Doctoral Dissertation
Doctoral Program in Materials Science and Technology (31th Cycle)

Design, synthesis and characterization of glass-ceramic and ceramic based materials for solid oxide electrolysis cell (SOEC) applications

By

Hassan Javed

* * * * * *

Supervisors
Prof. Federico Smeacetto
Dr. Christian Walter

Politecnico di Torino
2019

Declaration

I hereby declare that, the contents and organisation of this dissertation constitute my own original work and does not compromise in any way the rights of third parties, including those relating to the security of personal data.

…….....

Hassan Javed

Turin, 2019

This dissertation is presented in partial fulfillment of the requirements for **Ph.D. degree** in the Graduate School of Politecnico di Torino (ScuDo).

Summary

Efficient and durable electrochemical energy conversion solid oxide cell systems can be achieved only by a proper integration technology with a suitable joining and coating materials choice and processing. A crucial aspect in solid oxide electrolysis cell (SOEC) devices is given by the design of stable and reliable glass sealants and ceramic coatings, which must be used to join and coat dissimilar materials.

In SOEC planar configuration, the repeating units are combined together with the help of metallic interconnect. Sealants are also necessary in order to avoid the mixing and leakage of gases at both electrodes of cell. Glass-ceramic based sealants are the best choice thanks to the possibility of tuning their properties by adjusting their composition. For SOEC interconnects, the high Cr steels are most commonly used due to their remarkable properties in terms of high electrical conductivity and low cost. However, the Cr diffusion and evaporation from the interconnect cause poisoning of the other cell components.

This PhD research has been focused on two topics; i.e. design and synthesis of novel glass-ceramic based sealants and deposition of protective coatings on steel interconnect to avoid Cr diffusion. In this context different novel glass-ceramic sealants were designed and characterized to work in the real SOEC conditions and at the working temperature of 850 °C. The glass-ceramic sealants have been divided in to three series, depending either on the type of used modifiers or their respective concentration. The first and second series have SrO as main modifier, while the third series contains BaO. The crystallization and sintering behavior of glasses were analyzed by differential thermal analysis (DTA) and heating stage microscopy (HSM). The coefficient of thermal expansions (CTE) of as-casted glasses and respective glass-ceramics were measured by dilatometer. The compatibility of different glass-ceramics with the bare Crofer22APU interconnect and 3YSZ electrolyte was analyzed by scanning electron microscope (SEM) after

joining and thermal ageing (1000 hours, 850 °C). XRD analyses were carried out to investigate the crystalline phases in the as-joined and thermally aged glass-ceramics (1000 hours, 850 °C). In this thesis, the term as-joined glass-ceramic refers to the glass-ceramic after joining treatment and without any thermal ageing. The mechanical characterization of the glass-ceramics sandwiched between two Crofer22APU plates, was carried out at room temperature and 850°C. The electrical resistivity of the Crofer22APU/glass-ceramic/Crofer22APU joined samples was measured for 1000-3000 hours at 850 °C under the applied voltage of 1.7 V. In addition to static air, the electrical resistivity was also measured in dual atmosphere (simultaneously applied reducing and oxidizing) to simulate the working conditions of an SOEC. The SEM-EDS post mortem analyses were carried out to investigate the compatibility and any possible chemical interaction between glass-ceramics and the Crofer22APU. In order to deposit the glass at industrial scale, a new glass paste was formulated and deposited on the real dimensioned (16 cm x 18cm) Crofer22APU interconnects by a stencil printing technique.

$Mn_{1.5}Co_{1.5}O_4$ (MCO) spinel coating was deposited on the bare Crofer22APU substrate by electrophoretic deposition (EPD). The EDP process was also scaled up to coat the real dimensioned Crofer22APU plates. The morphology, uniformity and thickness of the as-deposited coatings on the flat and corrugated Crofer22APU substrates were analyzed by SEM. The area specific resistance (ASR) of MCO coated Crofer22APU was measured for 8600 hours at 850 °C, followed by the SEM-EDS post mortem analyses. CuO was also co-deposited with MCO by EPD process in order to investigate the properties of Cu-doped MCO. The morphology of the CuO doped MCO coating was studied by SEM and XRD after different sintering treatments. The effect of different concentrations of CuO doping on the densification, ASR and corrosion rate of MCO was also investigated for 2000 hours. Besides conventional sintering, flash sintering technique was also carried out to understand its effects on the densification of coatings.

This study shows that a suitable SrO/SiO_2 and BaO/SiO_2 ratio is very important to obtain the desired high CTE crystalline phases in SrO and BaO glass-ceramics respectively. Besides SrO/SiO_2 and BaO/SiO_2, a right balance of all constituents of a glass system, is also requited in order to avoid the formation of detrimental phases, such as Ba or Sr chromates. With a proper SrO/SiO_2 and BaO/SiO_2, the high CTE crystalline phases were formed in the 2^{nd} and 3^{rd} series glasses respectively. The newly designed glass-ceramic sealants showed excellent properties in terms of their sintering ability and thermo-mechanical compatibility.

The coefficient of thermal expansions (CTEs) of the as-joined and thermally aged glass-ceramics were closely matching with CTEs of other cell components. The long term testing showed that the Crofer22APU/glass-ceramic/Crofer22APU joined samples based on all glass systems, showed electrical resistivity higher than 10^4 Ω.cm, thus suitable for the SOEC applications to ensure electrical insulation. No evidence was found about the corrosion or chemical interaction between the glass-ceramic sealants and Crofer22APU interconnects after the long-term electrical resistivity test in dual atmosphere at 850 °C. Owing to these properties, these glass systems were found to be quite promising to be used as sealants in the SOEC conditions. The newly formulated glass paste also showed good rheological properties that make it suitable to deposit by stencil printing. However, some further modifications in the recipe of glass paste would be required for further optimization.

The EPD deposited $Mn_{1.5}Co_{1.5}O_4$ (MCO) spinel coating are quite uniform on the flat and corrugated Crofer22APU surfaces. The MCO coating has a thickness of ~ 10-15 µm after sintering. After suitable sintering treatment, MCO spinel showed low ASR (15-25 mΩ.cm^2) up to 5000 hours at 850 °C. The Cu doping was found to improve the sintering of the MCO spinel, however no significant effect of Cu doping on the ASR of MCO was noticeable. Moreover, the flash sintering was found to be a suitable technique to improve the densification of the coatings without formation of Cr oxide scale. No crack or delamination at the Crofer22APU/coating interface was observed as a result of the rapid heating/cooling carried out during the flash sintering.

The experiments reported in this PhD thesis were carried out in the framework of CoACH and GrInHy projects and under the co-supervision of Dr. Christian Walter (Sunfire GmbH, Dresden, Germany).

Acknowledgment

The project leading to this research has received funding from “The European Union’s Horizon 2020 research and innovation programme under the Marie Skłodowska-Curie grant agreement No 642557 (CoACH-ETN)”
and
“The Fuel Cells and Hydrogen 2 Joint Undertaking under grant agreement No 700300 (GrInHy Green Industrial Hydrogen via reversible high-temperature electrolysis)” and “European Union’s Horizon 2020 research and innovation programme and Hydrogen Europe and N.ERGHY”.

I would like to express my deepest gratitude to all the people who have helped me throughout my thesis, and more specifically to:

- Department of applied science and technology (DISAT), Politecnico di Torino, Italy; Sunfire GmbH, Dresden Germany; University of Erlangen, Germany; Institute of physics of materials (IPM), Brno, Czech republic; University of Padova, Italy and Nanoforce Ltd. UK for providing me the opportunity to work in their state of the art labs and for their collaborations during my entire PhD research period.
- Prof. Federico Smeacetto for his direct supervision of the research work, and for the great scientific freedom that I have enjoyed. It was indeed an honor to work with him. His guidelines would definitely be helpful in my entire career.
- Dr. Christian Walter for his expert opinions about the various aspects related to solid oxide electrolysis cells (SOECs) technology.
- Prof. Monica Ferraris and Prof. Milena Salvo for fascinating discussions and worthy advices related to the glass-ceramics.
- All my colleagues for their assistance during last three year.

- Finally, I would like to thanks my entire family back in Pakistan, my dearest wife and other friends for their kind support though out this journey. Without them, it would never been possible to achieve this milestone.

I would dedicate this thesis to my loving parents

Javed Iqbal

and

Azra Parveen

for their struggle, support and unconditional love throughout my life and educational carrier

"It is not defeat that destroys you, it is being demoralized by defeat that destroy you"

Imran Khan

Prime Minister of Pakistan

(2018-Present)

Introduction and Aim of Ph.D Thesis

Solid oxide electrolysis cell (SOEC) is a promising technology to convert electrical energy into chemical energy by high temperature electrolysis of steam. The high efficiency and almost no toxic by-products are the major benefits associated with an SOEC technology. The production of hydrogen in SOEC is fascinating, as hydrogen can be stored or transformed and subsequently used as an energy source.

Anyway, efficient and durable electrochemical energy conversion in solid oxide cell systems can be achieve only by a proper integration technology with a suitable joining and coating materials choice and processing. A crucial aspect in solid oxide electrolysis cell (SOEC) devices is given by the design of stable and reliable glass sealants and ceramic coatings, which must be used to join and coat dissimilar materials.

In order to achieve high efficiency, the single repeating units of an SOEC composed of a cell (cathode, anode, electrolyte), sealants and interconnect have to be joined to form a stack. The SOEC stack usually operates in the temperature range of 750-900 °C. The high working temperature usually results in the degradation of SOEC components. Furthermore, SOEC stack components should operate effectively for almost 40,000 hours in harsh operating conditions i.e. applied voltage, simultaneous oxidizing and reducing atmospheres, applied thermal cycles etc. which further restrict the selection of materials to be used in a SOEC device.

In SOEC, both the oxygen and fuel electrodes are separated by a solid ceramic electrolyte. In order to avoid the mixing and leakage of gases at each electrode, sealants are employed in planar SOEC stacks. The role of the sealant is crucial in order to assure high SOEC stack efficiency and durability. The sealants must show high gas tightness, thermo-chemical and thermo-mechanical compatibility with the adjacent materials, as well as stability in the relevant operating conditions for thousands of hours. Moreover, the sealants should also have high electrical resistivity in order to avoid any short circuit. Among various possibilities, the glass-ceramic based sealants are most attractive due to the possibility to tune their properties by modifying their compositions. Although the

glass-ceramics based sealants are chemically stable, electrically insulator and have high density, however due to variety of strict requirements, the synthesis of reliable glass-ceramic based sealants is not straight forward.

The first objective of this PhD research work is to synthesize new glass-ceramic based sealants for the SOEC applications having the working temperature of 850 °C. The novel glass-ceramic sealants are designed by using different modifiers in order to obtain the desired crystalline phases and coefficient of thermal expansion (CTE) suitable for the SOEC application. The thermo-mechanical and chemical compatibility of the novel glass-ceramic sealants with other cell components was investigated. The mechanical properties by means of shear strength evaluation of the glass-ceramic sealants were investigated at room temperature and at working temperature of 850 °C. The long term electrical properties of glass-ceramics were also investigated in simultaneously applied oxidizing and reducing atmospheres, and at 850 °C, in order to simulate the real working conditions of an SOEC stack. In order to deposit the glass at industrial scale, the new glass paste was formulated with the optimized rheological properties. The glass paste was deposited by the stencil printing technique.

In a SOEC stack the metallic interconnect provides electrical connection between adjacent repeating units and provide mechanical stability to the whole stack. High Cr steel interconnects are commonly used due their high electrical conductivity, low cost and CTE matching with other cell components. However, the high working temperature of an SOEC stack results in the evaporation of Cr from the steel interconnect. The Cr tends to poison other cell components and degrade their performances. The Cr also forms the Cr rich oxide scale at surface of interconnect, which is electrically insulating and consequently reduce the efficiency of the stack. The most promising solution to overcome this problem is the deposition of suitable coatings on the steel interconnect. The coating should have high electrical conductivity, CTE matching with the steel interconnect, be thermally and chemically stable in addition to hinder the Cr evaporation at high working temperature of an SOEC stack. Up to now, the manganese cobalt (MnCo) based coatings are considered to be the best option to work efficiently for SOEC applications.

The second objective of this PhD work is to deposit the MnCo spinel coating on the steel interconnect by electrophoretic deposition (EPD) technique. By keeping in review the industrial requirements, the EPD process was scaled up to coat the real dimensioned steel interconnects to be used in the SOEC stack. The effects of Cu doping and different sintering treatments (to improve densification) on the performance of MnCo coatings were also investigated.

The PhD thesis has been divided into six chapters. **Chapter 1** describes the literature background about the SOEC technology, the working principle, advantages and disadvantages, the different components of an SOEC in terms of their materials, fabrication methods and their purpose in stack. This chapter also briefly highlights the state of the art of different cell components. **Chapter 2** is dedicated to the state of the art of glass-ceramic sealants and MnCo based spinel protective coatings for interconnect. In detail, the chapter 2 describes the effect of different oxides on the chemical, thermal and thermo-mechanical properties of the glass-ceramics. The formulation of a suitable glass paste and stencil printing technique for the glass paste deposition are also discussed. This chapter also discusses the different coating materials used for the SOEC applications, different techniques to deposit coatings in addition to their pros and cons.

Chapter 3 deals with the experimental activities carried out in this PhD work. The methodology of glass synthesis, designing of different glass compositions, deposition of protective coatings on the steel interconnect and different characterization techniques used to analyze the properties of glass-ceramic based sealants and protective coatings are also discussed. **Chapter 4** and **chapter 5** discuss the results related to the glass-ceramic sealants and protective coatings respectively. In **chapter 4** the properties of the novel glass-ceramic sealants designed by using different modifiers are discussed. The thermal properties of the glasses are analyzed by differential thermal analysis (DTA) and heating stage microscopy (HSM), while the CTE analyses of glasses and glass-ceramics is carried out by dilatometer, The crystalline phases in glass-ceramics are analyzes performed by x-ray diffraction (XRD). Besides that, the chemical and thermo-mechanical compatibility of glass-ceramics with other cell components and long term electrical characterizations of the glass-ceramic sealants in dual atmosphere are also shown and discussed in detail.

Chapter 5 deals with the deposition of MnCo spinel coating by the EPD at lab scale as well as at industrial scale interconnects. The area specific resistance (ASR) of MnCo coating measured up to 8600 hours at 850 °C is presented. The effect of CuO doping on the morphology and electrical properties of the MnCo spinel are also reviewed and discussed. Finally, this chapter also discusses the effects of different sintering conditions carried out by conventional and flash sintering, on the morphology of un-doped MnCo, and MnCo spinel doped with CuO and Fe_2O_3.

In spite of a vast amount of research related to glass-based sealants and MnCo ceramic coatings for interconnects, it is still not possible to define “universal”

sealing or coating solutions. Both systems definitely depend on the SOEC working temperature and stack design.

The results obtained during this PhD research are very promising and effective in order to understand the long term performance of the glass-ceramic sealants and coatings in the SOEC operating conditions. These research findings will provide important insights for future sealing and coating development, their characterization and validation. This useful information will definitely contribute to the state of the art in these areas.

Contents

List of Tables

List of Figures

Chapter 1

Literature Survey

1.1 Solid oxide cells (SOC) - An overview

Natural and finite reservoirs such as coal and natural gas are the major energy sources[1]. However, the demand for energy is increasing at such a high rate that it would be difficult to maintain an energy balance in near future. In order to have a proper balance between energy demand and supply, it is required to develop some alternative energy sources. Solar cells, hydropowers and wind energies are considered the most promising sources to produce renewable energy. Besides possible energy crises in near future, the demand of energy also depends and varies by the climate change and from residential to industrial zone etc. therefore there should be some ways to store the excess of energy and use later when required. The renewable energy can be stored in different ways such as in batteries etc, but the batteries have limited lifetime and their efficiency can be reduced with time and therefore needs to be replaced [2].

High temperature solid oxide cells (SOC) have gained special attention as an alternative method to generate and store energy. SOC can work either in solid oxide fuel cell (SOFC) or in solid oxide electrolysis mode (SOEC), or as reversible solid oxide cell rSOC, where SOFC and SOEC modes operate alternatively [3–5]. Figure 1 describes the working principle of SOEC and SOFC modes in rSOC. The details about SOFC and SOEC are discussed below.

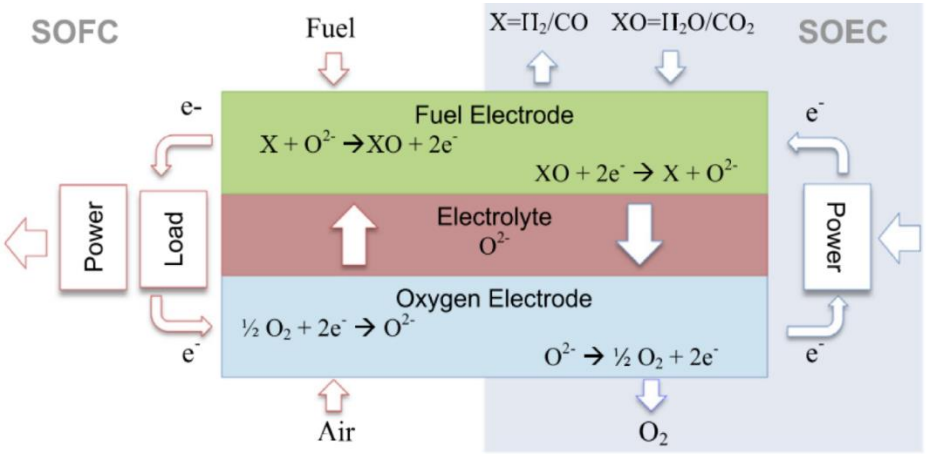

Figure 1. Working principle of reversible solid oxide cell. SOEC and SOFC mode [5]

1.1.1 Solid oxide fuel cell (SOFC)

Solid oxide fuel cell (SOFC) is a device that generates electrical energy by conversion of chemical energy such as different types of fuels. The working principle shown in Figure 1, indicates that the fuel is applied at the fuel electrode (anode) while oxygen is supplied at the air electrode (cathode). The oxygen ions are then migrate through the electrolyte causes oxidation of supplied fuel and consequently generate electricity. One of the major advantage associated with the SOFC technology is flexibility about the choice of the input fuel [6–8]. SOFC also has high efficiency and output due to its high working temperature typically 600-900°C. Figure 2 compares the efficiency of SOFC with other energy producing technologies, indicating that SOFC have higher efficiency and power output, thus making SOFC as most promising technology for energy generation.

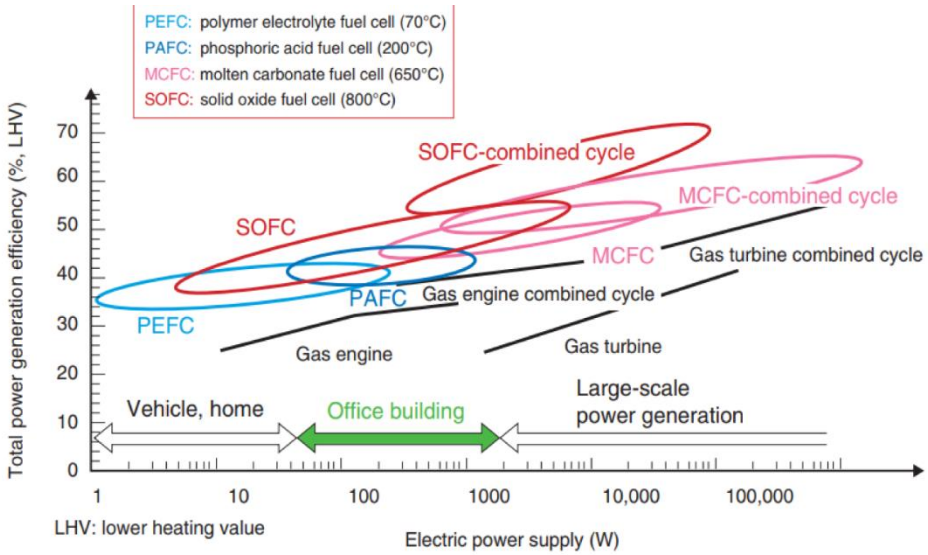

Figure 2. Efficiency comparison of SOFC with other energy sources [9,10]

1.1.2 Solid oxide electrolysis cell (SOEC)

Solid oxide electrolysis cell (SOEC) is a device that converts electrical energy obtained from different renewable energy sources (PV etc.) into chemical energy by direct high temperature electrolysis of water. It works on reverse principle as that of solid oxide fuel cells (SOFCs). By direct electrolysis of water in SOECs technology, pure hydrogen can be produce and subsequently can use as an energy source. In addition to that, a mixture of water and CO_2 can also be co-electrolyze to produce syngas (mixture of hydrogen and carbon monoxide) that can be utilized to synthesized a variety of hydrocarbons [11–15].

The production of hydrogen by the electrolysis of water is a well-known process initially demonstrated by Nicholson and Carlisle in 1800 and later by Faraday in 1820. In last century, the development of high temperature electrolyte ZrO_2 doped with Y_2O_3 laid the foundation of SOEC and SOFC technology. However, the first solid oxide electrolyze was made by Lurgi in 1951. Almost three decades ago, SOEC has gained attention as a promising technique to produce clean hydrogen at high efficiency; thanks to the work done by Donitz and co-workers [3,16,17]. Hydrogen energy produced by high temperature electrolysis of steam in SOEC, consumes less electrical energy due to generation of heat during the SOEC operation, thus make it more energy efficient [18].

The high energy efficiency, low emission of hazard by-products are the factors that shifted the research trend towards the rSOC. A lot of research has already been carried out in SOFC area as shown in Figure 3, however still the studies in the field of SOEC are limited. Nevertheless, the research for SOEC is also increasing gradually every year, indicating the importance of this field.

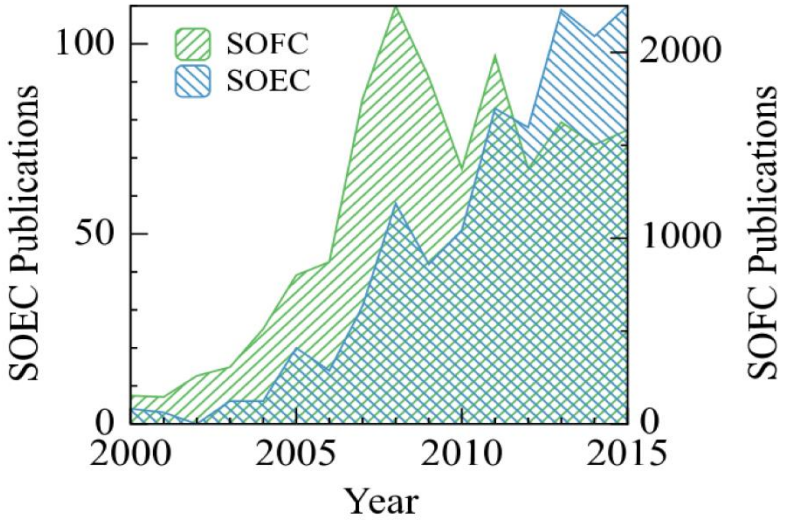

Figure 3. Number of publication made in recent year for SOFC and SOEC applications [5]

1.2 Solid oxide cell components

A single unit of solid oxide electrolysis cell is composed of two electrodes (cathode and anode) separated by a ceramic electrolyte. Fuel as steam is introduce at the fuel electrode while oxygen gas is produced at air electrode. In order to avoid any gas leakage and to prevent the mixing of gases at either electrode, sealants are employed in each unit cell. Besides that, in order to increase the power output, an SOEC stack is developed by repeating the different unit cells with the help of interconnects. The information about the function and materials selection for each component will be discussed in detail in next sections of this chapter.

The different reactions take place at both electrodes in SOEC conditions are:

At cathode: $H_2O + 4e \longrightarrow H_2 + 2O^{-2}$

At Anode: $2O^{-2} \longrightarrow O_2 + 4e$

Overall: $H_2O \longrightarrow H_2 + 1/2\ O_2$

In addition to hydrogen and oxygen, a significant amount of heat is also generated as a by-product. This heat is being recovered by heat exchangers and utilized by the SOEC system in order to preheat the feed water to the desired working temperature of SOEC [19]. Further details, functions and status of current research and development about each component of SOEC stack are provided below.

1.2.1 Cathode

Cathode is a negative charge electrode which causes the reduction of feed steam in SOEC conditions. The cathode in SOEC is commonly referred as fuel electrode. The selection of cathode material for SOEC application is quite challenging due to having higher partial pressure of steam. The cathode for SOEC should be porous in order to provide the active sites to facilitate the reduction of steam. It should have coefficient of thermal expansion (CTE) matching with other cell components, thermally stable at high working temperature and electrically conductive. Plenty of research has been carried out in past in order to investigate the performance and durability of various materials for SOEC cathode. In past the noble metals have been used as cathode for SOECs, but they are not first choice due to their high cost and formation of volatile species at high temperature. Nickel and yttrium stabilized zirconia (Ni-YSZ) based composites (often known as Ni-YSZ cermet) are considered to be the best choice due to having high electrical conductivity, sufficient catalytic activity and thermal stability [20]. However, in Ni-YSZ cermet it is difficult to increase the effective reaction zone due to having Ni and YSZ particles in micrometer range. As the performance of Ni-YSZ electrode mainly depends on the morphology, microstructure and distribution of Ni and YSZ grains, therefore recently research is being carried out to modify the microstructure of Ni-YSZ cermet in order to maximize the effective reaction zone [21,22]. Moreover, the oxidation of Ni into NiO can also reduce the performance of cathode. The performance of Ni-YSZ is more critical in SOEC conditions as

compared with SOFC. Figure 4 shows the comparison of potential losses as a function of current density, for cells operated in both SOEC and SOFC modes. The effect of different fuel compositions in terms to hydrogen/stream ratio in SOEC mode is also presented. In case of SOEC mode, higher cell resistance was measured as compared with the SOFC mode particularly at higher current density [23].

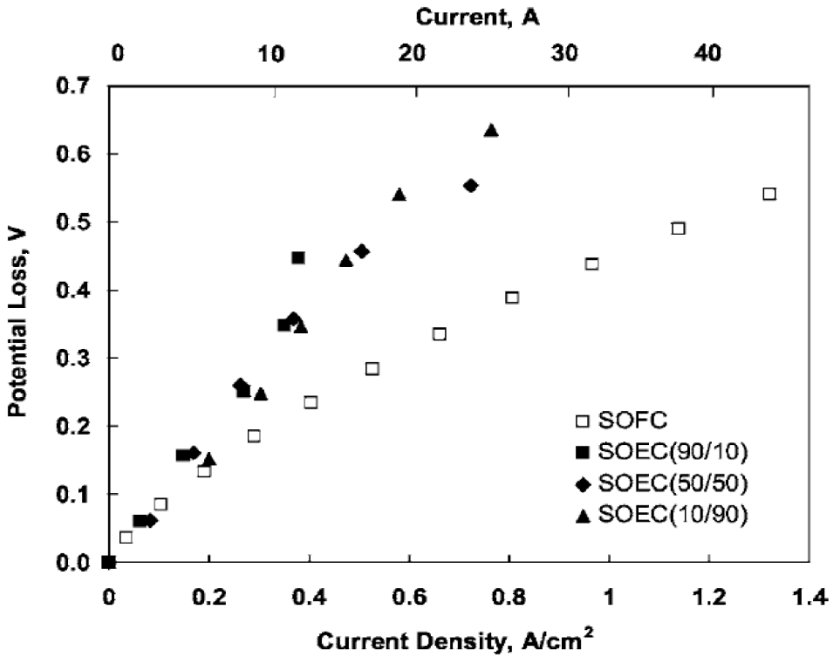

Figure 4. Potential losses vs current density for an Ni/YSZ-supported single cell operated in SOFC (open symbols) and SOEC (closed symbols), H_2/H2O = 90/10, 50/50, and 10/90 at 750°C [23]

Various methods have been reported in literature to produce the Ni-YSZ base cermet. Direct sintering of NiO and YSZ powders followed by reduction of NiO in hydrogen is commonly used method. Alternatively, ball milling, spray deposition and screen printing are also used for that purpose [22,24,25].

Currently Ni-YSZ cermet are most preferred and commonly used cathode for SOECs, nevertheless, the development of other materials as an alternative to Ni-YSZ cermet are also under research [23,26–28].

1.2.2 Anode

Anode in SOEC is an oxygen generating electrode, commonly referred as air electrode. Like SOEC cathode, the anode should also fulfill various requirements, such as; it should be thermally stable at high working temperature (700-850°C). The coefficient of thermal expansion should closely match with other components. Moreover, it should be chemically stable with low degradation rate in oxygen rich environment.

To be stable in oxidizing atmosphere, the use of noble metal as SOEC anode could be an option. However, their high cost limits their usage. The mixed oxides are considered to be the most promising anode materials in an SOEC technology.

These oxides have perovskite structure with high electronic conductivity and low production cost. So far, lanthanum strontium manganate $La_{1-x}Sr_xMnO_{3-\delta}$ (LSM) based perovskites are most commonly used materials for SOEC anode [5,18,20,29–37]. Figure 5 compares the area specific resistance (ASR) for different oxygen electrodes, indicating the LSM based perovskite have significantly higher conductivity.

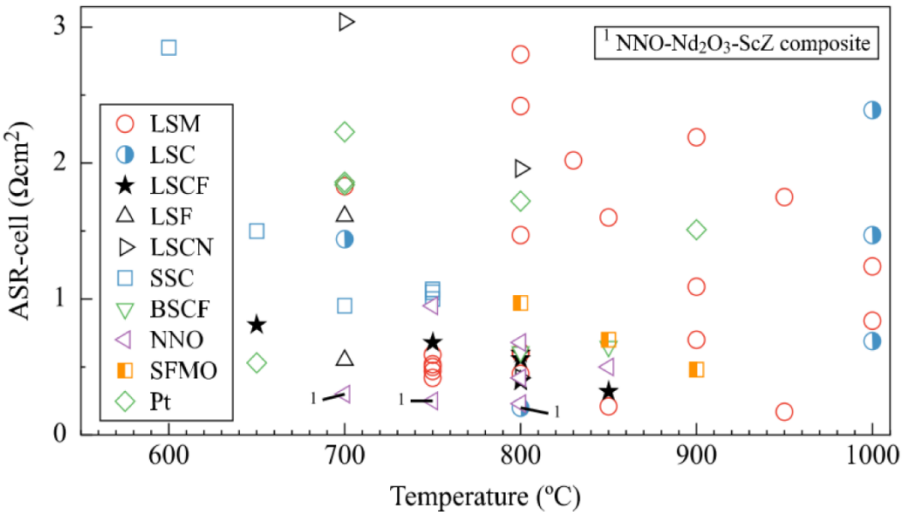

Figure 5. Area specific resistance vs. Temperature for different oxygen electrode materials in SOEC technology [5]

Besides the fact that LSM is the most common used material as an SOEC anode, it has certain limitations as well. Some undesirable reactions between LSM and other cell components are also frequently reported in literature. For instance, MnO_x may diffuse from LSM anode and poison neighboring cell components. It results in the formation of new phases with significantly lower conductivity, therefore the efficiency of cell reduces. Moreover, in LSM the only possible zone for reaction to occur is at triple phase boundary (TPB) between electrode and electrolyte. This significantly reduces the electronic conductivity and performance of the cell. The addition of ion conducting secondary phases is found to be a viable method to increase the reaction zone in LSM based materials. The addition of Co and Fe in LSM improved the oxygen reduction and electronic conductivity due to mixed ionic conductivity. A mixed conducting oxygen electrode $La_{1-x}Sr_xCo_{1-y}Fe_yO_{3-\delta}$ (LSCF) has been found to have high electro-catalytic activity, performance and stability as compared with LSM electrode [33,38–41].

Various methods such as dip coating, spray pyrolysis, sol gel, screen printing etc. are used to manufacture various oxygen electrodes [42–44]. The different manufacturing techniques have been summarized in Figure 6.

Oxygen electrode processing.

Material	Precursors	Powder synthesis	Processing	Thick (μm)	T (°C)
LSM	Acetates mixture	Calcination (900 °C)	Dip coating	–	1200
LSC	Acetates mixture	Calcination (900 °C)	Dip coating	–	1200
LCM	–	Spray pyrolysis (1200 °C)	Screen-printing	–	1300
LSF-YSZ	Nitrate salts	–	Dip coating	300	1250
LSC-YSZ	Nitrate salts	–	Dip coating	300	1250
LSM-YSZ	Nitrate salts	–	Dip coating	300	1250
LSM-YSZ	50LSM:50YSZ	Ball milling	Spray-painting	10	–
LSF-YSZ	Nitrate salts	Calcination (900 °C)	Dip coating (suspension 40 wt%)	300	900
Co/CeO_2	Nitrates-Oxides	Calcination	Dip coating (suspension 40 wt%)	15	–
BSCF-SDC	Acid-Nitrates	Calcination	–	–	1000
LSM/YSZ	–	Ball milling (2 h, 5 wt% ethyl-cellulose 95 wt% terpineol)	Screen-printing	50	1180
LSCF	–	–	Plasma Spraying	30	–
$Nd_2NiO_{4-\delta}$	Nd, Ni oxides in nitric acid	Annealing (1000 °C, 12 h)	Screen-printing	30	1100
SSC/BCZY	70SSC:30BCZY	Ball milling (in ethocel and abietyl alcohol)	Screen-printing	40	1100 (2 h)
SFMO	–	–	Screen-printing (binder as pore former)	70	1150 (5 h)
BSCF	Acid–Nitrates	Calcination	Screen-printing	30	1000 (1 h)
LSC	Nitrates	Spray pyrolysis	Screen-printing	36	1000 (1 h)
LSCF/GDC	–	–	Dip coating	30	–
LSCN	Oxides	Calcination (1100 °C, 18 h)	Screen-printing	10	1000 (2 h)

Figure 6. Processing of different oxygen electrodes in SOEC technology

For high performance in terms of catalytic activity, the anode should be porous to have sufficient surface area. In order to enhance the porosity and effective surface area, different types of additives are used. Carbon black and graphite can be used in this regard. The Figure 7 shows that with increasing concentration of graphite the porosity also increases. However, the effect of graphite to generate porosity varies from one material to other [44,45]

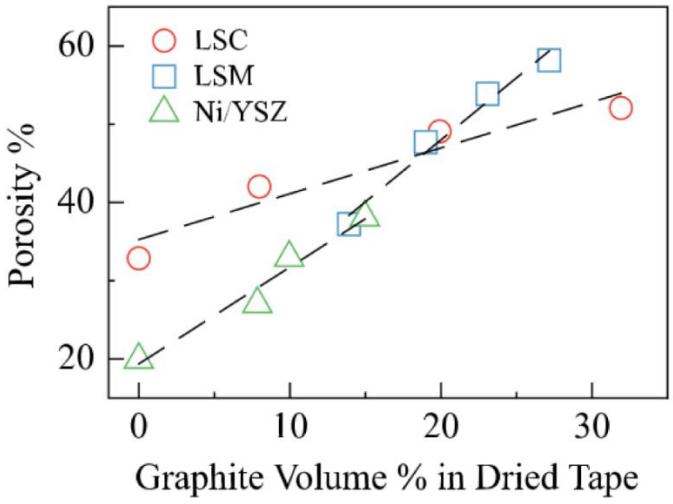

Figure 7. Effect of graphite concentration on porosity of different oxygen electrodes [5]

Besides LSM and LSCF based materials, recently few alternative materials such as $La_2NiO_{4+\delta}$ and $Nd_2NiO_{4+\delta}$ have also been studied and found to be promising for SOEC anode application [37,46–48]. However, the detailed studies on these new proposed materials in real SOEC conditions are still insufficient.

1.2.3 Electrolyte

An electrolyte is a key component of an SOEC cell that connects the cathode to the anode. For SOEC applications, the electrolyte should have higher ionic conductivity to facilitate the movement of oxygen ions from cathode to anode,

while no electric conductivity. It should be dense to avoid the recombination of gases produce at each electrode. It should also be thermally, chemically and mechanically stable at high working temperature and pressure.

Different materials such as Bi_2O_3, LaSrGaMg base perovskites, doped CeO_2 based oxides; $La_2Mo_2O_9$ etc. are reported in literature as suitable candidates for electrolyte in SOEC technology. However, their chemical stability at high working temperature limits their usage. Recently, $La_xNb_xW_xO_x$ has been also proposed as a novel electrolyte material for SOEC technology due to its chemical stability at high temperature. However, up to now the doped zirconia base ceramics (such as scandia stabilized zirconia, yttria stabilized zirconia, ZrO_2-Ln_2O_3) are considered as the most promising candidates for the electrolyte due to numerous advantages. Scandia stabilized zirconia (ScSZ) has highest ionic conductivity as compared with other zirconia stabilized electrolytes, however it has high cost that limits its uses [32,33,49–52]. Nevertheless, yttria stabilized zirconia (YSZ) is quite economical and therefore, frequently used in SOEC technology.

The conductivity of the ceramic electrolyte changes with temperature. Figure 8 compares the conductivity of three different electrolyte materials as a function of temperature. The ionic conductivity of doped ceria based oxides reduced above 600°C making them unsuitable for high temperature SOEC applications. Although LaSrGaMg base perovskites shows higher ionic conductivity as compared with YSZ, however their chemical reactivity with cathode is a huge problem in addition to the higher cost of Ga based oxide materials.

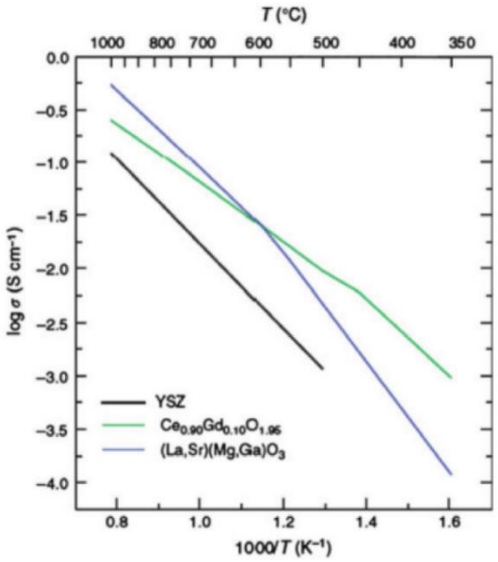

Figure 8. Electrical conductivity of different SOEC electrolyte materials as a function of temperature [53]

The YSZ electrolyte showed significant conductivity in addition to thermal, chemical and mechanical stability at high temperature in a wide range of oxygen partial pressures. A lot of research has already been carried out to study the

properties of YSZ using different amounts of yttria (3-8 mol%). Figure 9 shows the ionic conductivity of YSZ composite, as a function of different concentration of yttria (Y_2O_3). The ionic conductivity increased significantly by increasing the concentration of Y_2O_3 from 2 mol% to 3 mol% followed by slight decrease. Beyond 3 mol%, the reduction in ionic conductivity is due to phase transformation from tetragonal (with high specific conductive) to cubic (with low specific conductivity) [50].

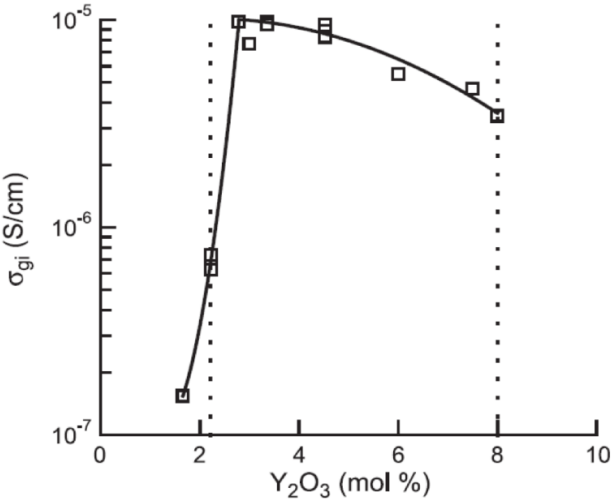

Figure 9. Ionic conductivity of yttria stabilized zirconia (YSZ), measured as a function of different yttria concentrationat 300°C [50]

Beside the materials selection, the thickness of electrolyte is also an important parameter to improving the efficiency of SOEC, as it directly affects the ohmic resistance. The ohmic resistance increases with thickness of electrolyte. Therefore, to achieve sufficient power density it is desirable to reduce the thickness of electrolyte while maintaining its mechanical integrity [52].

Yttria stabilized zirconia electrolyte can be fabricated by various methods. According to the literature, chemical vapor deposition, physical vapor deposition, spin coating, pulse layer deposition, electrophoretic deposition, atomic layer deposition, screen printing, tape casting, sol gel etc. are being used to prepare YSZ electrolyte of various thicknesses [34,52,54–58].

1.2.4 Sealants

In addition to the basic unit cell that composed of cathode, anode and electrolyte, another key component used in SOEC repeating unit is sealant. Sealants are used in planer SOEC along the edges of repeating unit cells. In order to achieve maximum efficiency of SOEC, it is very crucial to avoid the mixing of gases which are being generated at both electrodes. Sealants are used with a purpose to avoid mixing of these gases in addition to control any gas leakage. To satisfy these requirements, the sealants should be significantly dense with minimum porosity. They should have coefficient of thermal expansion matching

with other cell component and strongly bonded with them. The thermal, chemical and mechanical stability of sealants at high working temperature and in oxidizing and reducing environments is also very critical. Moreover, to be a successful sealant, they should have high electrical resistivity to avoid any short circuit during operation.

Table 1 summarizes the properties required by a sealant to work efficiently in the SOEC conditions [59].

Table 1. Properties required for sealants used in SOEC [15,59,60]

Thermal properties	Thermal expansion coefficient matching with other cell components Thermally stable for >30,000 hours at working temperature of 700-850°C
Chemical properties	Resistant to vaporization, chemical reaction and compositional change in oxidizing and reducing atmospheres at 700-850°C
Mechanical properties	Withstand external static and dynamic forces during transportation and operation Resistant to thermal cycling failure during start-up and shut-down of cell stacks
Electrical properties	Electrical resistivity $>10^4$ ohm.cm at operating temperature
Sealing ability	Withstand differential pressure up to 14–35 kPa across a cell or stack Total fuel leakage <1% for the duration of the cell life
Manufacturing flexibility	Flexible design, low processing cost, and high reliability

The sealants used in SOEC can be divided into three main categories namely: compressive sealants, compliant sealants and rigid sealants. All of these sealants have certain advantages and drawbacks, which are highlighted below.

Compressive sealants

Compressive sealants are usually made of deformable materials that can deform under the applied compressive stress. These sealants are not bonded with other cell components therefore the issues that can arise due to CTE mismatch are not relevant in this case. They also have high stability under thermal cycling. Typical examples of such sealants are mica-based hybrid seals, alumina-based hybrid seals and ceramic hybrid-based seals. Figure 10 (a) shows a typical compressive sealant where mica is used to join metal with ceramic-base electrolyte. A major disadvantage of these types of sealants is the leakage that can take place at interface of mica with metal or ceramic. One approach to overcome

this problem is to use compliant layer of metal or glass between mica and other joining components as shown in Figure 10 (b), but it is also not as effective. Moreover, an external compressive load is required in order to achieve gas tightness which increase their cost, reduce stability and make them unsuitable especially for the mobile applications.

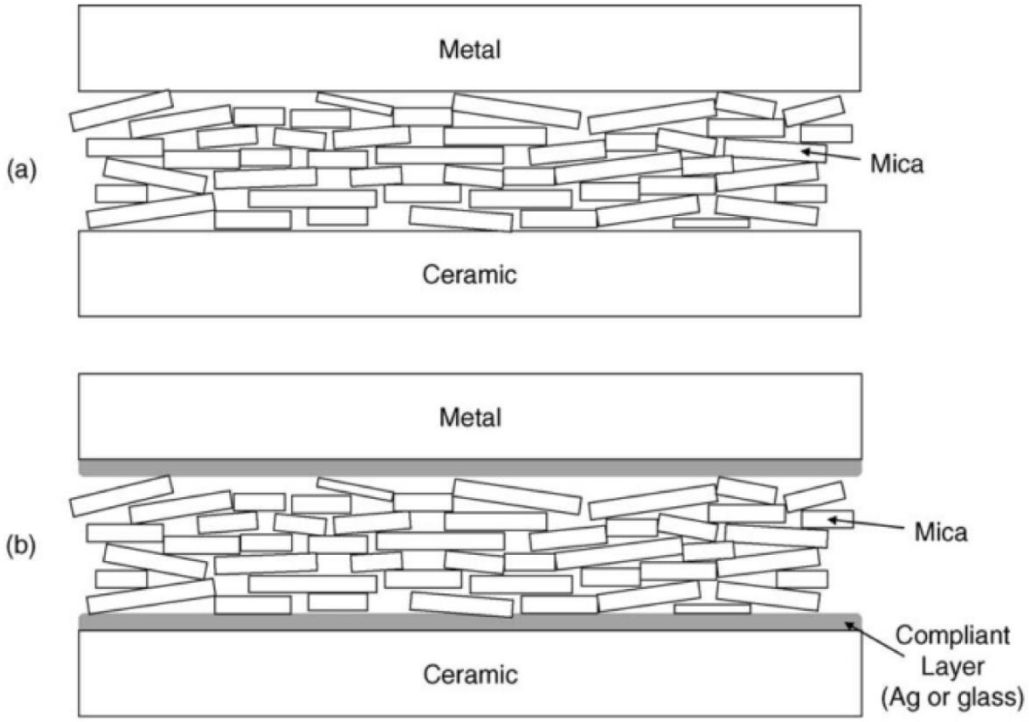

Figure 10. (a) Plane mica seal between metallic interconnect and ceramic electrolyte (b) addition of a compliant layer of glass or metal to improve gas tightening [59]

Compliant sealants

Compliant sealants are usually made of different metals and metal brazes. They can plastically deform and can accommodate the thermal stresses due to CTE mismatch. They are also quite dense and gas-tight. In order to avoid the problems of oxidation or hydrogen embrittlement in metal brazes, the different type of noble metals such as gold, silver platinum etc. can also use, thanks to their ductile behavior and corrosion resistance. However, these materials are very expansive. Another major drawback is that they have significantly high conductivity that make them non suitable for SOEC applications [59].

Composite sealants composed of metal matrix and ceramic reinforced are also used and their CTE can be tune according to requirements. For example, Ag reinforced Al_2TiO_5 composite is one of such kind. Figure 11 shows that increasing the concentration Al_2TiO_5 reinforcement from 0-20 wt% in Ag- Al_2TiO_5 composite, reduced the CTE from $22x10^{-6}$ K^{-1} to $12x10^{-6}$ K^{-1}, which is suitable for SOEC applications. However, at high working temperature the diffusion of Ag into porous neighboring components can cause contamination [61].

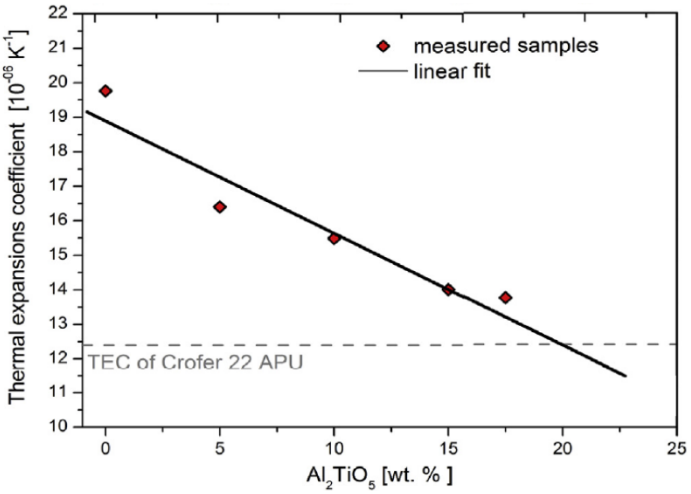

Figure 11. CTE of Ag-Al_2TiO_5 composite, as a function of Al_2TiO_5 concentration for SOC sealant [61]

Rigid sealants

Rigid sealants are usually glass and glass-ceramic base sealants and are hemetic seals due to joining with other neighboring components. They are more commonly used than compressive or compliant sealants due to flexibility in their composition and therefore their properties can be tailor easily. They become soft above their glass transition temperature and bond to other components due to their wettability. They have high electrical resistivity, low production cost and suitable for both stationary and mobile applications. Nevertheless, their chemical stability at high temperature can be critical issue and affect the life time of SOEC. The chemical stability of glass-ceramic sealant mainly depends in particular composition, therefore a lot of research is going on to improve the chemical stability of glass-ceramic sealants [59,62–66]. Many glass-ceramic compositions have been studied so far, and their details will discuss in chapter 2 (section 2.1)

Figure 12 summarizes the advantages and disadvantages of different types of sealants used for SOEC applications.

Advantages and disadvantages of different types of seals [12–15].

Seal type	Advantages	Disadvantages
Compressive seal	Easy replacement of seals in a malfunctioning cell stack Resistance to thermal cycling	Application of external load Complex design and high cost High gas leakage rate Unsuitable for mobile applications Poor stability Electrically conductive
Compliant seal	Low thermal stress	Non-wetting to other SOFC/SOEC components Poor oxidation resistance Hydrogen embrittlement Electrically conductive
Rigidly bonded seal	Hermetic sealing Tailorable performance by composition design High electrical resistivity Suitable for stationary and mobile applications Flexible in design and fabrication	Brittle at low temperatures Poor resistance to thermal cycling Chemical reaction with other cell components

Figure 12. Advantage and disadvantage of different types of sealants [15]

1.2.5 Interconnect

The single SOEC unit cell is not sufficient to generate sufficient output, therefore, at commercial scale many repeating unit are combine together to form an SOEC stack. The different repeating units in a stack are combine with each other by interconnects. Interconnects provide electrical connection between two adjacent unit cells and avoid the mixing of different gases at both electrodes. As interconnect separates cathode of one cell from anode of neighbor cell, therefore it protects fuel electrode (cathode) from being oxidize and oxygen electrode (anode) from reducing atmospheres. Besides that, interconnects also improve the mechanical integrity of overall stack.

In general, the interconnect for SOEC should be thermally and mechanically stable at working temperature of SOEC, typically in the range of 700-1000°C. It should have coefficient of thermal expansion matching with other cell components in addition to having high electrical conductivity. In SOEC stack, the interconnect can be in direct contact with H_2, O_2, CO_2 and CO, therefore it should be chemically stable in oxidizing and reducing atmospheres at high temperature. It should also be gas tight and economical [35].

Table 2 compares the properties of different interconnect materials used in SOEC technology. Among various options, the ferritic steels are considered to be the best choice. They have significant mechanical stability at high temperature, low production cost and coefficient of thermal expansion matching with other cell components. These ferritic steels have high chromium content (up 25%) which makes them highly conductive. Among ferritic stainless steels; the Crofer22APU, Crofer22H, Sanergy HT and 441 stainless steel are most widely studied and used as interconnect materials [67–70]. The chemical compositions for most commonly used ferritic steels (Crofer22APU and Crofer22H) are also shown in Table 3.

Table 2. Comparison of properties of different potential metallic interconnects used for SOECs/SOFCs [69]

Potential candidates	Oxidation resistance	Electrical conductivity	Manufacturability	Thermal expansion coefficient (RT-800°C)	Cost
Cr-based alloys	Good	Good	Difficult	11 - 12 $x10^{-6}$ K^{-1}	Very expensive
Fe stainless steel	Good	Good	Readily	11.5 - 14 $x10^{-6}$ K^{-1}	Inexpensive
Ni super alloys	Good	Good	Readily	14 -19 $x10^{-6}$ K^{-1}	Expensive

Table 3. Chemical composition (wt%) of Crofer22APU and Crofer22H steels [71,72]

		Cr	Fe	C	Mn	Si	Cu	Al	S	P	Ti	La			
Crofer22APU	**Max**	20.0	bal.		0.3						0.03	0.04			
	Min	24.0		0.03	0.8	0.5	0.5	0.5	0.02	0.05	0.2	0.2			
		Cr	Fe	C	Mn	Si	Cu	Al	S	P	Ti	La	Ni	W	Nb
Crofer22H	**Max**	20.0	bal.			0.1					0.02	0.02		1.0	0.2
	Min	24.0		0.03	0.8	0.6	0.5	0.1	0.006	0.05	0.2	0.2	0.5	3.0	1.0

The Figure 13 shows the electrical resistance of the Crofer22APU interconnect with other Cr containing alloys, measured at 800 °C in air. The Crofer22APU showed the lower order to resistance, which makes it one of the most suitable interconnect candidate in SOEC technology.

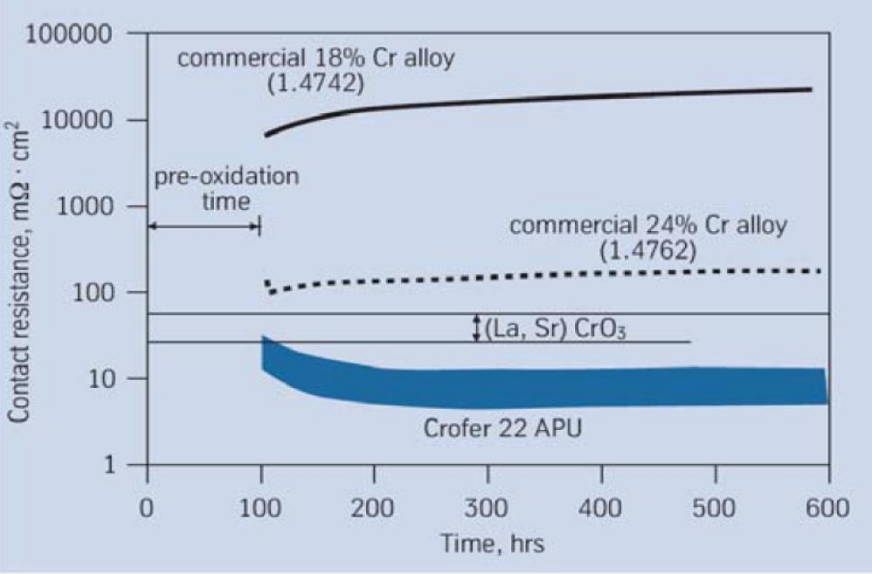

Figure 13. Comparison of contact resistance of Crofer22APU with other Cr-based alloys[71]

However, beside processing excellent mechanical, thermal and electrical properties the most common problem faced is the evaporation of Cr from interconnect at high temperature and consequent poisoning of neighbor cell components [73,74]. Cr evaporation also gradually degrades the properties of interconnect in terms of its electrical conductivity, especially in long term applications. The most prominent volatile species of Cr are CrO_3 and $CrO_2(OH)_2$.

Figure 14 shows the partial pressure of different species of Cr in air, as a function of temperature. The evaporation of all Cr species increases with increasing the temperature, therefore, in SOEC technology it increases the possibility of contaminating other cell components due to high working temperature of SOEC [74,75].

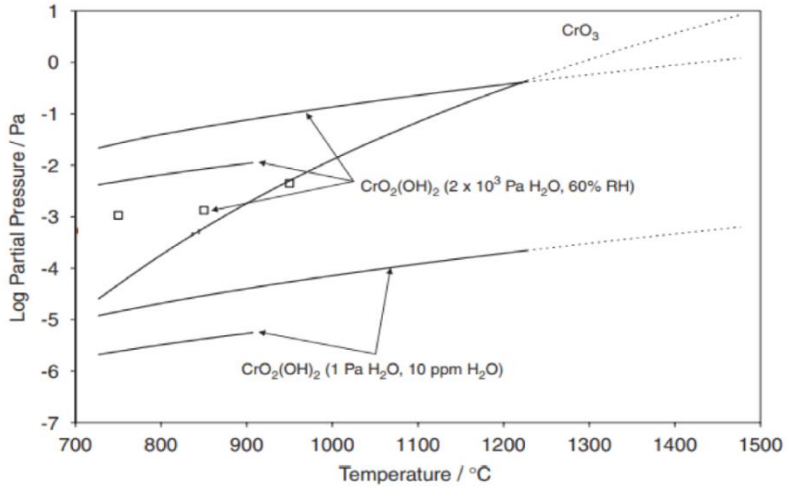

Figure 14. Partial pressure of different Cr species in air, as a function of temperature [74]

Different approaches have been used in order to overcome the issues related to Cr evaporation, either by modifying the steel interconnects composition or deposition of various coatings on these steel interconnects. For instance, 0.5 wt% of manganese in Crofer22APU and Crofer22H steel results in the formation of outer chromium manganese spinel that significantly reduces the evaporation of Cr from interconnect. Similarly different coatings are commonly deposited and found to be very beneficial in controlling Cr evaporation [69,73,76]. Further details about the different coating materials, deposition methods and their performance will be discussed in section 2.2.

1.2.6 Interaction of different stack components and cell degradation

Beside the properties and performance of the individual cell components, the interaction of each component with its neighboring components is very crucial to determine to overall efficiency and life time of an SOEC stack.

All materials must not be reactive with adjacent components at the SOEC operating temperature, and must have compatible thermal expansion coefficients.Significant mismatch of CTE can generate stress at interface during heating and cooling cycles, which can cause delamination and consequently can affect the efficiency of system. Table 4 shows the coefficient of thermal expansions of different stack components [77,78].

Table 4. Coefficient of thermal expansion (CTE) of different cell components of SOEC stack

Component	CTE (1 x 10^{-6}) K^{-1}	Reference
Ni-YSZ (Cathode)	12-12.5	[79]
LSM (anode)	10.5-11	[25]
YSZ (electrolyte)	10.5-10.8	[33]
Crofer22APU (interconnect)	10.3-12.7	[33,71]
Crofer22H (interconnect)	9.8-12.8	[72]
(Sanergy HT)	11-12	[80]

A strong bonding among different components does not grantee a completely efficient stack. Due to the high working temperature of an SOEC stack, the chemical stability of all components is also a key factor in this context. At high temperature the volatilization of different species from one of the cell component can deposit on another component within the stack. The diffusion of species into neighboring components in commonly observed problem particularly at high temperature. On the other hand, the microstructure of different cell components can also change over time. These issues can also significantly reduce the performance of cell components and affect the overall efficiency. A recent study was performed to analyze the microstructural and chemical changes that can occur in SOEC cell components during operation [13]. Figure 15 shows different cell components and their chemical interaction during operation, as investigated by SEM and EDS. At high working temperature, the presence of high vapor pressure of stream at cathode side resulted in the formation of $Si(OH)_4$ due to possible chemical reaction of steam with Si from glass sealants. On the other hand, at anode side, zirconia containing phases such a lanthanum zirconate (LZ) and manganese dioxide were formed at LSM-YSZ interface (Figure 15 c). These phase are undesirable due to various reasons. Firstly, they have low conductivity; secondly their CTEs are much lower than LSM anode and YSZ electrolyte. The Figure 15 (d) shows a crack/delamination at LSM-YSZ interface, which was formed due to CTE mismatch caused by the formation of low CTE phases [81,82].

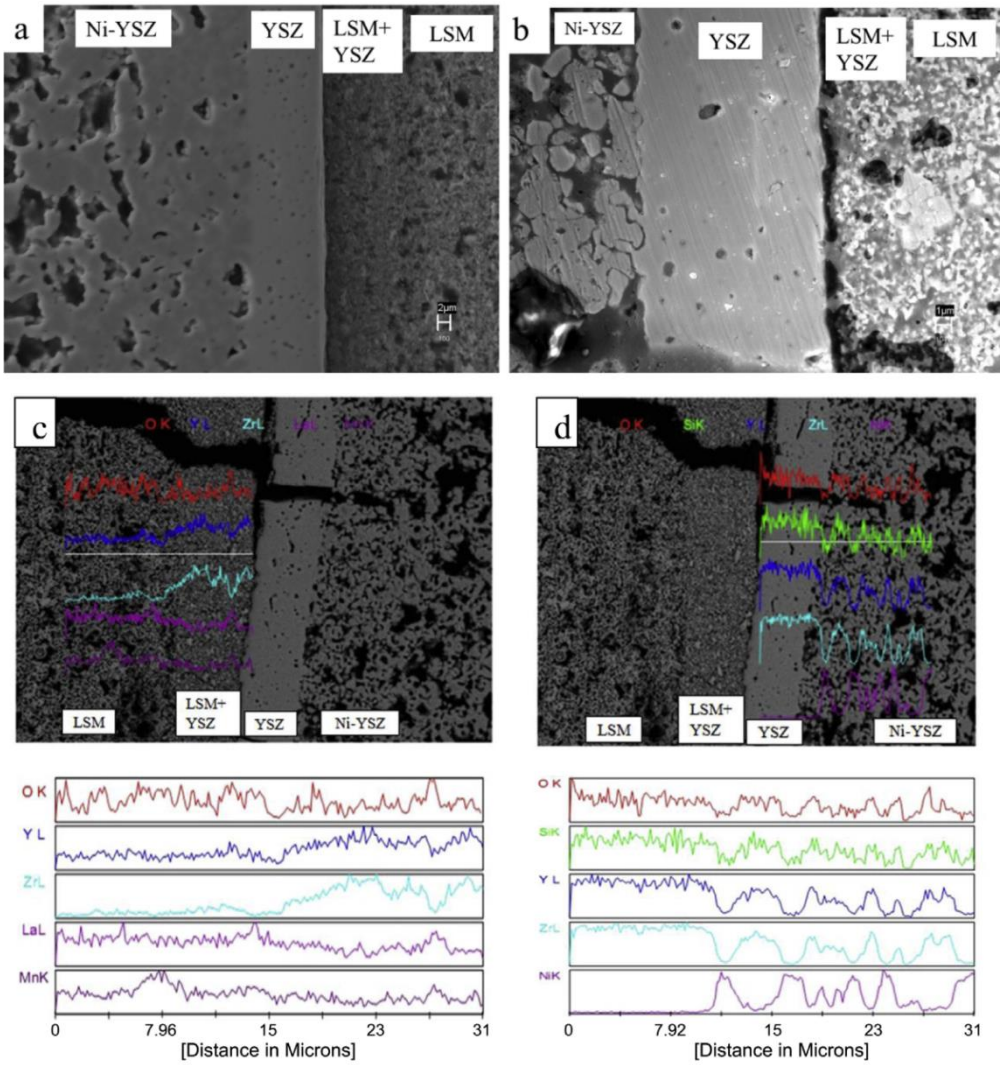

Figure 15. (a) FESEM micrograph of fresh sample, (b) FESEM micrograph of the delamination of anode layer from electrolyte. FESEM photograph and EDAX analysis of (c) anode and (d) cathode side respectively

The performance of cell also significantly affected due to volatile species from Cr-rich steel interconnects. At high temperature, chromium evaporation and consequently deposition on anode (LSM, LSCF) results in the formation of various secondary phases such as $LaCrO_3$, La_2CrO_6 etc. having higher electrical resistivity [83]. In addition to anode, the Cr also have detrimental effect on the glass-ceramic-based sealants. In SrO and BaO containing glasses, the formation of high CTE $SrCrO_4$ and $BaCrO_4$ phases are commonly reported in literature, that consequently lead to crack formation or delamination of sealant from the interconnect due to generation of thermal stresses [84–88].

The degradation of SOECs is another critical problem faced during operation of SOECs. The degradation problem is more severe in SOECs mode as compared with SOFCs mode due to harsh working conditions and high applied voltage. According to literature the lowest degradation rate for SOECs is 1.7%/1000h measured for up to for 3600 hours at working temperature of 850°C. However, the degradation rate tend to increase up to 3.8%/1000h when tested up to 9000 hours [89]. Other groups reported much higher degradation rates [90–92]. Moving from

single repeating cell to the SOEC stack, the degradation rate further increases due to the contaminations caused by interconnects and sealants. The degradation was found to increase the resistance of stack and cause significant current drop. The degradation mechanisms of different cell components have been discussed in detail in some recent articles [5,40,89,90,92]. However, still more research need to be carried out to understand the degradation mechanism in details.

References

[1] P. Lako, A. Kets, Resources and future availability of energy sources A quick scan, 2005.

[2] D. Honnery, P. Moriarty, Energy availability problems with rapid deployment of wind-hydrogen systems, International Journal of Hydrogen Energy. 36 (2011) 3283–3289. doi:10.1016/j.ijhydene.2010.12.023.

[3] DONITZ W, G. DIETRICH, E. ERDLE, R. STREICHER, ELECTROCHEMICAL HIGH TEMPERATURE TECHNOLOGY FOR HYDROGEN PRODUCTION OR DIRECT ELECTRICITY GENERATION, International Journal of Hydrogen Energy. 13 (1988) 283–287.

[4] S.D. Ebbesen, S.H. Jensen, A. Hauch, M.B. Mogensen, High Temperature Electrolysis in Alkaline Cells , Solid Proton Conducting Cells , and Solid Oxide Cells, Chemical Reviews. (2014) 10697−10734. doi:10.1021/cr5000865.

[5] S.Y. Gómez, D. Hotza, Current developments in reversible solid oxide fuel cells, Renewable and Sustainable Energy Reviews. 61 (2016) 155–174. doi:10.1016/j.rser.2016.03.005.

[6] R. Steinberger-Wilckens, Solid Oxide Fuel Cells, 2012. doi:10.1007/978-1-4471-2369-9_7.

[7] F. Ramadhani, M.A. Hussain, H. Mokhlis, S. Hajimolana, Optimization strategies for Solid Oxide Fuel Cell (SOFC) application: A literature survey, Renewable and Sustainable Energy Reviews. 76 (2017) 460–484. doi:10.1016/j.rser.2017.03.052.

[8] A. Choudhury, H. Chandra, A. Arora, Application of solid oxide fuel cell technology for power generation - A review, Renewable and Sustainable Energy Reviews. 20 (2013) 430–442. doi:10.1016/j.rser.2012.11.031.

[9] K. Hayashi, M. Yokoo, Y. Yoshida, H. Arai, Solid Oxide Fuel Cell Stack with High Electrical Efficiency, NTT Technical Review. 7 (2009).

[10] A. Nakajo, Thermomechanical and Electrochemical Degradation in Anode-Supported Solid Oxide Fuel Cell Stacks, EPFL, 2011.

[11] S.D. Ebbesen, M. Mogensen, Electrolysis of carbon dioxide in Solid Oxide Electrolysis Cells, 193 (2009) 349–358. doi:10.1016/j.jpowsour.2009.02.093.

[12] S. Fujiwara, S. Kasai, H. Yamauchi, K. Yamada, S. Makino, K. Matsunaga, M. Yoshino, T. Kameda, T. Ogawa, S. Momma, E. Hoashi, Hydrogen production by high temperature electrolysis with nuclear reactor, Progress in Nuclear Energy. 50 (2008) 422–426. doi:10.1016/j.pnucene.2007.11.025.

[13] A. Mahata, P. Datta, R.N. Basu, Microstructural and chemical changes after high temperature electrolysis in solid oxide electrolysis cell, Journal

of Alloys and Compounds. 627 (2015) 244–250. doi:10.1016/j.jallcom.2014.11.230.
[14] S.H. Jensen, C. Graves, M. Mogensen, C. Wendel, R. Braun, G. Hughes, Z. Gao, S.A. Barnett, Large-scale electricity storage utilizing reversible solid oxide cells combined with underground storage of CO_2 and CH_4, Energy Environ. Sci. 8 (2015) 2471–2479. doi:10.1039/C5EE01485A.
[15] M.K. Mahapatra, K. Lu, Glass-based seals for solid oxide fuel and electrolyzer cells - A review, Materials Science and Engineering R: Reports. 67 (2010) 65–85. doi:10.1016/j.mser.2009.12.002.
[16] W. Dönitz, E. Erdle, High-temperature electrolysis of water vapor-status of development and perspectives for application, International Journal of Hydrogen Energy. 10 (1985) 291–295. doi:10.1016/0360-3199(85)90181-8.
[17] W. Donitz, ECONOMICS AND POTENTIAL APPLICATION OF ELECTROLYTIC HYDROGEN IN THE NEXT DECADES, International Journal of Hydrogen Energy. 9 (1984) 817–821.
[18] A. Brisse, J. Schefold, M. Zahid, High temperature water electrolysis in solid oxide cells, International Journal of Hydrogen Energy. 33 (2008) 5375–5382. doi:10.1016/j.ijhydene.2008.07.120.
[19] N. M, L. MKH, L. DYC., Energy and exergy analysis of hydrogen production by solid oxide steam electrolyzer plant, International Journal of Hydrogen Energy. 32 (2007) 4648–4660.
[20] J.S. Herring, J.E. O'Brien, C.M. Stoots, G.L. Hawkes, J.J. Hartvigsen, M. Shahnam, Progress in high-temperature electrolysis for hydrogen production using planar SOFC technology, International Journal of Hydrogen Energy. 32 (2007) 440–450. doi:10.1016/j.ijhydene.2006.06.061.
[21] X.G. Cao, H.Y. Zhang, Development of Solid Oxide Electrolyzer Cell (SOEC) Cathode Materials, Advanced Materials Research. 476–478 (2012) 1802–1805. doi:10.4028/www.scientific.net/AMR.476-478.1802.
[22] H.S. Hong, U.S. Chae, S.T. Choo, K.S. Lee, Microstructure and electrical conductivity of Ni/YSZ and NiO/YSZ composites for high-temperature electrolysis prepared by mechanical alloying, Journal of Power Sources. 149 (2005) 84–89. doi:10.1016/j.jpowsour.2005.01.057.
[23] O.A. Marina, L.R. Pederson, M.C. Williams, G.W. Coffey, K.D. Meinhardt, C.D. Nguyen, E.C. Thomsen, Electrode Performance in Reversible Solid Oxide Fuel Cells, Journal of The Electrochemical Society. 154 (2007) B452. doi:10.1149/1.2710209.
[24] M. Liang, B. Yu, M. Wen, J. Chen, J. Xu, Y. Zhai, Preparation of NiO-YSZ composite powder by a combustion method and its application for cathode of SOEC, International Journal of Hydrogen Energy. 35 (2010) 2852–2857. doi:10.1016/j.ijhydene.2009.05.006.
[25] M. Ni, M.K.H. Leung, D.Y.C. Leung, Technological development of hydrogen production by solid oxide electrolyzer cell (SOEC), International Journal of Hydrogen Energy. 33 (2008) 2337–2354. doi:10.1016/j.ijhydene.2008.02.048.
[26] N. Osada, H. Uchida, M. Watanabe, Polarization Behavior of SDC Cathode with Highly Dispersed Ni Catalysts for Solid Oxide Electrolysis Cells, Journal of The Electrochemical Society. 153 (2006) A816. doi:10.1149/1.2177124.
[27] F.P.F.R.G. Ouweltjes, J P; van Tuel, M M A; van Berkel, Solid oxide electrolyzers for efficient hydrogen production, ECS Transactions. 7 (2007)

933–940.
[28] L. Zhang, Z. Wang, Z. Cao, L. Zhu, P. Li, J. Li, Z. Lü, High activity oxide Pr0.3Sr0.7Ti0.3Fe0.7O3−Δas cathode of SOEC for direct high-temperature steam electrolysis, International Journal of Hydrogen Energy. 42 (2017) 12104–12110. doi:10.1016/j.ijhydene.2017.03.043.
[29] P. Kazempoor, R.J. Braun, Hydrogen and synthetic fuel production using high temperature solid oxide electrolysis cells (SOECs), International Journal of Hydrogen Energy. 40 (2015) 3599–3612. doi:10.1016/j.ijhydene.2014.12.126.
[30] K. Chen, S.P. Jiang, Review — Materials Degradation of Solid Oxide Electrolysis Cells, Journal of The Electrochemical Society. 163 (2016) 3070–3083. doi:10.1149/2.0101611jes.
[31] M.A. Laguna-Bercero, Recent advances in high temperature electrolysis using solid oxide fuel cells: A review, Journal of Power Sources. 203 (2012) 4–16. doi:10.1016/j.jpowsour.2011.12.019.
[32] C. Tian, B. Ji, J. Xie, W. Bao, K. Liu, J. Cheng, Q. Yin, Preparation and characterization of Ce0.8La0.2-xYxO1.9as electrolyte for solid oxide fuel cells, Journal of Rare Earths. 32 (2014) 1162–1169. doi:10.1016/S1002-0721(14)60198-8.
[33] A.J. Jacobson, Materials for solid oxide fuel cells, Chemistry of Materials. 22 (2010) 660–674. doi:10.1021/cm902640j.
[34] W. Zhou, H. Shi, R. Ran, R. Cai, Z. Shao, W. Jin, Fabrication of an anode-supported yttria-stabilized zirconia thin film for solid-oxide fuel cells via wet powder spraying, Journal of Power Sources. 184 (2008) 229–237. doi:10.1016/j.jpowsour.2008.06.021.
[35] Y. Zheng, J. Wang, B. Yu, W. Zhang, J. Chen, J. Qiao, J. Zhang, A review of high temperature co-electrolysis of H2O and CO2 to produce sustainable fuels using solid oxide electrolysis cells (SOECs): advanced materials and technology, Chem. Soc. Rev. 46 (2017) 1427–1463. doi:10.1039/C6CS00403B.
[36] M. Palcut, L. Mikkelsen, K. Neufeld, M. Chen, R. Knibbe, P.V. Hendriksen, Improved oxidation resistance of ferritic steels with LSM coating for high temperature electrochemical applications, International Journal of Hydrogen Energy. 37 (2012) 8087–8094. doi:10.1016/j.ijhydene.2011.11.138.
[37] F. Chauveau, J. Mougin, F. Mauvy, J.M. Bassat, J.C. Grenier, Development and operation of alternative oxygen electrode materials for hydrogen production by high temperature steam electrolysis, International Journal of Hydrogen Energy. 36 (2011) 7785–7790. doi:10.1016/j.ijhydene.2011.01.048.
[38] M.J. López-Robledo, M.A. Laguna-Bercero, A. Larrea, V.M. Orera, Reversible operation of microtubular solid oxide cells using La0.6Sr0.4Co0.2Fe0.8O3-Δ-Ce0.9Gd0.1O2-Δoxygen electrodes, Journal of Power Sources. 378 (2018) 184–189. doi:10.1016/j.jpowsour.2017.12.035.
[39] Y. Takeda, Cathodic Polarization Phenomena of Perovskite Oxide Electrodes with Stabilized Zirconia, Journal of The Electrochemical Society. 134 (1987) 2656. doi:10.1149/1.2100267.
[40] X. Zhang, J.E. O'Brien, R.C. O'Brien, G.K. Housley, Durability evaluation of reversible solid oxide cells, Journal of Power Sources. 242 (2013) 566–574. doi:10.1016/j.jpowsour.2013.05.134.

[41] K.J. Lee, J.W. Seo, J.S. Yoon, H.J. Hwang, Electrode Performance in a Solid Oxide Electrolyzer Cell (SOEC), ECS Transactions. 57 (2013) 3255–3260. doi:10.1149/05701.3255ecst.
[42] J. Kong, Y. Zhang, C. Deng, J. Xu, Synthesis and electrochemical properties of LSM and LSF perovskites as anode materials for high temperature steam electrolysis, Journal of Power Sources. 186 (2009) 485–489. doi:10.1016/j.jpowsour.2008.10.053.
[43] J.C. Marrero, N.F.P. Ribeiro, C.F. Malfatti, M.M.V.M. Souza, Characterization of yttria-stabilized zirconia films deposited by dip-coating on La0.7Sr0.3MnO3 substrate: Influence of synthesis parameters, Journal of Advanced Ceramics. 2 (2013) 55–62. doi:10.1007/s40145-013-0042-4.
[44] A.K. Sahu, A. Ghosh, A.K. Suri, Characterization of porous lanthanum strontium manganite (LSM) and development of yttria stabilized zirconia (YSZ) coating, Ceramics International. 35 (2009) 2493–2497. doi:10.1016/j.ceramint.2008.11.012.
[45] M. Prestat, A. Morandi, A. Heel, L. Holzer, P. Holtappels, T.J. Graule, Effect of graphite pore former on oxygen electrodes prepared with La0.6Sr0.4CoO3-δnanoparticles, Electrochemistry Communications. 12 (2010) 292–295. doi:10.1016/j.elecom.2009.12.018.
[46] F. Chauveau, J. Mougin, J.M. Bassat, F. Mauvy, J.C. Grenier, A new anode material for solid oxide electrolyser: The neodymium nickelate Nd2NiO4+δ, Journal of Power Sources. 195 (2010) 744–749. doi:10.1016/j.jpowsour.2009.08.003.
[47] A. Egger, N. Schrödl, C. Gspan, W. Sitte, La2NiO4+δ as electrode material for solid oxide fuel cells and electrolyzer cells, Solid State Ionics. 299 (2017) 18–25. doi:10.1016/j.ssi.2016.10.002.
[48] A. Egger, N. Schrödl, W. Sitte, Evaluation of oxide ceramics as anodes for SOECs, Faraday Discuss. 182 (2015) 379–391. doi:10.1039/C5FD00021A.
[49] M.A. Laguna-Bercero, R.D. Bayliss, S.J. Skinner, LaNb0.84W0.16O4.08as a novel electrolyte for high temperature fuel cell and solid oxide electrolysis applications, Solid State Ionics. 262 (2014) 298–302. doi:10.1016/j.ssi.2013.11.039.
[50] M. Mogensen, D. Lybye, N. Bonanos, P. V. Hendriksen, F.W. Poulsen, Factors controlling the oxide ion conductivity of fluorite and perovskite structured oxides, Solid State Ionics. 174 (2004) 279–286. doi:10.1016/j.ssi.2004.07.036.
[51] I.R. De Larramendi, N. Ortiz-Vitoriano, I.B. Dzul-Bautista, T. Rojo, Designing Perovskite Oxides for Solid Oxide Fuel Cells, Perovskite Materials - Synthesis, Characterisation, Properties, and Applications. (2016). doi:10.5772/61304.
[52] H. Shi, R. Ran, Z. Shao, Wet powder spraying fabrication and performance optimization of IT-SOFCs with thin-film ScSZ electrolyte, International Journal of Hydrogen Energy. 37 (2012) 1125–1132. doi:10.1016/j.ijhydene.2011.02.077.
[53] B. Talic, PhD Thesis. Metallic Interconnects for Solid Oxide Fuel Cells: High Temperature Corrosion and Protective Spinel Coatings, 2016. https://brage.bibsys.no/xmlui/handle/11250/2404554.
[54] K. Chen, Y. Tian, Z. Lü, N. Ai, X. Huang, W. Su, Behavior of 3 mol% yttria-stabilized tetragonal zirconia polycrystal film prepared by slurry spin coating, Journal of Power Sources. 186 (2009) 128–132. doi:10.1016/j.jpowsour.2008.09.061.

[55] J.H. Shim, C.C. Chao, H. Huango, F.B. Prinz, Atomic layer deposition of yttria-stabilized zirconia for solid oxide fuel cells, Chemistry of Materials. 19 (2007) 3850–3854. doi:10.1021/cm070913t.
[56] E. Courtin, P. Boy, C. Rouhet, L. Bianchi, E. Bruneton, N. Poirot, C. Laberty-Robert, C. Sanchez, Optimized sol-gel routes to synthesize yttria-stabilized zirconia thin films as solid electrolytes for solid oxide fuel cells, Chemistry of Materials. 24 (2012) 4540–4548. doi:10.1021/cm302177s.
[57] H.J. Kim, M. Kim, K.C. Neoh, G.D. Han, K. Bae, J.M. Shin, G.T. Kim, J.H. Shim, Slurry spin coating of thin film yttria stabilized zirconia/gadolinia doped ceria bi-layer electrolytes for solid oxide fuel cells, Journal of Power Sources. 327 (2016) 401–407. doi:10.1016/j.jpowsour.2016.07.080.
[58] Y. Zou, W. Zhou, J. Sunarso, F. Liang, Z. Shao, Electrophoretic deposition of YSZ thin-film electrolyte for SOFCs utilizing electrostatic-steric stabilized suspensions obtained via high energy ball milling, International Journal of Hydrogen Energy. 36 (2011) 9195–9204. doi:10.1016/j.ijhydene.2011.04.187.
[59] J.W. Fergus, Sealants for solid oxide fuel cells, Journal of Power Sources. 147 (2005) 46–57. doi:10.1016/j.jpowsour.2005.05.002.
[60] H. Javed, A.G. Sabato, K. Herbrig, D. Ferrero, C. Walter, M. Salvo, F. Smeacetto, Design and characterization of novel glass-ceramic sealants for solid oxide electrolysis cell (SOEC) applications, International Journal of Applied Ceramic Technology. 15 (2018) 999–1010. doi:10.1111/ijac.12889.
[61] R. Kiebach, K. Engelbrecht, L. Grahl-Madsen, B. Sieborg, M. Chen, J. Hjelm, K. Norrman, C. Chatzichristodoulou, P.V. Hendriksen, An Ag based brazing system with a tunable thermal expansion for the use as sealant for solid oxide cells, Journal of Power Sources. 315 (2016) 339–350. doi:10.1016/j.jpowsour.2016.03.030.
[62] C.K. Lin, Y.A. Liu, S.H. Wu, C.K. Liu, R.Y. Lee, Joint strength of a solid oxide fuel cell glass-ceramic sealant with metallic interconnect in a reducing environment, Journal of Power Sources. 280 (2015) 272–288. doi:10.1016/j.jpowsour.2015.01.126.
[63] S.D. Kim, D.W. Seo, A.K. Dorai, S.K. Woo, The effect of gas compositions on the performance and durability of solid oxide electrolysis cells, International Journal of Hydrogen Energy. 38 (2013) 6569–6576. doi:10.1016/j.ijhydene.2013.03.115.
[64] Y. Ye, D. Yan, X. Wang, J. Pu, B. Chi, L. Jian, Development of novel glass-based composite seals for planar intermediate temperature solid oxide fuel cells, International Journal of Hydrogen Energy. 37 (2012) 1710–1716. doi:10.1016/j.ijhydene.2011.10.011.
[65] A. Rost, J. Schilm, M. Kusnezoff, A. Michaelis, Degradation of sealing glasses under electrical load, European Fuel Cell Forum. 80 (2010) 1–12. doi:10.4416/JCST2012-00002.
[66] M.K. Mahapatra, K. Lu, Effect of atmosphere on interconnect-seal glass interaction for solid oxide fuel/electrolyzer cells, Journal of the American Ceramic Society. 94 (2011) 875–885. doi:10.1111/j.1551-2916.2010.04020.x.
[67] J. Froitzheim, G.H. Meier, L. Niewolak, P.J. Ennis, H. Hattendorf, L. Singheiser, W.J. Quadakkers, Development of high strength ferritic steel for interconnect application in SOFCs, Journal of Power Sources. 178

(2008) 163–173. doi:10.1016/j.jpowsour.2007.12.028.
[68] W.J. Quadakkers, J. Piron-Abellan, V. Shemet, L. Singheiser, Metallic interconnectors for solid oxide fuel cells – a review, Materials at High Temperatures. 20 (2003) 115–127. doi:10.1179/mht.2003.015.
[69] J.C.W. Mah, A. Muchtar, M.R. Somalu, M.J. Ghazali, Metallic interconnects for solid oxide fuel cell: A review on protective coating and deposition techniques, International Journal of Hydrogen Energy. 42 (2017) 9219–9229. doi:10.1016/j.ijhydene.2016.03.195.
[70] J. Wu, X. Liu, Recent development of SOFC metallic interconnect, Journal of Materials Science and Technology. 26 (2010) 293–305. doi:10.1016/S1005-0302(10)60049-7.
[71] VDM ® Crofer 22 APU, (2010) 10. http://www.vdm-metals.com/fileadmin/user_upload/Downloads/Data_Sheets/Datenblatt_VDM_Crofer_22_APU.pdf.
[72] VDM ® Crofer 22 H, (2010) 1–11.
[73] J.G. Grolig, J. Froitzheim, J.E. Svensson, Coated stainless steel 441 as interconnect material for solid oxide fuel cells: Oxidation performance and chromium evaporation, Journal of Power Sources. 248 (2014) 1007–1013. doi:10.1016/j.jpowsour.2013.08.089.
[74] J.W. Fergus, Effect of cathode and electrolyte transport properties on chromium poisoning in solid oxide fuel cells, International Journal of Hydrogen Energy. 32 (2007) 3664–3671. doi:10.1016/j.ijhydene.2006.08.005.
[75] R. Sachitanand, M. Sattari, J.E. Svensson, J. Froitzheim, Evaluation of the oxidation and Cr evaporation properties of selected FeCr alloys used as SOFC interconnects, International Journal of Hydrogen Energy. 38 (2013) 15328–15334. doi:10.1016/j.ijhydene.2013.09.044.
[76] M. Stanislowski, J. Froitzheim, L. Niewolak, W.J. Quadakkers, K. Hilpert, T. Markus, L. Singheiser, Reduction of chromium vaporization from SOFC interconnectors by highly effective coatings, Journal of Power Sources. 164 (2007) 578–589. doi:10.1016/j.jpowsour.2006.08.013.
[77] M.K. Mahapatra, K. Lu, Seal glass for solid oxide fuel cells, Journal of Power Sources. 195 (2010) 7129–7139. doi:10.1016/j.jpowsour.2010.06.003.
[78] M. Kerstan, M. Mueller, C. Ruessel, Binary, ternary and quaternary silicates of CaO, BaO and ZnO in high thermal expansion seals for solid oxide fuel cells studied by high-temperature X-ray diffraction (HT-XRD), Materials Research Bulletin. 46 (2011) 2456–2463. doi:10.1016/j.materresbull.2011.08.031.
[79] S.T. Reis, M. Jérôme Schwartz, M. Zandi, Y. Narendar, SANBORNTE-BASED GLASS-CERAMIC SEAL FOR HIGH-TEMPERATURE APPLICATIONS, 2016.
[80] A.A. Reddy, A. Goel, D.U. Tulyaganov, M. Sardo, L. Mafra, M.J. Pascual, V. V. Kharton, E. V. Tsipis, V.A. Kolotygin, J.M.F. Ferreira, Thermal and mechanical stability of lanthanide-containing glass–ceramic sealants for solid oxide fuel cells, Journal of Materials Chemistry A. 2 (2014) 1834. doi:10.1039/c3ta13196c.
[81] J.A. Labrincha, J.R. Frade, F.M.B. Marques, La2Zr2O7 formed at ceramic electrode/YSZ contacts, Journal of Materials Science. 28 (1993) 3809–3815. doi:10.1007/BF00353183.
[82] A. Mitterdorfer, La2Zr2O7 formation and oxygen reduction kinetics of the

La0.85Sr0.15MnyO3, O2(g)|YSZ system, Solid State Ionics. 111 (1998) 185–218. doi:10.1016/S0167-2738(98)00195-7.

[83] B. Wei, K. Chen, L. Zhao, Z. Lü, S. Ping Jiang, Chromium deposition and poisoning at $La_{0.6}Sr_{0.4}Co_{0.2}Fe_{0.8}O_{3-\delta}$ oxygen electrodes of solid oxide electrolysis cells, Phys. Chem. Chem. Phys. 17 (2015) 1601–1609. doi:10.1039/C4CP05110F.

[84] Y.S. Chou, J.W. Stevenson, P. Singh, Effect of pre-oxidation and environmental aging on the seal strength of a novel high-temperature solid oxide fuel cell (SOFC) sealing glass with metallic interconnect, Journal of Power Sources. 184 (2008) 238–244. doi:10.1016/j.jpowsour.2008.06.020.

[85] B. Wei, K. Chen, C.C. Wang, Z. L??, S.P. Jiang, Cr deposition on porous La0.6Sr0.4Co0.2Fe0.8O3 - δ electrodes of solid oxide cells under open circuit condition, Solid State Ionics. 281 (2015) 29–37. doi:10.1016/j.ssi.2015.08.018.

[86] S.J. Kim, K.J. Kim, G.M. Choi, H. Khedim, H. Nonnet, F.O. Méar, L. Peng, Q. Zhu, A.A. Reddy, D.U. Tulyaganov, A. Goel, M.J. Pascual, V. V. Kharton, E. V. Tsipis, J.M.F. Ferreira, F. Smeacetto, M. Salvo, M. Santarelli, P. Leone, G.A. Ortigoza-Villalba, A. Lanzini, L.C. Ajitdoss, M. Ferraris, A. De Miranda, A. Chrysanthou, E. Bernardo, M. Secco, M. Bindi, M. Salvo, A.G. Sabato, M. Ferraris, X. Zhang, J.E. O'Brien, R.C. O'Brien, J.J. Hartvigsen, G. Tao, G.K. Housley, A novel solid oxide electrolysis cell (SOEC) to separate anodic from cathodic polarization under high electrolysis current, International Journal of Hydrogen Energy. 38 (2013) 20–28. doi:10.1111/jace.13219.

[87] M.J. Pascual, A. Guillet, A. Durán, Optimization of glass-ceramic sealant compositions in the system MgO-BaO-SiO2for solid oxide fuel cells (SOFC), Journal of Power Sources. 169 (2007) 40–46. doi:10.1016/j.jpowsour.2007.01.040.

[88] L. Peng, Q. Zhu, Thermal cycle stability of BaO-B2O3-SiO2 sealing glass, Journal of Power Sources. 194 (2009) 880–885. doi:10.1016/j.jpowsour.2009.06.018.

[89] J. Schefold, A. Brisse, F. Tietz, Nine Thousand Hours of Operation of a Solid Oxide Cell in Steam Electrolysis Mode, Journal of The Electrochemical Society. 159 (2012) A137. doi:10.1149/2.076202jes.

[90] A. Hauch, S.H. Jensen, S. Ramousse, M. Mogensen, Performance and Durability of Solid Oxide Electrolysis Cells, Journal of The Electrochemical Society. 153 (2006) A1741. doi:10.1149/1.2216562.

[91] J. Schefold, A. Brisse, H. Poepke, 23,000 h Steam Electrolysis With an Electrolyte Supported Solid Oxide Cell, International Journal of Hydrogen Energy. 42 (2017) 13415–13426. doi:10.1016/j.ijhydene.2017.01.072.

[92] P. Moçoteguy, A. Brisse, A review and comprehensive analysis of degradation mechanisms of solid oxide electrolysis cells, International Journal of Hydrogen Energy. 38 (2013) 15887–15902. doi:10.1016/j.ijhydene.2013.09.045.

Chapter 2

State of Art

2.1 Glass-ceramic sealants

The seal between the stainless steel interconnect and the ceramic SOEC components present significant challenges. Different areas are of interest by the presence of the seals in a solid oxide cell stack. As shown in Figure 16, there is an evidence that the sealant plays a key role for a successful integration between the cell to the metal frame, metal frame to the metal interconnect and the interconnect to spacer (for the electric insulation) [1].

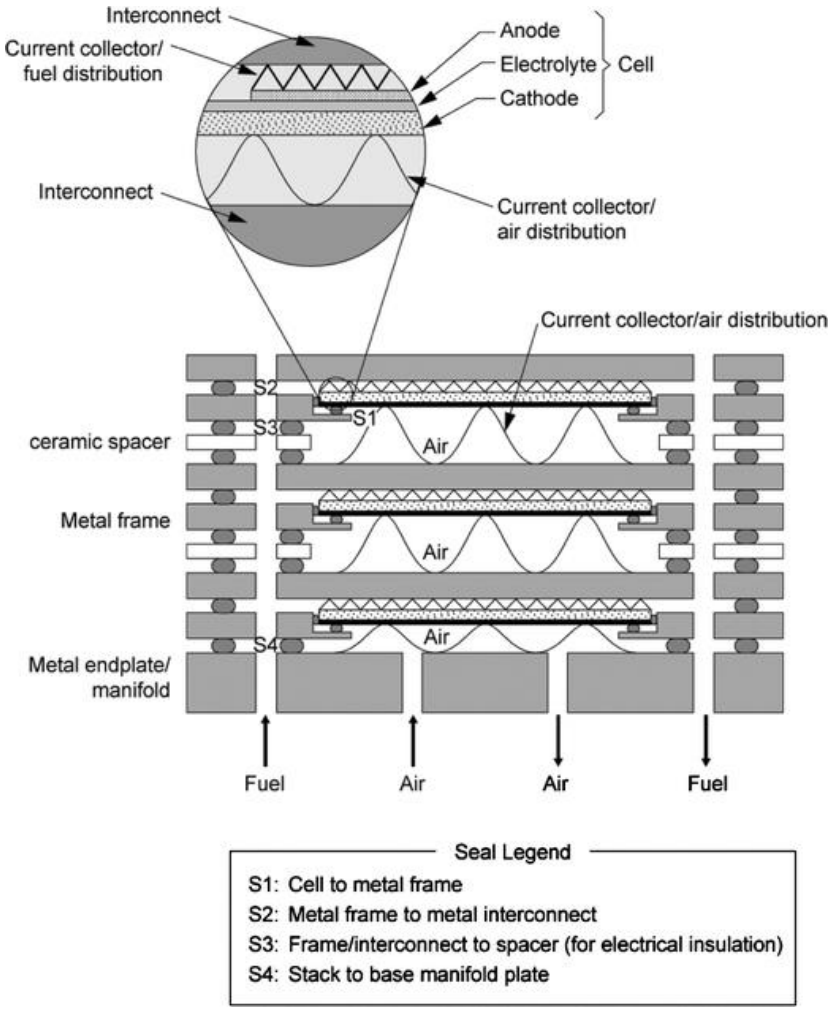

Figure 16. Role of sealants in solid oxide electrolysis cell (SOEC) stack [1]

Besides having strong adhesion with cell components, different parameters and critical issues must be taken in account while selecting a sealant for SOEC technology. For instance, a sealant should work effectively in the presence of harsh SOEC conditions such as high temperature in addition to simultaneous oxidizing and reducing atmospheres for >30,000 hours. The details about the different types of sealants and the essential properties required to work effectively in SOEC applications, have been already discussed in chapter 1.

Among different possibilities the glass-ceramic are considered the most successful and promising material for SOEC sealant applications, due to fact that their properties can be tuned according to the requirements by changing their compositions. Glasses are amorphous materials formed by melt quenching of liquid composed of various oxides. The most prominent properties of glasses are their brittle nature below glass transition temperature (T_g) and viscous behavior above glass transition temperature (T_g). Glass transition temperature indicates a temperature above which the glass shows a gradual transition from a hard brittle state to a viscous state.

Glass-ceramic is the crystalline form of glass, which is produce by heat treatment of glass to induce crystallization. The type and amount of crystals as well as their corresponding crystallization temperature (temperature to form

crystals) depends on the particular glass composition. The formation of crystals in glasses improves their mechanical and thermal stability thus make them suitable for SOEC applications [2–4]. The formed crystalline phases in the glass-ceramic are also responsible to determine their coefficient of thermal expansion (CTE).

Glasses are mainly composed of multi component oxides that can act as glass former, glass modifiers and intermediates [5]. Glass formers form the main structures of the glasses. They provide polyhedral units to the glass structure, have low coordination number (3-4) and high field strength. For sealants in SOEC applications, SiO_2, B_2O_3 and P_2O_5 are mostly used as glass formers. Glass modifiers are added with the purpose to disrupt the glass network. They occupy random sites in the glass network and therefore create non-bridging oxygen atoms (those who are not attached to the polyhedral units). They have low field strength and high coordination number of 8 [6]. They are important to control the characteristics temperatures and CTE of a glass system. On the other hand, intermediates have coordination number and field strength in between glass formers and modifiers. Al_2O_3 is mostly used intermediator in glass sealants. Beside glass former, modifier and intermediate, small amounts of other additives just as rare earth metal oxides and/or refractory metal oxides are also added to adjust the viscosity and to control the crystallization processes [5]. Further details about different components of glasses (glass former, modifier intermediates etc.) will be described in next section of this chapter. A typical glass network structure is illustrated in Figure 17.

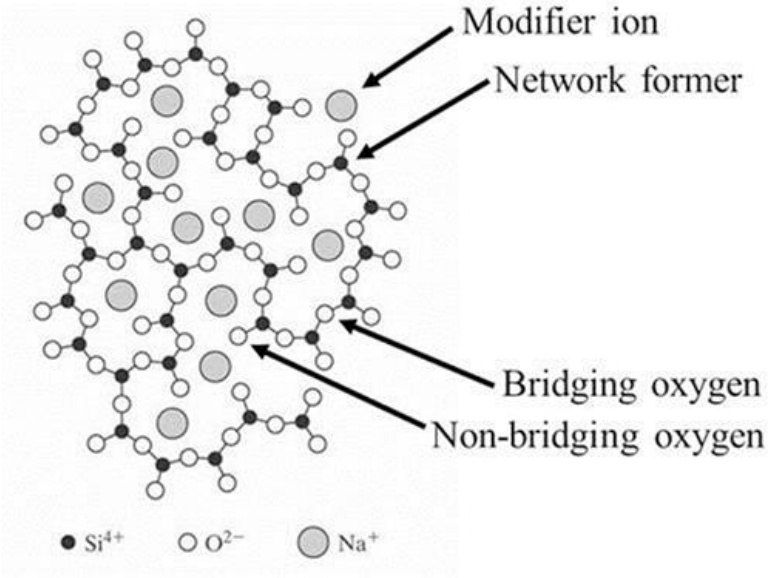

Figure 17. Schematic illustration of a glass network structure [7]

The Table 5 summarized the different elements oxides used in glasses for SOEC sealants. Their respective role in the glass structure is also described in table below.

Table 5. Examples and functions of typical oxides used in glass sealants composition [5,8]

Purpose	Oxides	Function
Glass network formers	SiO_2, B_2O_3, P_2O_5	Form glass network Determine thermal expansion coefficient Determine Tg and Ts
Glass modifiers	Na_2O, K_2O, CaO, MgO, SrO, BaO	Create non bridging oxygen (NBO) atoms Modify characteristic temperatures (Tg, Ts, Tx) of the glass Modify coefficient of thermal expansion of glass
Intermediated	Al_2O_3, Ga_2O_3	Hinder devitrification Modify glass viscosity
Additives	La_2O_3, Y_2O_3, ZnO, ZrO_2, TiO_2	Modify glass viscosity Improve coefficient of thermal expansion of glass Improve wettability and adhesion of glass with other components

Due to variety of strict working requirements, the designing of promising glass composition for SOEC sealants is not as straight forward. Extensive research has already been carried out to design and characterize glass-ceramic-based sealants for SOFC/SOEC technology. The requirements for SOEC sealants are almost similar to that of SOFC sealants. Beside various thermal, mechanical and chemical properties, the sealants in SOEC mode should be electrical insulation at higher voltage levels – typically > 1.2 V – compared to SOFC environment. Secondly, the stability of sealants under thermal cycling is also a fundamental requirement, especially when SOECs are operated in reversible systems for electricity storage, in which the cells are alternately working as SOECs or SOFCs with different temperature profiles. Moreover, the stability in high pressure is also a basic requirement for the sealants when SOECs operating in pressurized environments, which is a promising application showing improved cell performance at high current density [9,10].

2.1.1 Glass network former

Among different network formers mentioned in the Table 5, the P_2O_5 base glass-ceramics are least commonly used due to the fact the at high temperature the phosphorous becomes volatile and contaminate other cell components [5]. On the other hand, B_2O_3 base glass systems are also not highly recommended as B_2O_3 also become volatile due to its high vapor pressure and low melting point, thus

making it unsuitable for high temperature applications. However, small quantity of B_2O_3 can be beneficial to improve the wettability of a glass and to reduce the characterization temperatures of a glass such as glass transition temperature T_g, onset of crystallization temperature T_x and softening temperature T_s. The addition of B_2O_3 also reduces the viscosity of the glass system. In case of SiO_2 base glasses, although the formation of $Si(OH)_4$ species in the presence of steam degrades their performance, however, up to now the SiO_2 based glass-ceramics systems are most promising candidates for SOFC/SOEC applications due to their high thermal stability. Plenty of SiO_2 based glass compositions have been studied as sealant material and are reported in literature [5,11–23]. The presence of SiO_2 increases the glass transition and softening temperatures of a glass system. Commonly, the glass systems for SOEC applications have glass former concentration in the range of 40-60 mol%.

By increasing the concentration of SiO_2 in a glass, the crystallization temperature (T_x) also increases and consequently it delays the crystallization. Figure 18 shows that by increasing the SiO_2 content from 50 mol% to 60 mol%, almost 50°C increase in the devitrification temperature was observed in MgO-BaO-SiO_2 based glass system.

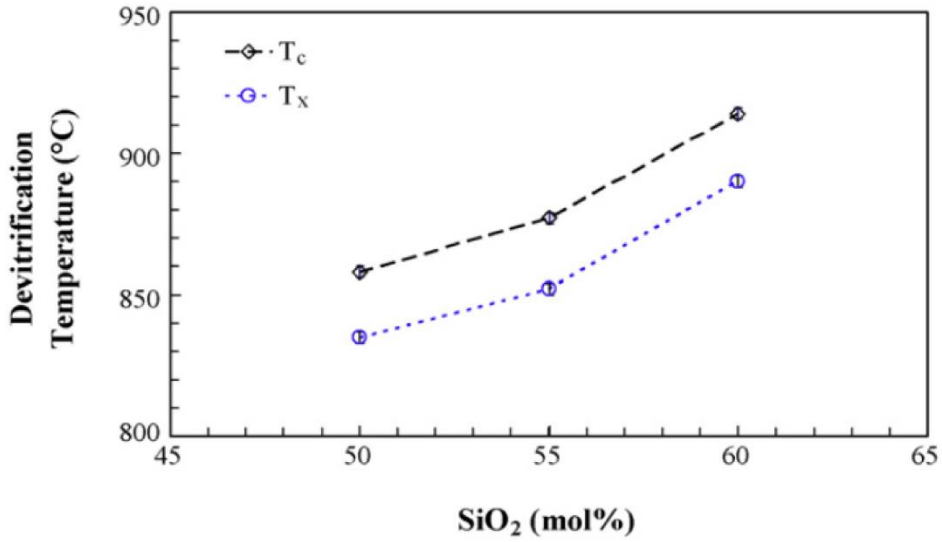

Figure 18. Dependence of devitrification temperatures on SiO_2 content in a MgO–BaO– SiO_2 glass system [24]

2.1.2 Glass modifiers

As discussed earlier, the purpose of modifiers is to break the network of the glass formers. With increasing concentration of a particular modifier, more disruption of glass network will occur and consequently form more non-bridging oxygen (NBO) atoms. It causes the reduction in their glass transition and softening temperatures and enhances the coefficient of thermal expansion of a glass.

Alkali metals and alkaline earth metals are most commonly used as modifiers in the glass-ceramics for SOEC sealants. Although alkali metal oxides enhance

the CTE, wettability and reduce the characterization temperatures of glass, however on the other hand their presence also reduces the electrical resistivity. This effect is due to their small ionic radius that makes their mobility easier under the applied voltage. They also have high potency to chemical react with other cell components as compared with alkaline earth metals. Due to these issues, the alkali metal oxides are not the first choice of selection particularly in large concentration [25,26].

Among alkaline earth metal oxides, BaO is most extensively used as compared to CaO and MgO. The addition of BaO improves the coefficient of thermal expansion of glass, wettability and sinter ability, and reduces the T_g and T_s. However, the excess amount of BaO reacts with the Cr of steel interconnect, resulted in the formation of $BaCrO_4$ phase. The $BaCrO_4$ is a high CTE phase and causes delamination at interconnect/glass-ceramic interface [15,21,27]. SrO has also been extensively studied in recent years as an alternative of BaO. Although it also forms a high CTE $SrCrO_4$ phase, however its tendency of formation is lower than $BaCrO_4$ [28]. SrO addition also enhances the CTE, improves wettability and adhesion of glass, reduces characteristic temperatures and improves sinter ability. Glass-ceramic based sealants for SOEC/SOFC have modifiers concentration commonly in the range of 25-40 mol% [12–14,16,22,29].

2.1.3 Glass intermediates

Based on coordination number, intermediates can act as either network former or modifier. The most commonly used intermediate in glass-based sealants is Al_2O_3. If coordination number of Al^{3+} is four, it will act as network former and its addition will enhance the glass transition and softening temperatures. On the other hand, if its coordination number is more than four, it will act as glass modifier and it will reduce the glass transition and softening temperatures. In a certain glass system the addition of Al_2O_3 can enhance the characteristics temperatures, while in other system it can show opposite effect. Al_2O_3 is also commonly used to hinder the crystallization process and to improve the stability of glass [5,30–32]. Typically, the concentration of Al_2O_3 in glass sealants is 5-10 mol%, however some systems have even higher concentration. Besides Al_2O_3, Ga_2O_3 can also use as intermediate to hinder the devitrification process, however the effect of Ga_2O_3 is still need to explore in detail.

2.1.4 Glass additives

In addition to the glass network formers, modifiers and intermediates, a small concentration (1-3 mol%) of additives is also used to tune to final properties of glass and glass-ceramic to make them suitable for desired SOEC/SOFC applications. Different additives reported in literature are La_2O_3, Y_2O_3, ZnO, ZrO_2, CeO_2 etc. [33–38]. The effect of different modifiers in glass sealants has been explained in detail in a review article by Tulyaganov et al. [31]. For instance, addition of La_2O_3 reduced the T_g and T_s, however no significant effect was observed on the CTE of glass system. The presence of ZnO reduces the

viscosity and T_g of glass, while enhances CTE and crystallization temperature. The addition of Nb_2O_5 in glass caused CTE mismatch between glass-ceramic sealant and Crofer22APU interconnect that lead to formation of crack at interface [35,39]. Recently Wang et al. [40] studied the effect of YSZ addition on stability of glass-ceramic sealants. The YSZ improved the CTE and gas tightening of glass ceramics. It also improved the interfacial compatibility and bonding of glass-ceramic sealants with the interconnect.

2.1.5 Recently developed promising glass-ceramic compositions

In the last decade, plenty of research has been already done to design novel glass-ceramic sealants with optimized properties. Most of the compositions available in literature were designed for SOFC having the working temperature of 700-800°C. Nevertheless, a significant work has also been carried out for SOEC applications. The sealants for SOEC applications have to work efficiently in harsh reducing atmosphere at the applied voltage, which is typically higher as compared with SOFC mode. The compositions available in literature for glass-ceramic sealants have been designed using various combinations of glass network formers, modifiers, intermediates and additives. Due to the high working temperature of SOEC, SiO_2 is mostly used as glass former with small amount of B_2O_3. On the other hand Al_2O_3 is most commonly used intermediate in different quantities. However, the selection of most suitable modifier (or combination of modifiers) in addition to their amounts is still an ongoing research. Various review articles are also available in literature that summarize recent developments in glass-ceramic sealants for SOEC/SOFC applications [5,30,31,41,42]. Some of the recently developed glass-ceramic compositions using different modifiers have been discussed below.

1. Few researchers developed glass systems using alkali metal oxides (Na_2O and K_2O) as main modifier in addition to other modifiers. The alkali metal oxides were added with the aim to improve wettability and CTE as well as to adjust the viscosity of system. For instance, Smeacetto et al. [43,44] investigated the thermal stability and compatibility of novel glass systems with the Crofer22APU interconnect for 500 hours at a working temperature of 800°C. The glass systems with alkali metal oxides showed excellent thermal and mechanical stability, a CTE of 10.6 - 10.9 x 10^{-6} K^{-1} for glass-ceramic and good compatibility with 3YSZ as well as with bare, pre oxidized and coated Crofer22APU interconnect [45–48]. The Cr diffusion was observed from bare Crofer22APU towards the glass-ceramic sealants, however in case of pre-oxidized and coated Crofer22APU, the migration of Cr across Crofer22APU/glass-ceramic sealant was depressed successfully. Anyways, no information has been provided for the electrical resistivity of these systems.

   Chou et al. [26] studied the effect of alkali metal oxides on the electrical properties of glass-ceramics for 1000 hours at 850°C. As shown in the Figure 19, the addition to 2-5mol% of K_2O was found to reduce the electrical resistivity of the system. Additionally, poor chemically stability was observed

between K_2O containing glass-ceramic sealants and Crofer22APU. Undesirable phases were formed at Crofer22APU/glass-ceramic interface resulted in debonding of sealant from the Crofer22APU interconnect. On the basis of these findings, the glass-ceramic sealants containing alkali metal oxides were not suggested to use in SOFC/SOEC applications. Anyway, a clear understanding of how Na contributes to the sealant degradation is still lacking. The experimental data are rather controversial, and there is no general agreement about the use of alkalis in SOC systems.

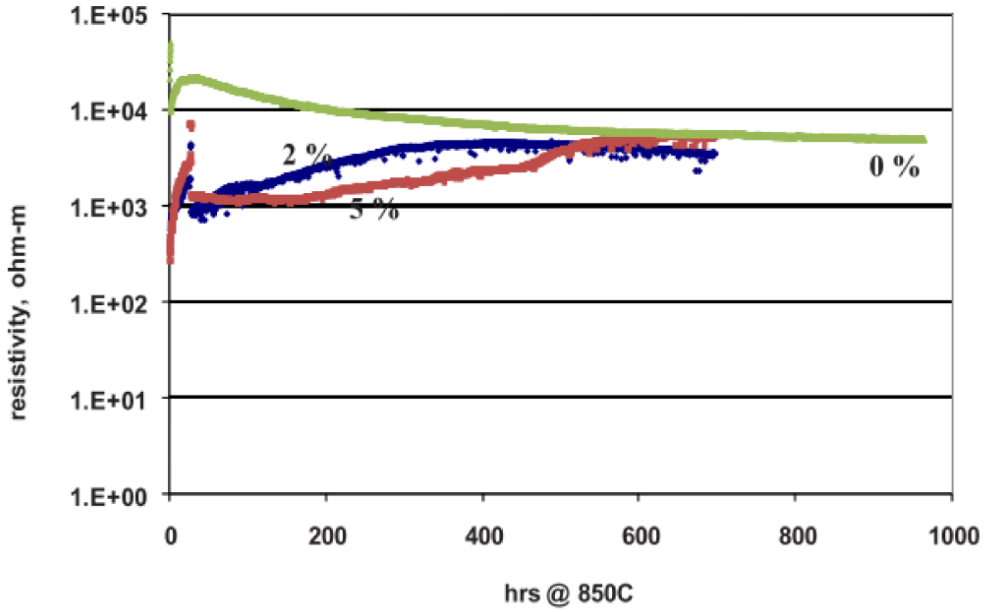

Figure 19. Electrical stability test of sealing glasses sandwiched between as-received Crofer22APU coupons in dual environment at 850°C with a dc load of 0.7 V. The numbers are the K_2O mol % in the glass [26]

2. The glass-ceramic systems containing alkaline earth metal oxides have been studied most intensively. For instance, many compositions contain either CaO or MgO as main modifiers, or both together. Like other modifiers, the addition of CaO and MgO is important to improve the CTE of system and to adjust the viscosity. Those compositions that contain both CaO and MgO as main modifiers are mainly designed to obtain $CaMgSi_2O_6$ diopside phase [21,44,49], having a CTE of 11 x 10^{-6} K^{-1}. Instead of using both CaO and MgO simultanously, the addition of only CaO as main modifier in silicate glass systems is usually made with aim to have $CaSiO_3$ and/or Ca_2SiO_4 phases with CTEs of 9.5-11x10^{-6} K^{-1}, while for MgO containing glass systems the $MgSiO_3$ has CTE of around 10 x 10^{-6} K^{-1} [7]. However, some articles also reported slightly different CTEs of $CaSiO_3$ and $MgSiO_3$ phases [30]. On the other hand, the formation of relatively low CTE $CaAl_2Si_2O_8$ (4.9 x 10^{-6} K^{-1}) and $Mg_2Al_4Si_5O_{18}$ (2 x 10^{-6} K^{-1}) phases could cause problems in these compositions.

3. SrO containing glass-ceramic compositions have gained special attention in recent years due to various advantages SrO could impart to the glass-ceramics [12–14,16,32,35,50]. Reddy et al. [51] developed different SrO (7-12 mol%) containing glass systems, and their thermal and mechanical properties were studied in detail at 850°C for 1000 hours. All these glass systems had excellent thermal and electrical stability, mechanical strength and compatibility with Sanergy HT metallic interconnect and 8YSZ electrolyte. The glass-ceramics shows CTE of 9.7-10.1 x 10^{-6} K^{-1} after joining with further increase when aged for 500 hours. However, the CTEs were slightly reduced for all studied glass-ceramic compositions, when ageing was done up to 1000 hours. However, the authors claimed that no new and undesirable phases were formed during ageing as confirmed by the XRD. The reported glasses showed excellent chemical stability with no chemical reaction at interface even up to 1000 hours at 850°C.

   Although addition of SrO has proven to be beneficial to improve various properties, nevertheless the excess amount of SrO also deteriorates the chemical stability of a glass system. Various researchers found the formation of $SrCrO_4$ phase at Crofer22APU/glass-ceramic sealant interface as a result of chemical reaction between SrO from glass sealant and Cr from steel interconnect. The formation of $SrCrO_4$ phase is thermodynamically favorable due to negative Gibbs free energy. The reaction takes place according to following equation:

$$2SrO + Cr_2O_3 + 3/2O_2 \rightarrow 2SrCrO_4 \qquad \Delta G_{800–900°C} = -(135–145)\ kJmol^{-1} \quad [52]$$

   The negative Gibbs free energy indicates that formation of $SrCrO_4$ can take place spontaneously in the air. The Sr present in the residual glassy phase favors the formation of $SrCrO_4$, instead of Sr in crystalline phases of a glass-ceramic. The $SrCrO_4$ is a detrimental phase as it has high CTE and consequently can cause delamination at Crofer22APU/glass-ceramic interface due to thermal stresses generated by CTE mismatch [52,53]. Figure 20 shows the interface between metallic interconnect and SrO containing glass-ceramic sealant. The excessive formation of undesirable $SrCrO_4$ was observed at point 1 and 2. The SrO containing glass system shown has SrO of 43 wt%.

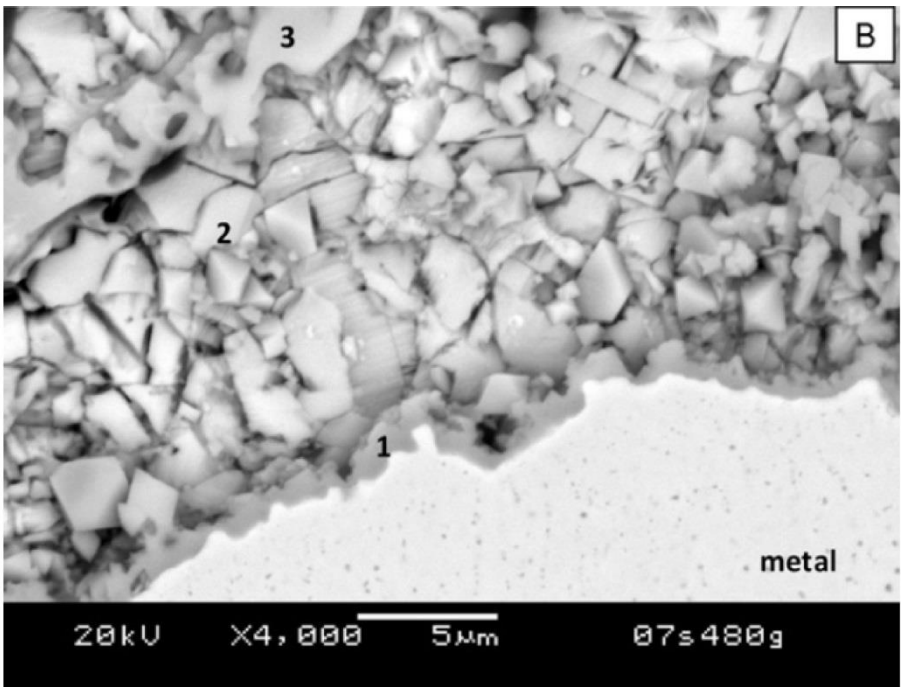

Figure 20. SEM micrograph shows the interfacial microstructure of the as-received Crofer22APU/glass sample after electrical stability test at 850◦C for ~500h in dual environment: The image corresponds to air side

Similar results have been reported in other systems where $SrCrO_4$ formation resulted in the delamination of glass-ceramic sealant and consequently deteriorate the mechanical integrity of joint [52,54,55].

4. BaO is probably most extensively used modifier in the glass-ceramics used for SOFC/SOEC sealants [11,13,15,24,37,38,56,57]. The effects of BaO are quite similar to that of SrO; such as reduce viscosity, increase CTE, reduce characteristics temperatures etc. However, like SrO, the glass-ceramic sealants contain BaO mostly suffer from the formation of undesirable $BaCrO_4$ phase due to chemical reaction between BaO from sealant and Cr from steel interconnect. The $BaCrO_4$ also has high CTE and its formations can take place according to following reaction [15]:

$$2Cr_2O_{3(s)} + 4BaO_{(s)} + 3O_{2(g)} \rightarrow 4BaCrO_{4(s)} \qquad \Delta G_{750\,^{\circ}C} = -205\ kJmol^{-1} \quad [58]$$

According to thermodynamics, the Gibbs free energy for the formation of $BaCrO_4$ in air is less than $SrCrO_4$ therefore; formation of $BaCrO_4$ is more favorable. Anyhow, plenty of compositions containing BaO as main modifier have been investigated. For instance; Peng et al. and co-workers [15,59,60] developed SiO_2-B_2O_3-BaO based glass system and investigated its chemical and thermal stability. The glass-ceramic showed strong adhesion with SS410 interface and 8YSZ electrolyte after joining with no undesirable phase formation. A high CTE $BaSi_2O_5$ phase was formed in glass-ceramic, which improved the thermo-mechanical compatibility of the glass sealant. However, the under the thermal cycling performed at 700°C the gas leakage was detected to take place at glass-ceramic/SS410 interface. The rate of leakage

was found to increase with the number of thermal cycles. Post mortem SEM-EDS analyses confirmed that the formation of undesirable phase $BaCrO_4$ took place at glass-ceramic/interconnect interface. The formation of that high CTE phase initiated the crack formation and consequently resulted in complete delamination at interface after 42 cycles at 700°C. Figure 21 shows the formation of crack at glass-SS441 interconnect interface due to presence of $BaCrO_4$ phase.

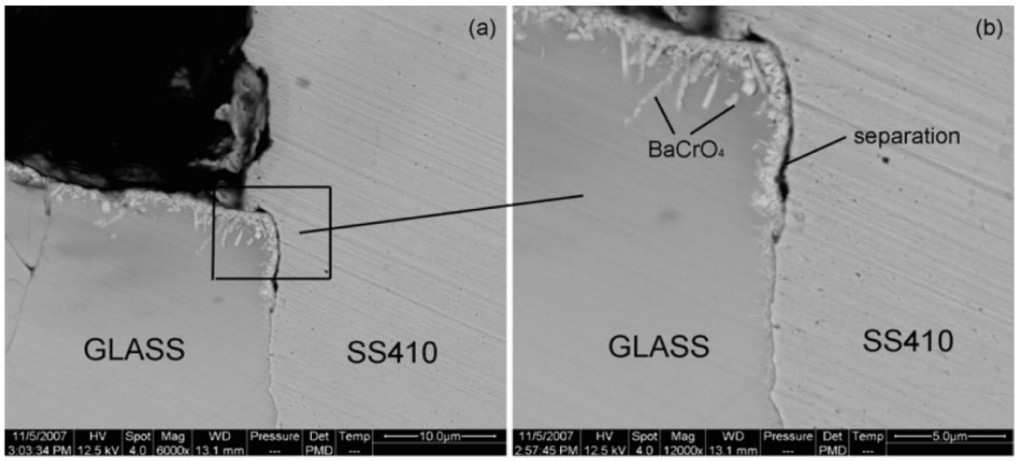

Figure 21. SEM micrographs of the air/glass/SS410 three phase boundaries after 42 thermal cycles: (a) a low magnification and (b) a high magnification of the marked area in (a) [15]

2.1.6 CTEs of different glass-ceramic phases in SOEC

The CTE of glass-ceramic is one the most critical parameter that need to adjust by keeping in view the CTEs of other cell components such as steel interconnects and YSZ electrolyte. Figure 22 shows the CTEs of different phases that can form in glass-ceramics depending upon the type and concentration of glass former, modifiers, intermediates and additives used. To obtain a glass-ceramic with the CTE in the range of 9.0-12 x 10^{-6} K^{-1}, the crystalline phases in the glass-ceramic should also have CTE in the range of 9-14 x 10^{-6} K^{-1}. To obtain the desire crystalline phase in a system, a careful design of composition is require by keeping in view the binary or tertiary phase diagrams of main components of a glass system.

CTEs of devitrified phases in seal glasses.

Devitrified phases	Formula	CTE ($\times 10^{-6}\,^{\circ}C^{-1}$)
Quartz	SiO_2	11.2–23.3
Enstatite	$MgSiO_3$	9.0–12.0
Clinoenstatite	$MgSiO_3$	7.8–13.5
Protoenstatite	$MgSiO_3$	9.8
Forsterite	Mg_2SiO_4	9.4
Wollastonite	$CaSiO_3$	9.4
Calcium orthosilicate	Ca_2SiO_4	10.8–14.4
Barium silicate	$BaSiO_3$	10.5–12.5
	$Ba_2Si_3O_8$	12.6
Barium borate	BaB_2O_4	$\alpha_a = 4.0$ $\alpha_c = 36.0$
Barium zirconate	$BaZrO_3$	7.9
Hexacelsian	$BaAl_2Si_2O_8$	6.6–8.0
Monocelsian	$BaAl_2Si_2O_8$	2.3
Orthorhombic celsian	$BaAl_2Si_2O_8$	4.5–7.1
Hexacelsian	$SrAl_2Si_2O_8$	7.5–11.1
Monocelsian	$SrAl_2Si_2O_8$	2.7
Orthorhombic celsian	$SrAl_2Si_2O_8$	5.4–7.6
Cordierite	$Mg_2Al_4Si_5O_{18}$	2.0

Figure 22. CTEs of different crystalline phases formed in the glass-ceramics [7]

2.1.7 Glass deposition by stencil printing

Various methods are being used and are reported in literature to manufacture different components of SOECs. Screen printing and stencil printing are arguably the most commonly applied method to deposit or manufacture different ceramic materials in SOEC stack. Stencil printing is an easy and cost efficient method that involves the squeezing of the paste or ink through a mesh on to a substrate. A mesh or stencil contains the image of desired pattern required on the substrate. Figure 23 shows the basic working principle of a stencil printing technique.

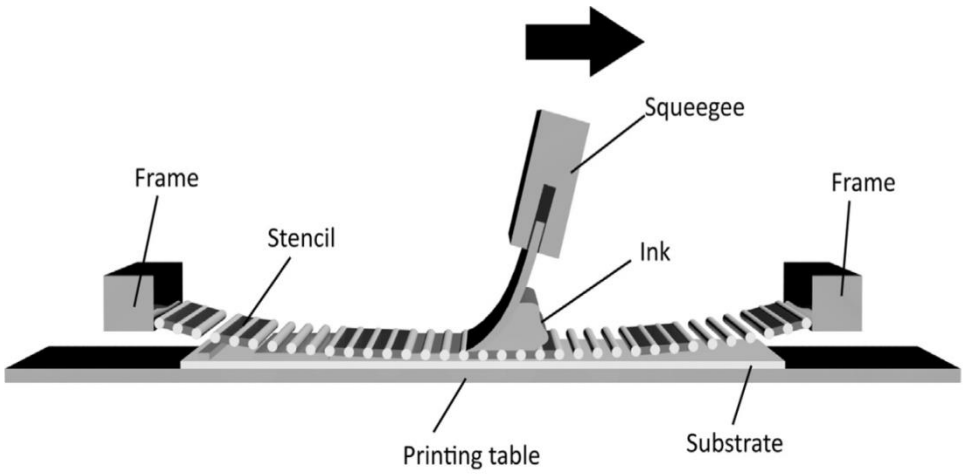

Figure 23. Working mechanism of stencil printing technique [61]

Stencil printing method can also be successfully employed to deposit glass in an SOEC technology. For stencil printing, the development of a suitable paste or ink is quite challenging. A typical paste is composed of solvent, binder, dispersant and solid content of final material to be deposit. The solvent is required to homogenize the solid particles while the binder is used to increase the inter-particle forces and connectivity. Dispersants are important to ensure the homogenous dispersion of the particle. Additionally, a small quantity of plasticizer can also be added to impart flexibility in the paste. For paste development, variety of solvents, binders, dispersants and plasticizers are being used to tune the properties of paste. In SOEC technology, the requirements of synthesized pastes change from one component to other, due to their different characteristics and operating demands. For instance, the anode and cathode in repeating unit cell should be porous after deposition and drying, due to fact that they need high surface area to facilitate the reactions. On the other hand, the electrolyte and sealants should be dense with minimum porosity. In this context, the selection of suitable components (solvent, binder, dispersant etc) and their corresponding quantities is very important to control the overall properties of a paste [62–70].

A lot of research has been carried out about the development of pastes for cathode, anode and electrolyte. However, very limited work has been reported about deposition technique or paste development for glass-ceramic based sealants for SOEC applications. Therefore, still there is need to do further research about paste development of glass based sealants.

2.2 Protective coatings on interconnects

As discussed in the chapter 1, the high chromium containing steels (Crofer22APU, Crofer22H, AISI 441 etc) are most suitable candidates for interconnects SOFCs and SOECs, due to remarkable properties in terms of low cost, high electrical conductivity and the CTE matching with other cell components. However, a major problem faced in these types of interconnects is

the evaporation of Cr at high working temperature. Cr can contaminate the other cell components and degrade their performances. Additionally, by the evaporation of Cr, the desired properties of the interconnect can also degrade with time [71,72].

In order to maximize the overall efficiency of the SOECs, the issues related to evaporation of Cr from interconnect must be addressed. Different methods have been proposed in the past to overcome this problem. Formation of barrier layer of Cr_2O_3 (oxide scale) by pre-oxidation of interconnect is probably the most easy solution. The chromia oxide scale has been found to reduce the evaporation of volatile species. Figure 24 compares the rate of Cr evaporation from Sanergy HT and Crofer22H interconnect at 850°C, as a function of time. The evaporation of Cr was found to decrease with time due to the formation of different Cr containing barrier layers on the surface of Cr steels [73,74].

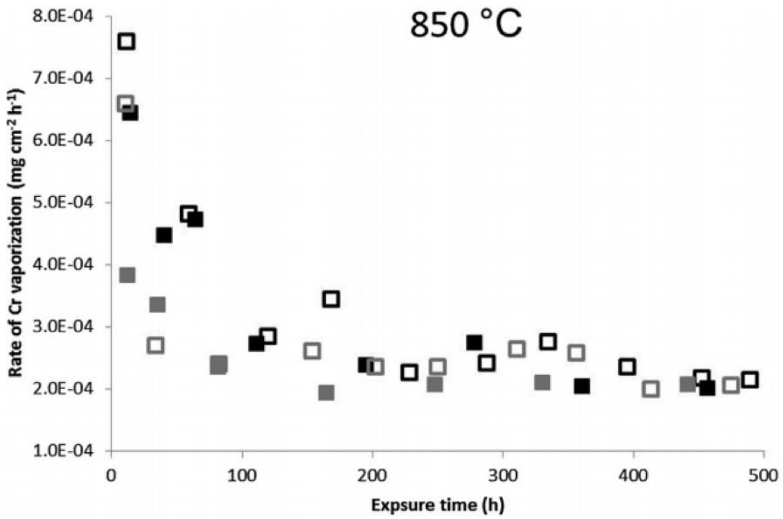

Figure 24. Rate of Cr vaporization as a function of time for Sanergy HT (black) and Crofer 22 H (grey) at 850 °C in air containing 3% H_2O (6000 sml min^{-1}). Filled and empty symbols represent the two individual isothermal exposures [75].

However, chromium oxide is thermodynamically not stable in humid conditions at high temperature and consequently can produce different Cr-containing volatile species. Secondly, the oxide scale also reduces the electrical conductivity of the interconnect. Another way could be the doping of Mn in to the steel interconnect, that can result in the formation of $(Cr,Mn)_3O_4$ spinel layer above the Cr-oxide scale and is more effective towards hindering of Cr from interconnect and improves the oxidation resistance. However, these methods do not provide sufficient barrier to hinder the Cr evaporation up to desired level. Therefore, it is important to choose some alternative ways that are more effective and durable. The deposition of protective coatings on the steel interconnects is widely studied topic in last decade, and is found to be the most promising way to minimize the evaporation of Cr from interconnect. In general, the coatings for SOECs should fulfill following requirements:

1. Must prevent the oxidation of volatile species such as Cr from steel based interconnect.
2. Should have low oxygen ion, to avoid formation of oxide scale.
3. Thermally stable at high working temperature (750-850°C).
4. Should have high electrical conductivity.
5. Coefficient of thermal expansion should match with interconnect.
6. Easy to deposit.

Various coating materials have been studied and their performance has been investigated in long terms [76–81]. On the other hand, different methods has been used to deposit these materials on the interconnect substrates [82–84]. The details about the different coating materials and deposition techniques are given below.

2.2.1 Coating materials

Metallic coatings

The interconnects in SOEC stack can be coated by metallic materials as well as rare earth metals to hinder the chromium evaporation, to reduce the rate of oxidation and area specific resistance (ASR) [77]. Metallic coatings can be more attractive than rare earth metals because they have low cost of raw materials and large availability. Metallic coatings also tend to oxidize at high working temperature and form a top barrier layer. Froitzheim and his co-workers [74,85–88] investigated the effect of 640 nm thin cobalt (Co) coatings on chromium retention capability up to 3000 hours at 850°C. The Co based coatings were found to reduce the Cr evaporation as compared with uncoated Sanergy HT interconnect. The difference in the performances of uncoated and Co-coated interconnects mainly arose from the formation of spinel layers. Although uncoated Sanergy HT interconnect and Co-coated coated showed the formation oxide scale of Cr_2O_3 after 3000 hours, as shown in Figure 25, however, uncoated coated substrate formed a $(Cr,Mn)_3O_4$ spinel layer on top of chromia oxide scale. This $(Cr,Mn)_3O_4$ layer give rise to evaporation of Cr at high temperature. On the other hand, a $(Co,Mn,Fe)_3O_4$ spinel layer was formed on Co-coated sample, therefore the Cr-evaporation rate was lower due to absence of Cr in outer most layer.

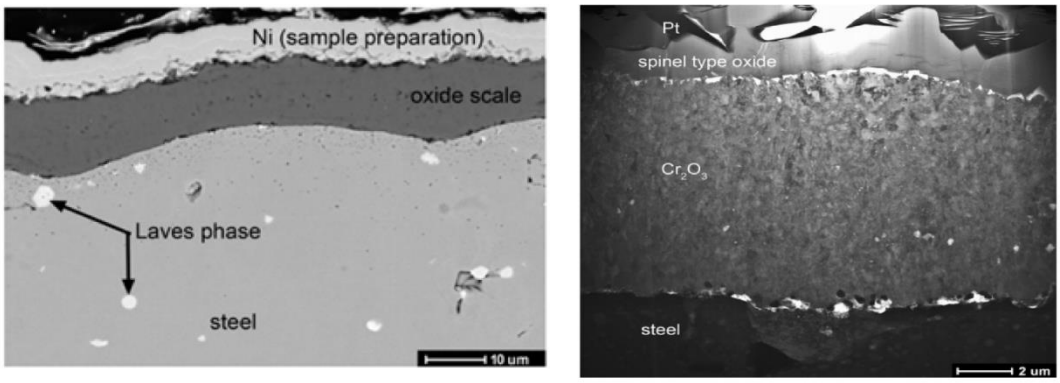

Figure 25. SEM backscattered electron image of a cross-section of the oxide scale of (Left) uncoated Sanergy HT (Right) Co-coated Sanergy HT sample after 3000 h exposure at 850 °C [88]

Another approach to further reduce the oxide scale growth is to deposit a very thin layer of cerium (Ce) below the Co coating. According to literature, a 10 nm thin Ce layer is beneficial not only to reduce the oxide scale growth but also to reduce its electrical resistivity [85,89–92].

Beside Co, other metallic coatings such as Ni and Cu have also been studied. These metallic materials can be deposited by various techniques on different interconnect materials. The metallic coatings were found to completely oxidized at working 800-850°C. The oxides of most of these metals have CTE matching with other cell components and therefore showed excellent adhesion with the substrate in the long term [93]. Additionally, these metallic coatings increase the electrical conductivity of interconnect and improve its oxidation resistance, therefore reduce the degradation. Figure 26 compares the CTE values of these metallic materials and their oxides with other cell components. The data of electrical conductivity is also shown in Figure 26 for comparison.

Name	$\alpha/10^{-6}\,K^{-1}$ (ΔT, °C)	σ (S cm^{-1}) T (°C)	Function
8YSZ	10.8(20–800) [47]	$(5.3–4.5) \times 10^{-2}$(800) [48]	Electrolyte
Crofer 22 APU	12.0(20–800) [49]	8.70×10^{3}(800) [49]	Interconnect
Cr_2O_3	9.6(20–1400) [50]	1.28(750) [50] 2.50(1000) [50]	Oxide scale
$MnCr_2O_4$	7.2(25–900) [43]	0.22(750) [43] 0.05(800) [43]	Oxide scale
Mn_2CrO_4	–	12.8–30.3(750) [43]	Oxide scale
Co	14.0(20–400) [51]	1.71×10^{4}(800) [51]	Coating
Co_3O_4	–	35.5(800) [52]	Coating
$CoCr_2O_4$	7.4(25–900) [43]	1.92(750) [43]	Coating
Ni	16.3(20–900) [51]	2.20×10^{4}(900) [51]	Coating
NiO	12.6(100–800) [50]	14.9(590) [50] 71.4(1000) [50]	Coating
$NiCr_2O_4$	7.6(25–900) [43]	62.5(750) [43]	Coating
Cu	20.3(20–1000) [51]	1.23×10^{5}(977) [51]	Coating
CuO	–	2×10^{3} (700) [50] 10^{5}(1000) [50]	Coating

Figure 26. Thermal expansion coefficients (CTEs), α, and electrical conductivities, σ, of the used coating materials and their oxides [93]

Perovskite coatings

Perovskite materials belong to the class having the chemical structure of ABO_3, where A and B represents the metallic cations. Usually the "A" is a large trivalent rare earth cation such as La or Y, whereas the "B" is usually a trivalent transition metal cations such as Cu, Co, Fe, Ni, Mn etc. Various perovskites materials such as $La_{1-x}Sr_xMnO_3$ (LSM) and $La_{0.6}Sr_{0.4}Co_{0.8}Fe_{0.2}O_3$ (LSCF),

$La_{0.8}Sr_{0.2}CrO_3$ (LSC) have been studied as protective coatings on different interconnects [94].

LSM has also been used as anode for SOEC applications and has a CTE matching with other cell components. That ensures its strong adhesion to the metallic interconnect. LSM coating has been found a promising coating candidate to hinders the transport of oxygen, therefore improves the oxidation and corrosion resistance of interconnect. Both LSM and LSCF also have high electrical conductivity that adds addition value towards their selection. However, some researcher detected an increase in the area specific resistance (ASR) after deposition of these coatings on steel interconnect. For instance, Figure 27 compares the ASR data of the bare Crofer22APU with Crofer22APU coated with LSM and LSCF materials. The LSM and LSCF coated Crofer22APU showed an increase in ASR as compared bare Crofer22APU, nevertheless the difference was quite negligible.

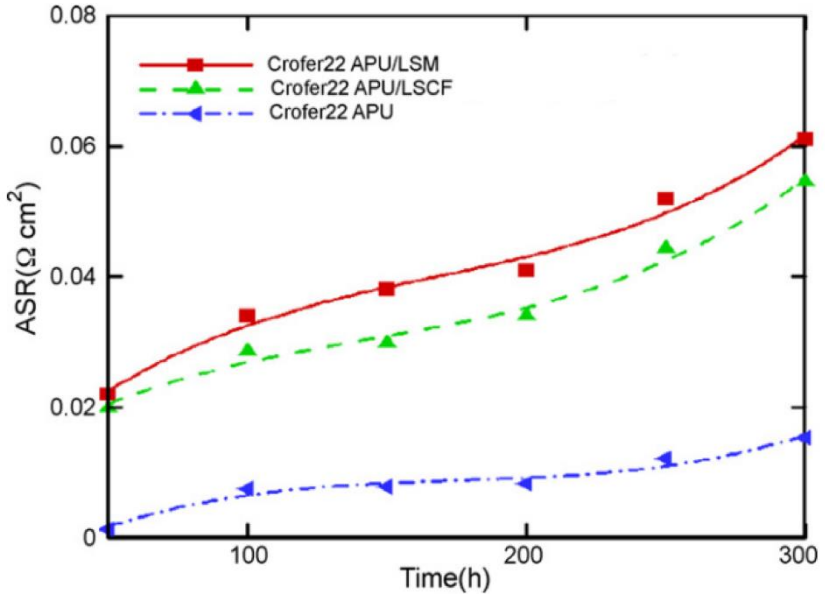

Figure 27. Comparison of area specific resistance of uncoated and LSCF/LSM coated Crofer22APU interconnect as a function of holding time at 800°C in hot air [95]

Although many researchers found that perovskite materials are effect to significantly reduce the Cr migration. However, few studies also revealed that these coatings are not best choice to hinder the Cr release [93,96,97]. The formation of pores due to crystallization of these materials makes them less effect to act as effective Cr-barrier coatings. Another disadvantage of these materials is their high cost and spallation especially during to the thermal cycling.[ref]

Spinel coatings

The general formula of the spinel materials is AB_2O_4, where A and B are divalent, trivalent or quadrivalent sites. By varying the cation at A and B positions, different spinel materials can be formed. The Figure 28 compares the CTEs and specific conductivities of different spinel materials [98]. In particular, manganese cobaltite MnCo spinel-based coatings have attracted great attention

due to their high electrical conductivities at 750-850 °C and CTE matching with the other cell components such as steel interconnect and YSZ electrolyte. By using different ratios between Mn and Co in $Mn_xCo_xO_4$, the properties of the MnCO spinel can be further tune [53,81,99].

	Mg	Mn	Co	Ni	Cu	Zn
Al	$MgAl_2O_4$ $\sigma = 10^{-6}$ $\alpha = 9.0$	$MnAl_2O_4$ $\sigma = 10^{-3}$ $\alpha = 7.9$	$CoAl_2O_4$ $\sigma = 10^{-5}$ $\alpha = 8.7$	$NiAl_2O_4$ $\sigma = 10^{-4}$ $\alpha = 8.1$	$CuAl_2O_4$ $\sigma = 0.05$ $\alpha = -$	$ZnAl_2O_4$ $\sigma = 10^{-6}$ $\alpha = 8.7$
Cr	$MgCr_2O_4$ $\sigma = 0.02$ $\alpha = 7.2$	$Mn_{1.2}Cr_{1.8}O_4$ $\sigma = 0.02$ $\alpha = 6.8$	$CoCr_2O_4$ $\sigma = 7.4$ $\alpha = 7.5$	$NiCr_2O_4$ $\sigma = 0.73$ $\alpha = 7.3$	$CuCr_2O_4$ $\sigma = 0.40$ $\alpha = -$	$ZnCr_2O_4$ $\sigma = 0.01$ $\alpha = 7.1$
Mn	$MgMn_2O_4$ $\sigma = 0.97$ $\alpha = 8.7$	Mn_3O_4 $\sigma = 0.10$ $\alpha = 8.8$	$CoMn_2O_4$ $\sigma = 6.4$ $\alpha = 7.0$	$NiMn_2O_4$ $\sigma = 1.4$ $\alpha = 8.5$	$Cu_{1.3}Mn_{1.7}O_4$ $\sigma = 225$ (750 °C) $\alpha = 12.2$	$ZnMn_2O_4$
Fe	$MgFe_2O_4$ $\sigma = 0.08$ $\alpha = 12.3$	$MnFe_2O_4$ $\sigma = 8.0$ $\alpha = 12.5$	$CoFe_2O_4$ $\sigma = 0.93$ $\alpha = 12.1$	$NiFe_2O_4$ $\sigma = 0.26$ $\alpha = 10.8$	$CuFe_2O_4$ $\sigma = 9.1$ $\alpha = 11.2$	$ZnFe_2O_4$ $\sigma = 0.07$ $\alpha = 7.0$
Co		$MnCo_2O_4$ $\sigma = 60$ $\alpha = 9.7$	Co_3O_4 $\sigma = 6.7$ $\alpha = 9.3$			

Figure 28. CTE and specific conductivity for different spinel materials at 800°C [99]

From the group of $Mn_xCo_xO_4$ spinels, $Mn_{1.5}Co_{1.5}O_4$ have been most extensively studied as an effective and potential coating material for SOEC technologies [53,55,84,100–104]. $Mn_{1.5}Co_{1.5}O_4$ has a dual-phase microstructure (cubic $MnCo_2O_4$ and tetragonal Mn_2CoO_4 spinel phases). The CTE of $Mn_{1.5}Co_{1.5}O_4$ is $12x10^{-6}$ K^{-1}, while has high electrical conductivity of 60 $S.cm^{-1}$. Figure 29 compares the area specific resistance (ASR) of uncoated and $Mn_{1.5}Co_{1.5}O_4$ coated Crofer22APU interconnect as studied up to 2500 hours at 800 °C. The $Mn_{1.5}Co_{1.5}O_4$ coated Crofer22APU showed lower values of ASR as compared with bare Crofer22APU [104]. Similar results about the ASR of $Mn_{1.5}Co_{1.5}O_4$ are also reported by other groups [97,105].

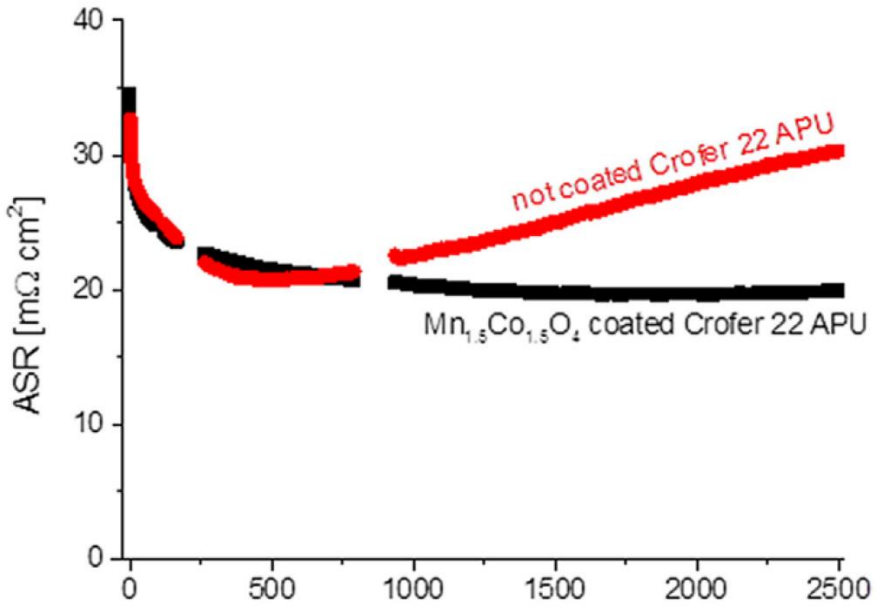

Figure 29. Area Specific Resistance (ASR) of uncoated and $Mn_{1.5}Co_{1.5}O_4$ coated Crofer22APU alloy tested at 800 °C under 500 mA cm^{-2} current load [104]

As discussed earlier, although other coating materials such as perovskites also showed high electrical conductivity and CTE matching with interconnect materials, however, the Cr-retention capability of perovkite materials could be a doubtful that can limit their usage. On the other hand, $Mn_{1.5}Co_{1.5}O_4$ spinel coatings beside processing excellent electrical and thermal properties, also have capability to reduce the Cr diffusion [81,98,105,106]. Unlike perovskite materials, $Mn_{1.5}Co_{1.5}O_4$ spinel showed effective barrier towards the migration of oxygen ions and reduced the oxide scale growth. Figure 30 shows EDS line scan analysis performed on $Mn_{1.5}Co_{1.5}O_4$ coated Crofer22PU after 1000 hours at 800°C. The Cr concentration drastically reduced at oxide scale/ $Mn_{1.5}Co_{1.5}O_4$ coating. No Cr was detected even in the spinel layer [84]. In addition to the electrical conductivity, another important requirement for the coating is the thermal expansion coefficient, which should be matched to other cell components, especially the steel substrate on which it is deposited.

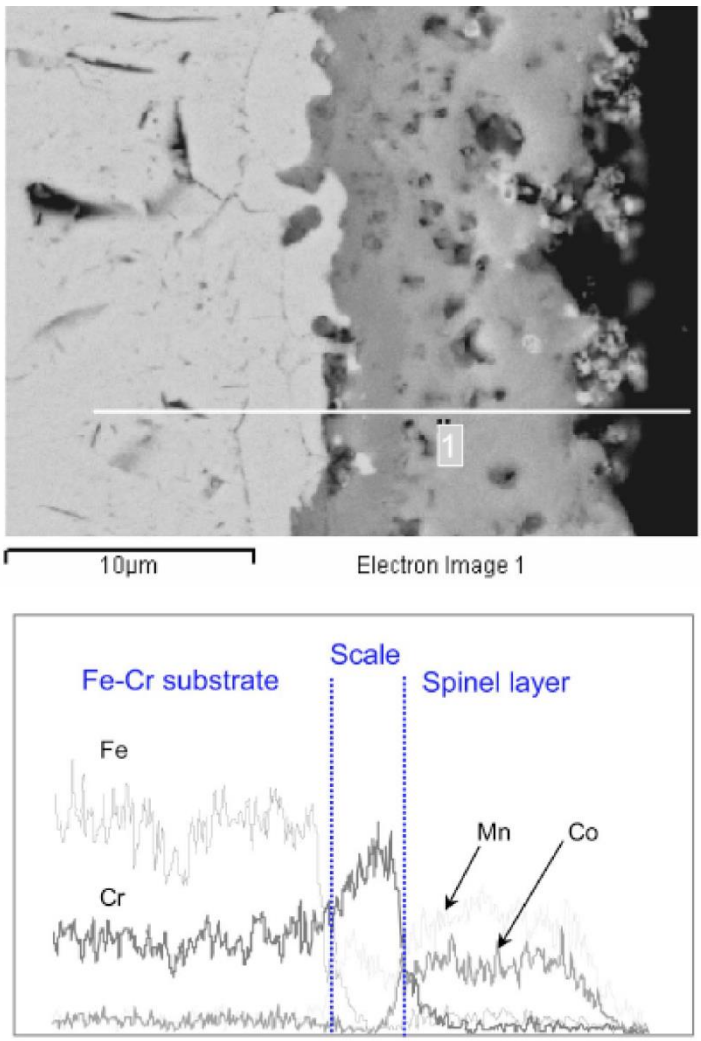

Figure 30. Microstructural and compositional analyses on the Mn1.5O1.5O4 protection layer subjected to an interfacial ASR measurement at 800°C in air [84]

Different methods have been used to modify the MCO spinel properties such as density, electrical conductivity etc. For instance, many studied are available in literature to increase the electrical conductivity and to tune the CTE of $Mn_{1.5}Co_{1.5}O_4$ coating. For the purpose, $Mn_{1.5}Co_{1.5}O_4$ can be doped with various transition metals such as Fe, Cu, Ni etc [107]. The addition of Cu improves the electrical conductivity and CTE of $Mn_{1.5}Co_{1.5}O_4$. The Cu doped $Mn_xCo_xO_4$ coatings were also found to enhance their densification, therefore improving their performance towards Cr-retention [108,109]. However, Cu doping can reduce the thermal stability of $Mn_xCo_xO_4$ based spinels [1]. On the other hand, the addition of Fe has been found to improve the thermal stability. Although the addition of FE tends to increases the ASR, but the conductivity measured for Fe-doped MnCo spinel ($MnCo_{1.7}Fe_{0.3}O_4$) at 800 °C (47 S cm−1) is significantly higher as compared with electrical conductivity of Cr_2O_3 (0.1–0.01 S cm^{-1}) [79].

Besides MnCo coating, recently Cu-Mn based spinel coatings are also receiving more attentions due to their higher electronic conductivity and low cost [110–113]. Sun et al. [112] found that $CuMn_{1.8}O_4$ spinel coatings as promising candidate to hinder the Cr-evaporation in addition to having low ASR values as

tested up to 500h at 850°C. Wang et al. [111] also compared the Cr-retention capability of Crofer22H coated with $CuMn_{1.8}O_4$ and $CuMn_2O_4$. The $CuMn_{1.8}O_4$ coating was most effective to hinder the Cr-diffusion, however $CuMn_2O_4$ coatings showed poor performance as barrier layer as studied at 800°C for almost 300 hours.

Although many researcher claims that $CuMn_{1.8}O_4$ spinel could be a potential candidate to act as barrier coating for SOEC interconnect, still there is a need to perform detailed and long-term characterizations in order to better understand these materials.

2.2.2 Coating deposition technique

Various methods are being used to deposit the protective barrier coatings on the SOEC interconnects. Each of these methods has certain advantages and limitations. The working principles, advantages and limitations of few methods are described below.

Magnetron sputtering

Direct current (DC) and radio frequency (RF) magnetron sputtering is a plasma assisted physical vapor deposition (PVD) method used to deposit thin and dense coatings of variety of materials. The target material as well as the desired deposition material is introduced into the chamber and plasma is created using argon gas near the target and is confined by using magnets. The positive ions in the plasma are bombarded on the negatively charged target that ejects the atoms of the target material. These ejected or sputtered target atoms are then deposited on the positively charged substrate material [114–119]. A simple illustration of the principle of magnetron sputtering process has been shown in Figure 31. Radio frequency magnetron sputtering is also used to deposit the non-conductive materials.

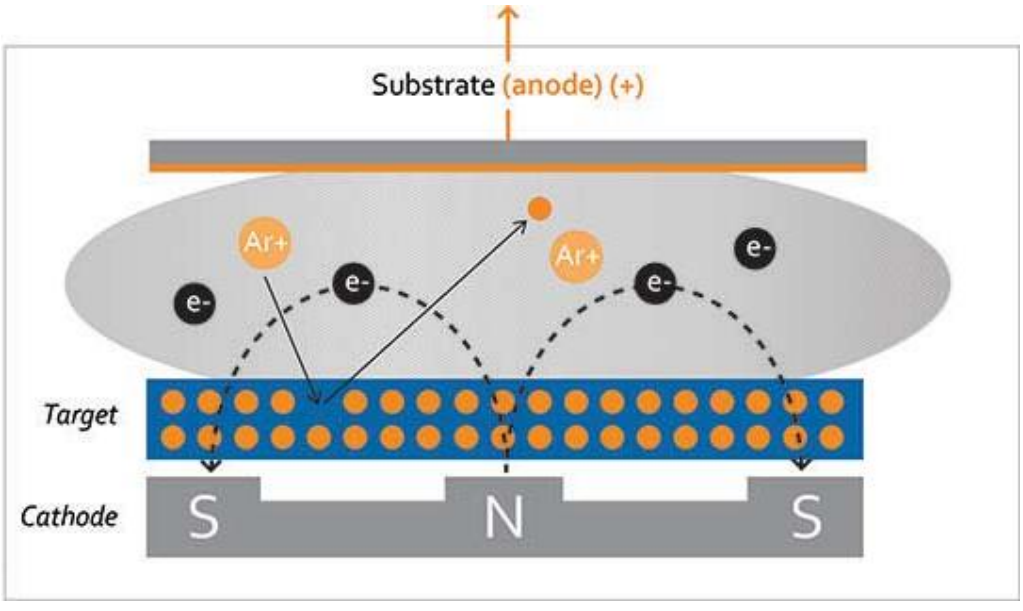

Figure 31. Illustration to demonstrate the working principle magnetron sputtering process [120]

Many groups used magnetron sputtering technique to deposit different materials such as perovskites and spinels, on steel interconnects used for SOECs applications [84,121–123]. The coatings produced by magnetron sputtering are dense and no post deposition treatments are required.

Electrophoretic deposition (EPD)

Electrophoretic deposition (EPD) is an electric field assisted process that employs the movement of charged particles in a liquid towards a charged electrode in an electric field. The working principle of EPD process has been shown in Figure 32. The basic requirement of EPD process is to produce a stable suspension of desire coating material in some solvent. In order to stabilize the particles and to avoid sedimentation some surfactants can also added in suspension. The conductive reference electrode and conductive substrate are dip into the suspension and with the help of external voltage the particles are deposited. The EPD technique requires simple apparatus that makes this process cost efficient and easy to use. The EPD is a wet deposition method that can be used to deposit variety of materials on different substrates for different application. In particular, it's commonly used to deposit different ceramic materials on the steel interconnects. The EPD can also be used to deposit particles of different materials simultaneously. The applications of EPD process are not limited to flat substrates, however, it is a promising method to deposit uniform coatings even on irregular surfaces having complex geometries [80,83,124,125].

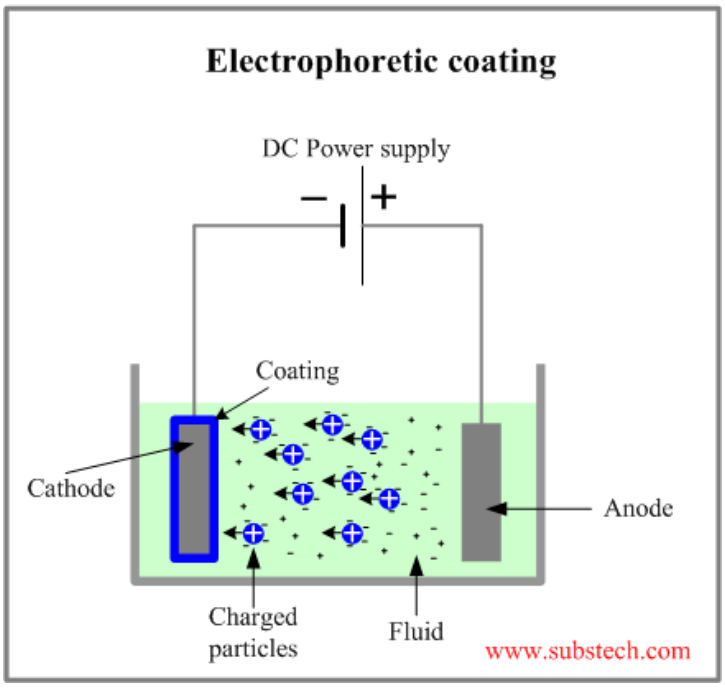

Figure 32. Working principle of EPD process [126]

The different parameters that can effect and contribute towards controlling the thickness and morphology of EPD deposited coating are:

I. Particle size and concentration
II. pH of the solution
III. Time of deposition
IV. Applied voltage during deposition
V. Distance between electrodes
VI. Drying conditions

For SOEC applications, the EPD has been used extensively to deposition $Mn_{1.5}Co_{1.5}O_4$ coatings on the steel interconnects [78,79,81,84,103,104,106,127]. The $Mn_{1.5}Co_{1.5}O_4$ coatings produced by the EPD were found to be uniform, crack free, with high capability to retain Cr-evaporation and consequently improve the oxidation and corrosion resistance of steel. The $Mn_{1.5}Co_{1.5}O_4$ coating with different thickness has been produce by adjusting deposition time, applied voltage and distance between electrodes. The comparative study about the electrical characterization of $Mn_{1.5}Co_{1.5}O_4$ coating showed that the EPD coated $Mn_{1.5}Co_{1.5}O_4$ showed superior properties in terms of low ASR and degradation rate as compared with Mn-Co coating deposited by other methods. This comparison about ASR values up to 5000hrs at 800°C has been shown in Figure 33.

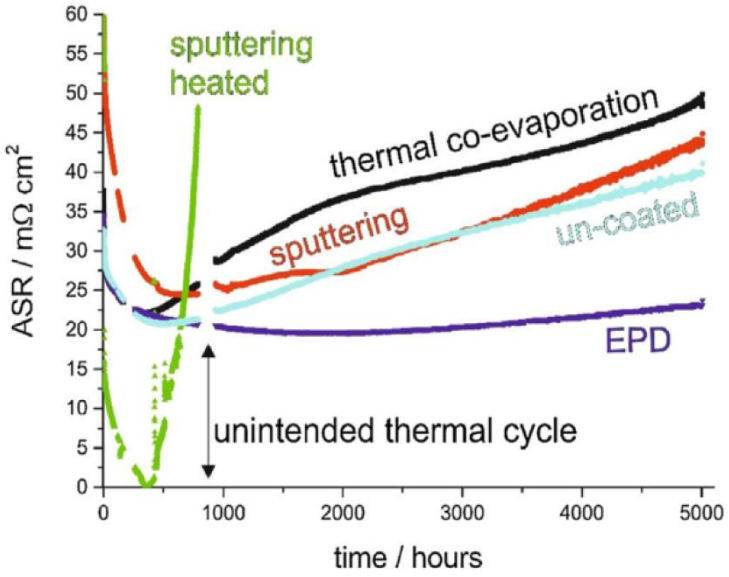

Figure 33. Area Specific Resistance measurement of samples at 800 °C under a current load of 500 mA cm^{-2} [84]

To act as effective barrier coating, to minimize the Cr evaporation from Crofer22APU and to hinder the oxygen ion conductivity, $Mn_{1.5}Co_{1.5}O_4$ coating should be significantly dense. The selection of sintering conditions plays an important role to control the densification of coatings deposited by EPD. EPD based $Mn_{1.5}Co_{1.5}O_4$ coatings are usually sintered at 900-1000°C. Among different sintering parameters, the most efficient method to produce dense coating is probably sintering at 800-950°C in two steps. In the first step the sintering is carried out in reducing atmosphere while second step involves sintering in

oxidizing atmosphere [14,35,45]. Few studies also reported high temperature sintering either in single step in air. High temperature sintering tends to improve the densification of coatings, nevertheless it can also increase the thickness of oxide scale [103,128], thus consequently contributing to higher ASR.

Various other methods such as sol-gel deposition [77], plasma spray deposition [94], spray pyrolysis [82] are also used to deposited different coatings on interconnects for SOEC applications. Figure 34 summarizes the pros and cons of different coating deposition methods.

Coating method	Advantage	Disadvantage
Sol–gel	• Simple • Applicable to ceramic coatings	• Thin, non-uniform coatings
MOCVD rf magnetron sputtering	• Applicable to ceramic coatings • Applicable to ceramic coatings	• Thin, non-uniform coatings • High cost • Dependent on line-of-sight • Cracked, porous coatings
PLD	• Applicable to ceramic coatings	• High cost • Dependent on line-of-sight
Slurry coatings	• Simple	• Non-uniform, porous coatings
Screen printing Plasma spraying	• Simple • Thick ceramic coatings possible	• Non-uniform, porous coatings • Porous coatings • Dependent on line-of-sight
Electrodeposition	• Simple • Applicable to complex shapes	• Difficulty for Mn deposition • Interdiffusion with substrate during oxidation leading to breakaway oxidation
Composite electrodeposition	• Simple • Applicable to complex shapes • REOs can be embedded into protective scale	• Difficulty for Mn deposition
Anodic deposition	• Simple • Applicable to complex shapes	• Limited coating thickness • Poor adhesion
LAFAD	• Applicable to ceramic coatings	• High cost • Dependent on line-of-sight

Figure 34. Advantages and disadvantages of different coating deposition methods [98]

References

[1] A.G. Sabato, S. Molin, H. Javed, E. Zanchi, A.R. Boccaccini, F. Smeacetto, Corrosion evaluation of pure and in-situ Cu doped MnCo-spinel coated Crofer22APU in air at 800°C, Journal of Power Sources. (Submiited (2019).

[2] N.M. Edelstein, Lanthanide and Actinide Chemistry and Spectroscopy, 1980. doi:10.1002/0470010088.

[3] J.M. Rincon, M. Romero, Characterization Techniques of Glasses and Ceramics, 1999. doi:10.1007/978-3-662-03871-0.

[4] J. Pepi, Strength properties of glass and ceramics, 2002.

[5] M.K. Mahapatra, K. Lu, Seal glass for solid oxide fuel cells, Journal of Power Sources. 195 (2010) 7129–7139. doi:10.1016/j.jpowsour.2010.06.003.

[6] H. Scholze, Glass: Nature, Structure and Properties, 1991. doi:10.1007/978-1-4613-9069-5.

[7] M.K. Mahapatra, K. Lu, Glass-based seals for solid oxide fuel and electrolyzer cells - A review, Materials Science and Engineering R: Reports. 67 (2010) 65–85. doi:10.1016/j.mser.2009.12.002.

[8] J. Wei, T. Osipova, J. Malzbender, M. Krüger, Mechanical characterization of SOFC/SOEC cells, Ceramics International. (2018). doi:10.1016/j.ceramint.2018.03.103.

[9] L. Bernadet, G. Gousseau, A. Chatroux, J. Laurencin, F. Mauvy, M. Reytier, Assessment of Pressure Effects on High Temperature Steam Electrolysis Based on Solid Oxide Technology, ECS Transactions. 68 (2015) 3369–3378. doi:10.1149/06801.3369ecst.

[10] P. Kazempoor, C. Wendel, R.J. Braun, Pressurized Regenerative Solid Oxide Cells for Electrical Energy Storage, ECS Transactions. 58 (2014) 45–54. doi:10.1149/05837.0045ecst.

[11] S.E. Lin, Y.R. Cheng, W.C.J. Wei, BaO–B2O3–SiO2–Al2O3 sealing glass for intermediate temperature solid oxide fuel cell, Journal of Non-Crystalline Solids. 358 (2012) 174–181. doi:10.1016/j.jnoncrysol.2011.09.013.

[12] B.M. Abel, J.M. Morgan, J.C. Mauro, M.M. Smedskjaer, Liquidus Temperature of SrO-Al2O3-SiO2 glass-forming compositions, International Journal of Applied Glass Science. 4 (2013) 225–230. doi:10.1111/ijag.12017.

[13] S. Rodríguez-López, J. Wei, K.C. Laurenti, I. Mathias, V.M. Justo, F.C. Serbena, C. Baudín, J. Malzbender, M.J. Pascual, Mechanical properties of solid oxide fuel cell glass-ceramic sealants in the system BaO/SrO-MgO-B2O3-SiO2, Journal of the European Ceramic Society. 37 (2017) 3579–3594. doi:10.1016/j.jeurceramsoc.2017.03.054.

[14] X. Wang, D.R. Ou, Z. Zhao, M. Cheng, Stability of SrO–La2O3–Al2O3–SiO2 glass sealants in high-temperature air and steam, Ceramics International. 42 (2016) 7514–7523. doi:10.1016/j.ceramint.2016.01.158.

[15] L. Peng, Q. Zhu, Thermal cycle stability of BaO-B2O3-SiO2 sealing glass, Journal of Power Sources. 194 (2009) 880–885. doi:10.1016/j.jpowsour.2009.06.018.

[16] P.K. Ojha, T.K. Chongdar, N.M. Gokhale, A.R. Kulkarni, Investigation of

crystallization kinetic of SrO-La2O3-Al2O3eB2O3-SiO2 glass and its suitability for SOFC sealant, International Journal of Hydrogen Energy. 36 (2011) 14996–15001. doi:10.1016/j.ijhydene.2010.12.120.
[17] H.C. Gupta, V. Luthra, Effects ofM2+ (M = Ca, Sr, and Ba) Addition on Crystallization andMicrostructure of SiO2-MgO-Al2O3-B2O3-K2O-F Glass, Vibrational Spectroscopy. 56 (2011) 235–240. doi:10.1016/j.vibspec.2011.03.002.
[18] S.B. Sohn, S.Y. Choi, G.H. Kim, H.S. Song, G.D. Kim, Suitable Glass-Ceramic Sealant for Planar Solid-Oxide Fuel Cells, Journal of the American Ceramic Society. 87 (2004) 254–260. doi:10.1111/j.1551-2916.2004.00254.x.
[19] M. Palcut, L. Mikkelsen, K. Neufeld, M. Chen, R. Knibbe, P. V. Hendriksen, Corrosion stability of ferritic stainless steels for solid oxide electrolyser cell interconnects, Corrosion Science. 52 (2010) 3309–3320. doi:10.1016/j.corsci.2010.06.006.
[20] S.-B. Sohn, S.-Y. Choi, G.-H. Kim, H.-S. Song, G.-D. Kim, Suitable Glass-Ceramic Sealant for Planar Solid-Oxide Fuel Cells, Journal of the American Ceramic Society. 87 (2004) 254–260. doi:10.1111/j.1551-2916.2004.00254.x.
[21] A.G. Sabato, G. Cempura, D. Montinaro, A. Chrysanthou, M. Salvo, E. Bernardo, M. Secco, F. Smeacetto, Glass-ceramic sealant for solid oxide fuel cells application: Characterization and performance in dual atmosphere, Journal of Power Sources. 328 (2016) 262–270. doi:10.1016/j.jpowsour.2016.08.010.
[22] H. Javed, A.G. Sabato, K. Herbrig, D. Ferrero, C. Walter, M. Salvo, F. Smeacetto, Design and characterization of novel glass-ceramic sealants for solid oxide electrolysis cell (SOEC) applications, International Journal of Applied Ceramic Technology. 15 (2018) 999–1010. doi:10.1111/ijac.12889.
[23] T. Osipova, J. Wei, G. Pecanac, J. Malzbender, Room and elevated temperature shear strength of sealants for solid oxide fuel cells, Ceramics International. 42 (2016) 12932–12936. doi:10.1016/j.ceramint.2016.05.064.
[24] C. Lara, M.J. Pascual, A. Durán, Glass-forming ability, sinterability and thermal properties in the systems RO-BaO-SiO2(R = Mg, Zn), Journal of Non-Crystalline Solids. 348 (2004) 149–155. doi:10.1016/j.jnoncrysol.2004.08.140.
[25] B. Kaur, K. Singh, O.P. Pandey, Microstructural study of Crofer 22 APU-glass interface for SOFC application, International Journal of Hydrogen Energy. 37 (2012) 3839–3847. doi:10.1016/j.ijhydene.2011.04.160.
[26] Q. Zhu, L. Peng, T. Zhang, Y.-S.S. Chou, J.W. Stevenson, J.-P. Choi, K.D. Meinhardt, Alkali Effect on the Electrical Stability of a Solid Oxide Fuel Cell Sealing Glass, Fuel Cell Electronics Packaging. 93 (2010) 618–623. doi:10.1111/j.1551-2916.2009.03466.x.
[27] A.A. Reddy, A. Goel, D.U. Tulyaganov, S. Kapoor, K. Pradeesh, M.J. Pascual, J.M.F. Ferreira, Study of calcium-magnesium-aluminum-silicate (CMAS) glass and glass-ceramic sealant for solid oxide fuel cells, Journal of Power Sources. 231 (2013) 203–212. doi:10.1016/j.jpowsour.2012.12.055.
[28] Y. Chou, J.W. Stevenson, P. Singh, Novel Refractory Alkaline Earth Silicate Sealing Glasses for Planar Solid Oxide Fuel Cells, Journal of The Electrochemical Society. 154 (2007) 644–651. doi:10.1149/1.2733868.

[29] A.A. Reddy, D.U. Tulyaganov, M.J. Pascual, V. V. Kharton, E. V. Tsipis, V.A. Kolotygin, J.M.F. Ferreira, Diopside-Ba disilicate glass-ceramic sealants for SOFCs: Enhanced adhesion and thermal stability by Sr for Ca substitution, International Journal of Hydrogen Energy. 38 (2013) 3073–3086. doi:10.1016/j.ijhydene.2012.12.074.
[30] J.W. Fergus, Sealants for solid oxide fuel cells, Journal of Power Sources. 147 (2005) 46–57. doi:10.1016/j.jpowsour.2005.05.002.
[31] D.U. Tulyaganov, A.A. Reddy, V. V. Kharton, J.M.F. Ferreira, Aluminosilicate-based sealants for SOFCs and other electrochemical applications - A brief review, Journal of Power Sources. 242 (2013) 486–502. doi:10.1016/j.jpowsour.2013.05.099 Review.
[32] M.K. Mahapatra, K. Lu, W.T. Reynolds, Thermophysical properties and devitrification of SrO-La2O3-Al2O3-B2O3-SiO2-based glass sealant for solid oxide fuel/electrolyzer cells, Journal of Power Sources. 179 (2008) 106–112. doi:10.1016/j.jpowsour.2007.12.101.
[33] S. Wang, Y. Wang, Y. Hsu, C. Chuang, Effect of additives on the thermal properties and sealing oxide fuel cell application, International Journal of Hydrogen Energy. 34 (2009) 8235–8244. doi:10.1016/j.ijhydene.2009.07.094.
[34] H. Liu, J. Huang, D. Zhao, H. Yang, T. Zhang, Improving the electrical property of CeO2- containing sealing glass – ceramics for Solid Oxide Fuel Cell applications : Effect of HfO2, Journal of European Ceramic Society. 36 (2016) 917–923. doi:10.1016/j.jeurceramsoc.2015.10.004.
[35] Q. Zhang, H. Yang, F. Zeng, S. Wang, D. Tang, T. Zhang, Development of the CaO – SrO – ZrO2 – B2O3 – SiO2 Sealing Glasses for Solid Oxide Fuel Cell Applications : Structure, RSC Advances. 5 (2015) 41772–41779. doi:10.1039/C5RA04781A.
[36] Q. Zhang, L. Fang, J. Shen, M.J. Pascual, T. Zhang, Tuning the Interfacial Reaction Between Bismuth-Containing Sealing Glasses and Cr-Containing Interconnect: Effect of ZnO, Journal of American Ceramic Society. 98 (2015) 3797–3806. doi:10.1111/jace.13779.
[37] A. Arora, K. Singh, O.P. Pandey, Thermal , structural and crystallization kinetics of SiO2 - BaO - ZnO - B2O 3 - Al2O3 glass samples as a sealant for SOFC, International Journal of Hydrogen Energy. 36 (2011) 14948–14955. doi:10.1016/j.ijhydene.2011.03.036.
[38] M.J. Da, J.F. Bartolomé, A.H. De Aza, S. Mello-castanho, Glass ceramic sealants belonging to BAS (BaO – Al2O3 – SiO2) ternary system modified with B2O3 addition : A different approach to access the SOFC seal issue, Journal of the European Ceramic Society. 36 (2016) 631–644.
[39] Q. Zhang, X. Du, S. Tan, D. Tang, K. Chen, T. Zhang, Effect of Nb 2 O 5 doping on improving the thermo-mechanical stability of sealing interfaces for solid oxide fuel cells, (2017) 1–8. doi:10.1038/s41598-017-05725-y.
[40] X. Wang, R. Li, J. Yang, D. Gu, D. Yan, J. Pu, B. Chi, J. Li, Effect of YSZ addition on the performance of glass-ceramic seals for intermediate temperature solid oxide fuel cell application, International Journal of Hydrogen Energy. (2018) 1–8. doi:10.1016/j.ijhydene.2018.03.023.
[41] K. Chen, S.P. Jiang, Review — Materials Degradation of Solid Oxide Electrolysis Cells, Journal of The Electrochemical Society. 163 (2016) 3070–3083. doi:10.1149/2.0101611jes.
[42] S. Ghosh, A. Das Sharma, P. Kundu, R.N. Basu, Glass-based sealants for application in planar solid oxide fuel cell stack, Transactions of the Indian

Ceramic Society. 67 (2008) 161–182. doi:10.1080/0371750X.2008.11078652.
[43] F. Smeacetto, M. Salvo, P. Leone, M. Santarelli, M. Ferraris, Performance and testing of joined Crofer22APU-glass-ceramic sealant-anode supported cell in SOFC relevant conditions, Materials Letters. 65 (2011) 1048–1052. doi:10.1016/j.matlet.2010.12.050.
[44] F. Smeacetto, A. De Miranda, A. Chrysanthou, E. Bernardo, M. Secco, M. Bindi, M. Salvo, A.G. Sabato, M. Ferraris, Novel glass-ceramic composition as sealant for SOFCs, Journal of the American Ceramic Society. 97 (2014) 3835–3842. doi:10.1111/jace.13219.
[45] F. Smeacetto, M. Salvo, M. Santarelli, P. Leone, G.A. Ortigoza-Villalba, A. Lanzini, L.C. Ajitdoss, M. Ferraris, Performance of a glass-ceramic sealant in a SOFC short stack, International Journal of Hydrogen Energy. 38 (2013) 588–596. doi:10.1016/j.ijhydene.2012.07.025.
[46] F. Smeacetto, A. Chrysanthou, M. Salvo, T. Moskalewicz, F. D'Herin Bytner, L.C. Ajitdoss, M. Ferraris, Thermal cycling and ageing of a glass-ceramic sealant for planar SOFCs, International Journal of Hydrogen Energy. 36 (2011) 11895–11903. doi:10.1016/j.ijhydene.2011.04.083.
[47] F. Smeacetto, M. Salvo, M. Ferraris, J. Cho, A.R. Boccaccini, Glass-ceramic seal to join Crofer 22 APU alloy to YSZ ceramic in planar SOFCs, Journal of the European Ceramic Society. 28 (2008) 61–68. doi:10.1016/j.jeurceramsoc.2007.05.006.
[48] F. Smeacetto, A. De Miranda, A. Ventrella, M. Salvo, M. Ferraris, Shear strength tests of glass ceramic sealant for solid oxide fuel cells applications, Advances in Applied Ceramics. 114 (2015) S70–S75. doi:10.1179/1743676115Y.0000000042.
[49] A.A. Reddy, D.U. Tulyaganov, A. Goel, M.J. Pascual, V. V. Kharton, E. V. Tsipis, J.M.F. Ferreira, Diopside - Mg orthosilicate and diopside - Ba disilicate glass-ceramics for sealing applications in SOFC: Sintering and chemical interactions studies, International Journal of Hydrogen Energy. 37 (2012) 12528–12539. doi:10.1016/j.ijhydene.2012.05.130.
[50] X. Wang, D.R. Ou, Z. Zhao, M. Cheng, Stability of SrO-La2O3-Al2O3-SiO2glass sealants in high-temperature air and steam, Ceramics International. 42 (2016) 7514–7523. doi:10.1016/j.ceramint.2016.01.158.
[51] A.A. Reddy, A. Goel, D.U. Tulyaganov, M. Sardo, L. Mafra, M.J. Pascual, V. V. Kharton, E. V. Tsipis, V.A. Kolotygin, J.M.F. Ferreira, Thermal and mechanical stability of lanthanide-containing glass–ceramic sealants for solid oxide fuel cells, Journal of Materials Chemistry A. 2 (2014) 1834. doi:10.1039/c3ta13196c.
[52] Y.S. Chou, J.W. Stevenson, P. Singh, Effect of pre-oxidation and environmental aging on the seal strength of a novel high-temperature solid oxide fuel cell (SOFC) sealing glass with metallic interconnect, Journal of Power Sources. 184 (2008) 238–244. doi:10.1016/j.jpowsour.2008.06.020.
[53] Y.S. Chou, J.W. Stevenson, G.G. Xia, Z.G. Yang, Electrical stability of a novel sealing glass with (Mn,Co)-spinel coated Crofer22APU in a simulated SOFC dual environment, Journal of Power Sources. 195 (2010) 5666–5673. doi:10.1016/j.jpowsour.2010.03.052.
[54] C.K. Lin, Y.A. Liu, S.H. Wu, C.K. Liu, R.Y. Lee, Joint strength of a solid oxide fuel cell glass-ceramic sealant with metallic interconnect in a reducing environment, Journal of Power Sources. 280 (2015) 272–288. doi:10.1016/j.jpowsour.2015.01.126.

[55] Y.S. Chou, J.W. Stevenson, J.P. Choi, Long-term evaluation of solid oxide fuel cell candidate materials in a 3-cell generic short stack fixture, Part II: Sealing glass stability, microstructure and interfacial reactions, Journal of Power Sources. 250 (2014) 166–173. doi:10.1016/j.jpowsour.2013.09.148.
[56] M.J. Pascual, A. Guillet, A. Durán, Optimization of glass-ceramic sealant compositions in the system MgO-BaO-SiO2for solid oxide fuel cells (SOFC), Journal of Power Sources. 169 (2007) 40–46. doi:10.1016/j.jpowsour.2007.01.040.
[57] M. Kerstan, M. Mueller, C. Ruessel, Binary, ternary and quaternary silicates of CaO, BaO and ZnO in high thermal expansion seals for solid oxide fuel cells studied by high-temperature X-ray diffraction (HT-XRD), Materials Research Bulletin. 46 (2011) 2456–2463. doi:10.1016/j.materresbull.2011.08.031.
[58] Z. Yang, K.D. Meinhardt, J.W. Stevenson, Chemical Compatibility of Barium-Calcium-Aluminosilicate-Based Sealing Glasses with the Ferritic Stainless Steel Interconnect in SOFCs, Journal of The Electrochemical Society. 150 (2003) A1095. doi:10.1149/1.1590325.
[59] L. Peng, Q. Zhu, The Development of Thermally Stable Sealing Glass in the BaO–B2O3–SiO2 System for Planar SOFC Applications, Journal of Fuel Cell Science and Technology. 5 (2008) 31210. doi:10.1115/1.2930768.
[60] Q. Zhu, L. Peng, T. Zhang, Stable Glass Seals for Intermediate Temperature (IT) SOFC Applications, Fuel Cell Electronics Packaging. (2007) 33–60. doi:10.1007/978-0-387-47324-6_2.
[61] J. Izdebska, S. Thomas, Printing on Polymers. Fundamentals and Applications, Elsevier, n.d.
[62] L.S. Mahmud, A. Muchtar, M.R. Somalu, Challenges in fabricating planar solid oxide fuel cells: A review, Renewable and Sustainable Energy Reviews. 72 (2017) 105–116. doi:10.1016/j.rser.2017.01.019.
[63] C. Lu, T. Sholklapper, C.P. Jacobson, S.J. Visco, L.C. Dejonghe, Modified LSM-YSZ Cathodes for Reduced Temperature Solid Oxide Fuel Cells (SOFC), (n.d.) 800–800.
[64] Y. Xia, Y. Hu, L. Ren, X. Luo, W. Gong, H. Zhou, Manufacturing a high performance film of CaO-B2O3-SiO2glass-ceramic powder with surface modification for LTCC application, Journal of the European Ceramic Society. 38 (2018) 253–261. doi:10.1016/j.jeurceramsoc.2017.08.003.
[65] F. Tietz, H.-P. Buchkremer, D. Stöver, Components manufacturing for solid oxide fuel cells, Solid State Ionics. 152–153 (2002) 373–381. doi:10.1016/S0167-2738(02)00344-2.
[66] M.R. Somalu, A. Muchtar, W.R.W. Daud, N.P. Brandon, Screen-printing inks for the fabrication of solid oxide fuel cell films: A review, Renewable and Sustainable Energy Reviews. 75 (2017) 426–439. doi:10.1016/j.rser.2016.11.008.
[67] W.J. Tseng, C. Chen, Effect of polymeric dispersant on rheological beha v ior of nickel Á terpineol suspensions, Materials Science and Engineering A. 347 (2003) 145–153. doi:10.1016/S0921-5093(02)00562-2.
[68] M.R. Somalu, V. Yufit, I.P. Shapiro, P. Xiao, N.P. Brandon, The impact of ink rheology on the properties of screen-printed solid oxide fuel cell anodes, International Journal of Hydrogen Energy. 38 (2013) 6789–6801. doi:10.1016/j.ijhydene.2013.03.108.
[69] M.R. Somalu, V. Yufit, N.P. Brandon, The effect of solids loading on the

screen-printing and properties of nickel/scandia-stabilized-zirconia anodes for solid oxide fuel cells, International Journal of Hydrogen Energy. 38 (2013) 9500–9510. doi:10.1016/j.ijhydene.2012.06.061.

[70] P. Ried, C. Lorenz, A. Brönstrup, T. Graule, N.H. Menzler, W. Sitte, P. Holtappels, Processing of YSZ screen printing pastes and the characterization of the electrolyte layers for anode supported SOFC, Journal of the European Ceramic Society. 28 (2008) 1801–1808. doi:10.1016/j.jeurceramsoc.2007.11.018.

[71] C. Collins, J. Lucas, T.L. Buchanan, M. Kopczyk, A. Kayani, P.E. Gannon, M.C. Deibert, R.J. Smith, D.S. Choi, V.I. Gorokhovsky, Chromium volatility of coated and uncoated steel interconnects for SOFCs, Surface and Coatings Technology. 201 (2006) 4467–4470. doi:10.1016/j.surfcoat.2006.08.053.

[72] M. V. Glazoff, S.N. Rashkeev, J.S. Herring, Controlling chromium vaporization from interconnects with nickel coatings in solid oxide devices, International Journal of Hydrogen Energy. 39 (2014) 15031–15038. doi:10.1016/j.ijhydene.2014.07.023.

[73] R. Sachitanand, M. Sattari, J.E. Svensson, J. Froitzheim, The Oxidation of Coated SOFC Interconnects in Fuel Side Environments, Fuel Cells. 16 (2016) 32–38. doi:10.1002/fuce.201500066.

[74] J. Froitzheim, L. Niewolak, M. Brandner, L. Singheiser, W.J. Quadakkers, Anode Side Diffusion Barrier Coating for Solid Oxide Fuel Cells Interconnects, Journal of Fuel Cell Science and Technology. 7 (2010) 31020. doi:10.1115/1.3182731.

[75] H. Falk-Windisch, J.E. Svensson, J. Froitzheim, The effect of temperature on chromium vaporization and oxide scale growth on interconnect steels for Solid Oxide Fuel Cells, Journal of Power Sources. 287 (2015) 25–35. doi:10.1016/j.jpowsour.2015.04.040.

[76] A. Gil, J. Wyrwa, T. Brylewski, Improving the Oxidation Resistance and Electrical Properties of Ferritic Stainless Steels for Application in SOFC Interconnects, Oxidation of Metals. 85 (2016) 151–169. doi:10.1007/s11085-015-9605-9.

[77] J.C.W. Mah, A. Muchtar, M.R. Somalu, M.J. Ghazali, J. Raharjo, Formation of sol–gel derived (Cu,Mn,Co)3O4 spinel and its electrical properties, Ceramics International. 43 (2017) 7641–7646. doi:10.1016/j.ceramint.2017.03.060.

[78] M. Bobruk, S. Molin, M. Chen, T. Brylewski, P. V. Hendriksen, Sintering of MnCo2O4coatings prepared by electrophoretic deposition, Materials Letters. 213 (2018) 394–398. doi:10.1016/j.matlet.2017.12.046.

[79] B. Talic, S. Molin, K. Wiik, P.V. Hendriksen, H.L. Lein, Comparison of iron and copper doped manganese cobalt spinel oxides as protective coatings for solid oxide fuel cell interconnects, Journal of Power Sources. 372 (2017) 145–156. doi:10.1016/j.jpowsour.2017.10.060.

[80] F. Shen, K. Lu, Co_3O_4 /Sm-Doped CeO_2 /Co_3O_4 Trilayer Coating on AISI 441 Interconnect for Solid Oxide Fuel Cells, ACS Applied Materials & Interfaces. 9 (2017) 6022–6029. doi:10.1021/acsami.6b14562.

[81] D. Szymczewska, S. Molin, V. Venkatachalam, M. Chen, P. Jasinski, P. V. Hendriksen, Assesment of (Mn,Co)33O4 powders for possible coating material for SOFC/SOEC interconnects, IOP Conference Series: Materials Science and Engineering. 104 (2016). doi:10.1088/1757-899X/104/1/012017.

[82] Y. Xie, W. Qu, B. Yao, N. Shaigan, L. Rose, Dense Protective Coatings for SOFC Interconnect Deposited by Spray Pyrolysis, ECS Transactions. 26 (2010) 357–362.
[83] J.C.W. Mah, A. Muchtar, M.R. Somalu, M.J. Ghazali, Metallic interconnects for solid oxide fuel cell: A review on protective coating and deposition techniques, International Journal of Hydrogen Energy. 42 (2017) 9219–9229. doi:10.1016/j.ijhydene.2016.03.195.
[84] S. Molin, A.G. Sabato, M. Bindi, P. Leone, G. Cempura, M. Salvo, S. Cabanas Polo, A.R. Boccaccini, F. Smeacetto, Microstructural and electrical characterization of Mn-Co spinel protective coatings for solid oxide cell interconnects, Journal of the European Ceramic Society. 37 (2017) 4781–4791. doi:10.1016/j.jeurceramsoc.2017.07.011.
[85] H. Falk-Windisch, J. Claquesin, M. Sattari, J.-E. Svensson, J. Froitzheim, Co- and Ce/Co-coated ferritic stainless steel as interconnect material for Intermediate Temperature Solid Oxide Fuel Cells, Journal of Power Sources. 343 (2017) 1–10. doi:10.1016/j.jpowsour.2017.01.045.
[86] J.F. Hannes Falk-Windisch, Ioannis Mertzidis, Jan-Erik Svensson, Pre-coated Ce/Co-coated Steel: Mitigating Cr Vaporization, Increasing Corrosion Resistance at Competitive Cost, ECS Transactions. 68 (2014) 1–5. doi:10.1007/s13398-014-0173-7.2.
[87] H. Falk-Windisch, J.E. Svensson, J. Froitzheim, The effect of temperature on chromium vaporization and oxide scale growth on interconnect steels for Solid Oxide Fuel Cells, Journal of Power Sources. 287 (2015) 25–35. doi:10.1016/j.jpowsour.2015.04.040.
[88] J. Froitzheim, S. Canovic, M. Nikumaa, R. Sachitanand, L.G. Johansson, J.E. Svensson, Long term study of Cr evaporation and high temperature corrosion behaviour of Co coated ferritic steel for solid oxide fuel cell interconnects, Journal of Power Sources. 220 (2012) 217–227. doi:10.1016/j.jpowsour.2012.06.092.
[89] J.G. Grolig, J. Froitzheim, J. Svensson, Coated stainless steel 441 as interconnect material for solid oxide fuel cells : Oxidation performance and chromium evaporation q, Journal of Power Sources. 248 (2014) 1007–1013. doi:10.1016/j.jpowsour.2013.08.089.
[90] S. Canovic, J. Froitzheim, R. Sachitanand, M. Nikumaa, M. Halvarsson, Surface & Coatings Technology Oxidation of Co- and Ce-nanocoated FeCr steels : A microstructural investigation, Surface & Coatings Technology. 215 (2013) 62–74. doi:10.1016/j.surfcoat.2012.08.096.
[91] A. Magraso, H. Falk-windisch, J. Froitzheim, J. Svensson, R. Haugsrud, Reduced long term electrical resistance in Ce / Co- coated ferritic stainless steel for solid oxide fuel cell metallic interconnects, International Journal of Hydrogen Energy. 40 (2015) 8579–8585. doi:10.1016/j.ijhydene.2015.04.147.
[92] J. Froitzheim, J.E. Svensson, Multifunctional Nano-Coatings for SOFC Interconnects, The Electrochemical Society. 35 (2011) 2503–2508.
[93] M. Stanislowski, J. Froitzheim, L. Niewolak, W.J. Quadakkers, K. Hilpert, T. Markus, L. Singheiser, Reduction of chromium vaporization from SOFC interconnectors by highly effective coatings, Journal of Power Sources. 164 (2007) 578–589. doi:10.1016/j.jpowsour.2006.08.013.
[94] J. Chen, K. Lin, Y. Yang, S. Yeh, Plasma-Sprayed LSM Protective Coating on Metallic Interconnect of SOFC, Coatings. 226 (2017). doi:10.3390/coatings7120226.

[95] S. Lee, C. Chu, M. Tsai, J. Lee, High temperature oxidation behavior of interconnect coated with LSCF and LSM for solid oxide fuel cell by screen printing, Applied Surface Science. 256 (2010) 1817–1824. doi:10.1016/j.apsusc.2009.10.013.
[96] L. Sr, M. Cathode, S. Oxide, F. Cells, Y. Larring, T. Norby, Spinel and Perovskite Functional Layers Between Plansee Metallic Interconnect (Cr-5 wt % Fe-1 wt % Y 2 O 3) and Ceramic (La0.85Sr0.15)0.91MnO3 Cathode Materials for Solid Oxide Fuel Cells, Journal of The Electrochemical Society. 147 (2000) 3251–3256.
[97] Z. Yang, G.G. Xia, G.D. Maupin, J.W. Stevenson, Conductive protection layers on oxidation resistant alloys for SOFC interconnect applications, Surface and Coatings Technology. 201 (2006) 4476–4483. doi:10.1016/j.surfcoat.2006.08.082.
[98] N. Shaigan, W. Qu, D.G. Ivey, W. Chen, A review of recent progress in coatings , surface modifications and alloy developments for solid oxide fuel cell ferritic stainless steel interconnects, Journal of Power Sources. 195 (2010) 1529–1542. doi:10.1016/j.jpowsour.2009.09.069.
[99] A. Petric, H. Ling, Electrical conductivity and thermal expansion of spinels at elevated temperatures, Journal of the American Ceramic Society. 90 (2007) 1515–1520. doi:10.1111/j.1551-2916.2007.01522.x.
[100] S.-I. Lee, J. Hong, H. Kim, J.-W. Son, J.-H. Lee, B.-K. Kim, H.-W. Lee, K.J. Yoon, Highly Dense Mn-Co Spinel Coating for Protection of Metallic Interconnect of Solid Oxide Fuel Cells, Journal of the Electrochemical Society. 161 (2014) F1389–F1394. doi:10.1149/2.0541414jes.
[101] Y. Zhang, A. Javed, M. Zhou, S. Liang, P. Xiao, Fabrication of Mn-Co spinel coatings on Crofer 22 APU stainless steel by electrophoretic deposition for interconnect applications in solid oxide fuel cells, International Journal of Applied Ceramic Technology. 11 (2014) 332–341. doi:10.1111/ijac.12013.
[102] Z. Yang, G.G. Xia, X.H. Li, J.W. Stevenson, (Mn,Co)3O4 spinel coatings on ferritic stainless steels for SOFC interconnect applications, International Journal of Hydrogen Energy. 32 (2007) 3648–3654. doi:10.1016/j.ijhydene.2006.08.048.
[103] J. Yoo, S.K. Woo, J.H. Yu, S. Lee, G.W. Park, La0.8Sr0.2MnO3 and (Mn1.5Co1.5)O4 double layer coated by electrophoretic deposition on Crofer22 APU for SOEC interconnect applications, International Journal of Hydrogen Energy. 34 (2009) 1542–1547. doi:10.1016/j.ijhydene.2008.12.005.
[104] F. Smeacetto, A. De Miranda, S. Cabanas Polo, S. Molin, D. Boccaccini, M. Salvo, A.R. Boccaccini, Electrophoretic deposition of Mn1.5Co1.5O4 on metallic interconnect and interaction with glass-ceramic sealant for solid oxide fuel cells application, Journal of Power Sources. 280 (2015) 379–386. doi:10.1016/j.jpowsour.2015.01.120.
[105] Z. Yang, G. Xia, J.W. Stevenson, Mn 1 . 5 Co 1 . 5 O 4 Spinel Protection Layers on Ferritic Stainless Steels for SOFC Interconnect Applications, Surface & Coatings Technology. (2005) 168–170. doi:10.1149/1.1854122.
[106] Z. Sun, S. Gopalan, U.B. Pal, S.N. Basu, Cu1.3Mn1.7O4 spinel coatings deposited by electrophoretic deposition on Crofer 22 APU substrates for solid oxide fuel cell applications, Surface & Coatings Technology. 323 (2017) 49–57. doi:10.1016/j.surfcoat.2016.09.028.
[107] A. Masi, M. Bellusci, J. Stephen, F. Padella, P. Reale, R. Steinberger-

wilckens, A. Masi, M. Bellusci, S.J. Mcphail, F. Padella, P. Reale, J. Hong, R. Steinberger-wilckens, The Effect of Chemical Composition on High Temperature Behaviour of Fe and Cu Doped Mn-Co spinels, Ceramics International. 43 (2016) 2829–2835. doi:10.1016/j.ceramint.2016.11.135.
[108] A. Masi, M. Bellusci, S.J. Mcphail, F. Padella, P. Reale, J. Hong, R. Steinberger-wilckens, M. Carlini, Cu-Mn-Co oxides as protective materials in SOFC technology: The effect of chemical composition on mechanochemical synthesis, sintering behaviour, thermal expansion and electrical conductivity, Journal of the European Ceramic Society. (2016). doi:10.1016/j.jeurceramsoc.2016.09.025.
[109] J. Li, C. Xiong, J. Li, D. Yan, J. Pu, B. Chi, L. Jian, Investigation of MnCu0.5Co1.5O4 spinel coated SUS430 interconnect alloy for preventing chromium vaporization in intermediate temperature solid oxide fuel cell, International Journal of Hydrogen Energy. (2017) 2–9. doi:10.1016/j.ijhydene.2017.05.074.
[110] W. Huang, S. Gopalan, U.B. Pal, S.N. Basu, Evaluation of Electrophoretically Deposited CuMn1.8O4 Spinel Coatings on Crofer 22 APU for Solid Oxide Fuel Cell Interconnects, Journal of The Electrochemical Society. 155 (2008) B1161. doi:10.1149/1.2975367.
[111] R. Wang, Z. Sun, U.B. Pal, S. Gopalan, S.N. Basu, Mitigation of chromium poisoning of cathodes in solid oxide fuel cells employing CuMn1.8O4spinel coating on metallic interconnect, Journal of Power Sources. 376 (2018) 100–110. doi:10.1016/j.jpowsour.2017.11.069.
[112] Z. Sun, R. Wang, A.Y. Nikiforov, S. Gopalan, U.B. Pal, S.N. Basu, CuMn1.8O4protective coatings on metallic interconnects for prevention of Cr-poisoning in solid oxide fuel cells, Journal of Power Sources. 378 (2018) 125–133. doi:10.1016/j.jpowsour.2017.12.031.
[113] Z. Sun, S. Gopalan, U.B. Pal, S.N. Basu, Cu1.3Mn1.7O4spinel coatings deposited by electrophoretic deposition on Crofer 22 APU substrates for solid oxide fuel cell applications, Surface and Coatings Technology. 323 (2017) 49–57. doi:10.1016/j.surfcoat.2016.09.028.
[114] T. Minami, Y. Ohtani, T. Miyata, T. Kuboi, Transparent conducting Al-doped ZnO thin films prepared by magnetron sputtering with dc and rf powers applied in combination Transparent conducting Al-doped ZnO thin films prepared by magnetron sputtering with dc and rf powers applied in combination, 1172 (2011). doi:10.1116/1.2748809.
[115] J.M. Schneider, W.D. Sproul, A. Matthews, Reactive ionized magnetron sputtering of crystalline alumina coatings, Surface and Coatings Technology. 98 (1998) 1473–1476. doi:10.1016/S0257-8972(97)00140-0.
[116] J.M. Schneider, W.D. Sproul, R.W.J. Chia, M. Wong, A. Matthews, Very-high-rate reactive sputtering of alumina hard coatings, 96 (1997) 262–266.
[117] P.. Kelly, R.. Arnell, Magnetron sputtering: a review of recent developments and applications, Vacuum. 56 (2000) 159–172. doi:10.1016/S0042-207X(99)00189-X.
[118] D. Constantin, M. Apreutesei, Magnetron Sputtering Technique Used For Coatings Deposition; Technologies And Applications, Materials Science. (2011) 24–26.
[119] J.G. Han, Recent progress in thin film processing by magnetron sputtering with plasma diagnostics, Journal of Physics D: Applied Physics. 42 (2009) 43001. doi:10.1088/0022-3727/42/4/043001.
[120] https://www.dentonvacuum.com/products-technologies/magnetron-

sputtering/, (n.d.).
[121] M. Palcut, L. Mikkelsen, K. Neufeld, M. Chen, R. Knibbe, P.V. Hendriksen, Improved oxidation resistance of ferritic steels with LSM coating for high temperature electrochemical applications, International Journal of Hydrogen Energy. 37 (2012) 8087–8094. doi:10.1016/j.ijhydene.2011.11.138.
[122] N. V. Gavrilov, V. V. Ivanov, A.S. Kamenetskikh, A. V. Nikonov, Investigations of Mn-Co-O and Mn-Co-Y-O coatings deposited by the magnetron sputtering on ferritic stainless steels, Surface and Coatings Technology. 206 (2011) 1252–1258. doi:10.1016/j.surfcoat.2011.08.036.
[123] Q. Fu, F. Tietz, D. Sebold, E. Wessel, H.P. Buchkremer, Magnetron-sputtered cobalt-based protective coatings on ferritic steels for solid oxide fuel cell interconnect applications, Corrosion Science. 54 (2012) 68–76. doi:10.1016/j.corsci.2011.08.051.
[124] H. Xu, I.P. Shapiro, P. Xiao, The influence of pH on particle packing in YSZ coatings electrophoretically deposited from a non-aqueous suspension, Journal of the European Ceramic Society. 30 (2010) 1105–1114. doi:10.1016/j.jeurceramsoc.2009.07.021.
[125] J.C. Marrero, N.F.P. Ribeiro, C.F. Malfatti, M.M.V.M. Souza, Characterization of yttria-stabilized zirconia films deposited by dip-coating on La0.7Sr0.3MnO3 substrate: Influence of synthesis parameters, Journal of Advanced Ceramics. 2 (2013) 55–62. doi:10.1007/s40145-013-0042-4.
[126] http://www.substech.com/dokuwiki/doku.php?id=electrophoretic_deposition, (n.d.).
[127] L. Ye, K. Wen, Z. Zhang, F. Yang, Y. Liang, W. Lv, Y. Lin, J. Gu, J.H. Dickerson, W. He, Highly Efficient Materials Assembly Via Electrophoretic Deposition for Electrochemical Energy Conversion and Storage Devices, Advanced Energy Materials. 6 (2016) 1–15. doi:10.1002/aenm.201502018.
[128] B. Talic, H. Falk-Windisch, V. Venkatachalam, P.V. Hendriksen, K. Wiik, H.L. Lein, Effect of coating density on oxidation resistance and Cr vaporization from solid oxide fuel cell interconnects, Journal of Power Sources. 354 (2017) 57–67. doi:10.1016/j.jpowsour.2017.04.023.

Chapter 3

Experimental

The experimental work has been divided into two main categories:

1. Synthesis, characterization and testing of novel glass-ceramic sealants for SOEC applications.

2. Deposition, characterization and testing of protective coatings on the Crofer22APU interconnect to hinder the Cr evaporation at high working temperature of SOEC.

3.1 Glass-ceramic sealants

The following sections will describe the methodology of glass synthesis, the novel compositions and different characterization techniques used to evaluate the thermo-mechanical properties and performance of glasses and glass-ceramics sealant according to the real working conditions of SOECs. The novel glass-ceramic sealants have been designed to operate at a working temperature of 850°C.

3.1.1 Synthesis of glasses

In this research work, novel glass-ceramics are designed by tailoring their compositions to obtain suitable sealants for SOEC applications. The novel glass compositions and their corresponding IDs are given in section 3.1.3. Glasses with specific compositions were synthesized by thoroughly mixing the different oxides and carbonates for at least 24 hours. The mixture of oxides and carbonates was then melted at 1600 °C in a Pt-Rh crucible for 1 hour to ensure the homogenization of the molten glass. Subsequently, the melted mixture was air quenched on a brass plate. The synthesized bulk glass was then crushed using ball milling and consequently sieved to obtain particles of a size <25um. The process of glass casting and sieving is summarized in Figure 35.

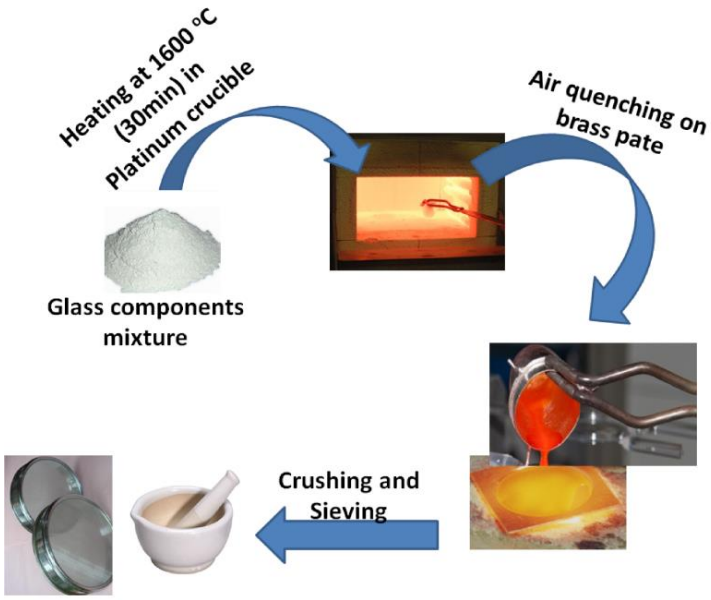

Figure 35. Systematic illustration of glass synthesis by melt quenching process

The different raw materials used to produce all the glass compositions are summarized in Table 6.

Table 6. List of raw materials used to synthesize different glasses

Raw Chemical	Desired oxide in glass	Purity
SiO_2	SiO_2	>99%
H_3BO_3	B_2O_3	99.99%
$CaCO_3$	CaO	>99%
$MgCO_3$	MgO	>99%
$SrCO_3$	SrO	>99%
$BaCO_3$	BaO	>99%
Al_2O_3	Al_2O_3	99.9%
Y_2O_3	Y_2O_3	99.99%

The pathway followed to synthesis and characterization of glasses and glass-ceramics has been summarized in Figure 36.

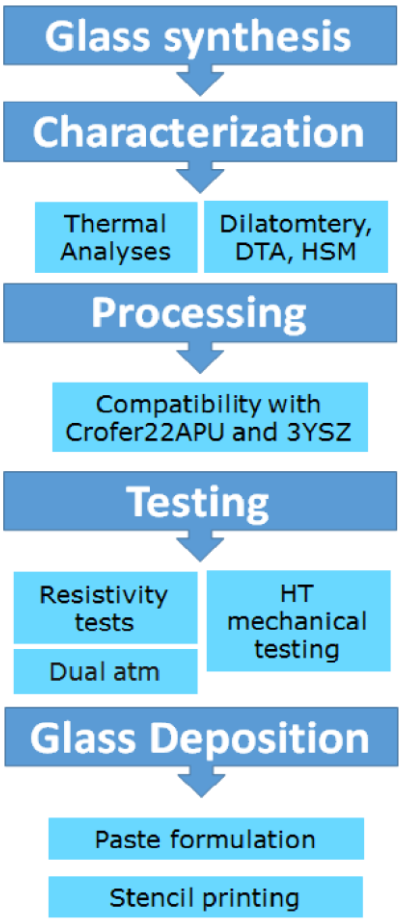

Figure 36. Systematic illustration of synthesis and testing workflow used to characterized the glasses

3.1.2 Characterizations of glasses and glass-ceramics

Thermal characterization of glasses

As-casted glasses were ground by using ball milling and consequently sieving by using mesh to obtain glass particles <25 µm. All the characterizations shown in this research will be carried out on the glasses with particle size <25 µm.

The first screening step for any glass system is to investigate its thermal properties. Therefore, to analyze the glass transition temperature (T_g), onset of crystallization temperature (T_x) and peak of crystallization temperature (T_p), differential thermal analysis (DTA Netzsch, Eos, Selb, Germany) was carried out. The DTA analysis was performed up to 1200 °C at a heating rate of 5 °C/min by using Pt-Rh crucibles. Before analyzing the behavior of a particular glass, a calibration (i.e. a baseline) is made by using the pure Al_2O_3 powder, which is thermally stable up to 1200 °C and does not undergo any phase change. After calibration, the thermal behavior of that particular glass powder was analyzed against the alumina (Al_2O_3) standard powder as reference. Three measurements were made for each glass composition in order to obtain the statistical data.

The sintering behavior of glasses was analyzed by heating stage microscopy (HSM, Hesse Instruments Germany) up to 1200 °C at a heating rate of 5 °C/min.

For HSM analysis, a cylindrical pellet of the glass powder was prepared by manual pressing in a steel mold. The cylindrical pellet has both a diameter and width of 3mm. The HSM instrument records the height of the pellet by photographing it for each degree rise in temperature. With the help of these images, HSM measures the shrinkage of the pellet against the temperature and consequently provides the first shrinkage temperature (T_{FS}), the maximum shrinkage temperature (T_{MS}) and the temperatures corresponding to when the cylindrical pellet becomes like a sphere (T_s) and starts flowing (T_F). Three measurements were carried out on each glass composition to ensure the reproducibility of the results. The peak crystallization temperature (T_p) as obtained from DTA, and maximum sintering temperature (T_{MS}) as obtained from HSM are important parameters to decide the joining treatment of a particular glass system, in order to obtain highly dense and sufficiently crystallized glass-ceramic with optimum thermo-mechanical properties.

The coefficient of thermal expansion (CTE) of the as-casted glasses was measured by using a dilatometer (Netzsch, DIL 402 PC/4) at a heating rate of 5°C/min up to the softening temperature of each type of glass. For the dilatometer analysis of the as-casted glasses, two opposite sides of the bulk glass were smoothly polished to make them plane parallel and to obtain a height of 4-5 mm. At least three measurements were performed on each composition to obtain reliable values.

XRD analysis was performed using X-Ray diffraction (PanAlytical X'Pert Pro PW 3040/60 Philips, The Netherlands), with CuK_α to investigate the amorphous nature of the as-casted glasses. These analyses were performed on the glass powders in the range of 2 theta 10° - 70°, with step size of 0.02626° and time per step of 10.20 sec.

Thermal characterization and compatibility analysis of glass-ceramics

Glass-ceramics were synthesized by heating the parent glass powders according to a proper heating treatment, based on the characteristic temperatures (crystallization and sintering temperatures) obtained from the DTA and HSM experiments. For each glass system, the temperature for glass-ceramic synthesis is higher than the crystallization temperature (T_p) and sintering temperature (T_{MS}) to ensure maximum crystallization and complete sintering in order to obtain fully dense glass-ceramics. The heat treatments of different glass-ceramics will be described in section 4.1.

For the dilatometer analysis on the glass-ceramics, first of all a pellet of glass powder with a diameter of 10 mm was prepared by pressing the powder in a mold. The corresponding glass-ceramic was prepared by heating the green pellet in a carbolite furnace (CWF 13/5) in static air. The synthesized pellet of glass-ceramic was then polished to make two sides perfectly parallel and to have a final height of 4-5 mm. Figure 37 shows the dilatometer samples for the as-casted glass and glass-ceramic. Three pellets were prepared for each glass composition and

dilatometer measurements were performed twice on each pellet. The dilatometer measurement was made up to 1000 °C (unless the glass-ceramic softened before) at a heating rate of 5°C/min.

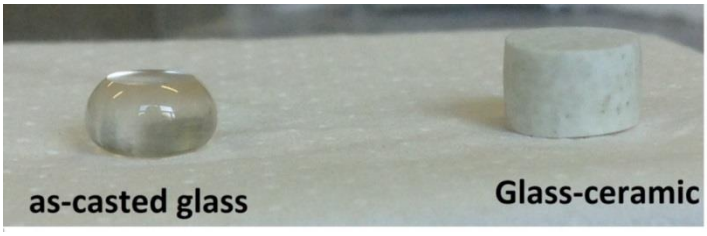

Figure 37. As-cast glass and glass-ceramic pellets for CTE measurement by dilatometer

XRD analysis was performed on the glass-ceramics to investigate the formation of different crystalline phases. XRD was carried out on the glass-ceramics in powder form, using the same parameters mentioned before i.e. in the range of 2 theta 10°-70°, with a step size of 0.02626° and time per step 10.20 sec. The different crystalline phases were identified by using the X-Pert software database.

To investigate the compatibility of the glass-ceramic sealants with the Crofer22APU interconnect and the 3YSZ electrolyte, the Crofer22APU/glass-ceramic/3YSZ joined samples were prepared in a carbolite furnace (CWF 13/5). Each substrate has dimensions of almost 15 mm x 15 mm. Before joining, the substrates were cleaned with acetone and deionized water to remove any surface contamination or dust. The glass was then deposited manually with the help of a spatula in the form of slurry containing the glass powder and ethanol in 70:30 wt%. For the joining process, a load of 15 g/cm^2 was used on the upper substrate to simulate the real pressure conditions as in the SOEC stack. The joining process is described in Figure 38. Joining of different glass systems was performed according to a certain heat treatment at different joining temperatures and by using different heating/cooling rates and holding times.

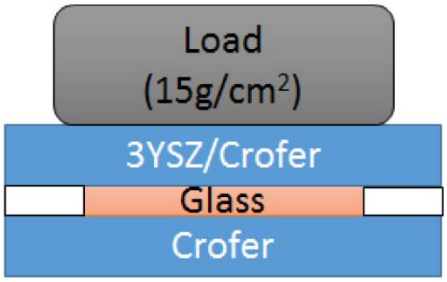

Figure 38. Joining process setup to prepare Crofer22APU/glass-ceramic/3YSZ joints

After joining, the Crofer22APU/glass-ceramic/3YSZ joints were polished up to 1µm using diamond paste and consequently coated with gold. The adhesion and interface of the glass-ceramic with Crofer22APU and 3YSZ, as well as the formation and distribution of different crystals within the glass-ceramic, were investigated by scanning electron microscope (FESEM, Merlin ZEISS). EDS point analysis was carried out to understand the chemical composition of any particular phase within the glass-ceramics. EDS line scans were also done at the

Crofer22APU/glass-ceramic interface to investigate the diffusion of elements across the interface. SEM and EDS analyses were performed after the joining of the Crofer22APU/glass-ceramic/3YSZ joined sample, as well as after ageing the joint for 1000 hours in static air at 850°C.

Electrical characterization of glass-ceramics in air

Sealants for SOEC applications must be electrical insulators with electrical resistivity > 10^4 Ω.cm [1,2]. To investigate the electrical properties of the sealants, Crofer22APU/glass-ceramic/Crofer22APU joined samples were processed in the furnace (Uhlig 424), at Sunfire, GmbH, Dresden Germany. Both the Crofer22APU plates (3x3 cm^2) of a joint were connected to the voltage source by using a platinum wire. Figure 39 shows the configuration of the setup to investigate the electrical resistivity.

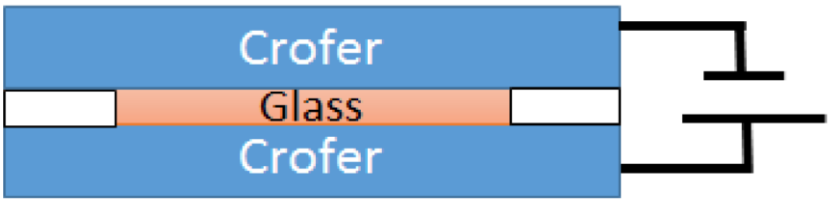

Figure 39. Illustration of electrical resistivity setup configuration. Tests were performed in static air

Figure 40 shows the deposition of glass slurry on the Crofer22APU plate to prepare the Crofer22APU/glass-ceramic/Crofer22APU joint to measure the resistivity in static air.

Figure 40. Crofer22APU/glass-ceramic/Crofer22APU joint preparation for resistivity test in static air

The electrical resistance of the glass-ceramics was investigated at an applied voltage of 1.6 V for 1000-3000 hours in static air. Subsequently, the resistance data was translated into the resistivity by using the following equation:

$$\rho = \frac{RA}{L}$$

where ρ represents the resistivity, R is resistance, and A/L represents the thickness of the glass-ceramic in the joint [3].

Post mortem analyses were carried out using FESEM and EDS to analyze the Crofer22APU/glass-ceramic interface in terms of compatibility, adhesion, diffusion of different elements across the interface and formation of new phases within the glass-ceramic and/or at the interface with the Crofer22APU. Moreover, the possible formation of chromates at Crofer22APU/glass-ceramics/air triple phase boundary and consequent corrosion was also investigated.

Electrical characterization of glass-ceramics in dual atmosphere

The sealants in the SOEC have to face severe conditions in terms of simultaneous oxidizing and reducing atmospheres. Therefore, the performance and reliability of sealants in dual atmosphere needed to be investigated. The chemical, thermal and thermo-mechanical stability of sealants in dual atmosphere becomes even more critical, especially at high working temperature and under electric load.

The electrical characterizations of glass-ceramics in dual atmosphere was carried out Politecnico di Torino, Italy. For this purpose, two 3x6 cm^2 Crofer22APU plates were joined using glass-ceramic to produce Crofer22AU/glass-ceramic/Crofer22APU joints. Before joining, the Pt wires were welded to the upper and lower Crofer22APU plates of Crofer22APU/glass-ceramic/Crofer22APU joined sample and connected to the external voltage source. Figure 41 shows the configuration of the setup used to test the Crofer22AU/glass-ceramic/Crofer22APU based joints in a dual atmosphere. The glass was deposited on the lower Crofer22APU plate by using a slurry, as described above, and the Crofer22APU/glass-ceramic/Crofere22APU joints were processed in a muffle furnace (FM 39, FALC instruments, Treviglio (BG), Italy) by placing over the Inconel base and by using a weight on the top. The lower Crofer22APU plate contains two holes as acting as inlet and outlet of the applied gases, as shown in Figure 41. In this study a mixture of hydrogen and steam in different ratio was applied to obtain the real conditions of an SOEC. A controlled evaporator mixer (CEM) and mass flow rate controller (MFC) were used to control the composition of gases and their flow rate, respectively. Thermocouples and pressure gauges were used to control and measure the temperature and pressure, respectively. A portable flow meter (MesaLabs' Bios DryCal Definer 220, LA, USA) was used to measure the output flow from the furnace.

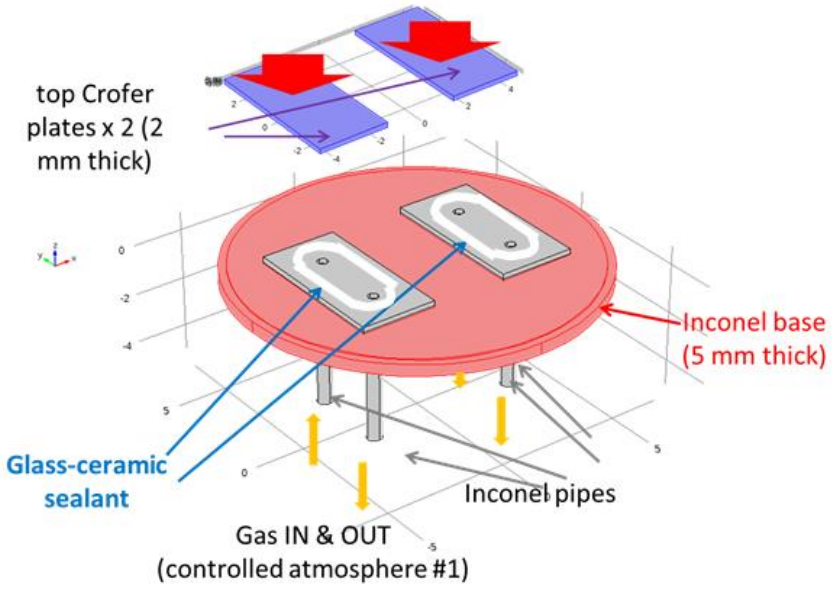

Figure 41. Configuration of dual test setup at Polito

The process setup to measure the electrical resistivity of the glass-ceramic sealants in dual atmosphere is illustrated in Figure 42. Figure 43 shows the Crofer22APU plates during glass deposition. The electrical resistance in dual atmosphere was measured under the applied voltage of 1.6V, while dual tests were conducted for the duration of 500, 1000 and 2000 hours at 850°C. Subsequently, the electrical resistivity was calculated using the data of measured resistance and the area of the glass-ceramic sealant in the joint.

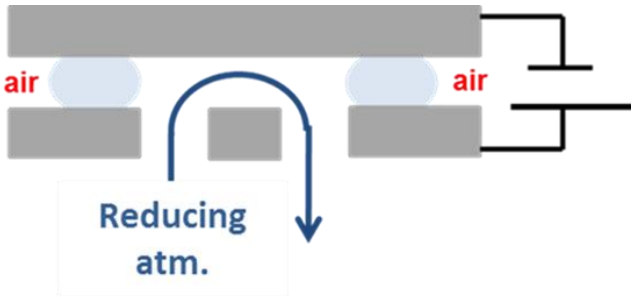

Figure 42. Illustration of setup used to measure the electrical resistivity of Crofer22APU/glass-ceramic/Crofer22APU joint in dual atmosphere

Figure 43 shows the sample preparation of a Crofer22APU/glass-ceramic/Crofer22APU joint, to be tested in dual atmosphere. Figure 43 also shows small pieces of YSZ with a thickness of almost 90 µm, used to ensure the final minimum height, by leveling the shrinkage of the glass during sintering.

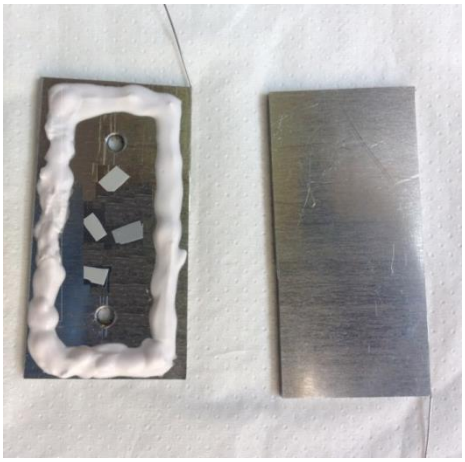

Figure 43. Crofer22APU plates with deposited glass slurry. Crofer22APU/glass-ceramic/crofer22APU joint to been tested in dual atmosphere

Test voltage was applied between upper and lower plates, connected to a voltage generator and a measuring circuit (Figure 44 (b)) by platinum wires. The platinum wires were covered by insulating sleeves, to avoid the electrical contact with metallic parts and short-circuits. The wires were collected in a braid and passed through the insulated hole on the back of the oven to be connected with the measuring circuit. The test-fixture has also a test position for a third sample, for which only the electrical connection was realized, thus the third sample can be tested with applied voltage in static-air in the furnace. The resistivity of the joint samples and static air sample – RS in Figure 44 (b) – were indirectly evaluated by measuring the voltage drop – Vm – on a known resistance Rm that was put in an electrical circuit in series with the Crofer22APU/glass-ceramic/Crofer22APU (see Figure 44 (b)). The voltage generator was regulated during the experiment in order to have the desired voltage on the samples (1.6 V), i.e. the sum of V and Vm was maintained equal to the fixed voltage value. By solving the circuit, the resistance RS was calculated: RS = Rm(V-Vm)/Vm, and consequently the resistivity from the geometry of the sealing frame.

A test-rig for verifying the leakage rate of the dual samples at ambient temperature after the dual-atmosphere tests has been built up, especially for the GrInHy project. The base is a stainless steel smooth plate with a central hole welded to a pipe and connected to a void pump, which is used to create void inside the joint sample in order to see if the glass ceramic is sealing the internal atmosphere. Sample is placed on the central hole with a rubber gasket on the border of the lower plate of the sample to ensure the sealing. The void pressure is measured and compared to a reference value obtained for a closed pipe. In case that the glass ceramic sealant has cracks, the void cannot be created and the void pressure level remain at levels higher than the reference one.

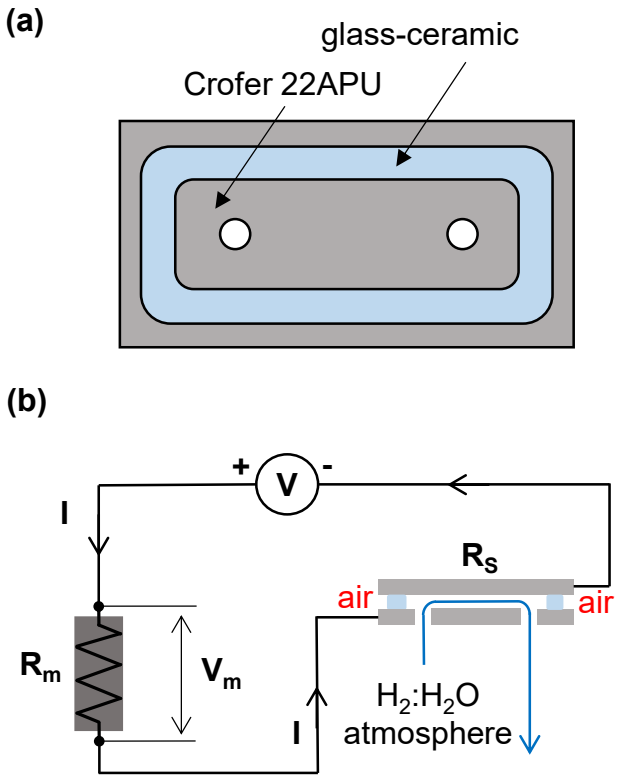

Figure 44. Schematic of sample and measuring setup.

To observe the thermo-mechanical integrity and compatibility of the sealants with Crofer22APU, post mortem analysis was carried out by FESEM and EDS both on the air and the fuel side (side of sealant facing steam and hydrogen gas mixture). For FESEM-EDS analysis, the Crofer22APU/glass-ceramic interfaces at air and fuel sides were polished up to 1 µm using the diamond paste and later coated with gold.

Mechanical characterization of glass-ceramic

The mechanical integrity of glass-ceramic sealants is also a key parameter to ensure their performance in harsh SOEC conditions. The importance of mechanical integrity becomes especially critical at high working temperatures [4–9]. To investigate this, the mechanical properties, such as shear strength, elastic modulus etc. of the Crofer22APU/glass-ceramic/Crofer22APU joints were determined at room temperature, 650°C and also up to 850°C at the Institute of Physics of Materials (IPM), Brno Czech Republic. The Cofer22APU/glass-ceramic/Crofer22APU joints were tested under shear compression load in quasi-static conditions.

For quasi-static shear testing the Crofer22APU/glass-ceramic/Crofer22APU joints were prepared using different glass-ceramics. Figure 45 illustrates the configuration and dimensions of the sample to be tested under shear compressive load. The real joined sample is also shown in Figure 45. Before joining, both plates of Crofer22APU were made plane parallel and polished to obtain the desired dimensions (25x12.5x12.5 mm^3) with a tolerance of ±0.1 mm. Each plate was cleaned by using acetone and subsequently the glass was deposited in the

form of a slurry containing the glass particles and ethanol. The joining was done in a furnace according to the heat treatment for the corresponding glass system by placing a weight on the upper plate. The details about the heat treatments of each glass system are given in chapter 4. After joining, the joint samples were again gently polished for a few minutes to make sure that both plates were perfectly parallel to each other. The red arrow in Figure 45 shows the direction of the applied load during shear testing.

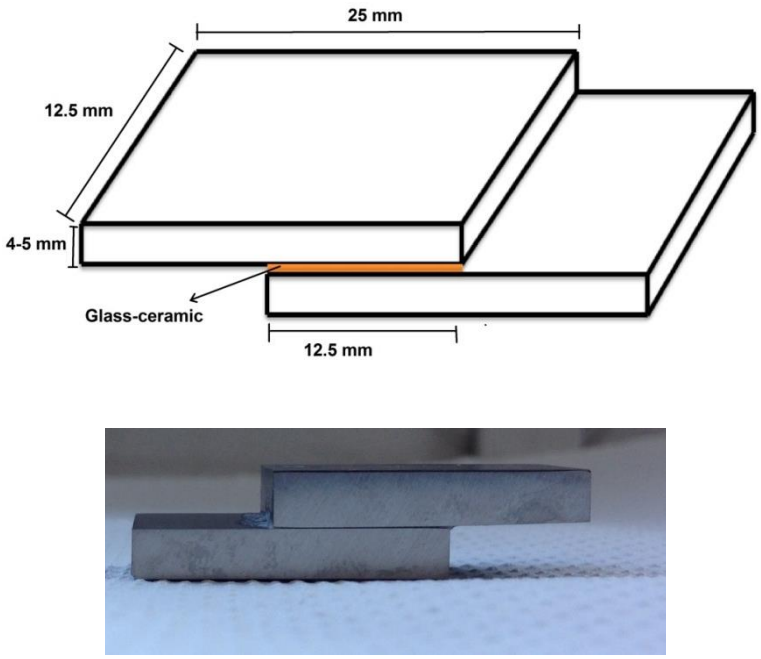

Figure 45. Symmetric illustration and real samples of Crofer22APU/glass-ceramic/Crofer22APU for shear testing

For testing the Crofer22APU/glass-ceramic/Crofer22APU joint samples, each sample was firmly placed inside the steel fixture, as shown in Figure 46, by using different supporting pins. Figure 46 also shows the mechanism of force applied during the shear testing, where the compressive force was applied on one of the joined plates of Crofer22APU, while the other plate was fixed. This configuration produced overall shear force at the joint.

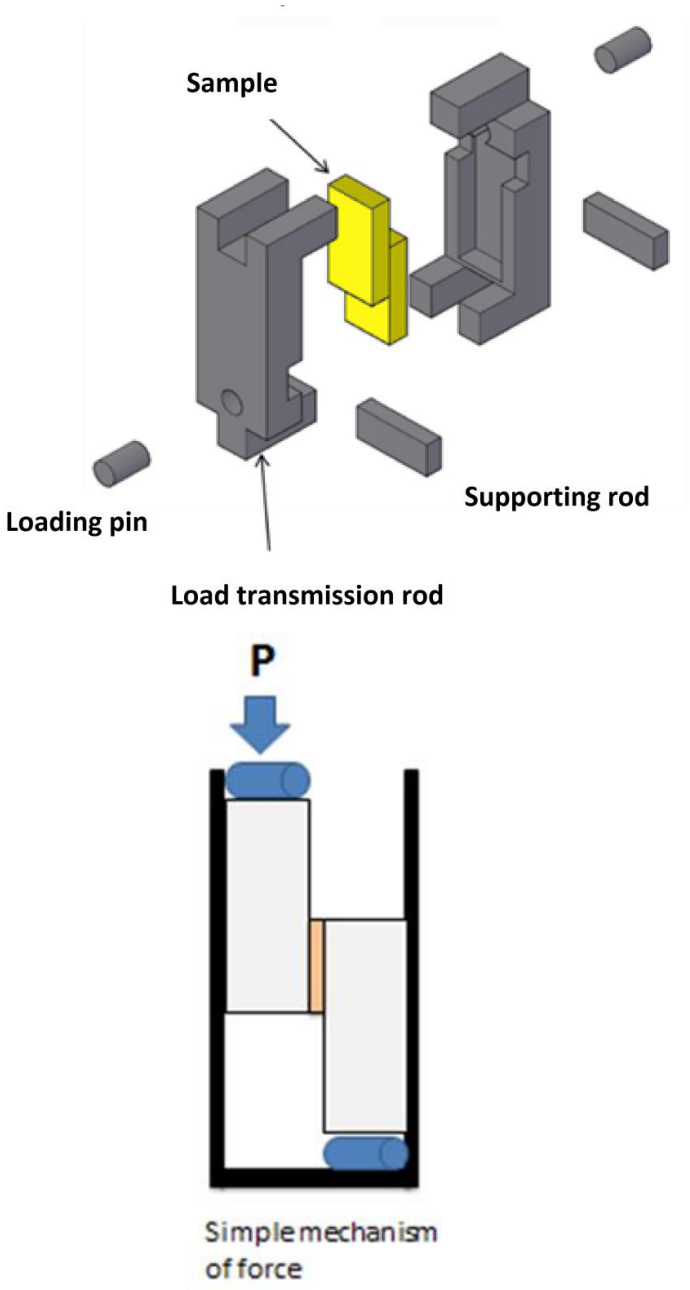

Figure 46. Shear testing fixture and applied force mechanism

Quasistatic shear testing was carried out at a constant machine cross-head rate of 50 µm/min. The loading fixture developed for the experiments is also shown in Figure 1. The red arrow in Figure 1 indicates the direction of the applied load. Tests were conducted at three different testing temperatures, namely room temperature, 650 °C and 850 °C. The applied load was measured by means of a system load cell. The displacement of the joined plates was quantified by using a system high temperature extensometer located outside the temperature chamber. The Zwick/Roell - Messphysik Kappa 50kN test system with a Maytec inert gas high temperature chamber was used for the experiments. Since the shrinkage of glasses, and thus a contact area between the glass-ceramic and Crofer22APU, can have a significant effect on the strength of the joining, the joint area of each

sample was measured separately after the shear test by using a light microscope with CCD camera and image analysis. The shear stress was then calculated by dividing the applied load by the real joint area.

All tests were conducted in an argon atmosphere. Before each test the sample was heated to the desired temperature and kept at that temperature for 3 hours, so as to make the temperature homogenous throughout the heating zone of the chamber. The temperature was measured by a thermocouple attached directly to the sample. In order to obtain statistically representative data, at least three samples of both compositions were tested at each temperature. The post mortem analysis of broken samples was carried out by SEM (Merlin ZEISS). For this purpose, cross sections of the Crofer22APU/glass-ceramic interfaces were metallographically polished up to 1 µm by diamond paste and investigated by SEM after being coated with gold. In addition to the Crofer22APU/glass-ceramic interface, the top fracture morphology of the glass-ceramics was also observed under SEM. EDS analysis was also performed to observe the possible diffusion of elements across the Crofer22APU/glass-ceramic interface during the high temperature testing.

The elastic modulus of pure the glass-ceramics was measured in the temperature range of 25°C-650°C by using the vibration method. For this purpose, a thin beam of each glass-ceramic with dimensions of 20mm x 2mm x 2mm was prepared. The high temperature impulse excitation technique, HT1600 system from IMCE, was applied for these analyses. The elastic modulus was determined by measuring the resonant frequency of the sample at the given temperature and then calculated from the specimen dimensions and density. The elastic modulus was measured during the heating as well as the cooling cycles. Above 650°C, the softening of the glass-ceramics did not provide sufficient vibrations to measure the elastic modulus.

3.1.3 Novel glass-ceramic compositions

Novel glass compositions were designed by using the SciGlass® database (Science Serve GmbH, SciGlass 6.6 software), by bearing in mind the required the CTE of glass-ceramic systems for SOEC applications, should be in the range 9-12 x 10^{-6} K^{-1}. The SciGlass database is the largest database of glasses that contains a collection of glass compositions form research articles and patents. The SciGlass database provides prediction about the variety of glass properties such as glass transition temperature, coefficient of thermal expansion, viscosity, softening temperature etc. therefore, act as a major tool in development of novel glass compositions for various applications.

The novel glass systems are divided into three series. The division of these series is based either on the selection of main modifiers or their respective quantities. The next section will discuss the compositions of these glass-ceramic systems in addition to highlighting the rationale behind the derivation of these compositions.

First series of glass-ceramic sealant

The first series of glasses contains two glass systems labeled as HJ3 and HJ4 respectively, and their compositions are shown in

Table 7. The glasses in the 1st series are free from alkali earth metal oxides as well as from BaO. In both glass systems, silica (SiO_2) was the main glass former to obtain high thermal stability. The concentration of SiO_2 in HJ3 and HJ4 glasses is 47.07 mol% and 57.06 mol% respectively. In addition to SiO_2, B_2O_3 was also used however its quantity is kept below 6 mol% to avoid the problems associated with the evaporation of B_2O_3 in case of its high concentration. In HJ3; CaO, MgO and SrO were used as modifiers with total concentration of 44.04 mol%. However, in HJ4 the CaO and MgO were completely removed and only SrO was used as the modifier in 28.84 mol%. Moreover, a small amount of Y_2O_3 was added as an additive to adjust the viscosity.

Table 7. Composition (mol%) of glass systems belonging to 1st series.

	1st Series of Glass Compositions (mol%)	
	HJ3	**HJ4**
SiO_2	47.07	57.06
B_2O_3	3.69	5.65
Al_2O_3	3.78	6.17
CaO	11.45	---
MgO	12.74	---
SrO	19.85	28.84
Y_2O_3	1.42	1.74

These Sr-based compositions (HJ3 and HJ4) were designed with the aim to maximize the possibility of the formation of Sr containing crystalline phases and consequently to minimize the concentration of SrO in the residual glassy phase in order to avoid the formation of an undesirable $SrCrO_4$ phase. Therefore, in HJ3 glass system, the concentration of SrO was kept higher as compared with other modifiers (CaO and MgO). However, according to the SiO_2-SrO binary phase diagram shown in Figure 47, it is clear that in order to obtain the high CTE $SrSiO_3$ phase, having a CTE of 10.9 x 10^{-6} K^{-1} [10], the ratio of SrO:SiO_2 should be 1:1. Therefore, in HJ4 glass system, the SrO was used only as modifier and in significantly high concentrations to maximize the possibility of formation of desired high CTE $SrSiO_3$ phase. Nevertheless, increasing the concentration of SrO also increases the risk of chromate formations, thus the concentration of SrO in HJ3 and HJ4 was kept lower as compared with SiO_2.

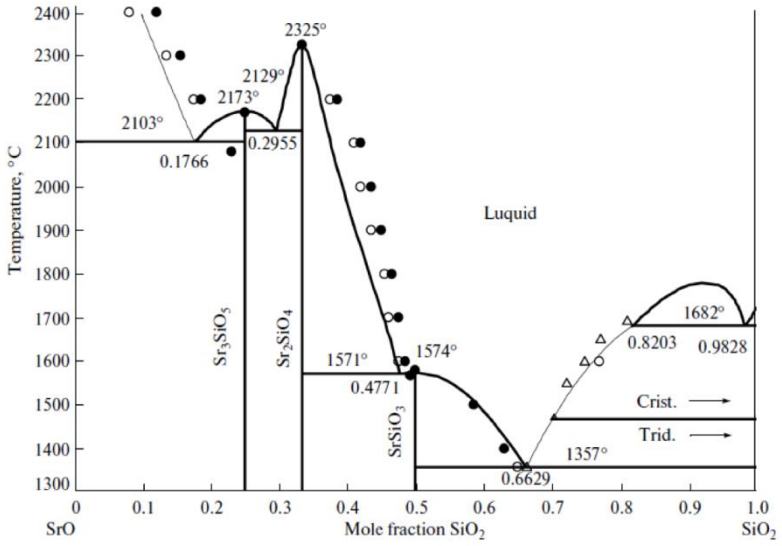

Figure 47. SiO_2-SrO binary phase diagram [11]

Second series of glass-ceramic sealants

The second series of glasses contains one glass system, labeled as HJ14. Table 8 shows the composition (mol%) of HJ14 glass. The 2nd series glass (HJ14) contains SrO as a main modifier, in addition to CaO. Like HJ3 and HJ4 glass systems (1st series), the HJ14 is also a silica bases glass with small amount (6 mol%) of B_2O_3. HJ14 is also free from alkali metal oxides and BaO.

Table 8. Composition (mol%) of the glass system belonging to the 2nd series.

2nd Series of Glass Compositions (mol%)	
	HJ14
SiO_2	55±5
B_2O_3	4±2
Al_2O_3	4±2
CaO	12±3
SrO	30±4

The HJ14 glass system is the further modification of SrO containing 1st series of glasses. The SrO-SiO_2 binary phase diagram in Figure 47 shows that in order to obtain only $SrSiO_3$ phase the SrO/SiO_2 (mol%) should be 1. SrO/SiO_2 (mol%) less than one will increase the possibility of devitrification of SiO_2 phase likely present in the form of cristobalite, in addition to $SrSiO_3$. Therefore, the SrO/SiO_2 in HJ14 was further increased as compared with HJ4 (1st series glass) with the

purpose of not only obtaining the high CTE $SrSiO_3$ phase, but also to reduce the possibility of formation of cristobalite (SiO_2) phase. The cristobalite phase has different polymorphs and shows a volume expansion around 270 °C as shown in Figure 48. This volume expansion can lead to cracks formation especially during the thermal cycling. Low concentration of Al_2O_3 was used in order to avoid the formation of low CTE $SrAl_2Si_2O_8$ phase. HJ14 glass also contains 12±3 mol% of CaO. The purpose of CaO was to reduce the viscosity and improve the CTE of residual glass, in addition to minimize the formation of cristobalite (SiO_2) phase.

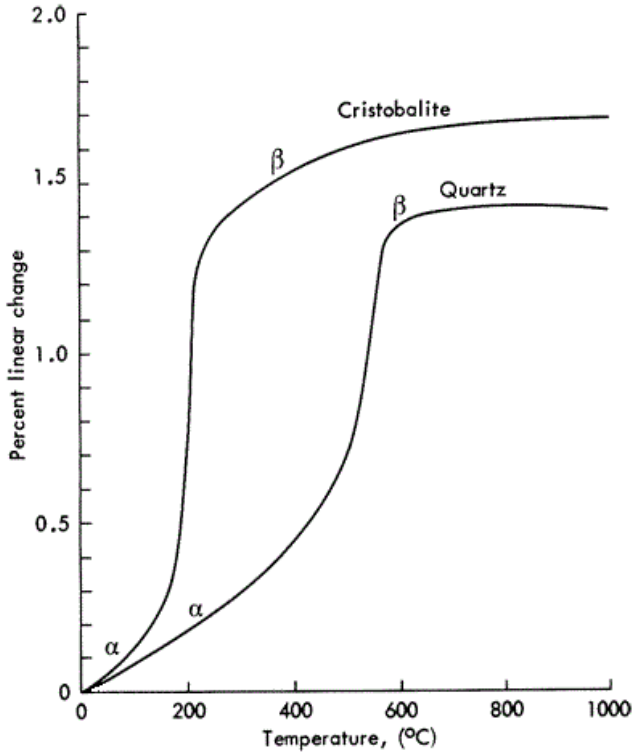

Figure 48. Temperature dependent specific volume of different forms of silica (SiO_2). Cristobalite shows volume expansion around 230 °C during heating and 270°C during cooling [12]

Third series of glass-ceramic sealants

The third series of glasses contains two glass systems, labeled as HJ11 and HJ28, their composition is reported in Table 9 (mol%). These compositions contain BaO as the main modifier, in addition to the CaO. Like 1st and 2nd series, the glass systems in the 3rd series are also silica (SiO_2) based and are also free from alkali metal oxides.

Table 9. Composition of the glass systems belonging to the 3rd series. The shown compositions are in mol%

	3rd series glass compositions (mol%)	
	HJ11	**HJ28**
SiO_2	50±5	60±5
B_2O_3	5±3	5±3
Al_2O_3	6±2	4±2
CaO	10±3	5±2
BaO	30±4	20±3
Y_2O_3	---	2±1

In HJ11 BaO is introduced as the main modifier. The BaO is most widely studied modifier, since it reduces viscosity, improves wettability, and forms high CTE $BaSi_2O_5$ phase (CTE 11-14 x10^{-6} K^{-1}) [11], in the SiO_2-BaO based glass systems. Figure 49 shows the BaO-SiO_2 binary phase diagram, indicating that the SiO_2/(BaO+SiO_2) should be around 0.67 to obtain $BaSi_2O_5$ phase. Higher SiO_2 contents will increase possibility of cristobalite (SiO_2) formation. In HJ11 glass system, the SiO_2/(BaO+SiO_2) was around 0.7 to ensure the formation of desired $BaSi_2O_5$ phase. Moreover, the concentration of Al_2O_3 was kept around 5 mol%.

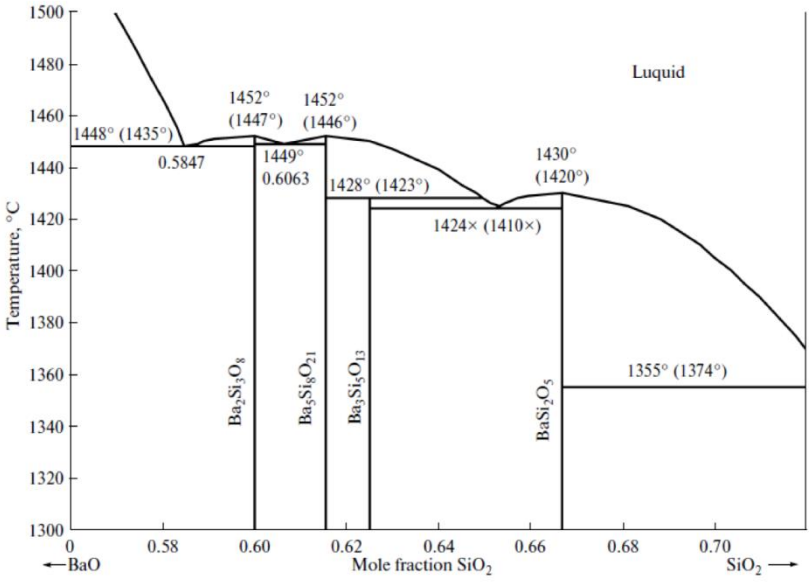

Figure 49. BaO-SiO_2 binary phase diagram [11]

HJ28 glass is also a BaO based glass with slight modifications as compared with HJ11, such as the concentration of Al_2O_3 in HJ28 was reduced, in order to avoid the formation of monocelsian $BaAl_2Si_2O_8$ phase having a CTE of 2.3 x 10^{-6} K^{-1}. Besides that, the concentration of SiO_2 was increased and concentration of BaO was reduced to avoid the formation of undesirable high CTE $BaCrO_4$ phase. In HJ28, about 1 mol% of Y_2O_3 was added to adjust the viscosity of system.

Like the 2nd series glass (HJ14), both the glasses of 3rd series also contain 5-10 mol% of CaO, with a aim to minimize the formation of cristobalite (SiO_2) phase.

3.1.4 Stencil printing of glasses

After successful characterization and analyses of glasses, the deposition of glass on the Crofer22APU substrate was up scaled. The glass was deposited by stencil printing method at Sunfire GmbH, Dresden Germany. For this purpose, a novel glass paste was developed by using glass powder in addition to solvent, binder, dispersant and plasticizer in a proper amount. The glass paste was developed in two steps: in the first step a mixture of solvent, binder, dispersant and plasticizer (further termed as pre-binder) was prepared in a proper ratio while in the second step this pre-binder was further mixed with the glass powder to form the glass-based paste.

In this research work, the glass pastes were developed by using HJ28 glass systems. The composition of the paste shown in Table 10. To prepare a paste, first of all the pre-binder was prepared by mixing the terpineol solvent with the plasticizer by heated at 70°C for 20 min with a constant stirring, followed by the addition of binder and dispersant. This mixture (pre-binder) was homogenized by continuous stirrer at 70°C for half an hour. In the second step, the synthesis of glass paste was carried out by mixing the pre-binder and glass powder at room temperature for at least half an hour to have a uniform distribution of glass powder particles.

Table 10. Composition of glass paste for stencil printing

Chemicals (Purpose)	Amount
Glass powder	72±2 wt%
Terpineol (solvent)	18±2 wt%
Ethyl cellulose N50 (binder)	5±2 wt%
Dispersant	5±1 wt%
Hexamol Dinch (plasticizer)	3±1 wt%

The rheological properties, such as viscosity, shear modulus and storage modulus of pre-binder and pastes, were analyzed using a rheometer (Physica, Anton Paar). The glass pastes were deposited on the real dimensioned Crofer22APU interconnect by manual stencil printer. Figure 50 shows the manual stencil printer along with the glass paste to be deposited.

After deposition, the glass paste was dried at 70°C for half an hour in an oven. The height of deposited glass paste was measured at different locations, before and after drying. Afterwards, the de-binding and subsequently the joining of glass

paste with the Crofer22APU was carried out according to the standard heat treatments for HJ11 and HJ28 glass systems. After joining, the Crofer22APU plate was cut and polished up to 1 µm by diamond paste, to observe the thermo-mechanical compatibility of Crofer22APU/glass-ceramic interface by SEM.

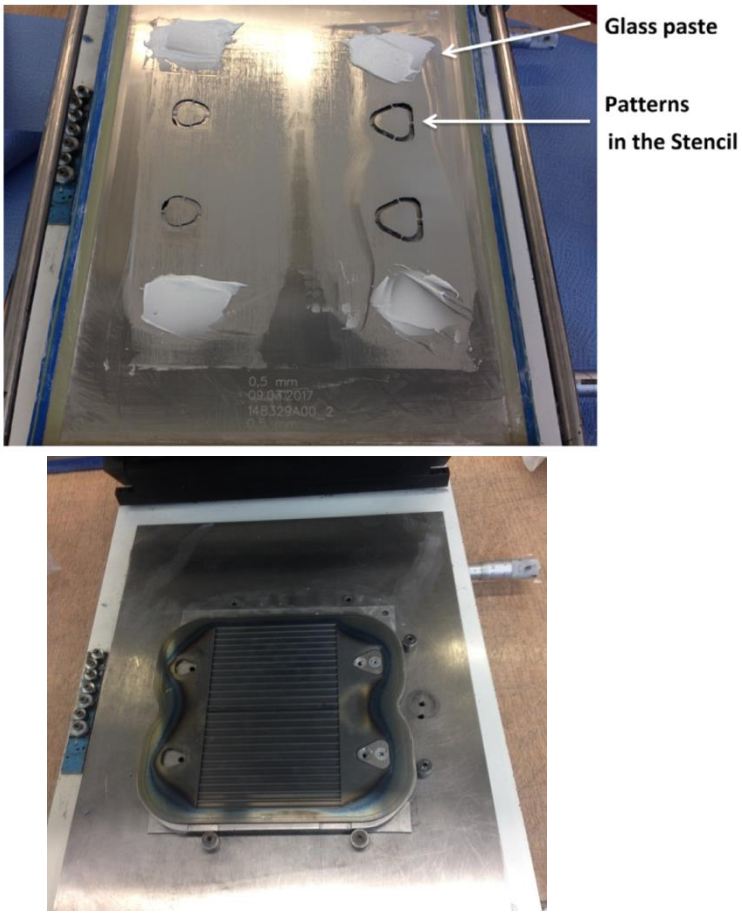

Figure 50. Manual stencil printer used to deposit glass paste on the Crofer22APU interconnect

3.2 Protective coatings

The following section will discuss the experiments regarding the deposition of different ceramic materials deposited on the Crofer22APU substrate to act as a barrier coating in order to hinder Cr evaporation at 850°C. The up-scaling of the coating deposition process, from lab to the industrial scale, as well as the characterization of the coatings in terms of their area specific resistance (ASR) will also be described in this section. At the end, the use of the flash sintering technique for the rapid sintering of the coatings will also be described.

3.2.1 Coating materials

$Mn_{1.5}Co_{1.5}O_4$ (MCO) spinel based coatings were studied in this research due to the fact that it's the most widely studied material and has been found to act as an efficient protective coating material in SOEC applications [13–16]. In addition to pure MCO, the Cu doped MCO coatings were also deposited by using CuO precursor.

3.2.2 Electrophoratic deposition of spinel coatings

In this work, the electrophoretic deposition technique (EPD) was used to deposit the MCO coatings on the Crofer22APU interconnect. The EPD was performed at Politecnico di Torino, Italy and the EPD setup is shown in Figure 51. Commercially available MCO powder from Fuelcellmaterials (USA), with a mean particle size of 0.36 µm and a specific surface area of 12.5 m^2/g was used.

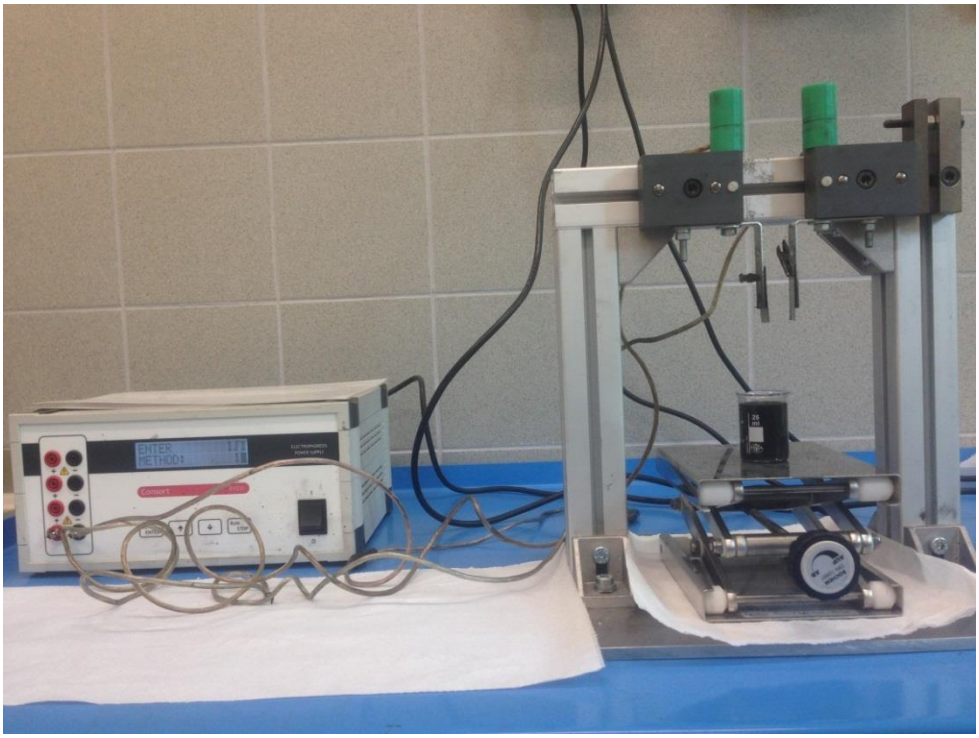

Figure 51. EPD setup at Polito, used to deposit spinel coatings on the Crofer22APU substrate

A pre-optimized process with consolidated deposition parameters was used to prepare the MCO powder based suspension and subsequently to deposit the coatings by EPD. The details of the process are described elsewhere [16]. The suspension of the MCO powder was produced in a solvent composed of mixture of ethanol and water in 40:60 by volume. 37.5 grams of MCO powder were added per liter of solution (ethanol + water), stirred and sonicated for half an hour in an ultrasonic bath in order to homogenize the suspension. The deposition was made on small (1.5 cm x 1.5 cm) Crofer22APU samples for 20 sec by using an electric field of 50 V cm^{-1} (as previously optimized [16]). A stainless steel sheet was used as a counter electrode with a distance of 1 cm between the two electrodes. Before deposition the Crofer22APU substrates were cleaned with acetone to remove any contamination. A new homogenous suspension was produced before every new deposition. Figure 52 shows the 1.5 x 1.5 cm^2 Crofer22APU sample freshly coated with MCO.

The freshly coated samples were dried in air for almost 24 hours. The sintering was carried out in two steps; in the first step, the sintering was done at 900°C at a heating rate of 10 °C/min for two hours in a reducing atmosphere

(1%H_2+Ar), while the second step involved sintering at 900°C at a heating rate of 10 °C/min, again for two hours in the static air (oxidizing atmosphere).

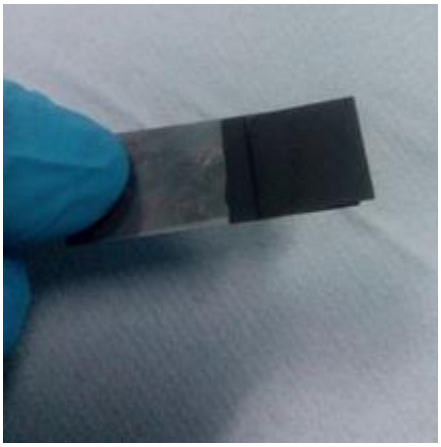

Figure 52. Freshly coated MCO on the Crofer22APU by EPD

Crofer22APU plates used in an SOEC stack are usually; corrugated (depending on the stack design), as shown in Figure 53. Therefore, in addition to flat surfaces, the EPD process was also used to deposit coatings on the corrugated Crofer22APU surfaces with dimensions of 1.5 cm x 1.5 cm. The deposition and sintering parameters for coating deposition on the corrugated surfaces were also kept the same as mentioned above for the flat surfaces.

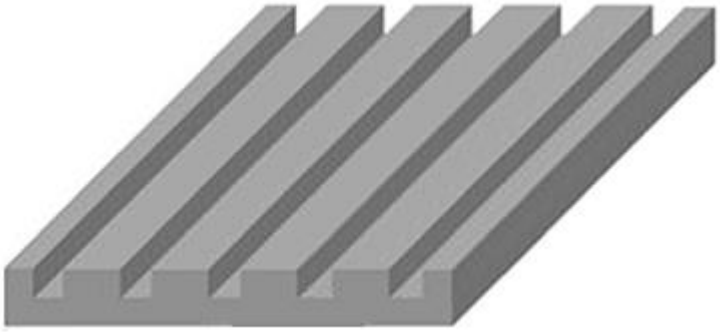

Figure 53. Sketch of steel interconnect with corrugated surfaces [17]

After sintering in two steps, the Crofer22APU/coating cross-section was polished up to 1 µm using diamond paste. The SEM analyses were performed at the interface to observe the thickness and uniformity of the coatings.

3.2.3 Scale up of EPD process

After the successful deposition of the MCO coatings on the small (1.5 cm x 1.5 cm) corrugated Crofer22APU samples, the EPD process was scaled up to coat the 16 cm x 18 cm corrugated Crofer22APU plates to be used in the SOEC stack. For this purpose, the same deposition parameters were used to deposit the coatings as for the small sized samples. Figure 54 shows the EPD setup to coat the

16 cm x 18 cm Crofer22APU plates. A counter steel electrode with the same dimensions as that of the Crofer22APU was used.

Figure 54. EPD scaled-up setup used to coated Crofer22APU interconnect with real dimensions

3.2.4 Area specific resistance (ASR) of MCO coated Crofer22APU

The area specific resistance (ASR) of coated Crofer22APU was measured at SUNFIRE, Dresden, Germany for 8600 hours at 850°C in the static air. Figure 55 shows the different steps followed to prepare the samples for the ASR test. For this purpose, the MCO coatings were first deposited on the real sized corrugated Crofer22APU substrate. In the second step, the cathode ribs were deposited on the coated Crofer22APU interconnect by screen printing. The third step involved the cutting of 3 x 3 cm^2 samples from the coated Crofer22APU plate. Afterwards, the Pt-wires were welded to the coated Crofer22APU by point welding, and were subsequently attached to the external circuit to measure the ASR. From the ASR data, the degradation rate for both coated materials was also calculated.

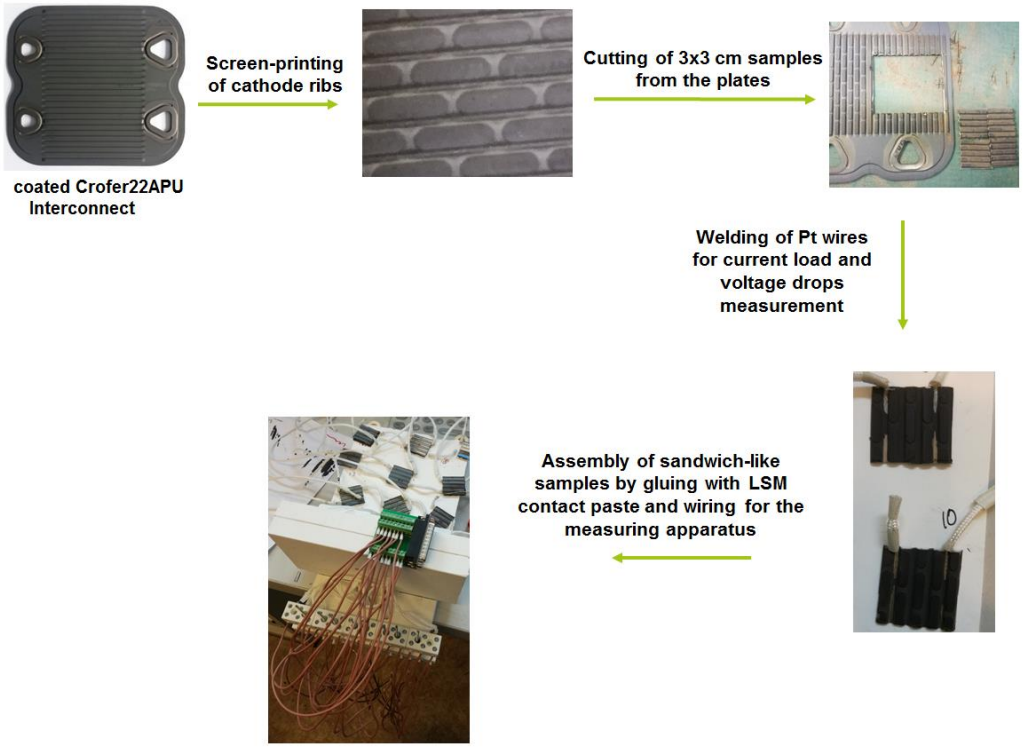

Figure 55. Procedure for the sample preparation to be tested under ASR test

The effect of different sintering conditions was also evaluated on the ASR values of both coating materials. For this purpose, the MCO coatings were sintered according to the following two different conditions:

1. Redox (Reduction + Oxidation): Two step sintering; 1st step in reducing atmosphere at 900°C for 2 hours at heating rate of 10°C/min and 2nd step in static air at 900°C for 2 hours at heating rate of 10°C/min
2. Oxi (Oxidation): One step sintering in static air at 950°C for 2 hours at heating rate of 10°C/min

After the ASR test (8.6 Kh, 850 °C, in air), the Crofer22APU/coating samples were polished up to 1 µm using diamond paste and observed under SEM for post mortem analyses.

3.2.5 EPD co-deposition of MCO with CuO

Mn-Co spinels are probably the most promising candidates for protective materials for steel based interconnects of solid oxide cells, thanks to their high electrical conductivity and CTE matching with metallic interconnects. Nevertheless, Cu is an attractive dopant for increasing both the sinterability and electrical conductivity of the spinel. The Cu doped spinel powders are typically prepared "ex-situ" (by soft chemistry or mechanochemical synthesis) in a separate process before the deposition, thus increasing the processing time and cost. However, in this research work, EPD process was employed to co-deposit the MCO and dopant (Cu) by adding a controlled amount of the second phase (CuO)

to the suspension, thus in only one deposition step. For this purpose, 0 wt%, 5 wt% and 10 wt% of the dopant (CuO), were added to the MCO suspension by maintaining the constant solid content (37.5 g/L) and solvent composition (60/40 vol of EtOH/H_2O) as described before. The sintering was also performed in two steps; first in the reducing atmosphere (900 °C-2hrs) and later in static air (900 °C-2hrs).

The corrosion analyses of the un-doped and Cu doped coated MCO spinel were performed for 2000 hours at 800 °C in a chamber furnace in static air. For each type of coated sample, five samples were analyzed in order to ensure the reproducibility and an average weight gains were measured. The ASR of the Cu doped $Mn_{1.5}Co_{1.5}O_4$ (MCO) coatings was measured for 1000 hours in addition to the un-doped MCO coating for better comparison. After the ARS test, the cross-sections of the coated samples were polished up to 1 µm and subsequently analyzed under SEM-EDS.

3.2.6 Flash sintering of coatings: MCO and MCO doped with CuO and Fe_2O_3

Besides conventional pressure-less sintering, the flash sintering technique was also used to sinter the EPD deposited coatings. The effect of flash sinter was compared with the conventional sintering in the furnaces, in terms of coatings density, crystalline phases and homogeneity. The flash sintering was carried out at Nanoforce Ltd, Queen Mary University of London. For this purpose, the coatings of the pure (MCO), and MCO doped with 10 wt% of CuO and Fe_2O_3 were deposited on the Crofer22APU substrate by EPD. For the flash sintering, the Crofer22APU substrates used were disc-shaped, with 15 ± 0.1 mm diameter and 2 mm thickness. Prior to coating, each Crofe22APU substrate was cleaned in an ultrasonic bath for 15 min. All three types of coatings were deposited by using the same deposition parameters i.e. deposition time of 20 secs, voltage of 50 V and distance of 1 cm between the two electrodes. After deposition, the coated Crofer22APU substrates were dried in air for 24 hours, followed by sintering treatments.

The coatings were sintered according to three different heat treatments, henceforth labeled as S1, S2 and S3.

1. S1 was a single step sintering treatment where the coatings were sintered only by the flash sintering technique.
2. S2 involved two step sintering, i.e. the first step involved sintering inside a tubular furnace in the presence of reducing atmosphere (Ar-1% H_2) at 900°C for two hours at a heating/cooling rate of 10°C/min, while in the second step sintering was done by using the flash sintering technique. Flash sintering was done in vacuum (1 m.bar) at 850°C using a pressure of 5 KN.
3. The S3 treatment involved three steps; the first two steps were similar to S1 (first in reducing atmosphere and second by flash sintering), however,

in the third, additional step the sintering was carried out in static air inside a tubular furnace at 900°C for 2 hours at a heating/cooling rate of 10°C/min.

The three heat treatments are also summarized in Table 11.

Table 11. Different heat treatments used to sinter the coated Crofer22APU by flash sintering

	S1	S2	S3
Step 1:	Flash sintering	Sintering in reducing atmosphere	Sintering in reducing atmosphere
Step 2:	---	Flash sintering	Flash sintering
Step 3:	---	---	Sintering in oxidizing atmosphere

For flash sintering, the disc-shaped coated Crofer22APU samples were introduced into a graphite die with an internal diameter of 15.2 ±0.1 mm, while the external diameter was 18.1 ±0.1 mm. Two cylindrical graphite punches were used to hold the sample in the die. Boron nitride (BN) was sprayed on the graphite punches in order to avoid direct contact between the graphite punches and the coated Crofer22APU samples. The white colored BN on the top of both punches is visible in Figure 56. BN is an insulating material and can be easily remove after the sintering due to its nonstick property. Because of the insulating nature of BN, a graphite sheet was wrapped around the Crofer22APU sample to provide electrical contact between the graphite punches and the coated Crofer22APU sample. Figure 56 shows the graphite die with graphite sheet, cylindrical graphite punches coated with BN and an MCO coated Crofer22APU sample.

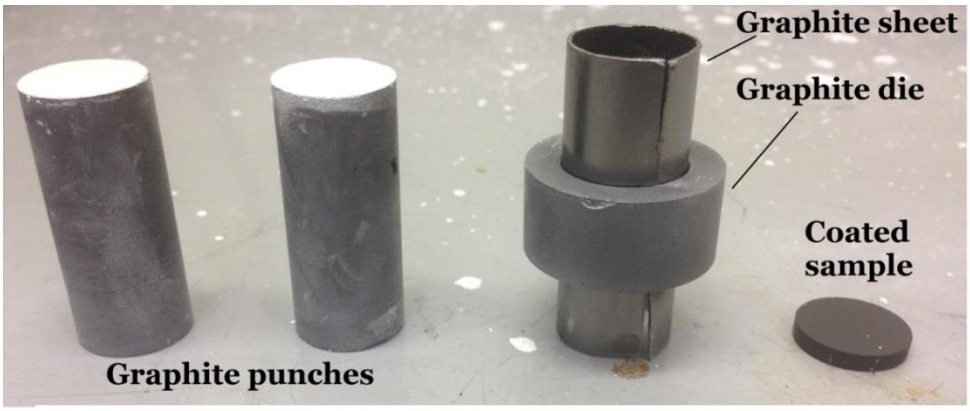

Figure 56. Different components of the assembly used for the flash sintering of coated Crofer22APU

The sample assembly was prepared by introducing the sample into the graphite die. Both graphite punches were inserted with one at each end of the disc-shaped sample. The sample assembly is shown in Figure 57. The sample assembly was then introduced into the chamber for flash sintering as shown in

Figure 57. A thermocouple was used to measure the temperature during the flash sintering process.

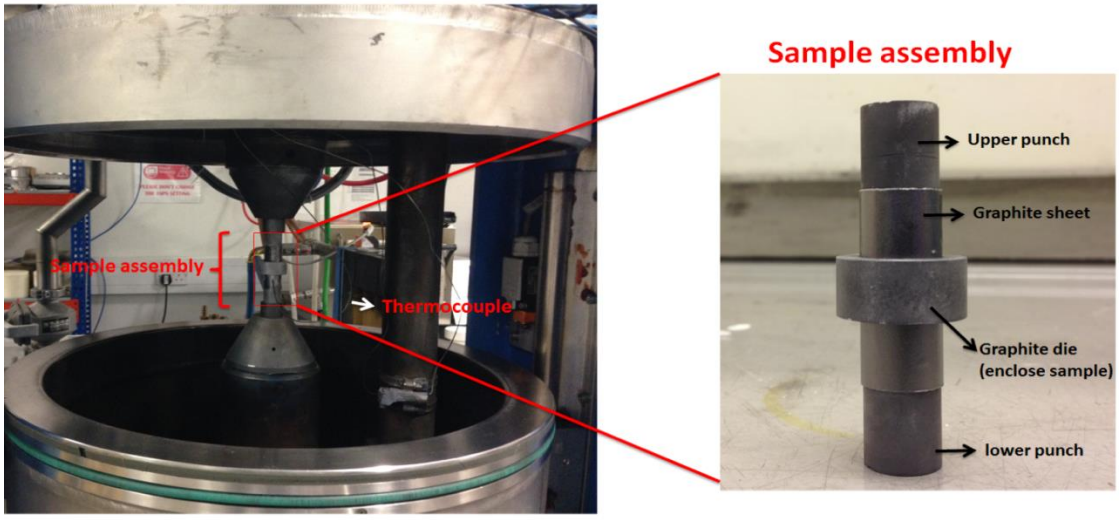

Figure 57. Flash sintering setup at Nanoforce Ldt, London and the sample assembly

The temperature profile to sinter the coatings by the flash sintering method is shown in Figure 58. Samples were initially heated up to 700°C at a heating rate of 200°C/min followed by a dwell of 1 min. Afterwards, a power pulse was applied in two steps for the total duration of two seconds i.e. initially 100% power (6.8 V) for the 1st sec and 70% powder for the 2nd sec. The power pulse increased the temperature up to 850 °C. Afterwards the sample was cooled down to room temperature at a heating rate of 200 °C/min. The rationale behind applying power in two steps was that the full power applied for 1 sec does not give sufficient density, while full power for 2 sec causes melting of the coatings. Therefore, intermediate power values (100 % (1st sec) and 70% (2nd sec)) were chosen.

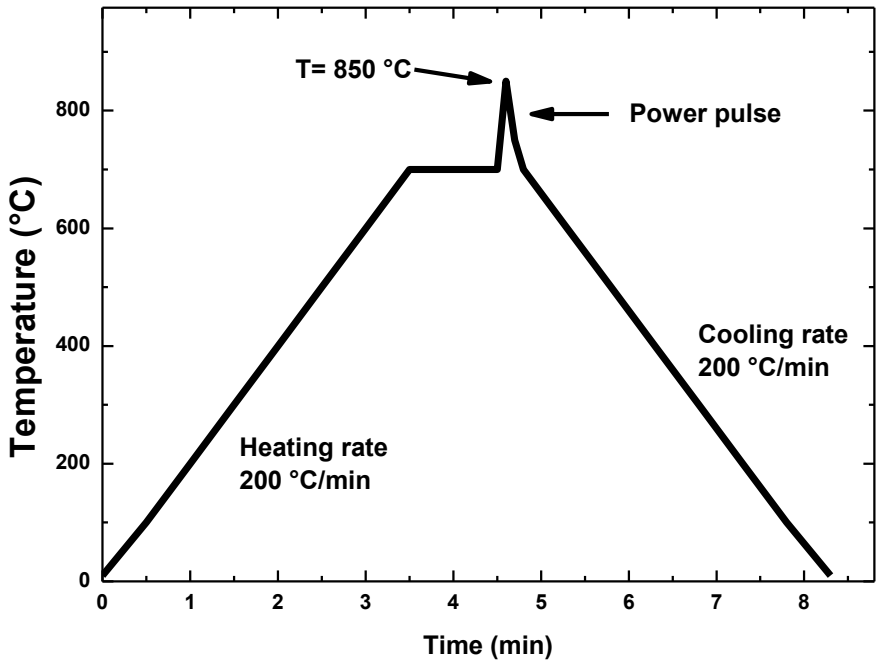

Figure 58. Temperature profile used during the flash sintering of coated Crofer22APU samples

References

[1] Q. Zhu, L. Peng, T. Zhang, Y.-S.S. Chou, J.W. Stevenson, J.-P. Choi, K.D. Meinhardt, Alkali Effect on the Electrical Stability of a Solid Oxide Fuel Cell Sealing Glass, Fuel Cell Electronics Packaging. 93 (2010) 618–623. doi:10.1111/j.1551-2916.2009.03466.x.

[2] A. Rost, J. Schilm, M. Kusnezoff, A. Michaelis, Degradation of sealing glasses under electrical load, European Fuel Cell Forum. 80 (2010) 1–12. doi:10.4416/JCST2012-00002.

[3] http://hyperphysics.phy-astr.gsu.edu/hbase/electric/resis.html, (n.d.). http://hyperphysics.phy-astr.gsu.edu/hbase/electric/resis.html.

[4] B. Cela Greven, S. Gross-Barsnick, T. Koppitz, R. Conradt, F. Smeacetto, A. Ventrella, M. Ferraris, Torsional shear strength of novel glass-ceramic composite sealants for solid oxide fuel cell stacks, International Journal of Applied Ceramic Technology. 15 (2018) 286–295. doi:10.1111/ijac.12819.

[5] Y. Zhao, J. Malzbender, S.M. Gross, The effect of room temperature and high temperature exposure on the elastic modulus, hardness and fracture toughness of glass ceramic sealants for solid oxide fuel cells, Journal of the European Ceramic Society. 31 (2011) 541–548. doi:10.1016/j.jeurceramsoc.2010.10.032.

[6] B. Cela Greven, S.M. Gross-Barsnick, D. Federmann, R. Conradt, Strength evaluation of multilayer glass-ceramic sealants, Fuel Cells. 13 (2013) 565–571. doi:10.1002/fuce.201200155.

[7] H. Abdoli, P. Alizadeh, D. Boccaccini, K. Agersted, Fracture toughness of glass sealants for solid oxide fuel cell application, Materials Letters. 115 (2014) 75–78. doi:10.1016/j.matlet.2013.10.013.

[8] B. Dev, M.E. Walter, G.B. Arkenberg, S.L. Swartz, Mechanical and thermal characterization of a ceramic/glass composite seal for solid oxide fuel cells, Journal of Power Sources. 245 (2014) 958–966. doi:10.1016/j.jpowsour.2013.07.054.

[9] M. Fakouri Hasanabadi, M.A. Faghihi-Sani, A.H. Kokabi, J. Malzbender, The analysis of torsional shear strength test of sealants for solid oxide fuel cells, Ceramics International. 43 (2017) 12546–12550. doi:10.1016/j.ceramint.2017.06.128.

[10] C. Thieme, C. Rüssel, Thermal expansion behavior of SrSiO3 and Sr2SiO4 determined by high-temperature X-ray diffraction and dilatometry, Journal of Materials Science. 50 (2015) 5533–5539. doi:10.1007/s10853-015-9100-3.

[11] A. Romero-Serrano, A. Cruz-Ramirez, B. Zeifert, M. Hallen-Lopez, A. Hernandez-Ramirez, Thermodynamic modeling of the BaO-SiO2 and SrO-SiO2 binary melts, Glass Physics and Chemistry. 36 (2010) 171–178. doi:10.1134/S1087659610020045.

[12] M.P. Bauleke, How to Solve the Problems of Body Cracking and Glaze Popping in Stoneware Bodies, (n.d.). http://www.kgs.ku.edu/Publications/Bulletins/211_4/bauleke.html (accessed April 9, 2019).

[13] J.C.W. Mah, A. Muchtar, M.R. Somalu, M.J. Ghazali, Metallic interconnects for solid oxide fuel cell: A review on protective coating and deposition techniques, International Journal of Hydrogen Energy. 42 (2017) 9219–9229. doi:10.1016/j.ijhydene.2016.03.195.

[14] D. Szymczewska, S. Molin, V. Venkatachalam, M. Chen, P. Jasinski, P. V. Hendriksen, Assesment of (Mn,Co)33O4 powders for possible coating material for SOFC/SOEC interconnects, IOP Conference Series: Materials Science and Engineering. 104 (2016). doi:10.1088/1757-899X/104/1/012017.

[15] N.J. Magdefrau, L. Chen, E.Y. Sun, J. Yamanis, M. Aindow, Formation of spinel reaction layers in manganese cobaltite-coated Crofer22 APU for solid oxide fuel cell interconnects, Journal of Power Sources. 227 (2013) 318–326. doi:10.1016/j.jpowsour.2012.07.091.

[16] F. Smeacetto, A. De Miranda, S. Cabanas Polo, S. Molin, D. Boccaccini, M. Salvo, A.R. Boccaccini, Electrophoretic deposition of Mn1.5Co1.5O4 on metallic interconnect and interaction with glass-ceramic sealant for solid oxide fuel cells application, Journal of Power Sources. 280 (2015) 379–386. doi:10.1016/j.jpowsour.2015.01.120.

[17] Q. Fu, F. Tietz, D. Sebold, E. Wessel, H.P. Buchkremer, Magnetron-sputtered cobalt-based protective coatings on ferritic steels for solid oxide fuel cell interconnect applications, Corrosion Science. 54 (2012) 68–76. doi:10.1016/j.corsci.2011.08.051.

Chapter 4

Glass-Ceramic Sealants - Results and Discussion

This chapter will discuss the results of 1st, 2nd and 3rd series of glass systems in terms of their thermal behavior, thermo-chemical compatibility with the Crofer22APU interconnect, 3YSZ electrolyte in addition to their high temperature mechanical properties. The effect of thermal ageing on the thermal properties such as coefficient of thermal expansion (CTE), the formation of crystalline phases and thermo-chemical compatibility of glass-ceramics will also be presented. The electrical properties and post mortem analyses of these glass systems in air and dual atmosphere will also be discussed. Finally, the novel glass paste development and subsequently paste deposition on the Crofer22APU interconnect by the stencil printing will also be discussed.

The text, data and images shown in this chapter are an adaptation of the results that were published in the following articles:

1. Javed, H.; Sabato, A.G.; Herbrig, K.; Ferrero, D.; Walter, C.; Salvo, M.; Smeacetto, F. Design and characterization of novel glass-ceramic sealants for solid oxide electrolysis cell (SOEC) applications, *International Journal of Applied Ceramic Technology* **2018**, 15, 999–1010. doi:10.1111/ijac.12889.
2. Javed, H.; Sabato, A.G.; Dlouhy, I.; Halasova, M.; Bernardo, E.; Salvo, M.; Herbrig, K.; Walter, C.; Smeacetto, F. Shear Performance at Room and High Temperatures of Glass–Ceramic Sealants for Solid Oxide Electrolysis Cell Technology. *Materials* **2019**, *12*, 298.

The results published in above-mentioned articles will be partially reproduced in this chapter with the incorporation of more results and slight modifications.

4.1 1st series of glass-ceramic systems

The 1st series of glasses contains two glass systems labeled as HJ3 and HJ4. The compositional details of both glasses have been discussed in chapter 3. The HJ3 glass system has CaO and MgO as main modifiers in addition to a minimal concentration of SrO. However, the HJ4 glass system has only SrO as a modifier.

4.1.1 Thermal analysis of glasses belonging to 1st series

To analyze the crystallization and sintering behaviors of glasses, the DTA and HSM analyses were carried out on the glass powders having a particle size < 25 μm. The information obtained from the DTA and HSM analyses will be important in order to decide the processing heat treatment parameters to obtain the corresponding glass-ceramics.

The DTA vs HSM curves corresponding to the HJ3 and HJ4 glass systems are shown in Figure 59. In Figure 59 the T_g, T_x and T_p labels on the DTA curves, correspond to the glass transition temperature, onset crystallization temperature and peak crystallization temperature, respectively. On the other hand, the T_{FS} and T_{MS} labels on the HSM curves represent the first and maximum sintering temperatures respectively. The T_{FS} (temperature of first shrinkage), corresponds to the temperature at which the sintering process was initiated by viscous flow, whereas T_{MS} corresponds to the maximum shrinkage temperature.

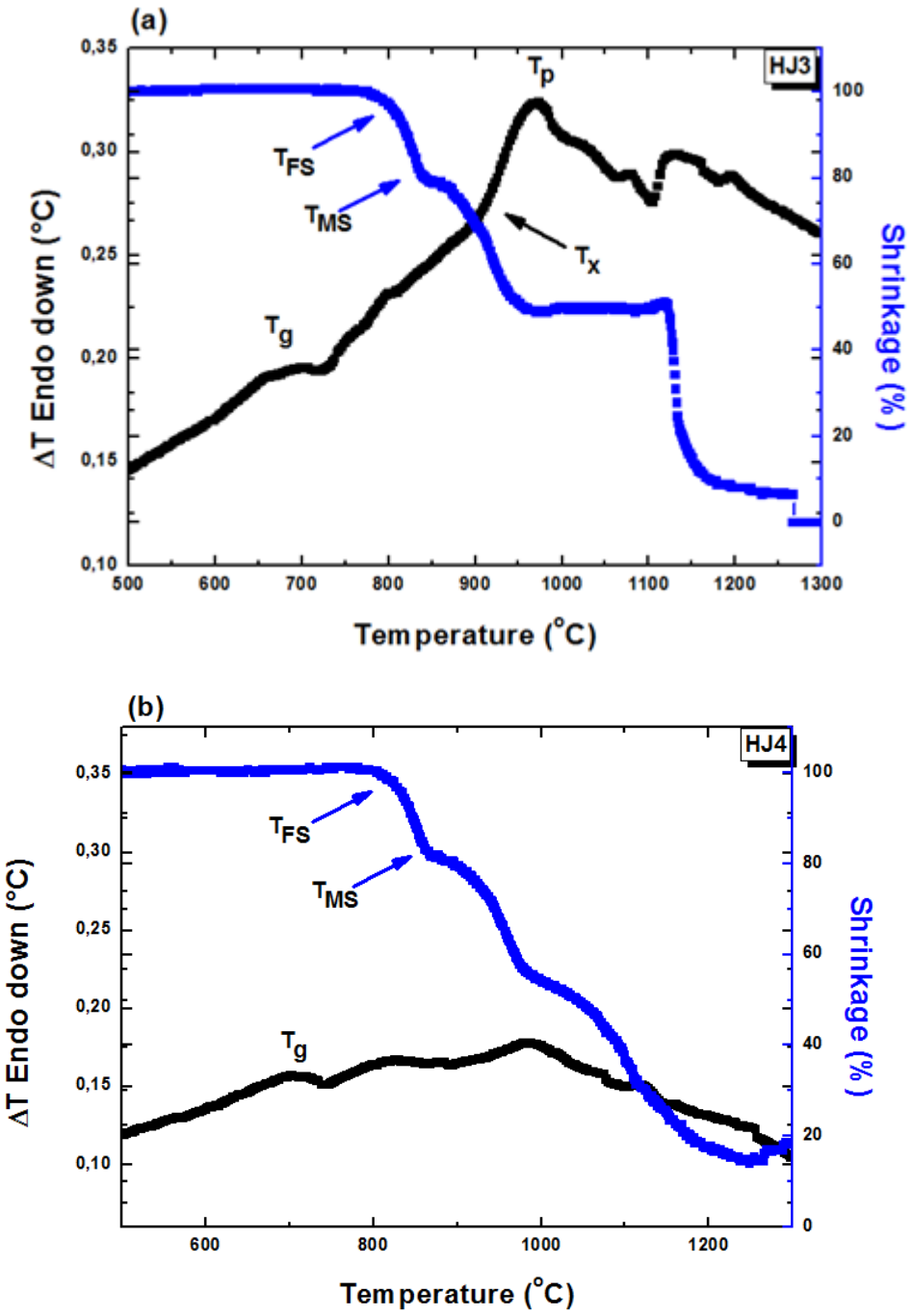

Figure 59. DTA vs HSM behaviors of (a) HJ3 and (b) HJ4 glass systems

The average characteristic temperatures (of three measurements) of HJ3 and HJ4 glasses, as obtained from the DTA and HSM analyses are summarized in Table 12

Table 12. Characteristic temperatures of HJ3 and HJ4 glasses (Heating rate: 5°C/min)

	HJ3	HJ4
Glass transition temperature T_g (°C)	722 ± 3	736 ± 4
Onset crystallization temperature T_x (°C)	893 ± 5	Not detected
Peak crystallization temperature T_p (°C)	936 ± 2	Not detected
First shrinkage temperature T_{FS} (°C)	773 ± 3	809 ± 5
Maximum shrinkage temperature T_{MS} (°C)	855 ± 2	875 ± 4
CTE of as-cast glass/1 x 10^{-6} K^{-1} (200 °C-500 °C)	9.7 ± 0.2	6.9 ± 0.1

Table 12 shows that the HJ3 and HJ4 glass systems have the T_g of 722°C and 736 °C respectively. In glasses, the addition of modifiers reduce the characteristic temperatures of glasses due to increase in the number of non-bridging oxygen atoms [1], [2]. The overall concentration of modifiers (CaO, MgO and SrO) in the HJ3 glass is 44.04 mol%, however, in the HJ4 glass the only used modifier SrO have the concentration of 28.84 mol%. The higher concentration of modifiers in HJ3 resulted in lowering the corresponding T_g as compared with HJ4.

From the DTA curves of HJ3 and HJ4 glass systems (Figure 59), it is apparent that the HJ3 glass system showed a crystallization temperature (T_p) peak at 936 °C. However, no crystallization peak was observed during the DTA analyses of the HJ4 glass system. In HJ4 glass, the absence of sharp crystallization peak indicates that the crystallization was not enough to be detected during the DTA analyses.

The HSM curves of both glass systems (Figure 59) show a clear difference in their sintering behaviors. The HSM analyses of the HJ3 system showed a constant shrinkage for a certain temperature range (955-1010 °C) after the completion of sintering at T_{MS}. On the other hand, in case of HJ4 glass, a continuous viscous flow of glass was observed at temperatures higher than the T_{FS}. As according to the DTA analyses, the HJ3 glass system showed more intensity of devitrification, therefore, the formation of crystalline phases improved the thermal stability of HJ3 glass system after T_p and T_{MS}. However, in case of HJ4 glass system, the continuous viscous behavior observed after T_p and T_{MS} was most likely due to the less devitrification.

The formation of dense and leakage free glass-ceramic sealants requires the sintering process to be completed before the crystallization starts ($T_{MS} < T_x$), in order to avoid the formation of porosity due to enhanced viscosity caused by the crystal formation [1]. As soon as the process of crystallization starts, the viscosity of glass increases drastically and consequently hinders the viscous flow of the glass and the adhesion to the metallic or ceramic substrates. Therefore, it is important that the crystallization mechanism of the glass-ceramic should be taken into account while choosing the heat treatment schedule. The characteristics temperatures mentioned for the HJ3 and HJ4 glass systems in the HSM analyses

are summarized in, shows that for both the glass systems, the sintering process was completed before the beginning of the crystallization.

To measure the coefficient of thermal expansion (CTE) of as-cast glasses, the dilatometer analyses was carried out at a heating rate of 5 °C/min up to the softening temperature. Figure 60 shows the dilatometer curves of HJ3 and HJ4 as casted glasses. The as-casted HJ3 and HJ4 glasses showed the CTEs of 9.7 x 10^{-6} K^{-1} and 6.9 x 10^{-6} K^{-1} respectively, as measured in the temperature range of 200-500 °C. The HJ3 as-casted glass showed higher CTE as compared with as-casted HJ4 glass. Like T_g, increasing modifiers concentration results in higher CTE of glass, due to the formation of non-bridging oxygen atoms. Therefore, the lower CTE of as-casted HJ4 glass system as compared with the HJ3 glass, is most likely due to the reduction in overall concentration of modifiers in the HJ3 system.

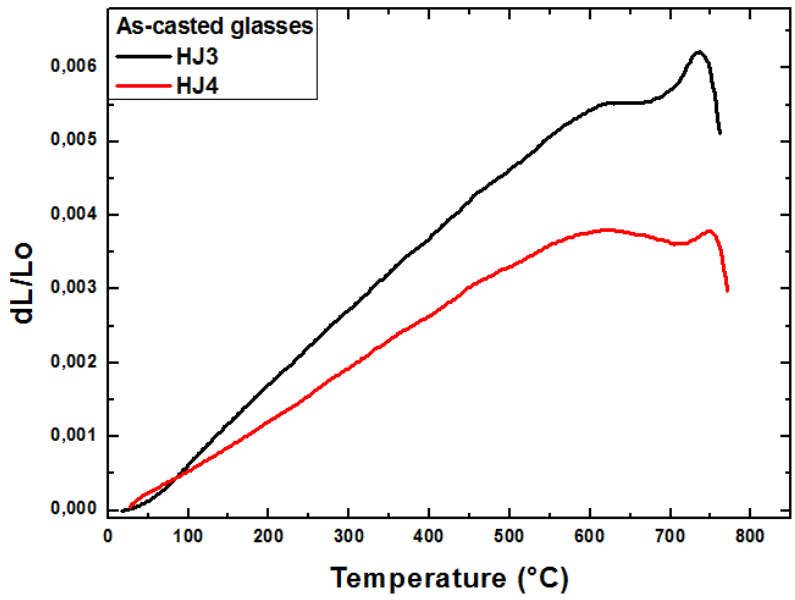

Figure 60. Dilatometer curve of HJ3 and HJ4 as-casted glasses

The XRD analyses was performed on the as-cast glasses (HJ3 and HJ4) in powder form. The corresponding XRD patterns given in the Figure 61 shows an amorphous hump without any sharp crystalline peak. It is a typical behavior of glasses due to the fact that glasses are amorphous in nature and lack long range ordered atomic structure [3].

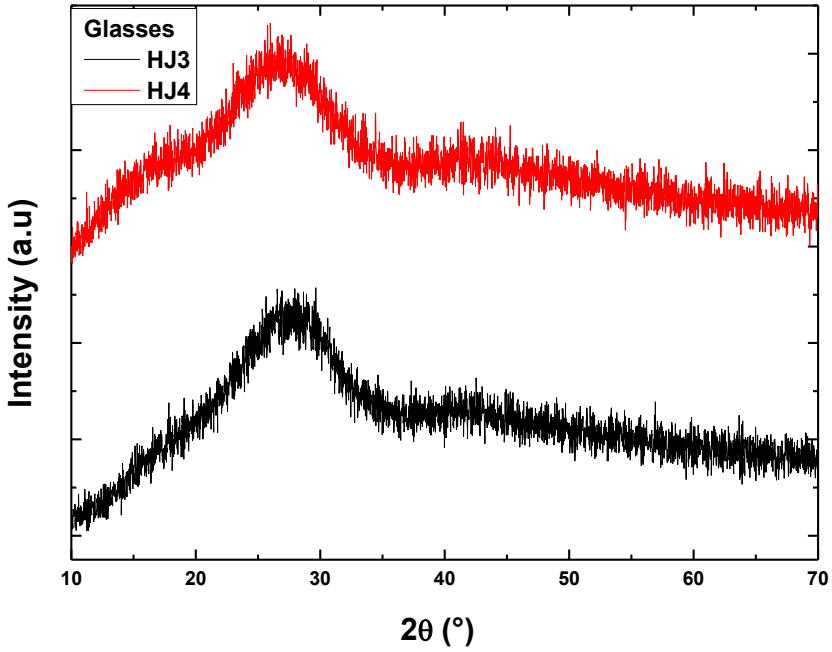

Figure 61. XRD of as-casted HJ3 and HJ4 glasses

4.1.2 Coefficient of thermal expansion and XRD phase analysis of the glass-ceramics belonging to 1st series

On the basis of the data obtained from the DTA and HSM analyses (HSM analyses are summarized in), a heat treatment of 950 ºC, for 1h at a heating rate of 5 °C/min, was selected to synthesize the as-joined HJ3 and HJ4 glass-ceramics. Glass-ceramics were synthesized at 950 °C to ensure maximum devitrification as well as good densification. The glass-ceramics were investigated in terms of their coefficient of thermal expansion (CTE) and phase analysis by XRD.

The dilatometer curves of the as-joined HJ3 and HJ4 glass-ceramics are shown in Figure 62. The corresponding CTE values of the as-joined HJ3 and HJ4 glass-ceramic are also summarized in Table 13. The as-joined HJ3 glass-ceramic has CTE of 10.2 x 10^{-6} K^{-1} (200-500°C), thus increased as compared with the HJ3 as-casted glass. However, on the other hand, the HJ4 glass-ceramic obtained by this heat treatment (950 °C, 1h, 5 °C/min) had a CTE of 7.0 x 10^{-6} K^{-1}, therefore negligibly increase as compared with the CTE of as-casted HJ4 glass (6.9 x 10^{-6} K^{-1}). This negligible increase was probably due to very negligible devitrification in HJ4 glass system. Therefore, to ensure sufficient devitrification, a slow heating rate of 2 ºC/min and a long dwelling time of 5 hours was chosen as a heat treatment to prepare the HJ4 glass-ceramic. After the long dwelling (5 hours), the HJ4 glass-ceramic showed the CTE of 9.3 x 10^{-6} K^{-1} and is within the desired range (9-12 x 10^{-6} K^{-1}), taking into consideration the CTEs of the other cell components (CTEs for Crofer22APU and 3YSZ are 12 x 10^{-6} K^{-1} and 10.5 x 10^{-6} K^{-1} respectively) [4]. The dilatometer curve of the as-joined HJ4 glass-ceramic

obtained after long dwelling (5 hours) and slow heating rate is also shown in the Figure 62.

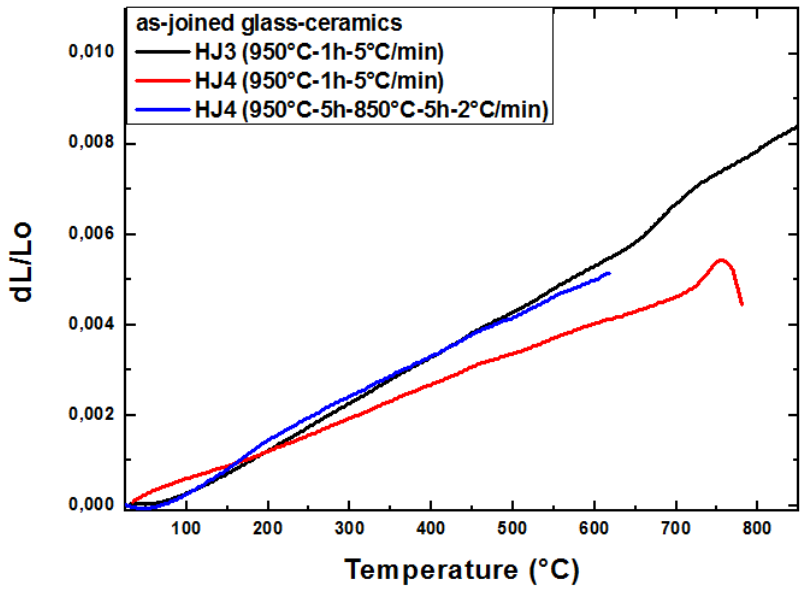

Figure 62. Dilatometer curves carried out at 5°C/min, on the as-joined HJ3 and HJ4 glass-ceramics

Table 13. CTEs of as-joined HJ3 and HJ4 glass-ceramics

	Heat treatment to obtain glass-ceramics	**CTEs of glass-ceramic /1 x 10^{-6} K^{-1} (200 ºC-500 ºC)**
HJ3 glass-ceramics	Room Temperature-950 °C (1 h), Heating/cooling rate 5 °C/min	10.2 ± 0.2
HJ4 glass-ceramics	Room Temperature-950 °C (1 h), Heating/cooling rate 5 °C/min	7.0 ± 0.1
	Room Temperature-950 °C (5 h), Heating/cooling rate 5 °C/min	8.2 ± 0.1
	Room Temperature-950 °C (5 h), Heating/cooling rate 2 °C/min	9.3 ± 0.1

XRD measurements were subsequently performed to identify the different crystalline phases formed in the glass-ceramics as a results of different heat treatments. The crystalline phases having CTEs of 9-14 x 10^{-6} K^{-1} is desirable in order to obtain the glass-ceramic sealant with a suitable CTE (9-12 x 10^{-6} K^{-1}) for

the SOEC applications. The presence of low CTE phase in a glass-ceramic generates the localized stresses within the glass-ceramic or at interface between glass-ceramic and neighboring component, and consequently leads to cracks generation and/or delamination.

The XRD patterns of the HJ3 and HJ4 as-joined glass-ceramics are shown in Figure 63. The as-joined HJ3 glass-ceramic (Figure 63 (a)) shows the presence of $Sr_2Al_2SiO_7$ as the main crystalline phase, while Sr-diopside ($Ca_{0.75}Sr_{0.2}Mg_{1.05}(Si_2O_6)$) and Akermanite ($Ca_2MgSi_2O_7$) were also present as secondary phases. Figure 63(b) shows the XRD patterns of the HJ4 system treated at different temperatures and for different dwelling times as mentioned in the Table 13. The HJ4 glass-ceramic obtained at 950°C for 1 hour, contains only $SrSiO_3$ as a crystalline phase in addition to the residual glassy phase. However, an increase in the dwelling time to five hours at 950°C, resulted in the formation of cristobalite (SiO_2) as a secondary phase in addition to the $SrSiO_3$ main phase. The XRD patterns of pure phases shown in Figure 63, corresponds to the simulated patters obtained from the X'Pert software data base.

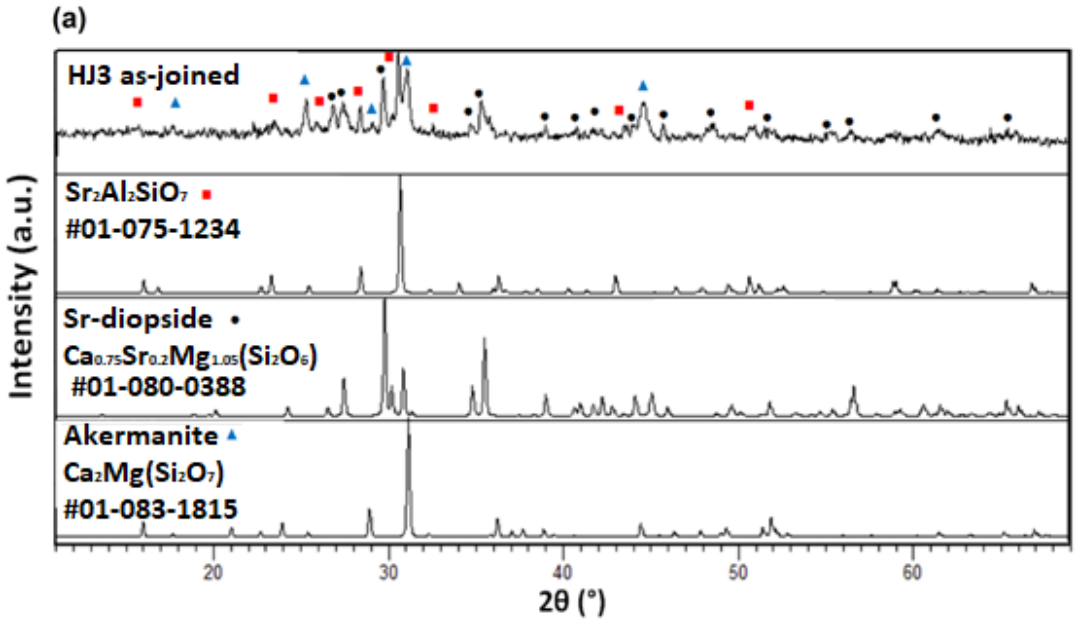

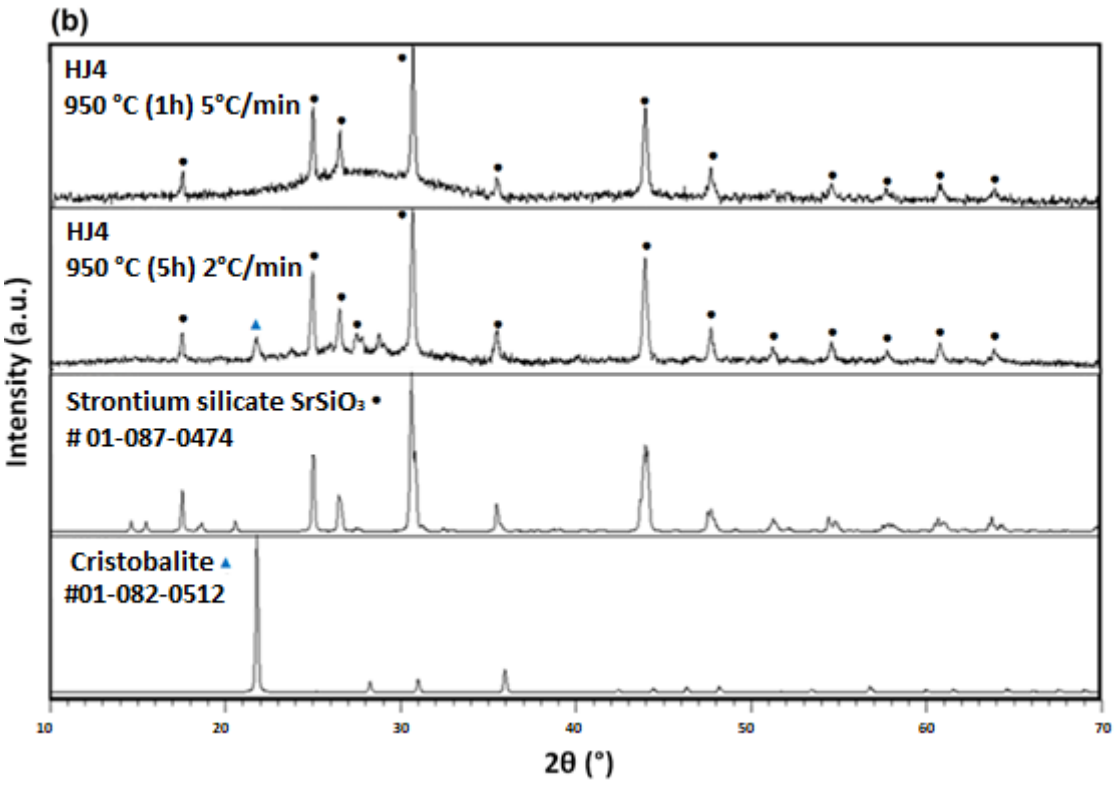

Figure 63. XRD patterns of as-joined (a) HJ3 and (b) HJ4 glass-ceramics

The different crystalline phases formed in the as-joined HJ3 and HJ4 glass-ceramics are summarized in Table 14.

Table 14. Crystalline phases (and relative ICCD reference number cards) present in the as-joined HJ3 and HJ4 glass-ceramics as detected by XRD

	Heat treatment to obtain glass-ceramic	Crystalline phases in as-joined glass-ceramics
HJ3 glass-ceramics	Room Temperature -950 °C, Dwell: 1 h, Heating/cooling rate 5 °C/min	$Sr_2Al_2SiO_7$ (# 01-075-1234) $Ca_{0.75}Sr_{0.2}Mg_{1.05}(Si_2O_6)$ (# 01-080-0388) $Ca_2Mg(Si_2O_7)$ (# 01-083-1815)
HJ4 glass-ceramics	Room Temperature -950 °C Dwell: 1 h, Heating/cooling rate 5 °C/min	$SrSiO_3$ (# 01-087-0474)
	Room Temperature-950 °C Dwell: 5 h, Heating/cooling rate 2 °C/min	$SrSiO_3$ (# 01-087-0474) SiO_2 (# 01-082-0512)

As shown in Figure 63 and Table 14, both the HJ3 and HJ4 as-joined glass-ceramics formed Sr containing crystalline phases. The formation of Sr based crystalline phases is beneficial to reduced its concentration into the residual glassy phase and consequently to minimize the possibility of formation of undesirable $SrCrO_4$ phase. However, at the same time, it is highly desirable that the formed phase in glass-ceramics should have the CTE in a desire range (9-12 x 10^{-6} K^{-1}) for SOEC applications.

Quantitative XRD analyses based on the Rietveld method were not feasible for the as-joined HJ3 and HJ4 glass–ceramics due to the complex crystalline phases and the corresponding XRD patterns. Consequently, in order to determine the relative quantities of the crystalline phases in the HJ3 and HJ4 as-joined glass–ceramics, an estimation could be made on the relative weight balance between the crystals in the glass–ceramics and the internal standard (ZnO), introduced in a defined quantity (20 wt.%). Therefore, the semi-quantitative analysis was performed by means of a Match software package (version 1.10, Crystal impact, Bonn, Germany), operating based on the reference intensity ratio method (RIR method) [8].

Figure 64(a) shows the XRD analyses performed on the as-joined HJ3 and HJ4 glass–ceramics. Due to the complex crystalline phases (especially in HJ3), some peaks are unidentified, as shown in Figure 64(a,b) shows the XRD patterns of both glass–ceramics after the inclusion of the standard (ZnO). Closer inspection of the XRD reported in Figure 64(b) shows the presence of a slightly more pronounced “amorphous halo” in the XRD pattern of the HJ4 glass–ceramic with respect to HJ3 system, thus undoubtedly indicating a relatively lower degree of crystallization in the HJ4 system. Even if the HJ4 system was processed for longer time in comparison with HJ3 (5 h vs. 1 h), it maintained a significant amount of amorphous phase, as further supported by the dilatometer curves of the as-joined HJ3 and HJ4 glass–ceramics shown in Figure 64, thus highlighting a significant difference between the two compositions. These results agree with the results obtained from the DTA, HSM and dilatometer analyses of these glass–ceramics i.e., the HJ4 glass–ceramic has a relatively higher quantity of residual glass than the HJ3 as-joined glass–ceramic.

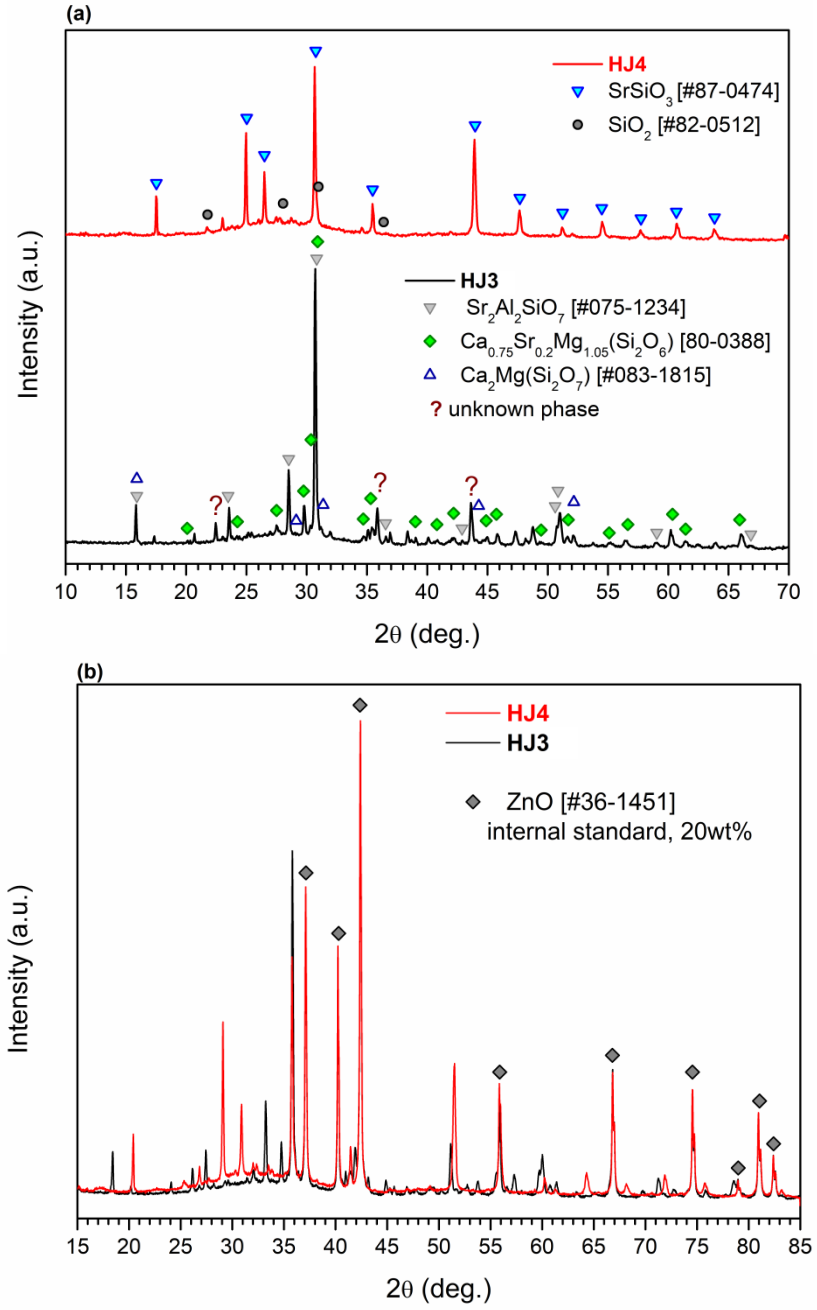

Figure 64. (a) Indexed XRD patterns of the HJ3 and HJ4 as-joined glass-ceramics (b) XRD pattern of as-joined glass-ceramics and ZnO standard

The HJ3 glass-ceramic contains $Sr_2Al_2Si_2O_7$ as main crystalline phase with CTE of 1.1 x 10^{-6} K^{-1}[5]. Although the presence of high CTE $Ca_{0.75}Sr_{0.2}Mg_{1.05}(Si_2O_6)$ [6] phase maintained the overall CTE of 10.2 x 10^{-6} K^{-1} in the as-joined HJ3 glass-ceramic, nevertheless the presence low CTE $Sr_2Al_2Si_2O_7$ phase can generate localized stresses within HJ3 glass-ceramic and can cause problem in long term tests. On the other hand, in case of HJ4 glass-ceramic, the higher SrO content and a suitable SiO_2/SrO resulted in the formation of desired high CTE $SrSiO_3$ having CTE of 10.9 x 10^{-6} K^{-1}[7]. The long dwelling time (5 hours) also resulted in the devitrification of a secondary SiO_2 phase (cristobalite)

in addition to parent $SrSiO_3$ phase. For SOEC applications, as the glass-ceramic sealant has to be subjected to several thermal cycles, the presence of cristobalite phase could be an issue due to the fact that it has phase transformation around 270°C (with a change in the specific volume) and can lead to the generation of thermo-mechanical stresses with possible crack formation. Therefore, it can affect the long-term integrity of SOEC stack subjected to thermal cycles.

4.1.3 Effect of thermal ageing on the cofficient of thermal expansion and XRD phase analysis of the glass-ceramics belonging to 1st series

The XRD analysis was performed on the aged HJ3 and HJ4 glass-ceramics to investigate crystalline phases after ageing. The XRD analyses were carried out on the glass-ceramics in powder form, obtained by crushing and ball milling the aged pallets of glass-ceramics. The corresponding XRD patterns are shown in Figure 65, while the different crystalline phases are summarized in Table 15. The Table 15 shows that the thermal ageing for 1000 hours at 850°C does not resulted in the formation of new phases in both (HJ3 and HJ4) glass-ceramics. All the crystalline phases after ageing (Table 15) are similar to those detected in the as-joined HJ3 and HJ4 glass-ceramics (Table 14).

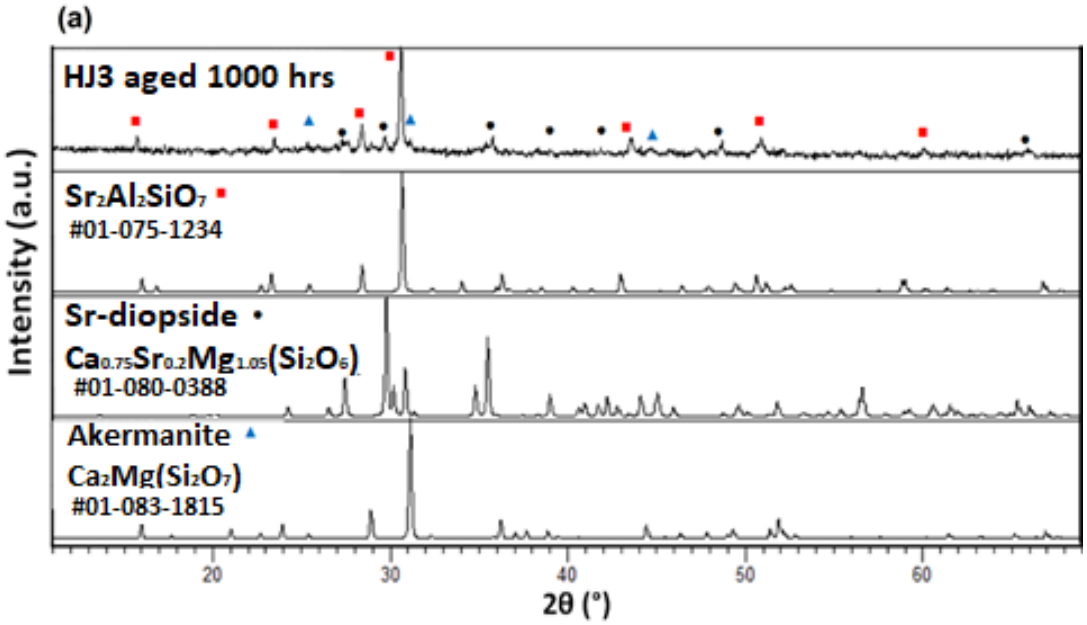

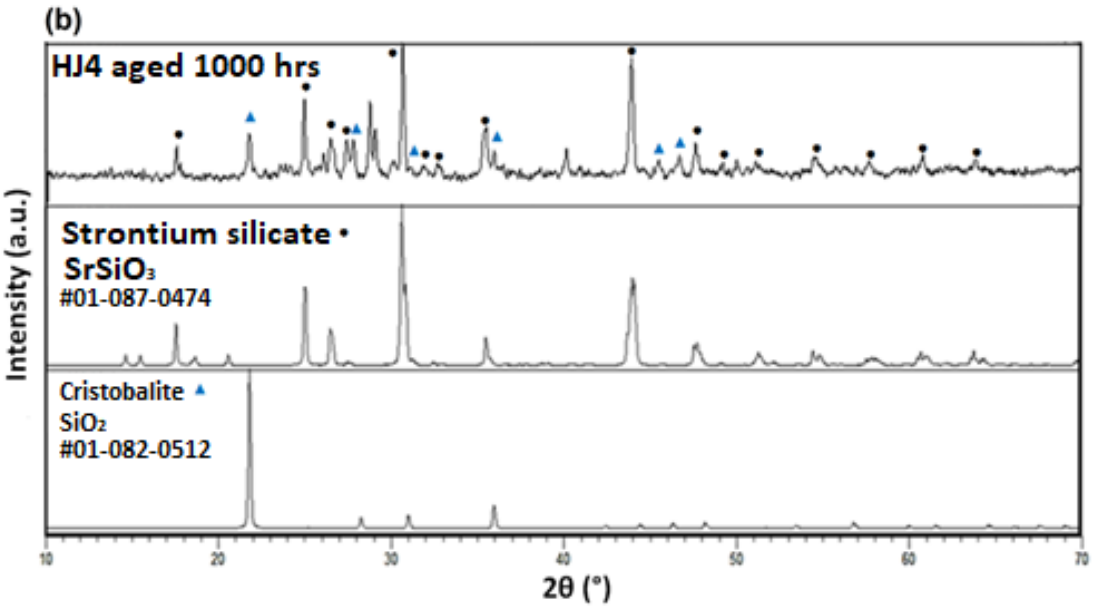

Figure 65. XRD patterns of (a) HJ3 and (b) HJ4 glass-ceramics, aged for 1000 hours at 850°C

Table 15. Crystalline phases (and relative ICCD reference number cards) present in the HJ3 and HJ4 glass-ceramics after ageing for 1000h at 850 °C, as detected by the XRD

Glass-ceramics (aged- 1000 hours, 850 °C)	Crystalline phases
HJ3	$Sr_2Al_2SiO_7$ (# 01-075-1234) $Ca_{0.75}Sr_{0.2}Mg_{1.05}(Si_2O_6)$ (# 01-080-0388) $Ca_2Mg(Si_2O_7)$ (# 01-083-1815)
HJ4	$SrSiO_3$ (# 01-087-0474) SiO_2 (# 01-082-0512)

The CTEs of the HJ3 and HJ4 glass-ceramics after the thermal ageing for 1000 hours at 850°C in static air were also measured and are reported in Table 16. The CTE of the HJ3 glass-ceramic after ageing remained unchanged as compared with the as-joined HJ3 glass-ceramic. On the other hand, thermal ageing further increased the CTE of the HJ4 glass-ceramic. Therefore, the CTEs of both glass-ceramics after ageing are in the desirable range (9-12) x 10^{-6} K^{-1} for SOEC applications.

Table 16. CTEs of HJ3 and HJ4 glass-ceramic after ageing aged for 1000 h at 850°C

	HJ3	HJ4
CTEs of glass-ceramic aged for 1000 h at 850 °C (200 °C-500 °C) 1 x 10^{-6} K^{-1}	10.1 ± 0.2	9.6 ± 0.1

Due to the presence of similar crystalline phases in the HJ3 and HJ4 glass-ceramics after joining and thermal ageing, the CTEs of both the glass systems remained almost unchanged after the ageing. Thermally aged HJ3 glass-ceramic showed CTE of 10.1 x 10^{-6} K^{-1} in spite of having a low CTE $Sr_2Al_2Si_2O_7$ phase (Table 16). The presence of a high CTE Sr-diopside phase was responsible for retaining the overall CTE of the HJ3 glass-ceramic. In case of HJ4 glass-ceramic, the increase in CTE after ageing was probably due to an increase in the quantity of the high CTE $SrSiO_3$ phase.

4.1.4 Joining of 1st series glass-ceramics with Crofer22APU and 3YSZ

In order to investigate the compatibility and adhesion of the HJ3 and HJ4 glass-ceramics with the Crofer22APU and 3YSZ substrates, Crofer22APU/glass-ceramic/3YSZ joined samples were prepared. The SEM analyses was carried out to observe the adhesion of glass-ceramics with the neighboring components, while EDS analyses was done to detect diffusion of different element across the Crofer22APU/glass-ceramic interface and to investigate the composition of residual glassy phases in HJ3 and HJ4 as-joined glass-ceramics. Figure 66 shows the SEM cross-section images of the as-joined Crofer22APU/HJ3 glass-ceramic/3YSZ and Crofer22APU/HJ4 glass-ceramic/3YSZ samples. The Crofer22APU/HJ3 glass-ceramic/3YSZ joined sample was processed at 950 °C for 1 hour at a heating/cooling rate of 5 °C/min. However, the Crofer22APU/HJ4 glass-ceramic/3YSZ joined sample was processed at 950°C for 5 hours at a heating/cooling rate of 2 °C/min. The slow heating/cooling rate and long dwelling time for HJ4 system was chosen to ensure sufficient degree of crystallization in HJ4 glass-ceramic. The SEM analyses show continuous interfaces of both HJ3 and HJ4 glass-ceramics with the Crofer22APU and 3YSZ, thus confirming a strong adhesion. No evidence of cracks or delamination was observed at both interfaces. The SEM microstructure of both glass-ceramics is uniform and dense throughout the joining region.

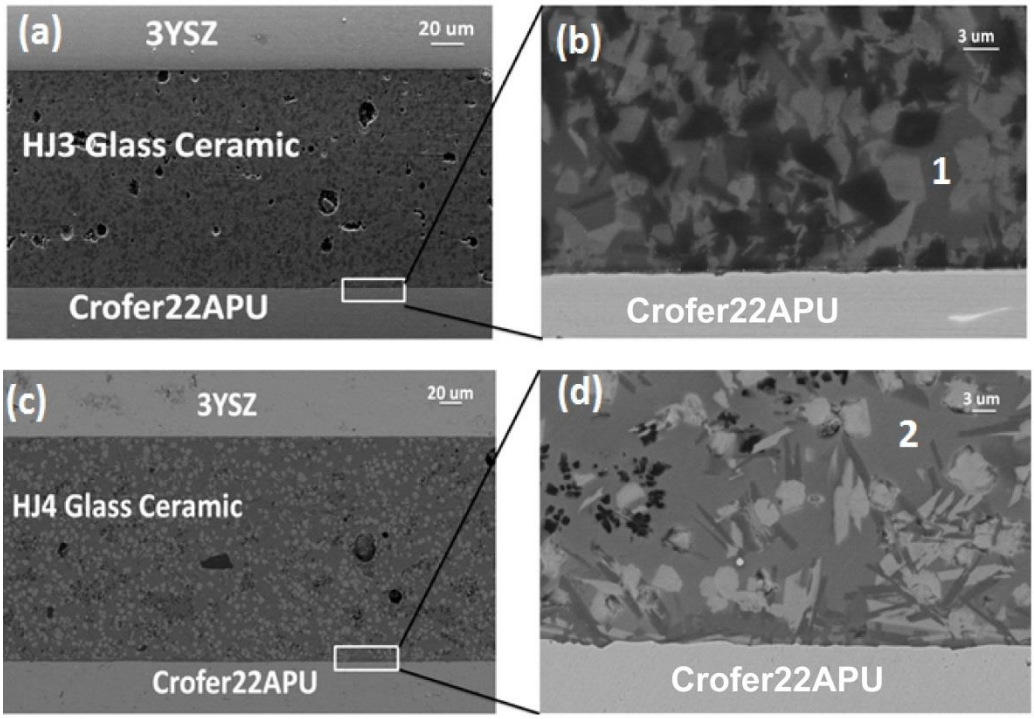

Figure 66. SEM image of (a) Crofer22APU/HJ3 glass-ceramic/3YSZ joint, (b) Crofer22APU/HJ3 glass-ceramic interface, (c) Crofer22APU/HJ4 glass-ceramic/3YSZ joint, and (d) Crofer22APU/HJ4 glass-ceramic interface

The SEM microstructure of the HJ3 glass-ceramic (Figure 66 (a) and (b)) showed different crystalline phase as well as the residual glassy phase. The residual glassy phase of the HJ3 glass-ceramic is labeled as point 1 in the Figure 66. The Figure 66 (c) and (d) show quite dense HJ4-based joint with a little porosity. A significant residual glassy phase can be seen in HJ4 glass-ceramic (Figure 66 (d)-Point 2), that impart viscous behavior to HJ4 glass-ceramic. The "viscous character" of this system led to a negligible level of porosity during the joining treatment.

The EDS point analyses carried out at the residual glassy phases of HJ3 and HJ4 as-joined glass-ceramics are given in Table 17. The EDS analyses shown in the Table 17 corresponds to the point 1 and 2 labeled in the Figure 66. It is important to note that the residual glassy phases of both glass systems contain Sr less than 10 at %. This minimal concentration of Sr is beneficial not only to maintain the viscous behavior of glassy phase but also to avoid the potential formation of undesirable $SrCrO_4$ phase.

Table 17. The EDS point analyses (at. %) at the residual glassy phase of as-joined HJ3 and HJ4 glass-ceramics shown in the Figure 66

Elements	HJ3 (Point 1)	HJ4 (Point 2)
O	66.3	72.3
Mg	5.2	---
Al	1.4	2.8
Si	14.2	16.4
Ca	2.9	---
Sr	9.4	7.1
Y	0.6	1.4

The microstructure of the HJ4 glass-ceramic processed at different heat treatments is shown in Figure 67. The microstructure of HJ4 glass-ceramic obtained after the heat treatment of 950°C, 1h (Figure 67(a)) shows the presence of only one crystalline phase (Figure 67(a)-point 2) in addition to the residual glass phase (Figure 67(a)-point 1). According to XRD (Figure 63(b)) that crystalline phase corresponds to the $SrSiO_3$. On the other hand, the heat treatment at 950°C, 5h at a heating/cooling rate of 2 °C/min resulted in the significant evolution of microstructure. Apparently, long dwelling of 5 hours not only increased the volume fraction of the initially formed $SrSiO_3$ phase but also resulted in the devitrification of a new phases (Figure 67(b)- point 4 and 6).

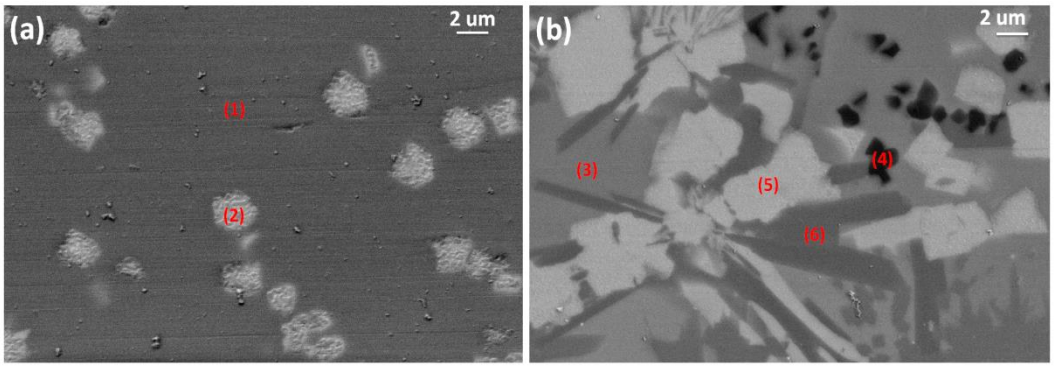

Figure 67. SEM images correspond to the HJ4 glass-ceramic synthesized at (a) 950°C for 1 h, heating/cooling rate 5 °C/min and (b) at 950 °C for 5 h, heating/cooling rate 2 °C/min.

The EDS point analysis performed on the HJ4 glass-ceramic microstructures (Figure 67) evolved as a result of different heart treatments, are shown in Table 18. According to EDS analysis, the point 1 and 2 in the Figure 67 correspond to the residual glassy phase and $SrSiO_3$ phase respectively. The point 3 in Figure 67 (b) represents the residual glass in the HJ4 glass-ceramic formed after the long dwelling time. The comparison of residual glass compositions before (Table 18-

point 1) and after long dwelling (Table 18-point 3) shows that the Sr concentration reduced form 13.9 at. % to 7.1 at.%. The long dwelling increased in the concentration of $SrSiO_3$ phases, thus cause reduction in Sr concentration into the residual glass and consequently further minimized the possibility of $SrCrO_4$ phase formation.

The EDS analyses carried out at dark phase in the Figure 67 (b)-point 4, indicated a SiO_2 rich phase thus refer to cristobalite as investigated by XRD. The detection of Sr and Al at point 4, is most likely due to the surrounding environment of the point where the EDS analysis was carried out. The EDS analyses of point 6 is similar to point 2, thus indicates $SrSiO_3$ phase. The different contrast between point 2 and 3 was probably due to the presence of very thin glass layer on the crystals at point 6. These EDS results validate the XRD analyses of HJ4 at different heat treatments, as discussed earlier in this section.

Table 18. The EDS point analyses (at.%) performed at the HJ4 glass-ceramics shown in the Figure 67

	1	2	3	4	5	6
O	58.8	53.6	72.3	74.3	68.6	75.1
Al	4.5	0.7	2.8	3.8	0.4	1.3
Si	21.5	20.3	15.0	16.4	15.6	17.3
Sr	13.9	25.4	7.1	5.5	14.9	6.4
Y	0.9	---	1.4	0.0	0.5	0.0
Cr	---	---	0.7	---	---	---
Mn	---	---	0.6	---	---	---

Figure 68 shows the EDS line scans across the Crofer22APU/ as-joined glass-ceramics (HJ3 and HJ4). According to EDS line scans, no Cr diffusion was observed from Crofer22APU into glass-ceramics, nor diffusion or segregation of any element of glass-ceramics at Crofer22APU/glass-ceramic interface was detected. The EDS line scan also confirmed that no undesirable chromates were formed.

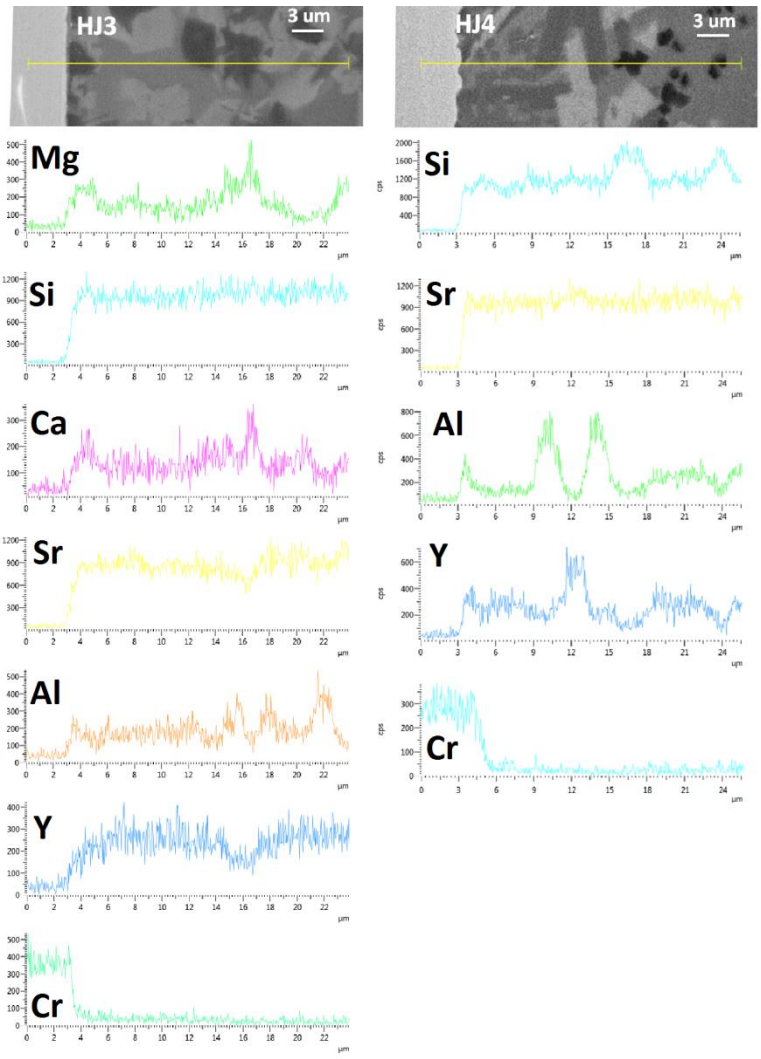

Figure 68. EDS line scan across (a) Crofer22APU/as-joined HJ3 glass-ceramic and (b) Crofer22APU/as-joined HJ4 glass-ceramic

To investigate the effect of thermal ageing on the compatibility of HJ3 and HJ4 glass-ceramics with Crofer22APU, the Crofer22APU/glass-ceramics joined samples were aged at 850°C for 1000 hours in static air. The corresponding SEM images of Crofer22APU/glass-ceramics interfaces after the thermal ageing are shown in Figure 69. Both the glass-ceramics showed excellent compatibility with the Crofer22APU after thermal ageing. The Crofer22APU/aged glass-ceramic interfaces uniform and crack free. The microstructures of both glass-ceramics is similar to their as-joined microstructures (Figure 66).

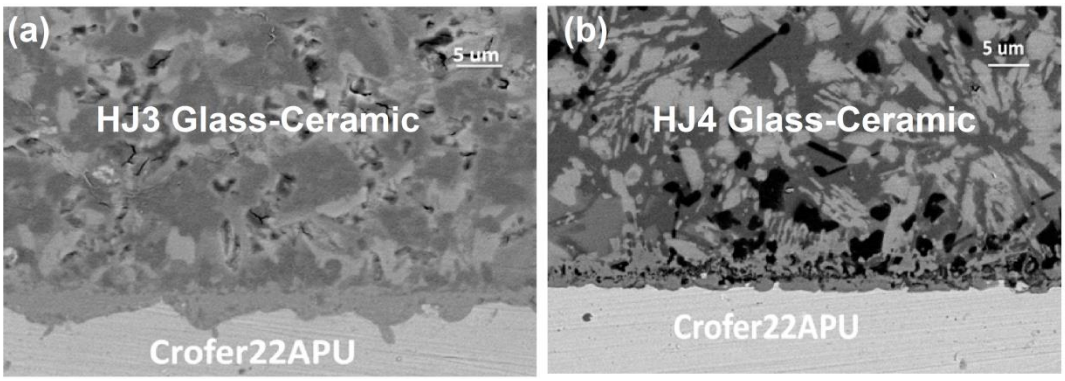

Figure 69. SEM images of (a) Crofer22APU/HJ3 glass-ceramic and (b) Crofer22APU/HJ4 glass-ceramic, after thermal ageing for 1000 hours at 850°C

The EDS line scans across the Crofer22APU/HJ3 and the Crofer22APU/HJ4 interfaces after thermal ageing are shown in Figure 70. The EDS line scan analyses showed the formation of Cr rich layer at the Crofer22APU surface. The formation of Cr-based scale is due to the long-term thermal ageing (1000 hrs) at 850°C. Nevertheless, from the EDS line scans, no Cr diffusion was detected in HJ3 and HJ4 glass-ceramics after the thermal ageing. These SEM-EDS results excluded the formation of $SrCrO_4$ and the consequent possible delamination at the Crofer22APU/glass-ceramic interface. The presence of low CTE $Sr_2Al_2SiO_7$ phase in HJ3 and cristobalite phase (with different polymorphs) [1] in HJ4 did not determine cracks within the glass-ceramics or at the interface with Crofer22APU even after 1000 hours at 850 °C.

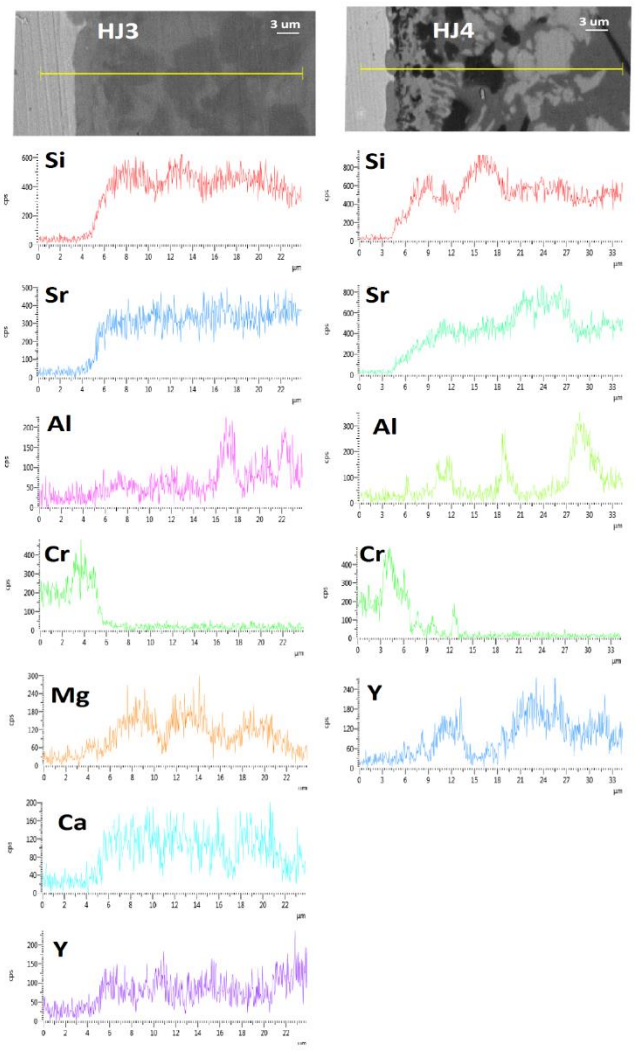

Figure 70. EDS line scan across (a) Crofer22APU/aged HJ3 glass-ceramic, and (b) Crofer22APU/aged HJ4 glass-ceramic

4.1.5 Mechanical properties and post mortem analysis of glass-ceramics belonging to 1st series

To provide a reliable integration of components within a solid oxide electrolysis cell stack, it is fundamental to evaluate the mechanical properties of the glass–ceramic sealing materials, as well as the stability of the metal–glass–ceramic interface. In this context, the mechanical properties of HJ3 and HJ4 glass–ceramics were investigated under the shear compressive load at room temperature, 650 °C and at 850 °C.

In order to investigate the mechanical integrity of the HJ3 and HJ4 glass-ceramics at room and high temperature, the Crofer22APU/glass-ceramic/Crofer22APU joints were tested. The configuration of Crofer22APU/glass-ceramic/Crofer22APU samples and the testing parameters have been discussed in detail in the chapter 3.

Figure 71 shows the shear stress vs. load displacement curves for the HJ3 and HJ4 joint samples, tested at three different temperatures. For the sake of simplicity, only one curve has been shown for each temperature measurement. The traces reflect that the high temperatures significantly affect the deformation history and fracture behavior of joints made by two different glass-ceramics. Note that slope of linear part of traces does depend not only on the Young's modulus level but may be partly affected by inexact determination of the joint area as carried out by post mortem from fracture surfaces of broken joints. For Crofer22APU/glass-ceramic/Crofer22APU joints made of both glass-ceramics, when tested at room temperature and at 650 °C (lower than T_g), the fracture occurred in the linear mode once the applied stress reached to maximum shear strength. This behavior reflects almost elastic deformation and brittle response of the glass ceramic joint. However, at 850 °C (T higher than T_g), the joints showed enhanced displacement under the applied load and extensive non-linear behavior of the trace. This effect is due to the stress relaxation and softening of the residual glassy phase above T_g and partly also due to viscous flow of the glassy phase present in the material of joint. Thus, although both systems were crystallized at 950 °C, the residual glassy phase seemed to be the main factor in controlling the mechanical behavior of the joint. As both glass systems were designed for the working temperature of 850 °C, the stress relaxation phenomena are favorable in reducing the thermal stresses that could generate due to thermal mismatch at high temperature changes associated with the cell operation. Moreover, this behavior (remaining glassy phase exhibiting viscous flow component) could also be beneficial for the self-healing and consequently can enhance the long-term stability of the sealant. Chang et al. [9] observed the stress relaxation phenomena for the as-joined and aged glass-ceramic when tested in the temperature range of 650 °C - 750 °C and attributed it as the viscoelastic behavior of residual glassy phase. Similarly, Zhao et al. [10] also observed transition from elastic to non-elastic fracture of glass-ceramic with increasing temperature from room temperature to 800 °C.

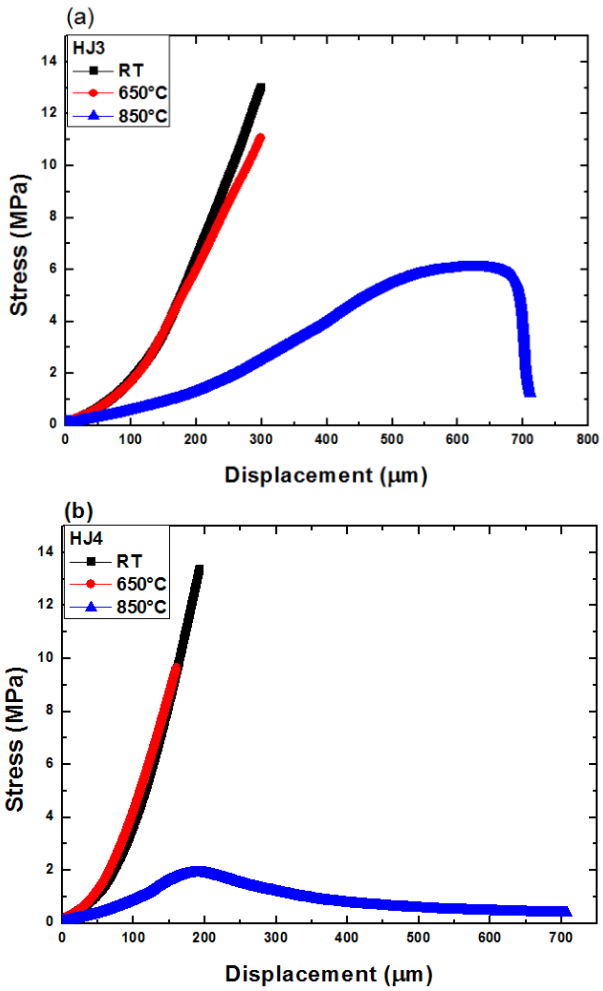

Figure 71. Shear stress vs. displacement curves for HJ3 and HJ4 joints tested under shear loads at three different temperatures

The shear strength values as determined and calculated from the above shown stress displacement curves (Figure 71) are shown in Figure 72(a). The Figure 72(a) shows the average shear strength and corresponding load displacements at fracture as obtained from three samples for each composition and at each test temperature. The shear strength of joints made by both glasses is observed to decrease with increasing testing temperatures. For HJ3 based joints the strength reduced from 14.1 (at 25 °C) to 5.5 MPa (850 °C), while for HJ4 based joints, the shear strength dropped from 13.9 MPa (25 °C) to 1.8 MPa (850 °C). The observed reduction in the strength with increasing temperature was according to expectations due to softening of residual glassy phase at high temperature and its viscous flow (creep deformation). While increasing testing temperature from 650°C to 850°C, the shear strength of HJ4 glass-ceramics reduced more drastically as compared with HJ3 glass-ceramic. This is most likely due to low volume fraction of crystalline phases and more residual glassy phase in HJ4, and consequently softening of residual glassy phase reduce the mechanical rigidity of HJ4. Osipova et al. [11] also investigated the shear strength of glass-ceramics at room temperature, 600°C and 800°C and found similar behavior of enhanced reduction in shear strength at 800°C, due to softening of remaining glassy phase.

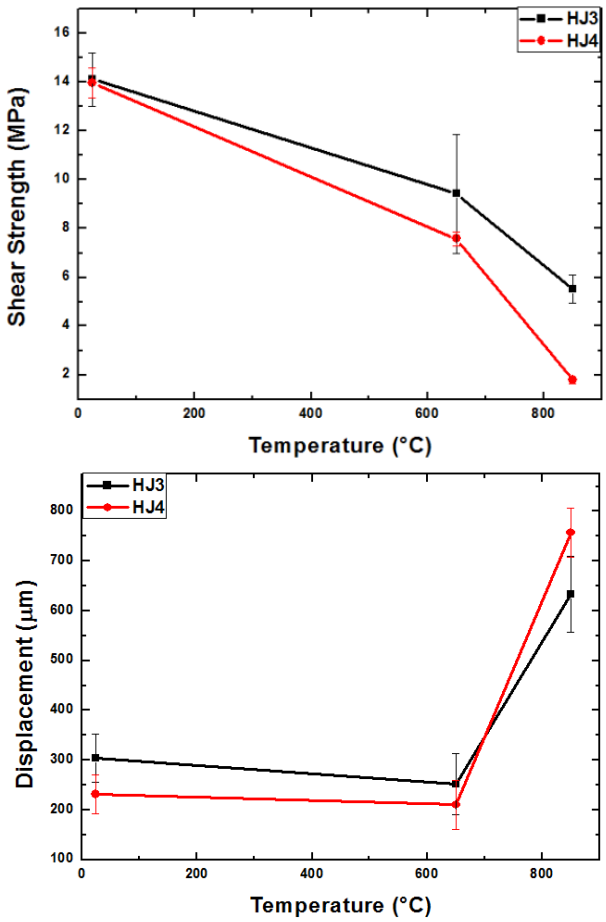

Figure 72. Comparison of shear strength (left) and load displacement (right) corresponding to fracture of both different glass systems as the function of test temperature

The displacement to fracture of both glass-ceramics joints, showed quite interesting results. For both glass systems, by increasing the testing temperature from room temperature to 650 °C, caused the fracture at displacement slightly lower than at room temperature (Figure 72(b)). For both glass systems (HJ3 and HJ4), as the test temperature of 650 °C is lower than their corresponding glass transition temperatures and glass-ceramics were still rigid, the reduction in shear strength was responsible to cause the reduction in displacement to fracture. On contrary to this, joined samples showed noticeable increase in the displacement preceding the fracture at 850 °C due to softening of residual glassy phases. Both the systems showed enhanced displacement under the applied stress as also evident from stress-displacement curves at 850 °C (Figure 71).

Table 19 summarizes the dominant fracture mode for broken joints made of both glass-ceramics tested at three different temperatures. The HJ3 based joints gave cohesive fracture (fracture occurred within the glass-ceramic joint); while HJ4 based joints fractured in adhesive manner (fracture occurred at Crofer22APU/glass-ceramic interface), as first visually observed and further confirmed by light microscope. The Figure 73 illustrates the cohesive and adhesive mode of fractures for the better understanding.

Table 19. Fracture mechanism of Crofer22APU/glass-ceramic/Crofer22APU joints made by HJ3 and HJ4 glass-ceramic, tested under shear conditions at room temperature, 650 °C and 850 °C

	Room Temperature	650 °C	850 °C
HJ3	Cohesive	Cohesive	Cohesive
HJ4	Adhesive	Adhesive	Adhesive

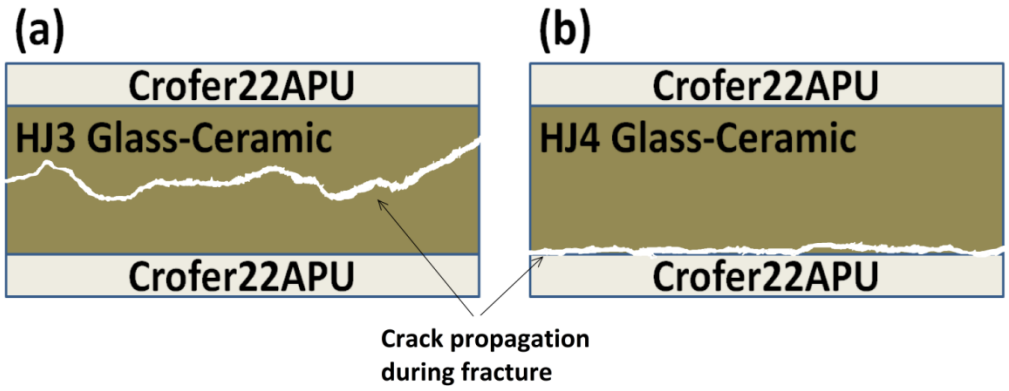

Figure 73. Illustration of (a) cohesive fracture for HJ3 and (b) adhesive fracture for HJ4 glass system, in Crofer22APU/glass-ceramic/Crofer22APU joints

Figure 74 shows the SEM images of the fracture surfaces of joints based on both glass systems. For HJ4 based systems, the SEM images corresponds to the Crofer22APU plate containing all the HJ4 glass-ceramic. Table 19 and Figure 74 shows that in case of HJ3 system the cohesive mode of fracture occurred, when the tests were performed at room temperature, 650 °C and at 850 °C. Corresponding SEM images (Figure 74(a) and (b)) of Crofer22APU/HJ3/Crofer22APU samples tested at room temperature and at 650 °C shown that the glass-ceramics completely adhered throughout the joining area of both Crofer22APU plates. However, for the HJ3 system based joint tested at 850 °C, the glass-ceramic was also partially detached from one the Crofer22APU plate as shown in Figure 74(c). The fracture was probably initiated within the glass-ceramic bulk as in case of low temperature testing and then propagated to the interface. On the other hand, for the Crofer22APU/HJ4/Crofer22APU system tested at room and high temperatures, the adhesive fracture occurred at one of the two Crofer22APU/HJ4 glass-ceramic interfaces, which resulted in complete delamination of HJ4 glass-ceramic at one interface. Nevertheless, when evaluating the quality of the sealing material, the fracture surfaces in Figure 74 exhibit quite dense glass-ceramics structure with slight porosity. In particular, the

high sintering ability of HJ4 glass (as discussed in section 4.1.1) makes it highly dense sealant.

The thermal expansion coefficient (CTE) of the glass-ceramics as well as that of individual crystal phases in a glass-ceramic system can play a key role towards the fracture behavior as they can create the stress concentration regimes, either within the glass-ceramics and/or at interface. The HJ3 glass-ceramic has CTE of 10.2 $\times 10^{-6}$ K^{-1} [12] that is closely matching with CTEs of Crofer22APU (12 $\times 10^{-6}$ K^{-1}) [4], however, the presence of $Sr_2Al_2SiO_7$ as main crystalline phase with CTE of 1.1 $\times 10^{-6}$ K^{-1} [5] can generate localized stresses within the glass-ceramics. The localized stress concentration at a crystalline phase can act as nucleation site for crack initiation particularly during externally applied shear load. HJ4 system has $SrSiO_3$ as main crystalline phase having CTE of 10.9 $\times 10^{-6}$ K^{-1} [7] thus excluding the possibility of localized stresses formation within the glass-ceramics. In our previous paper, it has been shown that HJ4 glass-ceramic had strong interface with Crofer22APU, but the as-joined HJ4 glass-ceramic has CTE of 9.3 $\times 10^{-6}$ K^{-1} [12] which is slightly less than that of Crofer22APU, therefore it can lead to generate stresses at Crofer22APU/HJ4 glass-ceramics interface and make adhesive fracture more favorable under the externally applied load.

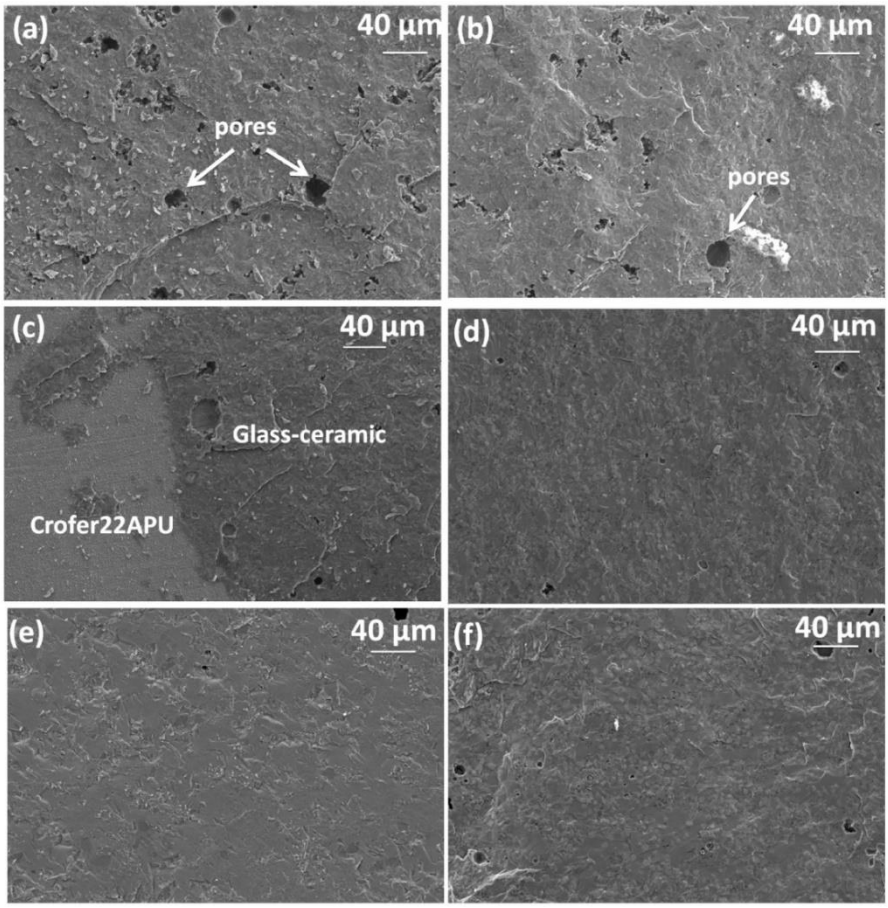

Figure 74. SEM images of top morphology of fracture surfaces of broken joint material; samples (a) HJ3 tested at RT, (b) HJ3 tested at 650 °C, (c) HJ3 tested at 850 °C, (d) HJ4 tested at RT, (e) HJ4 tested at 650 °C, (f) HJ4 tested at 850 °C

Figure 75 shows the SEM images of the Crofer22APU/glass-ceramic interface of fractured samples for both the glass systems, tested at three different temperatures under shear load. For HJ4 system, the images corresponding to the Crofer22APU/HJ4 contained all the joined glass-ceramics well adhered to Crofer22APU surface after the fracture. The SEM images showed a strong bonding of both glass-ceramics with the Crofer22APU at room temperature as well as at high testing temperatures. A uniform and dense microstructure was observed with no pores or crack. For a particular glass system, the Crofer22APU/glass-ceramic interfaces showed similar morphology for all the testing temperatures. Further details about the microstructure can be found elsewhere [12].

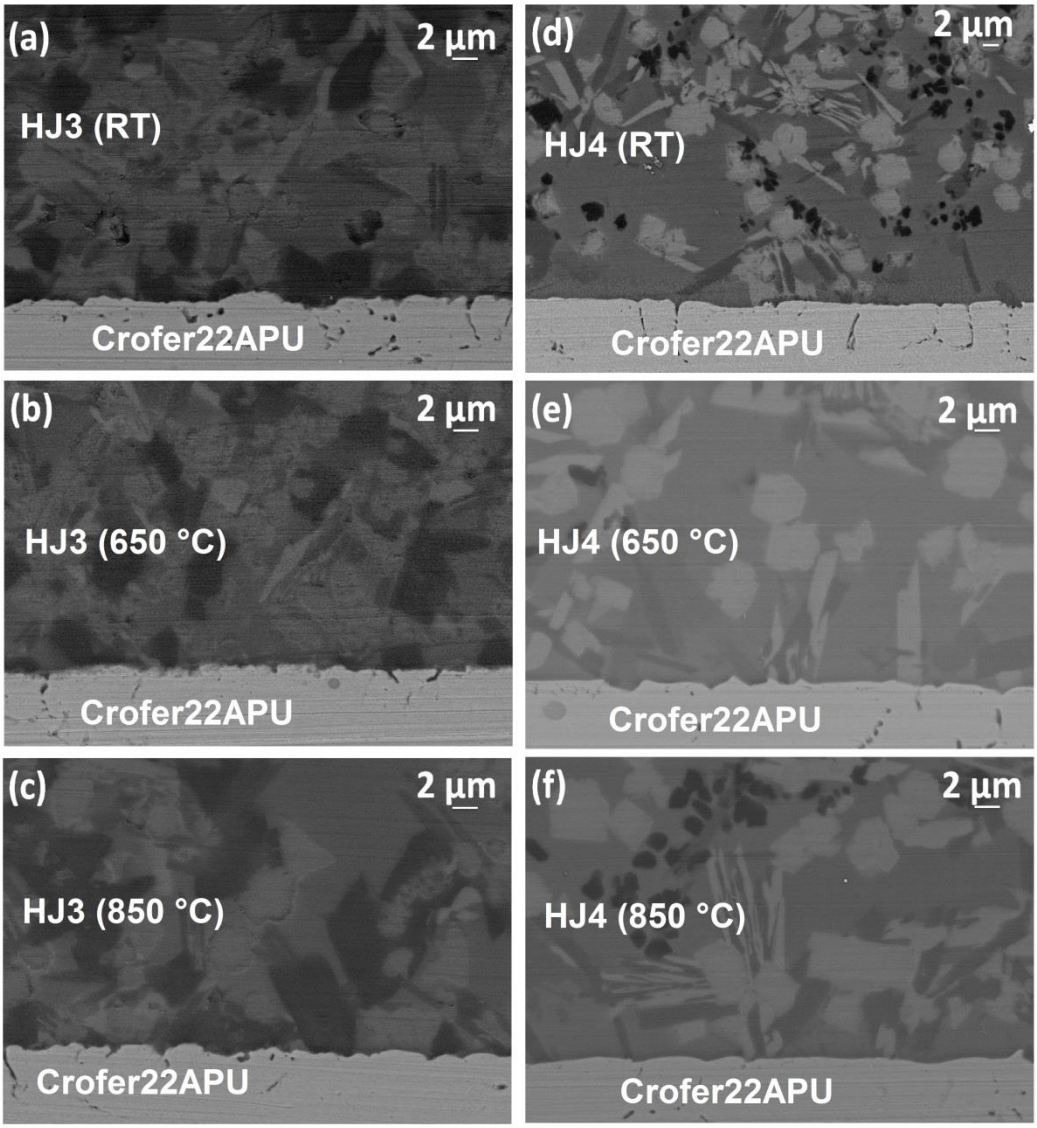

Figure 75. SEM images of interface of Crofer22APU with (a) HJ3 tested at RT, (b) HJ3 tested at 650 °C, (c) HJ3 tested at 850 °C, (d) HJ4 tested at RT, (e) HJ4 tested at 650 °C, (f) HJ4 tested at 850 °C.

The elastic moduli of as-joined glass-ceramics for both systems are shown in Figure 76. Measurements were performed up to 650°C and elastic modulus was measured both during heating and cooling. Above 650 °C, the obtained resonance

frequencies were not sufficient to measure the reliable values due to possible softening of the glass-ceramics. Direct comparison (Figure 76) shows that HJ3 glass-ceramic have higher values of elastic modulus as compared with HJ4 system. The higher volume fraction of crystals in HJ3 glass-ceramics made this system stiffer than HJ4 glass-ceramics. Similar behavior were observed by Milhans et al. [13] where reduced modulus was observed to increase with increasing volume content of the crystalline phases in glass-ceramics, as measured by nanoindentation. Zhao et al. [14] also compared the elastic modulus of different glass-ceramic systems having different amounts of residual glassy phases. The glass-ceramic with less quantity of residual glassy phase showed higher elastic modulus. The elastic modulus also increased after ageing (500 hrs), due to increase in the concentration of crystalline phases. Nevertheless, both of our glass-ceramics systems (HJ3 and HJ4) showed linear reduction in their corresponding elastic modulus with temperature due to possible softening. For HJ3 glass-ceramics, the elastic modulus reduced from 100 GPa (at room temperature) to 92 GPa (650°C), whereas for the HJ4 glass-ceramic it decreased from 80 GPa (room temperature) to 75 GPa (650°C). Zhao el al. [10] also observed almost 10% reduction in elastic modulus of different glass-ceramics when testing temperature was increased from room temperature to 650°C, however above 650°C the softening of glassy matrix strongly reduced the elastic modulus. The elastic modulus curve for HJ4 glass-ceramic (Figure 6) also shows discontinuities around 230°C during heating cycle and around 230 °C – 270 °C during cooling. This is due to the presence of cristobalite (SiO_2) phase in HJ4 [12] that has different polymorphs and cause volume expansion around 250 °C [15]. Nevertheless, the obtained elastic moduli for both systems (HJ3 and HJ4) are comparable or slightly higher than the elastic modulus of glass-ceramics available in the literature (50-80 GPa) [13], [14], [16]–[19].

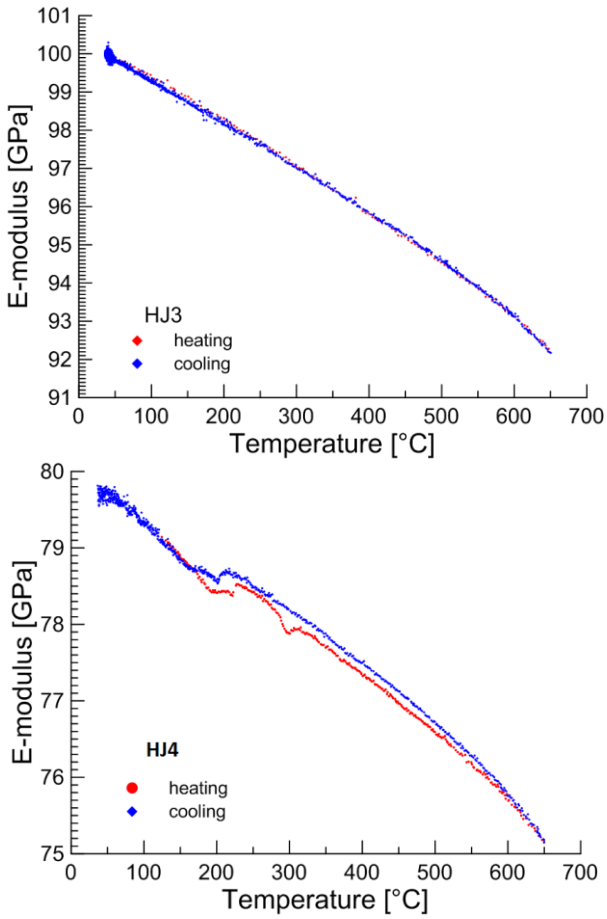

Figure 76. Elastic modulus of HJ3 and HJ4 glass-ceramics after joining, measurement was done from room temperature to 650°C

4.1.6 Electrical properties of 1st series glass-ceramics in air and post mortem analysis

The electrical resistivity of the Crofer22APU/HJ3 glass-ceramic/Crofer22APU and the Crofer22APU/HJ4 glass-ceramic/Crofer22APU joined samples was measured for 2800 hours in static air. For this purpose, the glass was deposited manually in the form of slurry on the Crofer22APU substrates having dimensions of 3 cm x 3 cm. The electrical resistivity was measured at 850°C under the applied voltage of 1.6 V. The electrical resistivity curves of Crofer22APU/glass-ceramics/Crofer22APU joined samples for both HJ3 and HJ4 systems are shown in Figure 77.

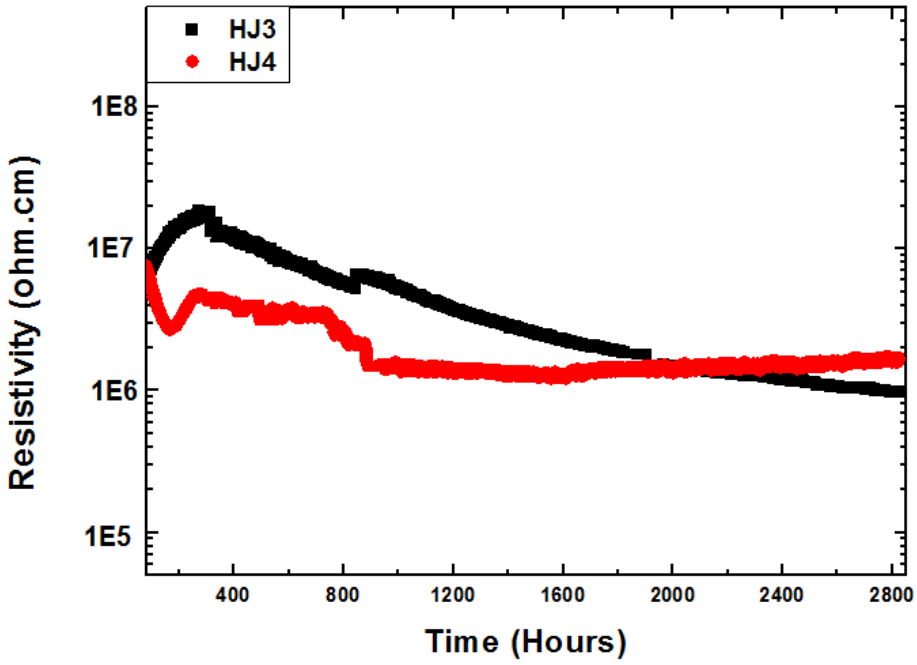

Figure 77. Electrical resistivity of Crofer22APU/glass-ceramics/Crofer22APU joined samples for HJ3 and HJ4 glass-ceramics. These measurements were carried out at 850 °C with 1.6 V applied

Figure 77 depicts that the resistivity of both the joined samples is in the range of (10^6-10^7 Ω.cm). These resistivity values are higher than the minimum threshold (10^4 Ω.cm) required for the sealants to work effectively in the SOEC conditions in order to ensure the electrical insulation between two conductive Crofer22APU plates [20].

The electrical resistivity analyses for both the joined samples as shown in Figure 77, were conducted independently and under slight different conditions. The electrical resistivity of HJ4 system was measured without any interruption while during the electrical resistivity test of HJ3 glass-ceramic based joint the test was stopped after 300 hours, 800 hours and 2000 hours due to some maintenance issues and later restarted, therefore, the HJ3 based joint sample undergo some thermal cycles. During the thermal cycles the Crofer22APU/HJ3 glass-ceramic/HJ3 joined sample was cool down from 850°C to the room temperature at a cooling rate of 2 °C/min and reheated to the testing temperature of 850 °C at a heating rate of 2 °C/min for further ageing. The slight discontinuity in the resistivity curve of HJ3 based joined sample after 300, 800 and around 2000 hours, corresponds to thermal cycle. However, after each thermal cycle, the HJ3 based joined sample reached the same resistivity values as before that thermal cycle. The electrical resistivity curve for the HJ3 based joint (black curve) shows a slight and gradual reduction in resistivity over the time. Nevertheless, the resistivity after 2800 hours is still higher than 10^6 Ω.cm and no abrupt change was noticed during the whole testing duration. Moreover, the stability in the electrical resistivity values of HJ3 based joined samples also suggests that no chemical interaction took place between the HJ3 glass-ceramic and the Crofer22APU plates, thus excluding the possibility of corrosion.

For HJ4 system based joint, the electrical resistivity initially reduced up to 200 hours followed by a constant behavior up to 800 hours. After 800 hours, some discontinuity was again observed and the resistivity values showed a reduction, followed by a steady constant behavior till the end of test. The initial gradual reduction up to 200 hours is most likely due to the presence of free ions, as HJ4 glass-ceramic has significantly low fraction of crystallization. The free ions in the residual glassy phase can move under the high applied voltage of 1.6 V and testing temperature of 850 °C, therefore consequently reduce the resistivity. The second discontinuous behavior noticed after 800 hours is probably due to any chemical interaction between the HJ4 glass-ceramic and the Crofer22APU substrates, or thermal stresses generated during cooling of samples. However, after 800 hours the resistivity values for HJ4 based joint became constant until the end of test (2800 hours). Nevertheless, like HJ3 based joined sample, the electrical resistivity of HJ4 based joint is also higher than 10^6 Ω.cm as tested up to 2800 hours, therefore it ensured the electrical insulating behavior of the HJ4 glass-ceramic.

After the long term electrical resistivity tests in the static air, the compatibility of both the glass-ceramics with the Crofer22APU substrates was examined by SEM. EDS analyses were also conducted to investigate the possible diffusion of elements across the Crofer22APU/glass-ceramics interfaces and to detect the possible chromates formation in specially in case of HJ4 glass system.

The SEM post mortem image of the positive polarized Crofer22APU/HJ3 glass-ceramic, after the electrical resistivity test, is shown in Figure 78. A dense microstructure (with low porosity) of HJ3 glass-ceramic is clearly evident from the Figure 78. The HJ3 glass-ceramic is strongly bonded with the positive polarized Crofer22APU substrate. No cracks were detected at positive polarized Crofer22APU/HJ3 glass-ceramic interface. An oxide scale can be seen at Crofer22APU/HJ3 glass-ceramic interface, which is formed due to the long-term (2800 hours) exposure of Crofer22APU to a high temperature of 850 °C.

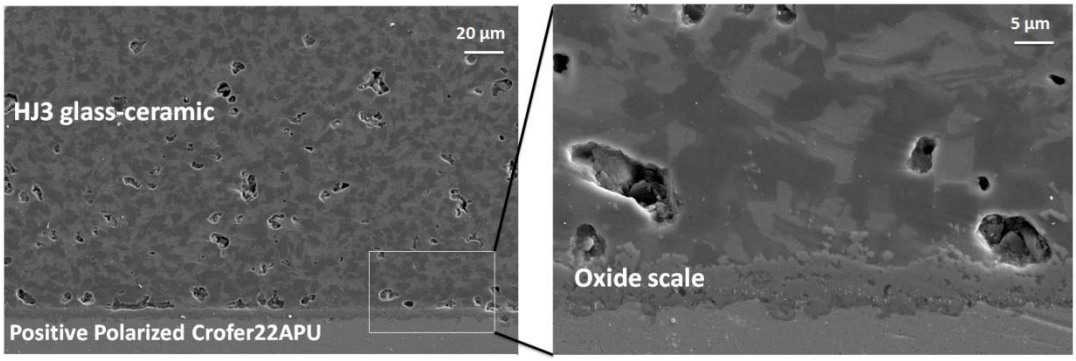

Figure 78. Post mortem SEM image of the positive polarized Crofer22APU/HJ3 glass-ceramic interface, after the electrical resistivity test for 2800 hours in the static air, under a voltage of 1.6 V

An EDS mapping carried out at the positive polarized Crofer22APU/HJ3 glass-ceramic interface after the electrical long-term resistivity test is shown in

Figure 79. The EDS analysis shows that no diffusion across the positive polarized Crofer22APU/glass-ceramic interface was detected. Due to the minimal concentration of Sr in the HJ3 glass composition, no formation of undesirable high CTE $SrCrO_4$ phase was detected. Moreover, the EDS mapping also confirms the presence of a Cr rich scale at the Crofer22APU surface.

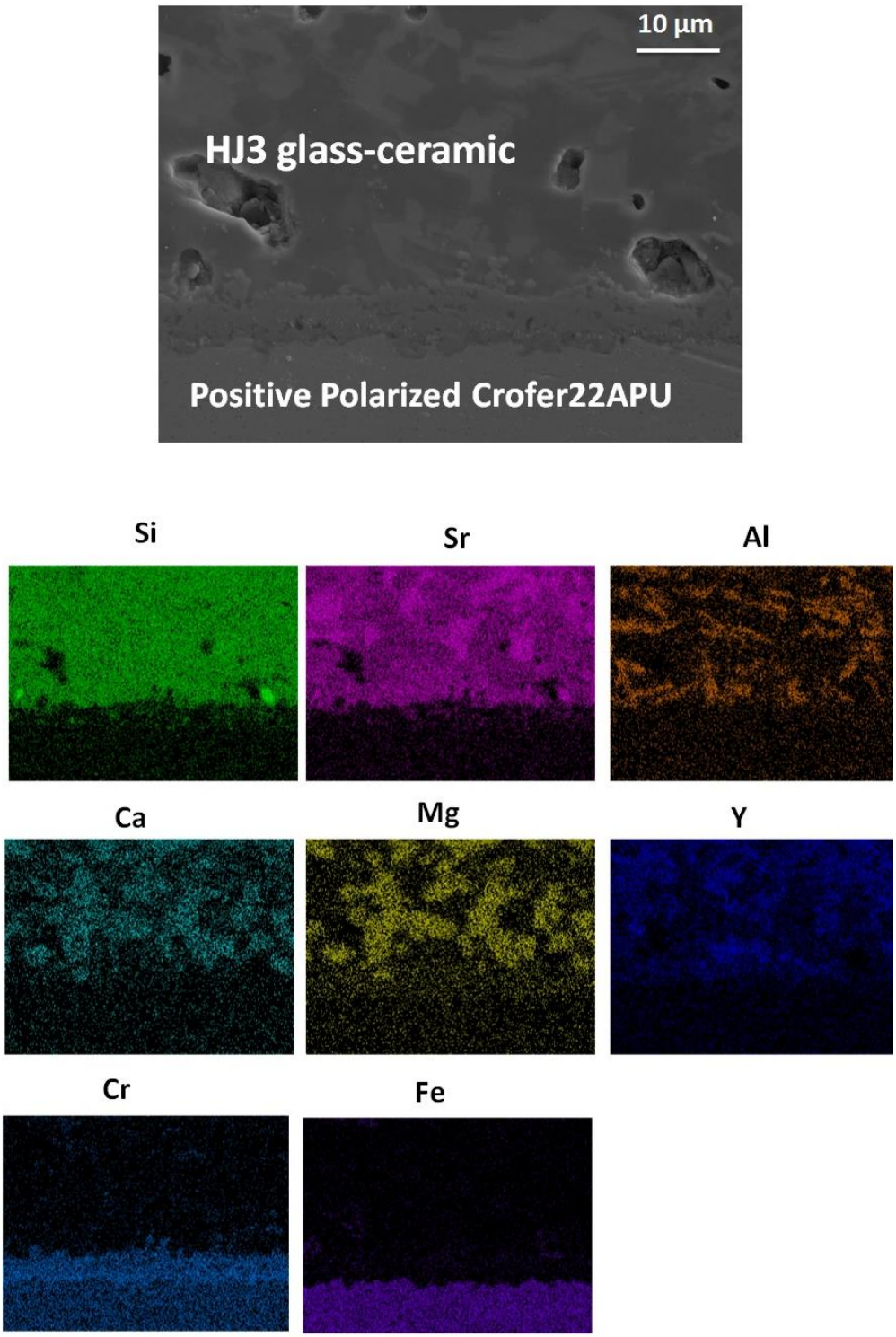

Figure 79. EDS mapping of the SEM image corresponding to the post mortem analyses of positive polarized Crofer22APU/HJ3 glass-ceramic interface, after the electrical resistivity test for 2800 hours in static air, under a voltage of 1.6V

After the resistivity test, the 3cm x 3cm Crofer22APU/HJ3 glass-ceramic/Crofer22APU joined sample was fractured at negative polarized Crofer22APU/HJ3 glass-ceramic interface, during the cutting (as required for SEM analyses). This fracture is probably due to stresses generated during cutting. Therefore, in this thesis the post mortem analyses of negative polarized Crofer22APU/HJ3 glass-ceramic have not been shown.

The Figure 80 shows the SEM post mortem image of the positive polarized Crofer22APU/HJ4 glass-ceramic interface after the electrical resistivity test in the static air. The microstructure of the HJ4 glass-ceramic is homogenous, dense with slight presence of porosity and similar to its microstructure after 1000 hours as shown in Figure 69. The SEM image shows that the positive polarized Crofer22APU/glass-ceramic interface is free of any crack or delamination thus confirmed strong bonding and good compatibility. The long-term (2800 hours) thermal ageing also resulted in the formation of an oxide scale at Crofer22APU/HJ4 glass-ceramic interface as shown in the Figure 80.

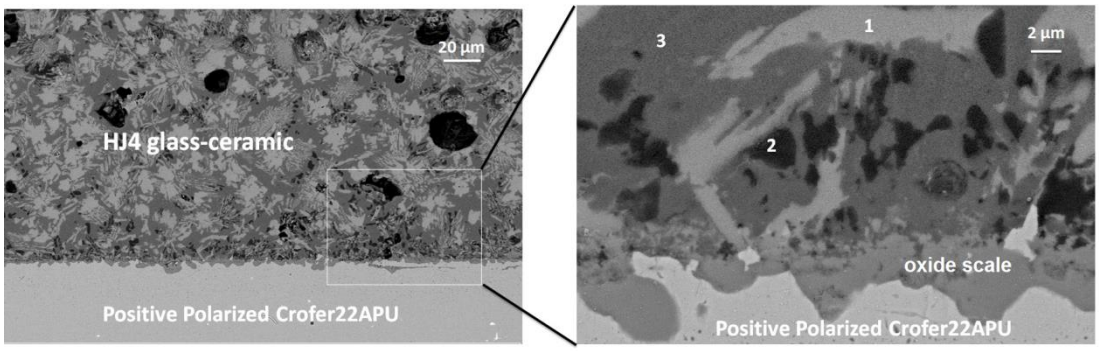

Figure 80. Post mortem SEM image of the positive polarized Crofer22APU/HJ4 glass-ceramic interface, after the electrical resistivity test for 2800 hours in static air, under a voltage of 1.6 V

The EDS point analyses were performed at different regions of HJ4 glass-ceramic after the electrical resistivity test. These regions are marked in the Figure 80 and their corresponding EDS analyses are given in Table 20. The EDS analyses carried out at point 1 shows that it corresponds to $SrSiO_3$ phase, similar to one observed in the HJ4 glass-ceramic after joining (Figure 66) and after thermal ageing for 1000 hours (Figure 69). The EDS analyses performed at point 2 (black phase) confirmed cristobalite (SiO_2) phase. A 3.1 at % of aluminum was also detected at point 2, most likely due to the surrounding environment of the EDS point analysis, however, the morphology of black phase (point 2) is similar to cristobalite phase observed in the Figure 66 and Figure 69. Point 3 in Figure 80 corresponds to the residual glassy phase. The residual glassy phase contains 7.4 at % of Sr, which is beneficial to maintain viscous behavior of residual glass. The SEM image (Figure 80) also shows that even after thermal ageing of 2800 hours

at 850 °C, a significant residual glass is still present. This residual glass can promote the self-healing above the glass transition temperature (T_g).

Table 20. EDS point analyses (at.%) performed on HJ4 glass-ceramic shown in Figure 80, after electrical resistivity test for 2800 hours in static air

	Point 1	Point 2	Point 3
O	71.2	75.6	73.4
Si	21.5	21.3	16.2
Sr	7.2	---	7.4
Al	---	3.1	2.0
Y	---	---	0.7

Figure 81 shows the EDS mapping of the positive polarized Crofer22APU/HJ4 glass-ceramic interface after the resistivity test. The EDS mapping confirmed that no evidence of Cr diffusion from the positive polarized Crofer22APU into the HJ4 glass-ceramic side was found, thus eliminating the possibility of the formation of undesirable $SrCrO_4$ phase. Besides that, no other element of glass-ceramic diffused or segregate at interface with Crofer22APU. These results also confirmed that HJ4 glass-ceramic is chemically stable after high temperature and long term ageing under electric load.

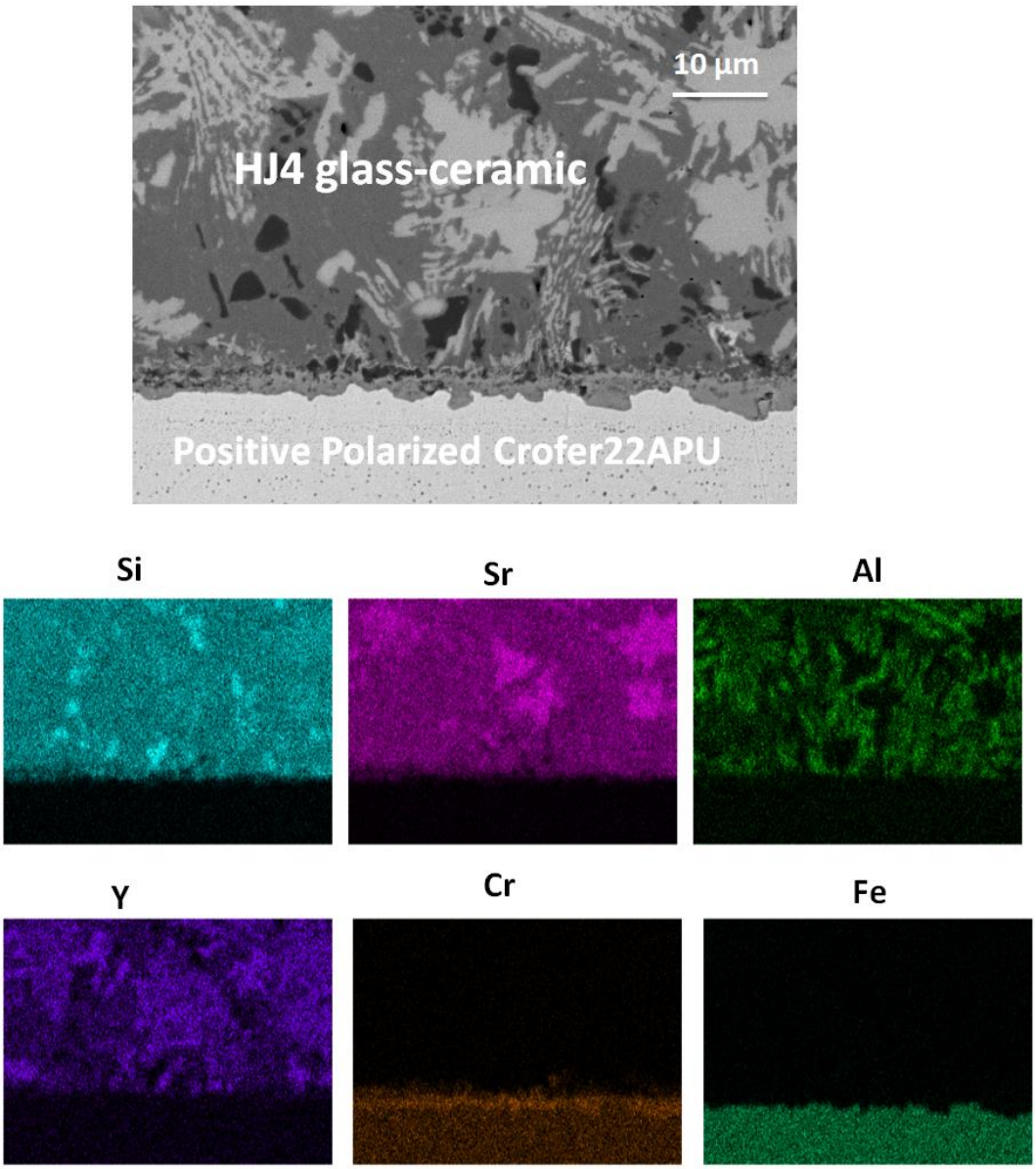

Figure 81. EDS mapping of the SEM image corresponding to the post mortem analyses of positive polarized Crofer22APU/HJ4 glass-ceramic interface, after the electrical resistivity test for 2800 hours in static air, under a voltage of 1.6V

The SEM post mortem analysis of the negative polarized Crofer22APU/HJ4 glass-ceramic interface after the resistivity test is shown in Figure 82, while the corresponding EDS analyses carried out at the HJ4 glass-ceramic are given in Table 21. A uniform and dense microstructure of HJ4 glass-ceramic in addition to excellent compatibility with the Crofer22APU substrate is evident from the SEM post mortem analyses. The EDS point analyses confirmed the presence of the $SrSiO_3$ (point 1) and cristobalite (point 2) phases in addition to the residual glassy phase (point 3).

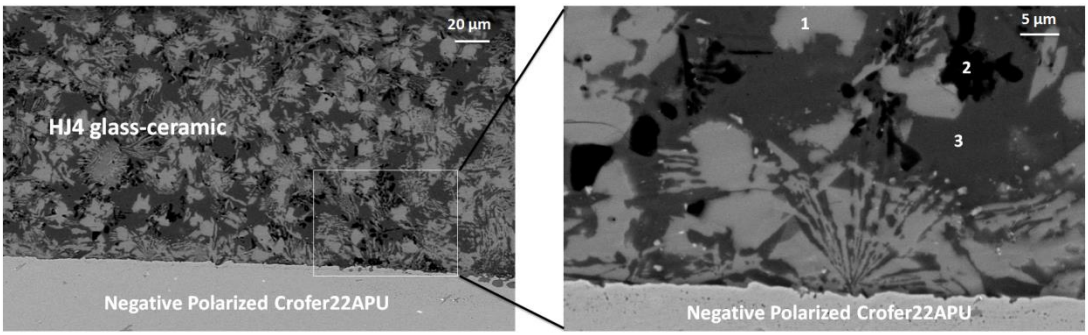

Figure 82. Post mortem SEM image of negative polarized Crofer22APU/HJ4 glass-ceramic interface, after the electrical resistivity test for 2800 hours in static air, under a voltage of 1.6V

Table 21. EDS point analyses (at.%) performed on HJ4 glass-ceramic shown in Figure 82, after electrical resistivity test for 2800 hours in static air

	Point 1	Point 2	Point 3
O	57.6	65.1	67.1
Si	23.0	34.9	20.1
Sr	19.4	---	9.3
Al	---	---	3.2
Y	---	---	0.3

The EDS mapping performed at the negative polarized Crofer22APU/HJ4 glass-ceramic after the electrical resistivity test, is shown in Figure 83. Like the positive polarized Crofer22APU/HJ4 glass-ceramic interface, no diffusion of glass-ceramic elements across the interface was detected. On the other hand, the EDS mapping indicates that a small concentration of Cr has been diffused from the Crofer22APU interconnect towards the HJ4 glass-ceramic side. Nevertheless, no chemical interaction or traces of formation of $SrCrO_4$ phase were found from SEM-EDS analyses.

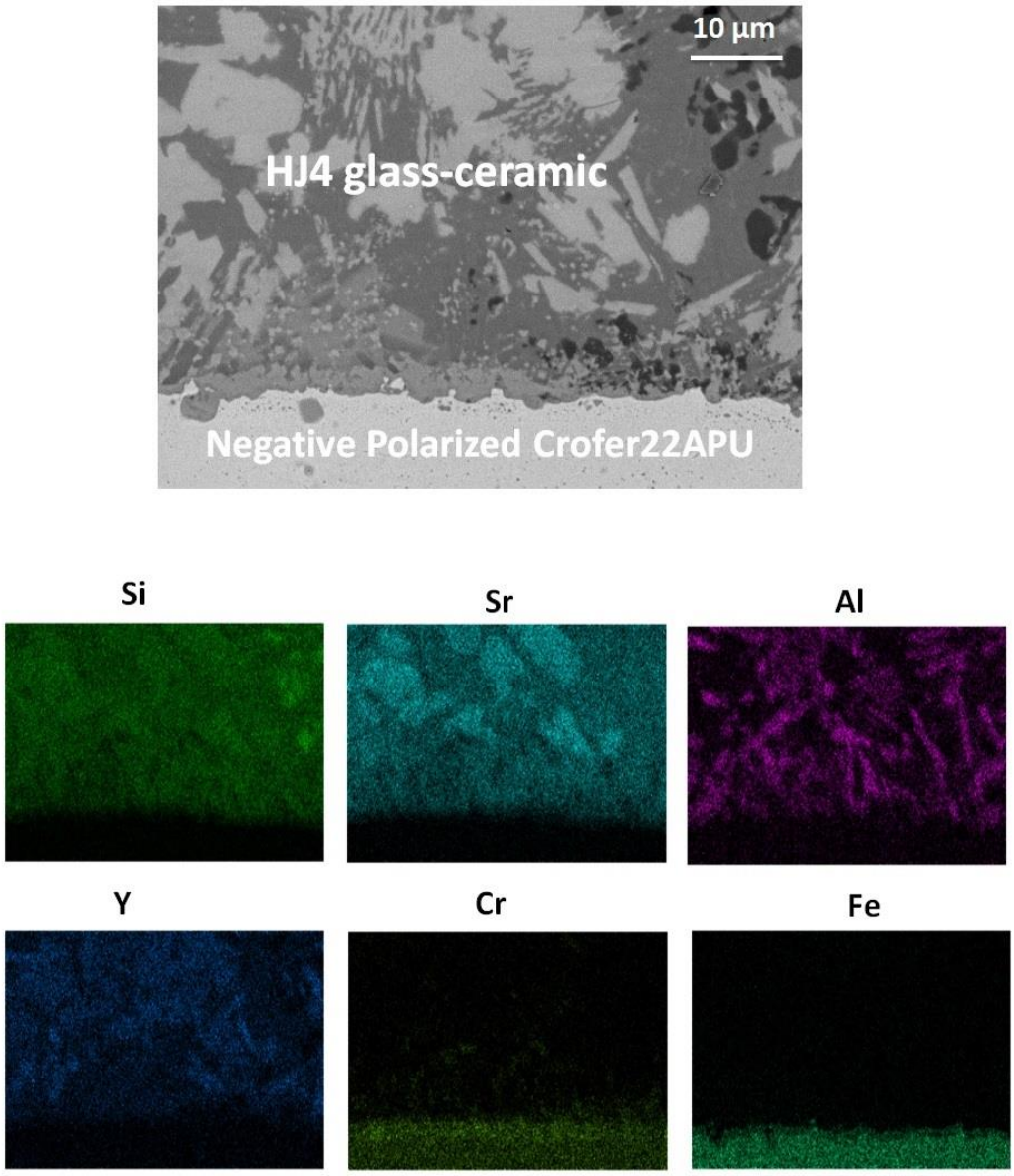

Figure 83. EDS mapping of SEM image corresponding to post mortem analyses of negative polarized Crofer22APU/HJ4 glass-ceramic interface, after the electrical resistivity test for 2800 hours in static air, under a voltage of 1.6V

Summary

Both the glass systems (HJ3 and HJ4) of the 1st series showed excellent thermo-chemical properties and CTE matching with other cell components after joining as well as after the thermal ageing. The microstructures of both glass-ceramics are quite dense to act as gas tight sealants. High electrical resistivity of Crofer22APU/glass-ceramic/Crofer22APU joined samples was observed for both the glass-ceramics as measured up to 2800 hours at 850 °C in the static air. The SEM-EDS post mortem analyses confirmed that no undesirable chromates were formed after long-term thermal ageing under an electrical load. However, the presence of low CTE $Sr_2Al_2SiO_7$ phase in the HJ3 glass-ceramic while cristobalite (SiO_2) phase in the HJ4 glass-ceramic can cause problems in long terms i.e. low CTE $Sr_2Al_2SiO_7$ phase can generate localized stresses within the glass-ceramic

while cristobalite phase can cause crack initiation due to its volume expansion during the thermal cycling. In this context, it is important to slightly modify this composition in order to avoid the formation of $Sr_2Al_2SiO_7$ and cristobalite phases.

4.2 2nd series of glass-ceramic systems

The 2nd series contains one glass-ceramic, termed as HJ14. The HJ14 contains SrO as main modifier. The 2nd series of glass is designed to obtain the desire high CTE $SrSiO_3$ phase and to avoid the formation of low CTE $SrAl_2Si_2O_8$ phase as well as cristobalite (SiO_2).

4.2.1 Thermal analysis of glasses belonging to 2nd series

Figure 84 shows the DTA and HSM analyses carried out on the HJ14 glass powder (<25 µm) up to 1200°C at a heating rate of 5°C/min. In Figure 84, the T_g, T_x, and T_p labels on the DTA curve correspond to the glass transition temperature, the onset of crystallization temperature and the peak crystallization temperature, respectively. The T_{FS} and T_{MS} labels on the HSM curve (Figure 84) represent the first sintering and maximum sintering temperatures, respectively. The corresponding characteristic temperatures are also summarized in Table 22.

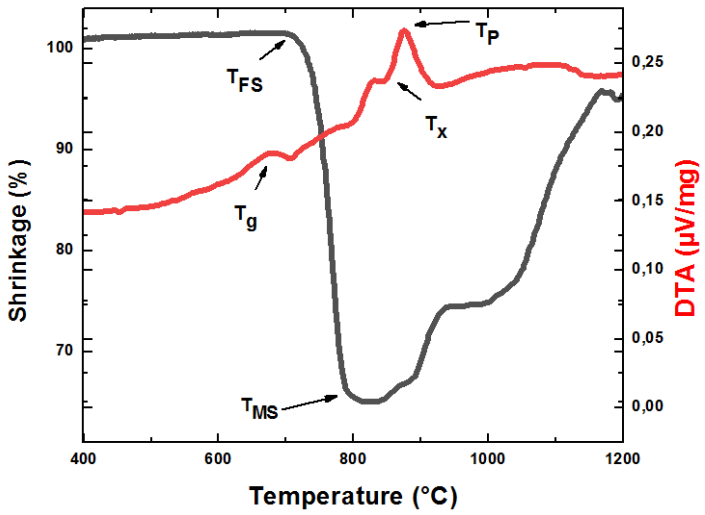

Figure 84: DTA vs HSM curves for HJ14 glass system, analyses carried out at a heating rate of 5°C/min

Table 22: Characterization temperatures of HJ14 glass as measured by DTA and HSM (measurements carried out at 5°C/min)

Glass transition temperature T_g (°C)	On set crystallization temperature T_x (°C)	Peak crystallization temperature T_p (°C)	First shrinkage temperature T_{FS} (°C)	Maximum shrinkage temperature T_{MS} (°C)
695 ± 3	854 ± 5	876 ± 5	716 ± 2	820 ± 3

As reported in Table 22, the HJ14 glass showed T_g and T_p of 695°C and 876°C, respectively, as measured by DTA. On the other hand, the sintering process was initiated at 716°C as measured by HSM. Beyond the first sintering temperature (T_{FS}), the shrinkage continued until it attained maximum shrinkage at 820°C. In order to obtain a good densification of the sealant, it is necessary that sintering is completed prior to the initiation of the crystallization process. As soon as the crystallization occurs, the glass viscosity will drastically increase, hindering the viscous flow of the glass and the adhesion to the metallic or ceramic substrates. Therefore, the crystallization mechanism of the glass-ceramic should be controlled and taken into account in the heat treatment schedule [21]. From the data given in Table 22, it is clear that for the HJ14 glass system the sintering process was completed before the start of the crystallization.

4.2.2 Coefficient of thermal expansion and XRD phase analysis of the of as-joined and thermally aged glass-ceramics belonging to the 2nd series

On the basis of the DTA and HSM data, the joining treatment at 950°C for 1 hour with a heating/cooling rate of 2°C/min was selected to obtain a dense as-joined HJ14 glass-ceramic. The coefficients of thermal expansion (CTEs) of the as-casted glass, as-joined glass-ceramic and aged glass-ceramic (850°C, 1000 hours) are given in Table 23. The as-joined HJ14 glass-ceramic showed a CTE of 10.3 x10^{-6} K^{-1}, thus closely matching other cell components. The CTE of the HJ14 glass-ceramic after ageing showed a slight reduction (0.5 ±0.1 x10^{-6} K^{-1}), however this reduction is negligible so it will not affect the performance of the glass-ceramic sealant for SOEC applications.

Table 23. Coefficient of thermal expansion (CTE) of HJ14 glass and glass-ceramic, in as-joined condition and after ageing

as-casted glass	as-joined glass-ceramic (950°C, 1h)	aged glass-ceramic (850 °C, 1000 hours)
(9.1 ±0.1) x10^{-6} K^{-1}	(10.3 ±0.2) x10^{-6} K^{-1}	(9.8 ±0.1) x10^{-6} K^{-1}

In general, the change in the CTE of the glass-ceramic after thermal ageing is likely due to the formation of new crystalline phases, however in the case of HJ14, no new phases were formed as a result of ageing (1000 hours, 850°C), as will be discussed below. Another possible reason could be the change of residual glass/crystalline phase concentration. The XRD quantification of as-joined and thermally aged HJ14 glass-ceramic is under progress. Therefore, the exact reason behind a slight reduction of HJ14 CTE after ageing is not clear.

The XRD phase analyses performed on the as-joined and aged (850°C, 1000 hours) HJ14 glass-ceramics are shown in Figure 85. $SrSiO_3$ was detected as the only crystalline phase in the as-joined as well as the thermally aged HJ14 glass-

ceramics. The formation of only a $SrSiO_3$ phase validated the rationale behind the design of the HJ14 composition i.e. to produce a high CTE $SrSiO_3$ phase and to avoid the formation of low CTE celsian ($SrAl_2Si_2O_8$), as well as cristobalite (SiO_2) phases. The XRD patterns of the HJ14 glass-ceramics after thermal ageing is similar to the as-joined glass-ceramic, with no new peak, thus confirming that the HJ14 system is stable after ageing. The XRD pattern of the $SrSiO_3$ phase (reference number: 01-077-0233) retrieved from X'Pert data base, is also shown in Figure 85 for a good comparison.

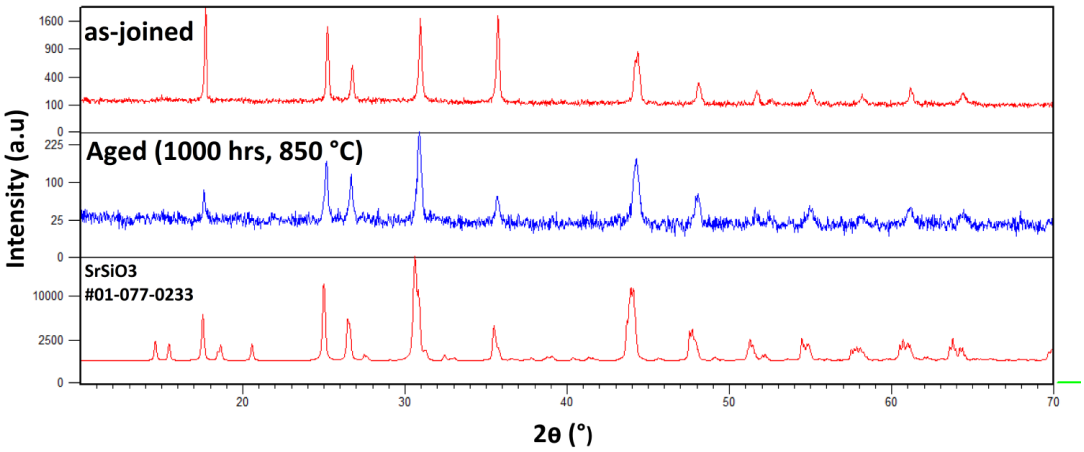

Figure 85. XRD patterns of HJ14 glass-ceramic in as-joined condition and after thermally aged (1000 hours, 850°C)

4.2.3 Joining of 2nd series glass-ceramic with Crofer22APU and 3YSZ

Figure 86 shows the SEM image of the Crofer22APU/HJ14 glass-ceramic/3YSZ joined sample processed at 950°C for 1 hour at a heating rate of 2°C/min. The selection of a suitable joining treatment produced a very dense glass-ceramic microstructure. The HJ14 glass-ceramic contains a uniform distribution of crystals. A good CTE match of the HJ14 glass-ceramic with the neighboring components (Crofer22APU and 3YSZ) resulted in a crack-free joint, in addition to which no delamination was observed at the Crofer22APU/glass-ceramic and 3YSZ/glass-ceramic interfaces. Two different types of phases are present in the glass-ceramic and are labeled as 1 and 2 in Figure 86. The corresponding EDS point analyses are given in Table 24. Table 24 shows that the dark phase (point 1) corresponds to the residual glassy phase and contains all the constituent elements of the HJ14 glass. The EDS analyses performed on the bright phase (point 2) show a Sr and Si rich phase and thus refer to the $SrSiO_3$ phase as detected by XRD. However, some diffusion of Ca was also detected in the $SrSiO_3$ phase. Moreover, the concentration of Sr measured at point 1 (residual glass) is lower compared with its concentration at point 2, which is beneficial to minimize the possibility of the formation of an undesirable $SrCrO_4$ phase in the long term. Additionally, the presence of Sr in the residual glassy phase is important to maintain a viscous behavior in the glass.

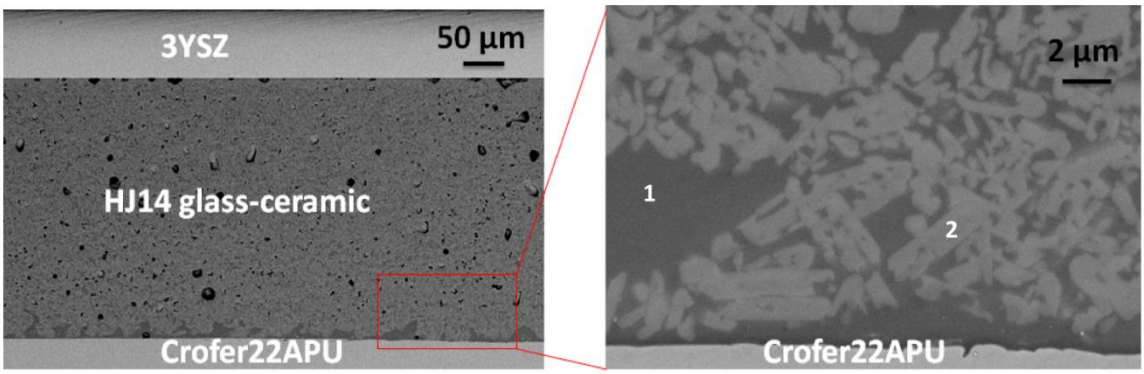

Figure 86. SEM image of as-joined Crofer22APU/HJ14 glass-ceramic/3YSZ joined sample

Table 24. EDS point analyses performed on as-joined HJ14 glass-ceramic

	O	Al	Si	Ca	Sr
Point 1	47.4	5.9	29.3	4.0	13.5
Point 2	41.8	---	30.1	6.1	22.0

4.2.4 Electrical characterization of 2nd series glass-ceramic in dual atmosphere and post mortem analysis

Figure 87 shows the electrical resistivity curve of the Crofer22APU/HJ14 glass-ceramic/Crofer22APU joined sample measured under the applied voltage of 1.6V, for 1000 hours at 850°C in a dual atmosphere. The electrical resistivity values for the HJ14 glass-ceramic based joint, are higher than 1 x10^5 Ω.cm and are comparable with the electrical resistivity of other glass-ceramics discussed in the literature [4], as tested under dual atmosphere. A high electrical resistivity ensures the insulating behavior of the HJ14 glass-ceramic sealant sandwiched between the two conducting Crofer22APU plates, thus excluding the possibility of a short circuit. The interaction of the glass-ceramic with the Crofer22APU interconnect can lead to the possibility of a short circuit and the consequent degradation of the cell. The presence of a dual atmosphere, high working temperature and applied voltage not only facilitate this interaction but also cause the formation of some conductive species, such as Fe_3O_4 and FeO, due to the volatilization of iron from the Crofer22APU [22], [23]. However, in the case of the HJ14 glass-ceramic based joint, no short circuit was observed during electrical resistivity measurements, even in the presence of a high steam content, a high working temperature (850°C) and an applied voltage of 1.6V. Furthermore, no formation of iron based (Fe_3O_4 and FeO) conductive oxides or interaction of the glass-ceramic with the Crofer22APU was detected during post mortem analyses.

The electrical resistivity trend reported in Figure 87 shows an increase of the resistivity in the first period of the test, with a maximum around 200 h, and then an almost linearly decreasing behavior. This trend is similar to that of other glass-

ceramics tested under SOFC voltage conditions for shorter periods [24], with the resistivity reaching a plateau within 300 h of testing for some of the samples in [24]. A longer test would be needed to investigate if the resistivity of HJ14 would also evolve towards an asymptotic value after a longer exposition to dual atmosphere conditions and voltage.

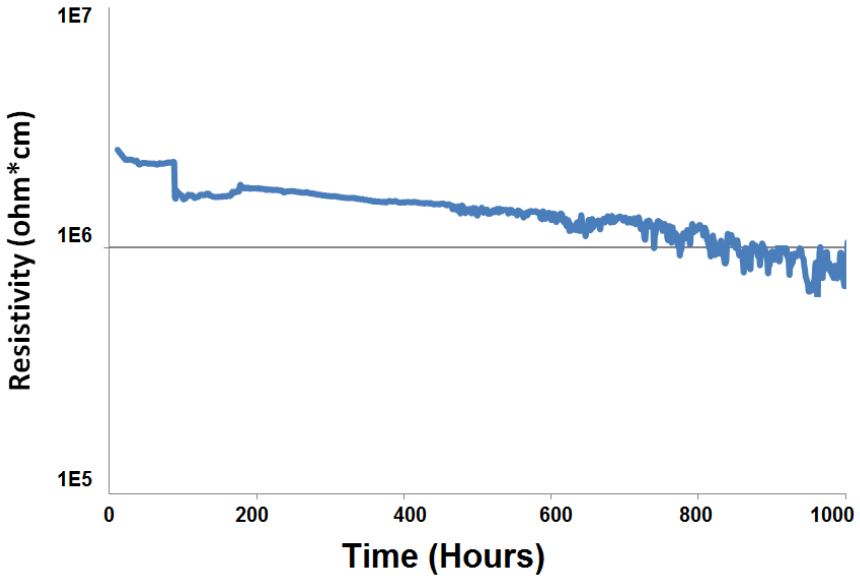

Figure 87. Electrical resistivity of Crofer22APU/HJ14 glass-ceramic/Crofer22APU joined sampled, measured for 1000 hours at 850°C in dual atmosphere

After the long-term resistivity analysis in dual atmosphere , the SEM-EDS post mortem analyses were carried out on the Crofer22APU/HJ14 glass-ceramic/Crofer22APU joined sample in order to investigate the thermo-mechanical compatibility of the glass-ceramic with the Crofer22APU and the possible formation of chromates at the Crofer22APU-glass-ceramic-air triple phase boundary. SEM-EDS analyses were performed both at air and fuel sides after testing the joined sample under electric load at 850°C for 1000 hours.

Air side

Figure 88 shows the Crofer22APU/HJ14 glass-ceramic/Crofer22APU joined sample facing the air side during the electrical resistivity test. Good interfacial bonding and thermo-mechanical compatibility between the Crofer22APU and the HJ14 glass-ceramic are evident from Figure 88. The EDS mapping carried out confirms that no chromates were formed at Crofer22APU-glass-ceramic-air triple phase boundary.

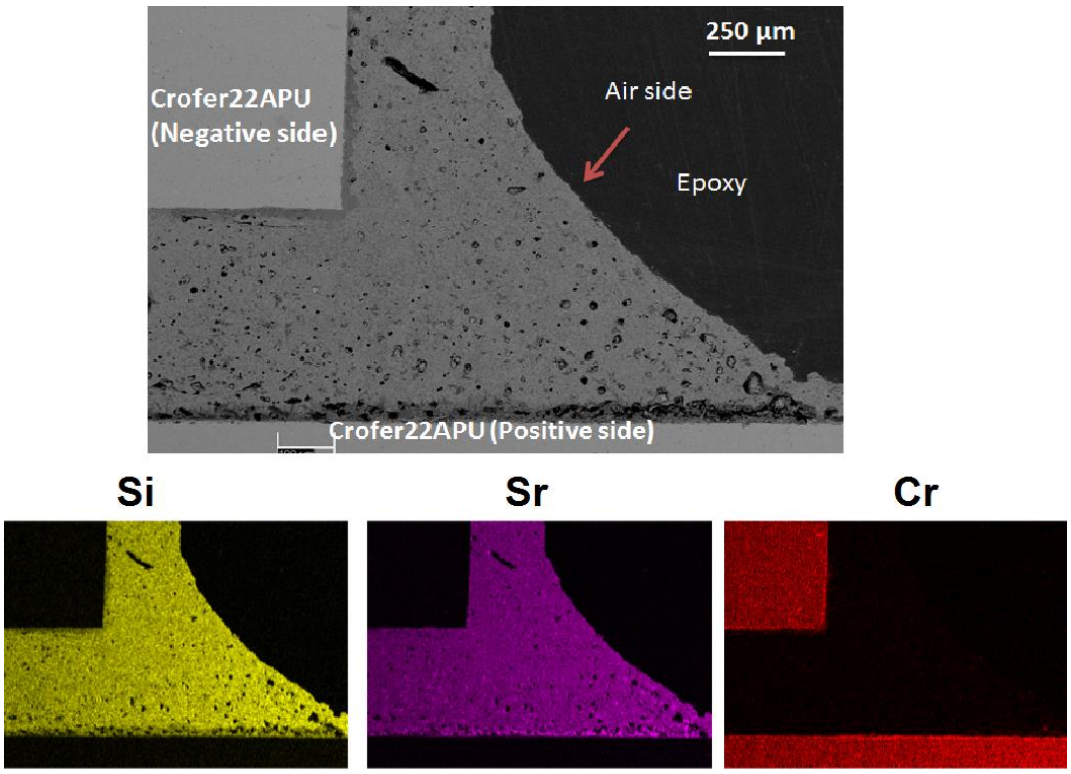

Figure 88. SEM post mortem analyses of Crofer22APU/HJ14 glass-ceramic/Crofer22APU joined sampled, after thermal ageing of 1000 hours at 850°C on air side under the applied voltage of 1.6V

Figure 89 shows the magnified SEM image and EDS mapping of the positive polarized Crofer22APU/HJ14 glass-ceramic interface at the air side. No cracks within the HJ14 glass-ceramic nor delamination were observed at the Crofer22APU/glass-ceramic interface. The different crystals are uniformly dispersed (bright regions) in the HJ14 glass-ceramic. The corresponding EDS point analyses performed on these different phases in the HJ14 glass-ceramic are given in table 5. The EDS analyses carried out at point 1 (Figure 89) correspond to the $SrSiO_3$ phase, thus validating the XRD analyses as discussed in section 4.2.2. However, some diffusion of Ca into the $SrSiO_3$ phase was also detected by EDS, similar to the EDS analyses performed on the as-joined glass-ceramic. The EDS analyses at Point 2 (Figure 89) correspond to the residual glassy phase, as it contains all the constituent components of the HJ14 glass system. In contrast with point 1, a lower concentration of Ca was detected in the residual glassy phase due to its diffusion into the $SrSiO_3$ phase. The residual glassy phase also contains 9 at. % Sr, which is beneficial to maintain the glass transition temperature (T_g) and to produce viscous behavior in the residual glass. A negligible concentration (0.3 at. %) of Cr was also detected in the residual glassy phase, and is present close to the Crofer22APU interface. The residual glassy phase (dark regions) is mainly present along the Crofer22APU substrate, which is beneficial to promote self-healing at the Crofer22APU/ glass-ceramic interface above T_g. The EDS analysis at point 3 is similar to point 1, thus indicating the presence of $SrSiO_3$ with little diffusion of Ca. The presence of a black phase was also observed by SEM at the Crofer22APU/glass-ceramic interface as indicated by point 4. The corresponding

EDS at point 4 (table 5) confirms that this phase corresponds to a cristobalite phase (SiO_2). However, the SEM image of the HJ14 (Figure 89) shows that the concentration of cristobalite is very negligible and is only crystallized along the Crofer22APU substrate.

The EDS mapping shown in Figure 89, and the EDS point analyses performed at different regions on the HJ14 glass-ceramic joined to the positive polarized Crofer22APU did not detect the diffusion of Cr, therefore excluding the possibility of the formation of an undesirable $SrCrO_4$ phase.

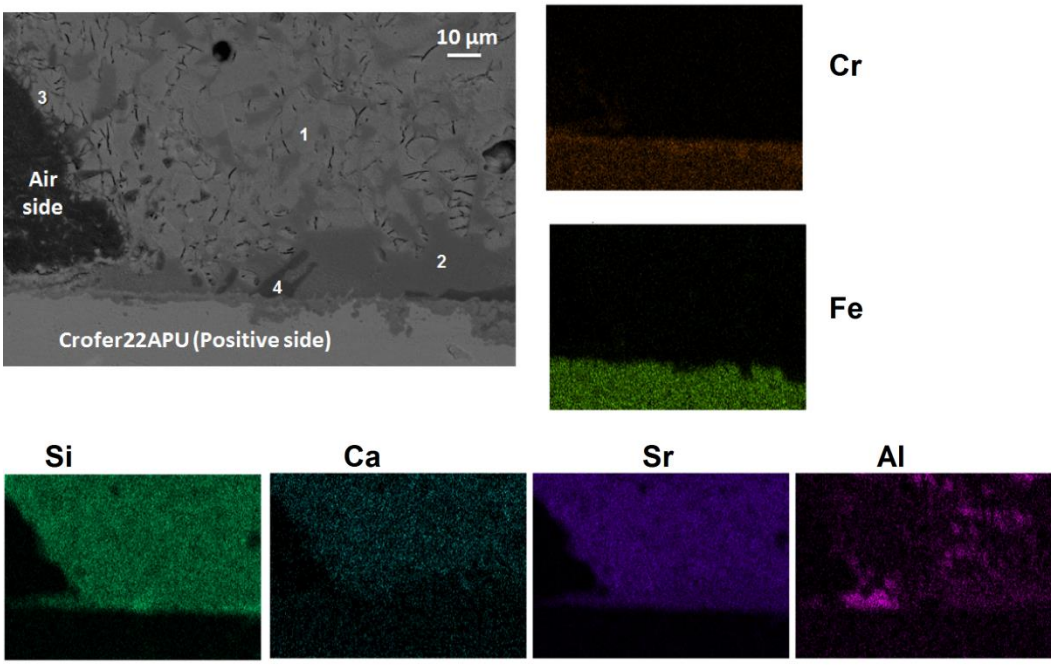

Figure 89. SEM image and EDS mapping of positive polarized Crofer22APU/HJ14 glass-ceramic interface at air side

Table 25. EDS point analyses performed on HJ14 glass-ceramic, bonded to positive polarized Crofer22APU on air side

	O	Al	Si	Ca	Cr	Sr
Point 1	57.2	---	21.9	4.3	---	16.5
Point 2	66.9	3.1	20.1	0.7	0.3	8.9
Point 3	54.6	---	24.0	4.4	---	17.0
Point 4	66.5	---	33.5	---	---	---

The SEM image and EDS mapping of the negative polarized Crofer22APU/HJ14 glass-ceramic interface at air side is shown in Figure 90. A strong bonding was observed between the negative polarized Crofer22APU and the HJ14 glass-ceramic, with no delamination. The glass-ceramic seems to be significantly dense (with little porosity), ensuring gas tightness during the SOEC operation. The corresponding EDS analyses performed in different regions are

given in table 6. The EDS analyses at point 1 in Figure 90 correspond to the residual glassy phase, which is mainly present close to the interface with the Crofer22APU. The concentrations of Sr, Si and Ca in the residual glassy phase are comparable at both polarized Crofer22APU sides (Table 5 and 6). However, a slightly higher concentration of Cr was observed in the residual glassy phase at the negative polarized Crofer22APU/HJ14 glass-ceramic interface. The EDS mapping in Figure 90 also shows the presence of Cr in the residual glassy phase. The EDS analysis at point 2 shows the presence of a $SrSiO_3$ phase with slight diffusion of Ca. As at the positive polarized Crofer22APU/HJ14 glass-ceramic interface, no chromates were detected at the negative polarized Crofer22APU/HJ14 glass-ceramic interface, thus excluding the possibility of any corrosion. Moreover, unlike the negative polarized Crofer22APU/HJ14 glass-ceramic interface (air side), no black (cristobalite) phase was detected at the positive polarized Crofer22APU/HJ14 glass-ceramic interface (air side).

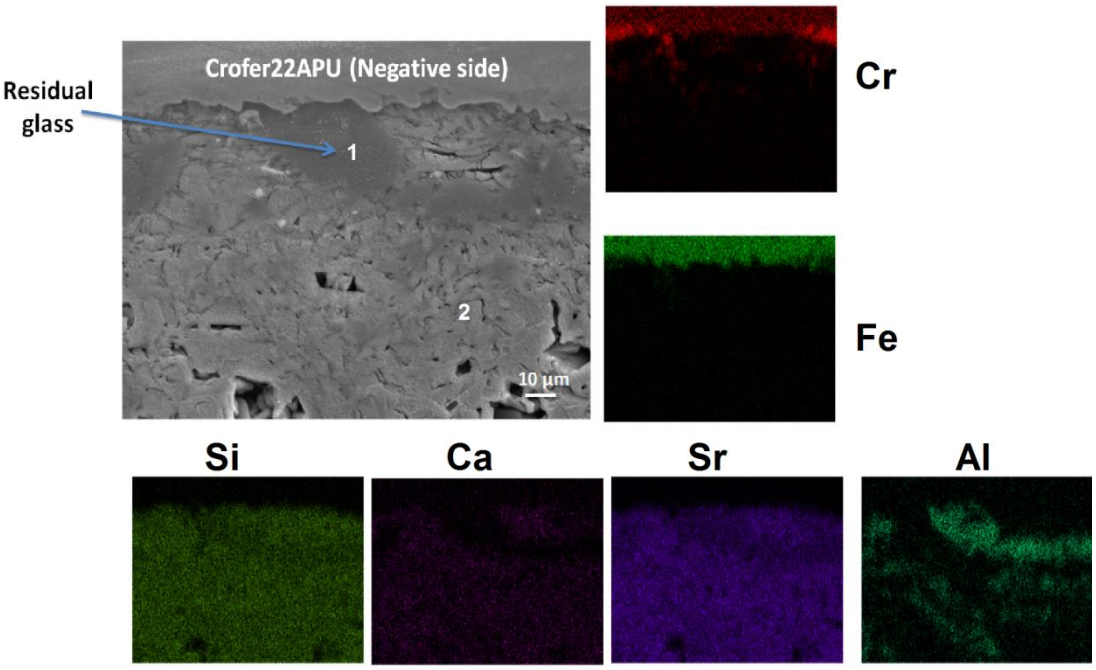

Figure 90. SEM image and EDS mapping of negative polarized Crofer22APU/HJ14 glass-ceramic interface at air side

Table 26. EDS point analyses performed on HJ14 glass-ceramic, bonded to negative polarized Crofer22APU on air side

	O	Al	Si	Ca	Cr	Sr
Point 1	58.5	11.8	20.1	0.7	1.2	7.4
Point 2	56.8	---	23.0	4.6	---	15.7

Figure 91 compares the EDS line scan performed across the Crofer22APU/HJ14 glass-ceramic interface, where the Crofer22APU has positive (Figure 91 (a)) and negative polarities (Figure 91(b)). Both the interfaces shown in Figure 91 correspond to the air side. A direct comparison shows that in the case of the negative polarized Crofer22APU, a diffusion of Cr can be seen from the Crofer22APU into the glass ceramic, while no Cr diffusion was detected from the positive polarized Crofer22APU. On the other hand, no diffusion or segregation of the glass-ceramic elements was detected across the Crofer22APU/HJ14 glass-ceramic interface. These results are in agreement with the EDS point analyses given in table 5 and 6, where a slight amount of Cr diffusion was detected from the negative polarized Crofer22APU into the glass-ceramic side.

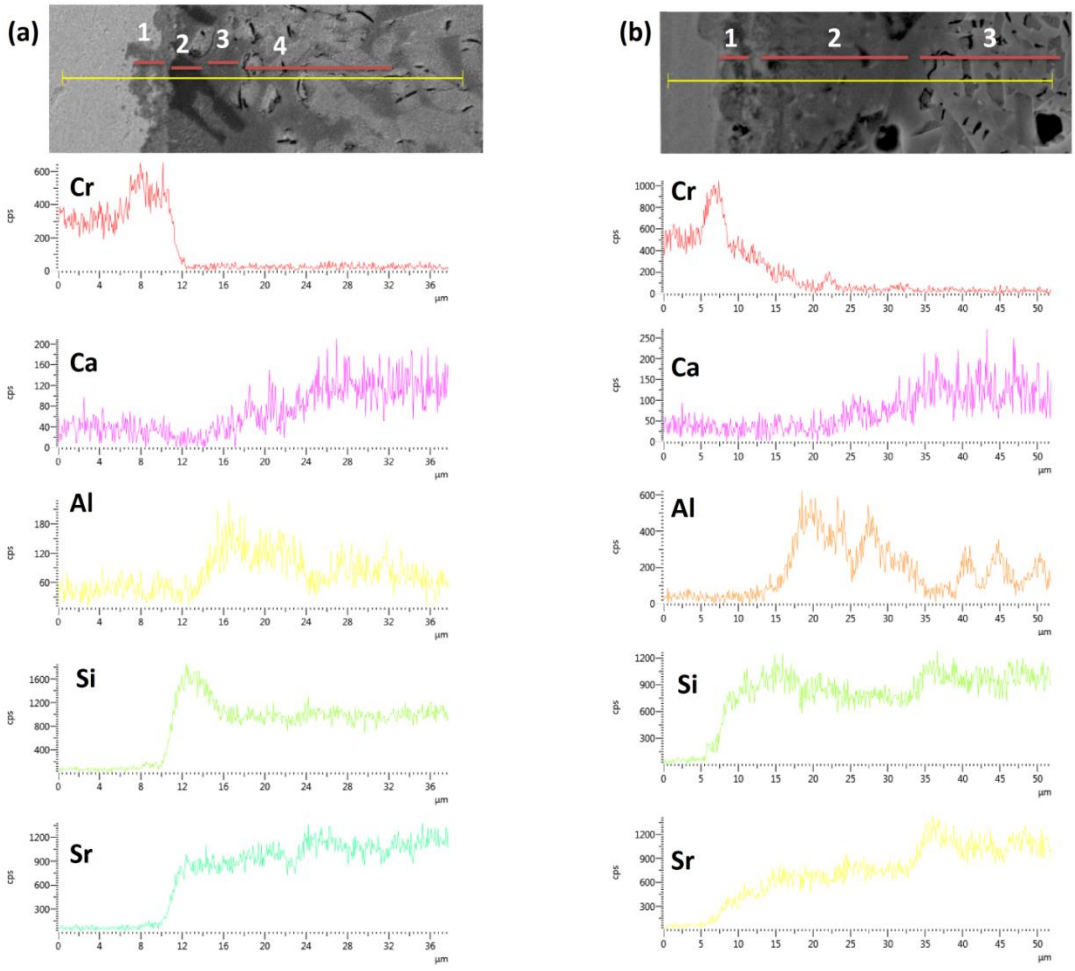

Figure 91. EDS line scan across (a) positive polarized Crofer22APU/HJ14 glass-ceramic and (b) negative polarized Crofer22APU/HJ14 glass-ceramic interfaces at air side

Figure 91 shows that the Crofer22APU/HJ14 glass-ceramic interface can be divided into different regions based on different phases. In Figure 91 (a), region 1 corresponds to a Cr-oxide scale of ~3 µm thickness. The formation of the oxide scale is as expected and is formed during high temperature ageing. Region 2 (black phase) shows a high concentration of Si, and it corresponds to the

cristobalite phase. Region 3 is the residual glassy phase, as its contains a high concentration of Al, Si and Sr, in addition to a small concentration of Ca. In region 4, the concentration of Al reduces compared with region 3, while it contains a significantly high concentration of Si and Sr, thus referring to the $SrSiO_3$ phase. Moreover, the concentration of Ca also increases in region 4 compared with region 3, thus confirming its diffusion into the $SrSiO_3$ phase as discussed before.

Similarly, for Figure 91 (b), region 1 is a Cr rich area, thus referring to the Cr-oxide scale. Region 2 has a high concentration of Al, Si and Sr, in addition to a small quantity of Ca, and therefore corresponds to the residual glassy phase. In region 3, the Si and Sr concentration increased while the Al concentration reduced compared with region 2, thus region 3 contains mainly the $SrSiO_3$ phase. As in Figure 91(a), the concentration of Ca is higher at the $SrSiO_3$ region compared with the residual glass due to its possible diffusion during thermal ageing.

Fuel side

Figure 92 shows the SEM post mortem image of the Crofer22APU/HJ14 glass-ceramic/Crofer22APU joined sample on the fuel side, after the electrical resistivity test for 1000 hours at 850°C. Like the air side, the HJ14 glass-ceramic has some porosity, however the glass-ceramic seems to be significantly dense enough to work effectively as a gas tight sealant in SOEC conditions. Moreover, no cracks were detected within the glass-ceramic.

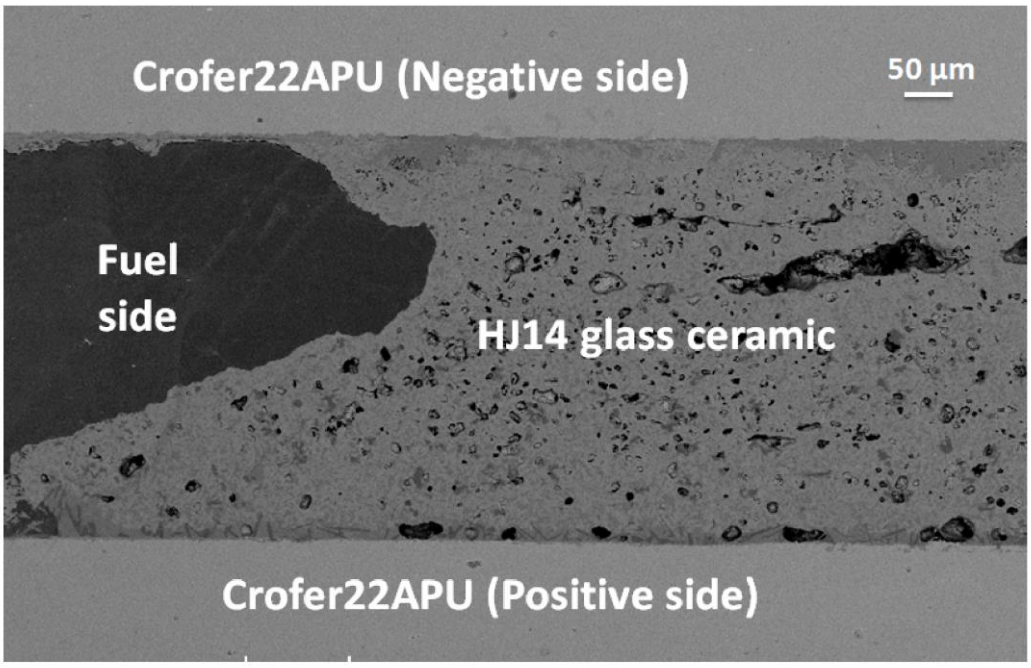

Figure 92. SEM post mortem analyses of Crofer22APU/HJ14 glass-ceramic/Crofer22APU joined sampled, after thermal ageing of 1000 hours at 850°C on fuel side under the applied voltage of 1.6V

Figure 93 shows the magnified SEM post mortem image of the positive polarized Crofer22APU/HJ14 glass-ceramic interface. The HJ14 glass-ceramic shows good adhesion with the Crofer22APU, with no delamination or cracks at the interface. The SEM image (Figure 93) shows the presence of different crystalline phases within the glass ceramic, and their detailed EDS point analyses are given in table 7. The EDS analyses carried out at the black region (point 1) show a silica-rich phase, thus referring to the cristobalite (SiO_2) phase. The EDS at points 2 and 3 shows that these regions contain a high concentration of Si and Sr, with no Al, thus referring to the $SrSiO_3$ phase. A small concentration of Ca was also detected at points 2 and 3, due to its diffusion into the $SrSiO_3$ phase as discussed before. Point 4 is a residual glassy phase, as it contains all the constituents (Si, Sr, Al, Ca) of the HJ14 glass system. The composition of the residual glassy phase is similar to that discussed before for the HJ14 glass-ceramic. A negligible concentration of Cr and Mn was also found in the residual glass phase, however no evidence for the formation of unwanted $SrCrO_4$ was noticed.

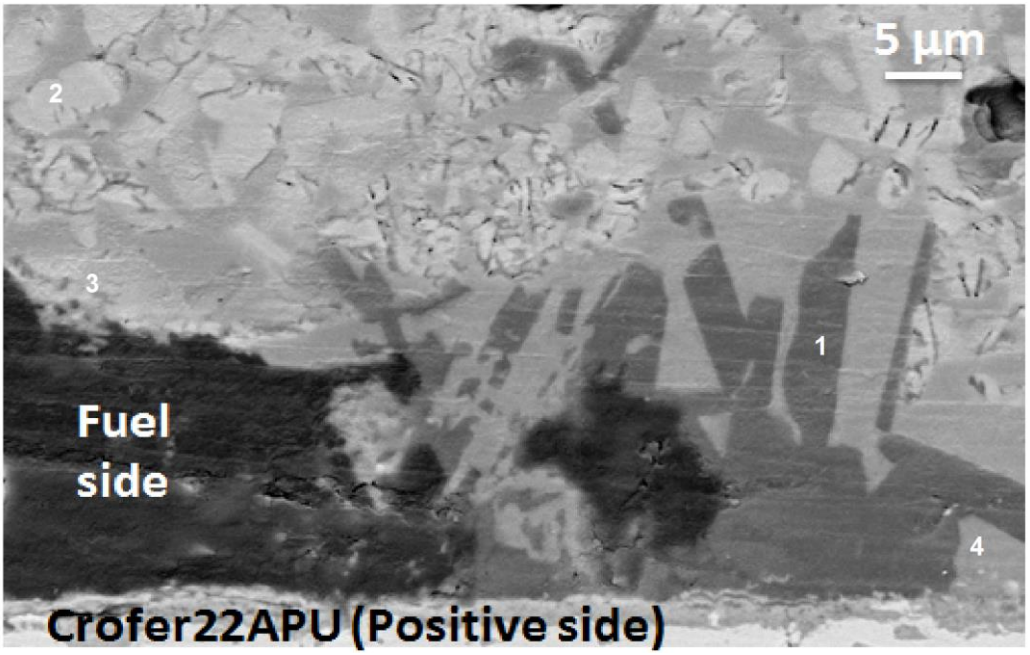

Figure 93. SEM image of positive polarized Crofer22APU/HJ14 glass-ceramic interface at fuel side

Table 27: EDS point analyses (at. %) performed at HJ14 glass-ceramic joined with positive polarized Crofer22APU at fuel side

	O	Al	Si	Ca	Cr	Sr	Mn
Point 1	63.0	---	37.0	---	---	---	---
Point 2	55.9	---	22.4	4.5	---	17.2	---
Point 3	57.6	---	20.8	3.9	---	17.7	---
Point 4	65.6	3.1	17.3	2.4	0.5	9.78	1.4

The negative polarized Crofer22APU/HJ14 glass-ceramic interface at the fuel side is shown in Figure 94 and is also similar to the Crofer22APU/HJ14 glass-ceramic interfaces observed at the air side in terms of good adhesion and the presence of crystal phases. As at the positive polarized Crofer22APU/HJ14 glass-ceramic interface, no black silica-rich (cristobalite) phase was observed at the negative polarized Crofer22APU/HJ14 glass-ceramic interface on the fuel side. The EDS point analyses performed at the different regions of Figure 94 are in given table 8. The EDS point analyses confirmed the presence of a high concentration of Cr and O at point 1 in Figure 94, thus indicating the formation of a Cr_2O_3 oxide scale layer. In addition to this, a significant concentration of Mn was also detected at point 1 (Figure 94). Point 2 is the $SrSiO_3$ phase with a small concentration of Ca, as discussed in detail in the previous section. No Cr was detected at point 2, thus confirming that Cr is only diffused close to the Crofer22APU/HJ14 glass-ceramic interface.

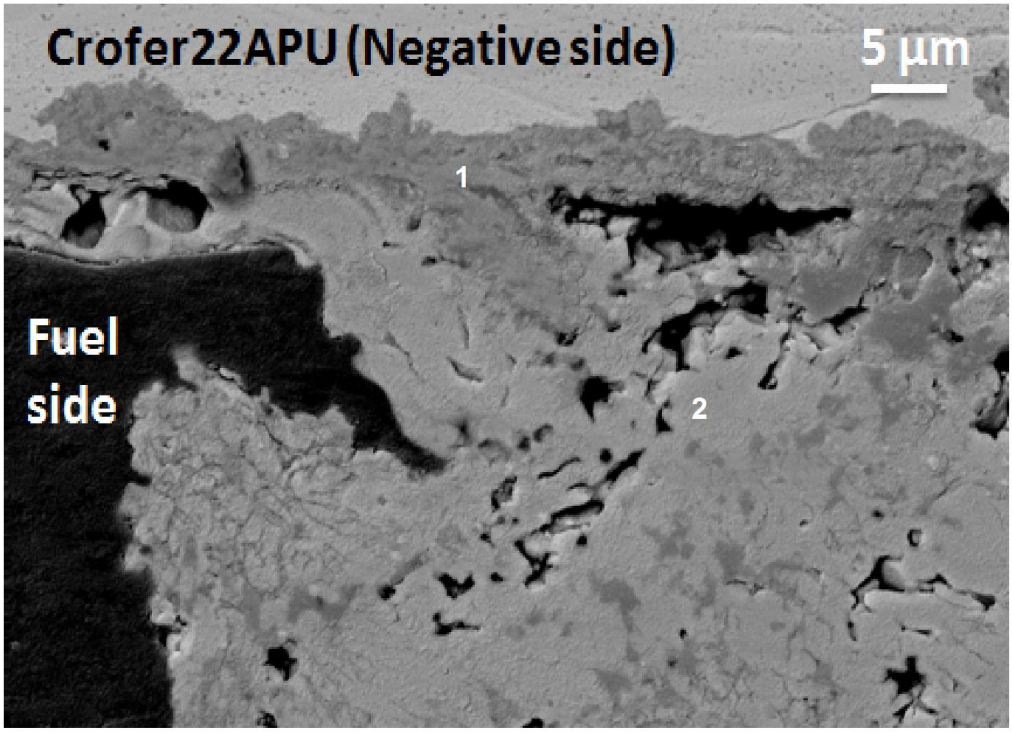

Figure 94. SEM image of negative polarized Crofer22APU/HJ14 glass-ceramic interface at fuel side

Table 28. EDS point analyses (at. %) performed at HJ14 glass-ceramic joined with negative polarized Crofer22APU at fuel side

	O	Al	Si	Ca	Cr	Sr	Mn	Fe
Point 1	55.2	2.4	1.0	0.7	25.6	---	14.3	0.9
Point 2	59.1	---	21.7	4.1	---	15.1	---	---

Summary

By adjusting the SiO_2/SrO, the suitable $SrSiO_3$ phase was obtained in the 2nd series glass-ceramic (HJ14) after joining and thermal ageing for 1000 hours at 850 °C. The long term ageing does not result in the devitrification of any undesirable phase. The thermal properties such as the glass transition temperature, the sequence of crystallization and sintering phenomena were found to be suitable to obtain a dense glass-ceramic sealant in order to ensure gas tightness. The HJ14 glass-ceramic showed coefficients of thermal expansion of 10.3 x 10^{-6} K^{-1} and 9.8 x 10^{-6} K^{-1} after joining and thermal ageing (1000 hours, 850°C), respectively, thus closely matching that of the neighboring cell components. An excellent thermo-mechanical compatibility of the glass-ceramic with the Crofer22APU interconnect and 3YSZ was observed. A high electrical resistivity (>10^5 Ω.cm) was measured for the glass-ceramic sandwiched between the two conductive Crofer22APU plates, thus excluding the possibility of a short circuit. No formation of undesirable chromates nor diffusion of elements across the Crofer22APU/glass-ceramic interface were detected after post mortem analyses of the Crofer22APU/glass-ceramic/Crofer22APU joined samples treated in dual atmosphere for 1000 hours at 850°C. Owing to these properties, the HJ14 glass system is a promising candidate for the SOEC sealant at 850°C.

4.3 3rd series of glass-ceramic systems

The 3rd series of glasses contains two glass systems termed as HJ11 and HJ28. Both the glass systems contain BaO as the main modifier. The compositions of these glass systems are given in chapter 3. Both of these glass systems were analyzed in terms of their thermal properties, thermo-mechanical compatibility with Crofer22APU and 3YSZ substrates, and long term electrical analysis in the dual atmosphere.

4.3.1 Thermal analysis of glasses belonging to 3rd series

To investigate the characteristic temperatures of the HJ11 and HJ28 as-casted glass systems, the DTA and HSM analysis were carried out at 5 °C/min, on the glass powder having the particle size <25 μm. The DTA and HSM curves for HJ11 and HJ28 glasses are shown in Figure 95. The characteristic temperatures such as glass transition (T_g), onset of crystallization (T_x) and peak crystallization temperature (T_p) obtained from DTA, as well as the first sintering temperature (T_{FS}) and maximum sintering temperature (T_{MS}) obtained from HSM analyses are given in Table 29.

From the DTA analysis, the HJ11 glass showed the glass transition (T_g) of 677 °C and the onset crystallization (T_x) of 833 °C. The DTA curve of HJ11 (Figure 95 (a)) also showed a clear exothermal peak at 887 °C corresponding to the peak crystallization temperature (T_p). The HSM curve of HJ11 glass shows that the sintering process started at 675 °C, while the sintering completed at 778 °C. After the completion of the sintering process (T_{MS}), the HJ11 glass showed

slight viscous flow, followed by the constant shrinkage behavior. The constant shrinkage behavior after (T_{MS}) is due to the initiation of the crystallization process that enhanced the thermal stability of the glass.

The DTA analysis of the HJ28 glass (Figure 95(b)) showed that T_g of 685 °C. However, no sharp and clear crystallization peak was detected during the DTA analysis of HJ28 glass. As discussed before for the HJ4 glass system (1st series of glass), this is due to the fact that the degree of devetrification in the HJ28 glass is not significant to be detected during the DTA analysis. The HSM analysis of HJ28 (Figure 95(b) and Table 29) showed that the sintering started at 717 °C while completed at 829 °C. After the completion of sintering process, the HJ28 glass showed more significant viscous flow compared to HJ11 glass (Figure 95 a)

Table 29 shows that the HJ11 glass has lower characteristic temperatures i.e. T_g, T_{FS}, T_{MS} etc. compared with the HJ28 glass system. The higher characteristic temperatures of HJ28 glass system is most likely due to the reduction in the total concentration of modifiers (especially BaO) in the HJ28 glass system as compared with HJ11 glass.

As discussed before, in order to obtain a dense sealant, the sintering should be completed before the start of crystallization phenomena. From the Figure 95 and characteristic temperatures mentioned in the Table 29, it is clear that the sintering process of both the glass systems completed prior to the initiation of crystallization (T_x).

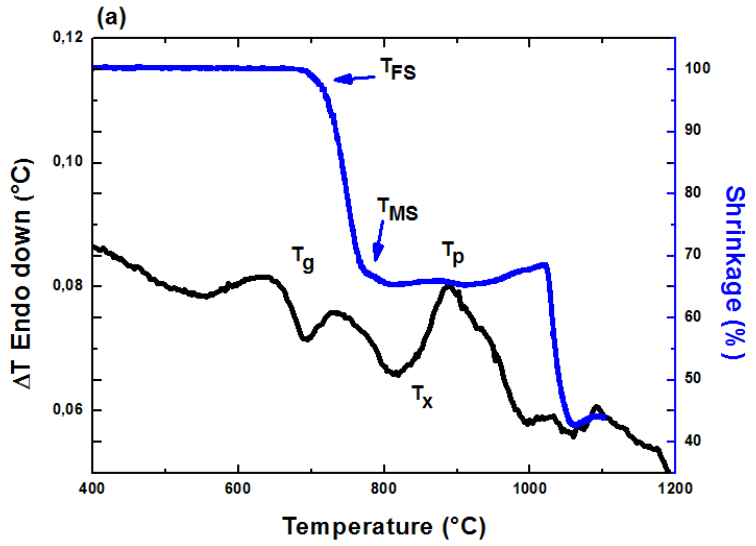

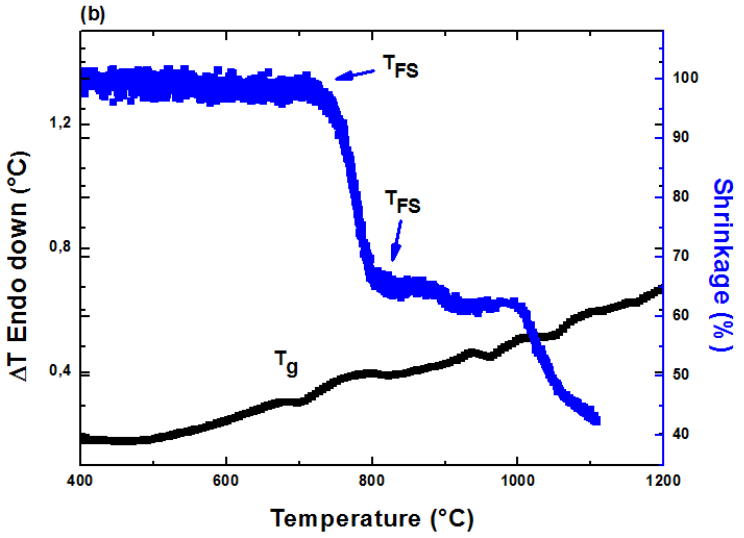

Figure 95. DTA and HSM curves of (a) HJ11 and (b) HJ28 glasses. Analyses were carried out at 5 °C/min

The dilatometeric curves of the HJ11 and HJ28 as-casted glasses are shown in the Figure 96 and the corresponding CTE values are reported in Table 29. The as-casted HJ11 and HJ28 glasses showed the coefficient of thermal expansion (CTE) of 9.1 x 10^{-6} K^{-1} and 8.6 x 10^{-6} K^{-1} respectively, as measured in the temperature range of 200-500 °C. The softening temperature (T_s) of 720 °C and 739 °C (Table 29.) were measured for the HJ11 and HJ28 as-casted glasses, respectively. As discussed before, the presence of modifiers such as BaO tends to increase the CTE of as-casted glass; therefore, the higher BaO content in the HJ11 is responsible for its higher CTE compared with the HJ28 as-casted glass.

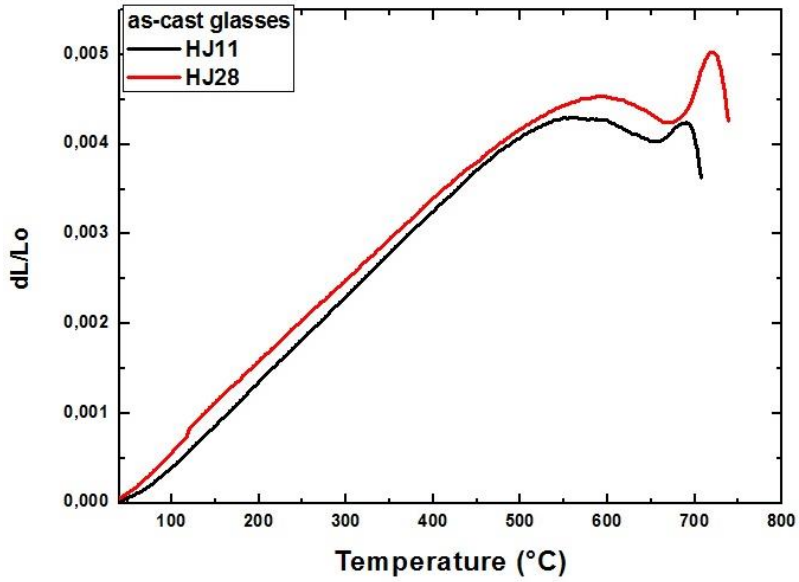

Figure 96. Dilatometeric curves of HJ11 and HJ28 as-casted glasses obtained at a heating rate of 5 °C/min

Table 29. Characteristic temperatures and CTE s of HJ11 and HJ28 glasses, obtained from DTA, HSM and dilatometer at a heating rate of 5 °C/min

	HJ11	HJ28
Glass transition temperature T_g (°C)	677 ± 3	685 ± 2
Onset crystallization temperature T_x (°C)	833 ± 5	Not detected
Peak crystallization temperature T_p (°C)	887 ± 2	Not Detected
First shrinkage temperature T_{FS} (°C)	675 ± 4	717
Maximum shrinkage temperature T_{MS} (°C)	778± 3	829
CTE of as-cast glass/1 x 10^{-6} K^{-1} (200 °C-500 °C)	9.1 ± 0.2	8.6 ± 0.1
Softening temperature T_s (°C)	720 ± 5	739 ± 3

4.3.2 Cofficient of thermal expansion and XRD phase analysis of the of as-joined glass-ceramics belonging to the 3rd series

In order to synthesize the HJ11 and HJ28 glass-ceramics, a heat treatment of 950 °C was chosen. The selection of heat treatment was based on the crystallization and sintering data obtained from the DTA and HSM analyses, and was chosen to obtain maximum densification as well as sufficient crystallization. The dwelling time for the HJ11 was kept 1 hour. However, due to the fact that the HJ28 glass showed considerably less devetrificaiton during the DTA analyses, the HJ28 glass-ceramic was synthesize at 950 °C for 2 hours to increase the possibility of crystallization. The HJ11 and HJ28 glass-ceramics were synthesized at heating/cooling rate of 2 °C/min in order to minimize the possibilities of stress generation due to fast heating/cooling rates. The XRD and dilatometer analysis were performed to investigate the crystalline phases and the CTE of HJ11 and HJ28 as-joined glass-ceramic.

The XRD patterns of the as-joined HJ11 and HJ28 glass-ceramics are shown in Figure 97. According to the XRD analyses, the as-joined HJ11 and HJ28 glass-ceramics contain only $BaSi_2O_5$ crystalline phase. The reference pattern of $BaSi_2O_5$ is also shown in Figure 97. The $BaSi_2O_5$ is a high CTE phases with CTE in the range of 11-14 x 10^{-6} K^{-1} [25] and is important to obtain a high CTE (9-12 x 10^{-6} K^{-1}) glass-ceramic sealant, for the SOEC applications [1]. These XRD results also validate the rationale behind designing the HJ11 and HJ28 glass compositions i.e. to have high CTE $BaSi_2O_5$ phase and to minimize the formation of cristobalite (SiO_2) phase.

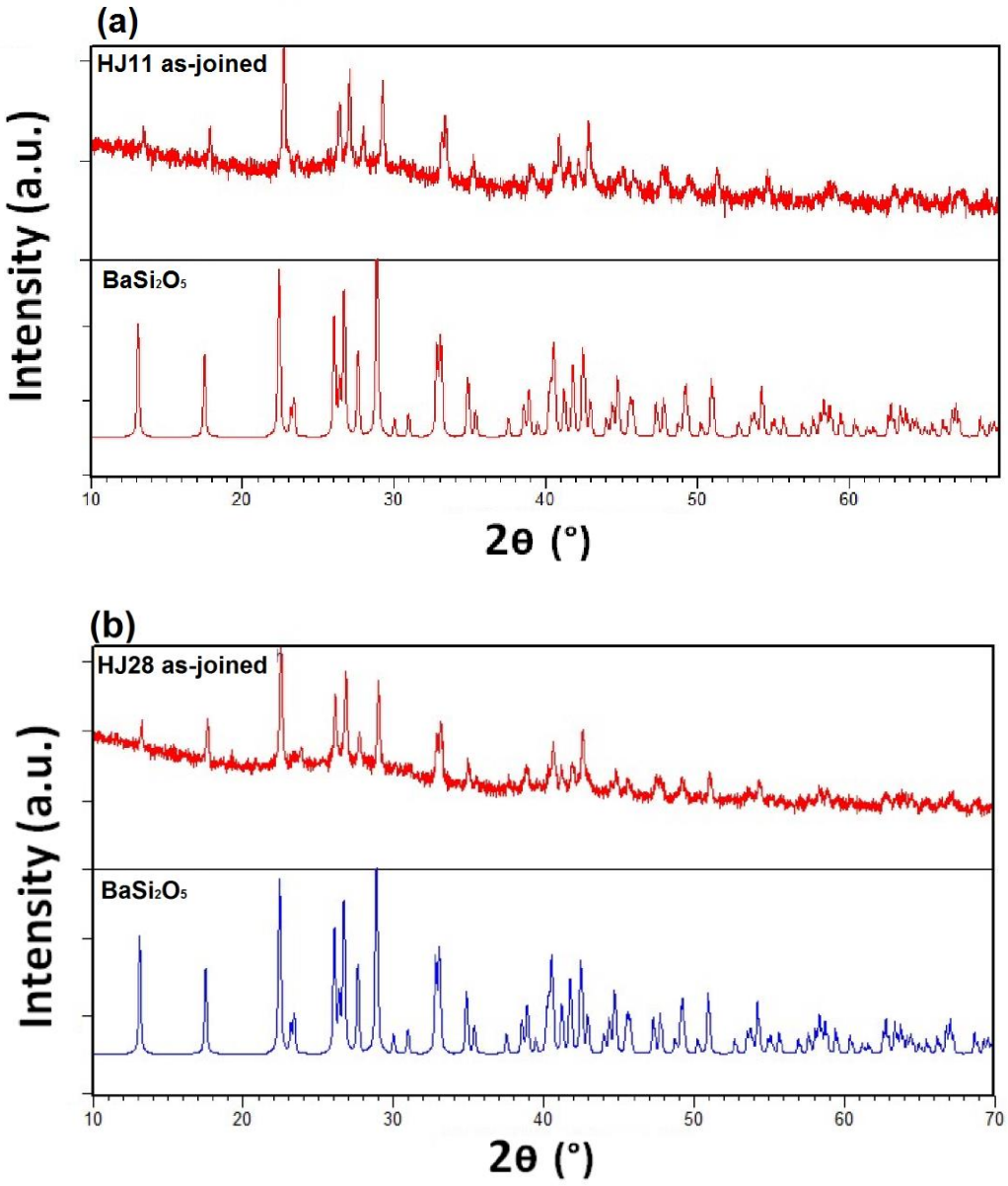

Figure 97. XRD patterns of (a) HJ11 glass-ceramic synthesized at 950 °C (1h) , and (b) HJ28 glass-ceramic synthesized at 950 °C (2h)

The dilatometer analyses was carried out on the as-joined HJ11 and HJ28 glass-ceramic pellets to investigate their CTEs. The dilatometer curves of both the glass-ceramics are shown in Figure 98 and their respective CTEs are reported in

Table 30. The as-joined HJ11 glass-ceramic has the CTE of 11.4 x 10^{-6} K^{-1} while the CTE of as-joined HJ28 glass-ceramic is measured as 9.2 x 10^{-6} K^{-1}. The CTEs of HJ11 and HJ28 glass-ceramics are matching with other cell components i.e. Crofer22APU and 3YSZ [1], [26] and are suitable for the SOEC applications. The dilatometer curves of the HJ11 and HJ28 as-joined glass-ceramics also showed a hump around 700 °C. This is most likely due to the softening of the residual glassy phase around the glass transition temperatures (T_g).

A significant increase in the CTE of the HJ11 as-joined glass-ceramic as compared with the as-casted HJ11 glass is due to the higher degree of

devetrification of the high CTE $BaSi_2O_5$ phase. Although, the as-joined HJ28 glass-ceramic also have the high CTE $BaSi_2O_5$ phase, however, a low degree of devetrification in HJ28 is probably the reason for its low CTE as compared with the as-joined HJ11 glass-ceramic.

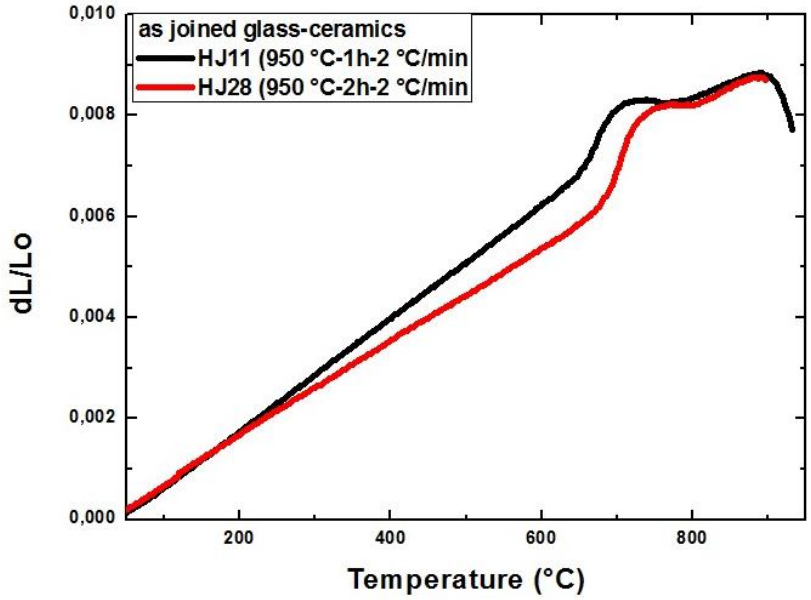

Figure 98. Dilatometer curves of as-joined HJ11 and HJ28 glass-ceramics. Measurements were carried out at a heating rate of 5 °C/min

Table 30. CTEs of as-joined HJ11 and HJ28 glass-ceramics

	Heat treatments to obtain glass-ceramic	**CTEs of glass-ceramic /1 x 10^{-6} K^{-1} (200 ºC-500 ºC)**
HJ11 glass-ceramics	Room Temperature-950 °C, Dwell: 1 h, Heating/cooling rate: 2 °C/min	11.4 ± 0.3
HJ28 glass-ceramics	Room Temperature-950 °C Dwell: 2 h, Heating/cooling rate 2 °C/min	9.2 ± 0.1

4.3.3 Joining of 3rd series glass-ceamics with Crofer22APU and 3YSZ

The compatibility and bonding of the HJ11 and HJ28 glass-ceramics with the Crofer22APU interconnect and 3YSZ electrolyte were investigated by producing the Crofer22APU/glass-ceramic/3YSZ joined samples according to the heat treatments mentioned above. The SEM images of the Crofer22APU/HJ11 glass-ceramic/3YSZ and Crofer22APU/HJ28 glass-ceramic/3YSZ joints cross sections are shown in Figure 99. Both the glass-ceramics showed good interfacial bonding with the Crofer22APU and 3YSZ substrates, with no crack or delamination at either interface. Some isolate pores can be seen in the as-joined glass-ceramics; however, these pores are not interconnected and could be formed as a result of

manual glass deposition. Moreover, no crack within the as-joined glass-ceramics was observed.

The microstructure of the HJ11 glass-ceramic after joining is quite homogenous. The crystalline phases are uniformly distributed throughout the joining area. The EDS point analysis performed at different regions of as-joined HJ11 glass-ceramic (Figure 99) are given in Table 31. The EDS analyses at the bright phase (point 1) indicates the $BaSi_2O_5$ phase while the dark region corresponds to the residual glassy phase. The EDS analyses shows that the Ba concentration in the residual glassy phase is around 11 at %, which would be favorable to maintain the CTE and to impart a viscous behavior to the residual glass.

Similar to HJ11, the microstructure of the HJ28 glass-ceramic is also uniform and homogenous. The morphology of the crystalline phases in HJ28 glass-ceramic is similar to that of HJ11 glass-ceramic. The EDS analysis reported in

Table 31 confirmed that the bright phase (point 3) in the HJ28 as-joined glass-ceramic is the $BaSi_2O_5$ phase similar to one observed in the HJ11 as-joined glass-ceramic. However, the dark phase (phase 4) is the residual glassy phase. The small Ca concentration detected at point 3 is most likely due to the effect of surrounding area of this EDS point analysis. Despite of the fact that as compared with HJ11 glass system the HJ28 glass has lower concentration of BaO, the residual glassy phases of both the as-joined glass-ceramics contain almost same Ba contents as reported in

Table 31. This is due to the relatively less devetrification of $BaSi_2O_5$ phase in the HJ28 as-joined glass-ceramic. One the other hand, the residual glass of HJ28 glass-ceramic has higher Si concentration as compared with HJ11, due to having higher SiO_2 content in its corresponding glass composition.

The SEM-EDS analyses performed on the as-joined HJ11 and HJ28 glass-ceramics are in agreement with the XRD results of the as-joined HJ11 and HJ28 glass-ceramics.

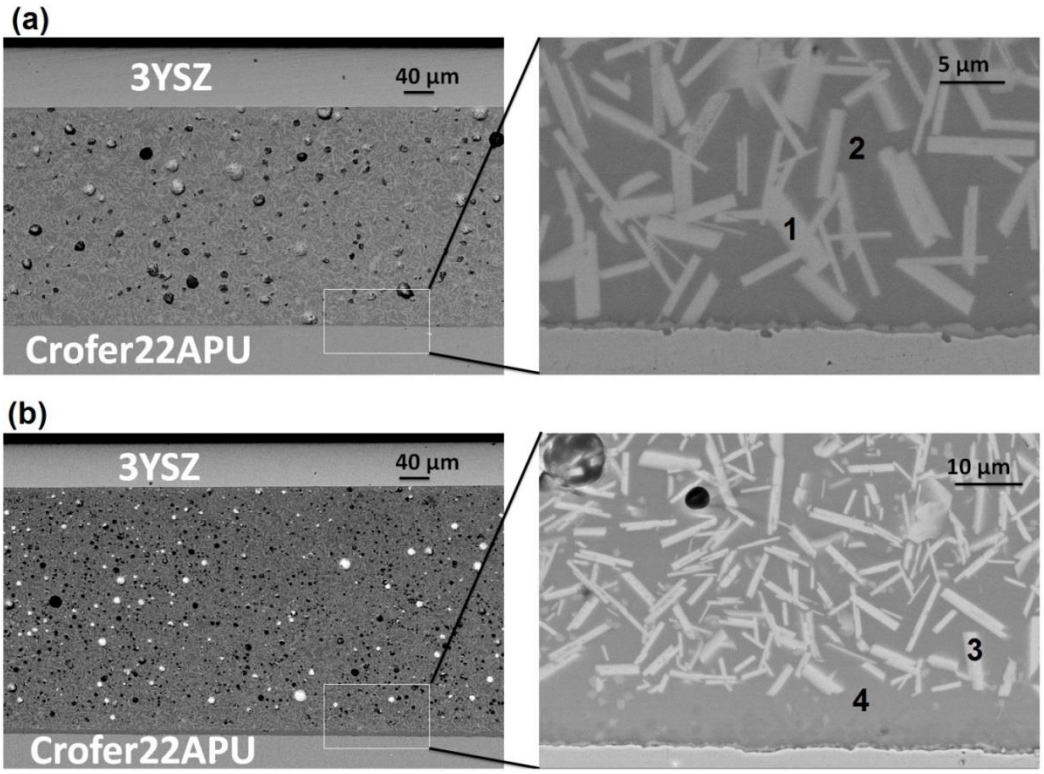

Figure 99. SEM images of as-joined (a) Crofer22APU/HJ11/3YSZ and (b) Crofer22APU/HJ28/3YSZ joined samples

Table 31. EDS point analyses performed on the HJ11 (point 1 and 2) and HJ28 (point 3 and 4) glass-ceramics as shown in Figure 99

	Point 1	Point 2	Point 3	Point 4
O	46.3	51.2	48.0	49.7
Si	35.6	25.5	35.2	31.6
Ba	18.1	11.2	15.1	10.1
Ca	---	4.8	1.7	3.7
Al	---	7.2	--	4.3
Y	---	---	---	0.6

4.3.4 Effect of thermal ageing on the Coefficient of thermal expansions and XRD phase analyses of the glass-ceramics belonging to 3rd series

The XRD was carried out on the HJ11 and HJ28 glass-ceramics after the thermal ageing for 1000 hours and 2000 hours respectively at 850°C. The XRD analyses was carried out on the glass-ceramics powder obtained by ball milling of the aged pallet. The corresponding XRD patterns are shown in Figure 100. Long-

term ageing resulted in the devetrification of a secondary phase ($BaAl_2Si_2O_8$), in both the glass-ceramics. The newly formed $BaAl_2Si_2O_8$ phase has low CTE [27] and therefore, can lead to generation of thermal stresses either within the glass-ceramic or at Crofer22APU/glass-ceramic interface. These thermal stresses can produce a crack and consequently reduce the mechanical integrity of sealants. Nevertheless, the XRD patterns of both the glass-ceramics (HJ11 and HJ28) contain an unidentified peak at $2^{\theta} = 23.7°$.

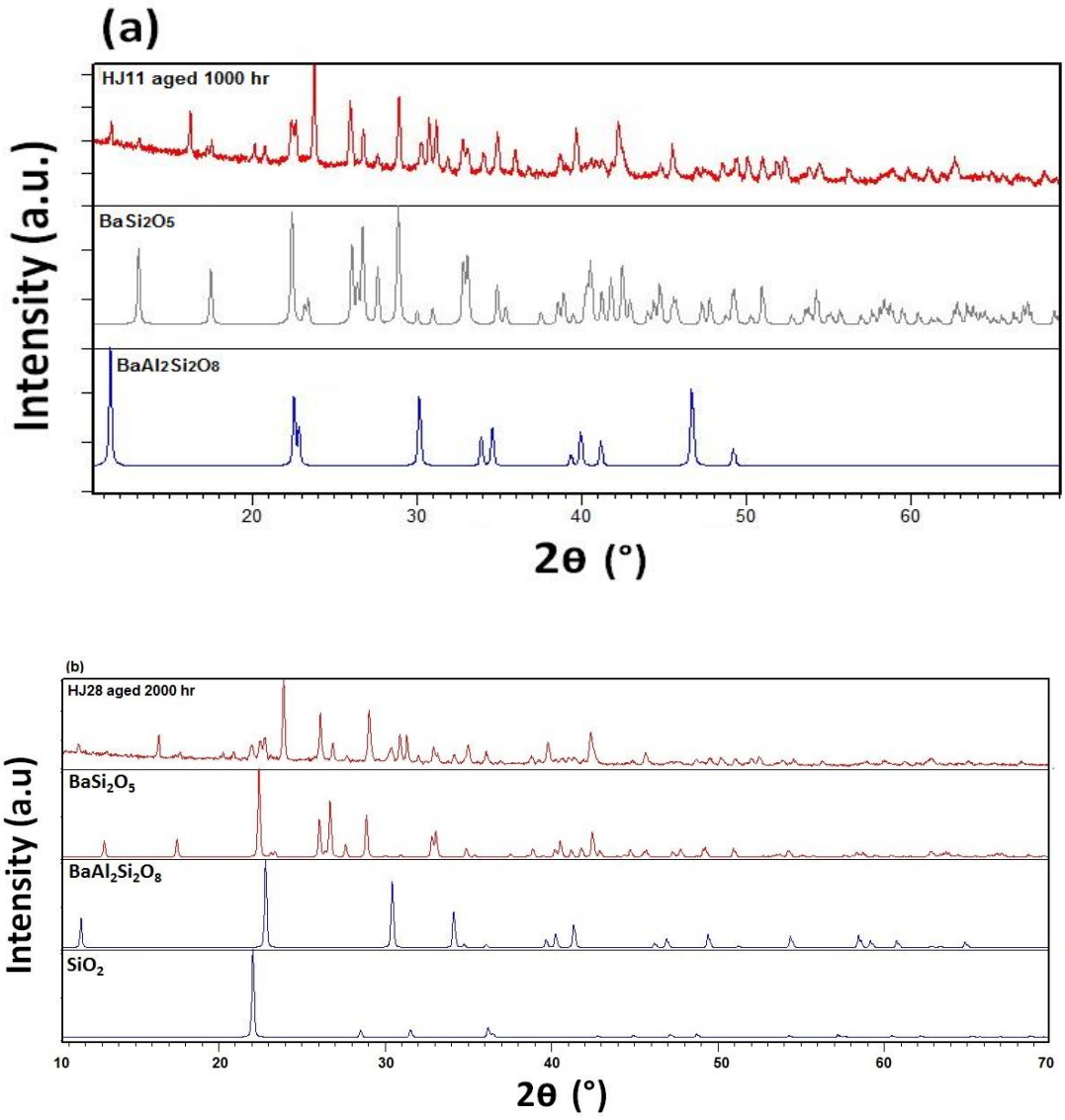

Figure 100. XRD patterns of thermally aged (a) HJ11 and (b) HJ28 glass-ceramics

Table 32 summarizes the different crystalline phases present in the as-joined and thermally aged HJ11 and HJ28 glass-ceramics.

Table 32. Crystalline phases present in the thermally aged HJ11 and HJ28 glass-ceramics

	HJ11	HJ28
After joining	$BaSi_2O_5$	$BaSi_2O_5$
After thermal ageing	$BaSi_2O_5$ $BaAl_2Si_2O_8$	$BaSi_2O_5$ SiO_2 $BaAl_2Si_2O_8$

From the dilatometeric analyses performed on the aged HJ11 glass-ceramic (1000 hours, 850 °C), a CTE of 9.7 x 10^{-6} K^{-1} was measured in the temperature range of 200-500 °C. The reduction is the CTE of HJ11 glass-ceramic after the ageing is most likely due to the devetrification of low CTE $BaAl_2Si_2O_8$ phase as detected by the XRD. Another reason of reduction in CTE could be the change in the composition of residual glass due to devetrification of new phase and/or change in the concentration of initially formed $BaSi_2O_5$ phase. Although, after the ageing the CTE of the HJ11 glass-ceramic is in the desire range (9-12 x 10^{-6} K^{-1}) for SOEC applications, nevertheless the low CTE phase can lead to stress generation and cause problem in terms of long term stability of the sealant.

The CTE of the HJ28 glass-ceramic was measured after the thermal ageing of 2000 hours. The corresponding dilatometer curve is shown in Figure 101. The CTE of the thermally aged HJ28 glass-ceramic was 9.4 x 10^{-6} K^{-1} as measured in the temperature range of 250-500 °C. The dilatometer curve of the HJ28 glass-ceramic shows a significant change in slope around 230 °C. This change in slope was due to the presence of cristobalite phase that undergo phase transformation around 230 °C. While measuring the CTE of the aged HJ28 glass-ceramic, the measurement below 250 °C were exempt to avoid the effect of cristobalite. The CTE of the aged HJ28 glass-ceramic does not showed any change compared with as-joined HJ28 glass-ceramic (9.3 x 10^{-6} K^{-1}). Nevertheless, the CTE after ageing is also in desire range for the SOEC applications.

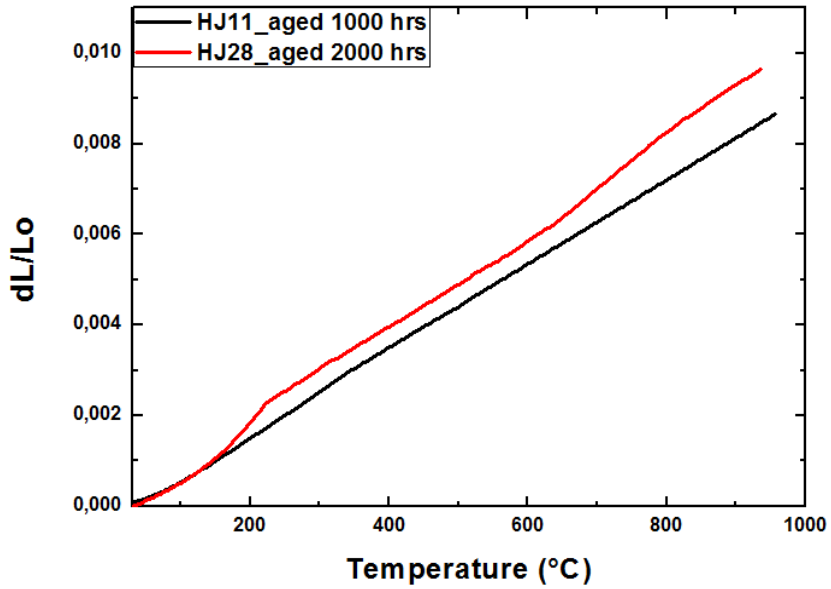

Figure 101. Dilatometer curves of HJ11 and HJ28 glass-ceramics after the thermal ageing of 1000 hours and 2000 hours respectively

4.3.5 Electrical characterization of 3rd series glass-ceramic in dual atmosphere and post mortem analysis

The electrical resistivity of the Crofer22APU/HJ11 glass-ceramic/Crofer22APU joined sample was measured in the dual atmosphere for 800 hours at 850 °C. For this purpose, the glass was manually deposited in the form of slurry, and joining was carried out at 950 °C for 1 hour, followed by the ageing at 850 °C for 800 hours without any interruption. The electrical characterization was performed under the applied voltage of 1.6V.

The electrical resistivity data of the Crofer22APU/HJ11 glass-ceramic/Crofer22APU joined sample is shown in Figure 102. The electrical resistivity curve shows a slight reduction in the beginning of test (up to 20 hours), followed by a steady and stable behavior. The initial reduction is probably as a result of mobility of some free ions before the sufficient crystallization occurred. Afterward, the resistivity curve showed a very stable behavior up to 500 hours. After 500 hours, a discontinuity in the resistivity data can be seen, that caused reduction in the resistivity. The discontinuity in electrical resistivity could be due to some polarization effect. However, soon after this interruption, the resistivity curve again became stable and remained uniform until the end of the test. During the entire testing period, the electrical resistivity values of the Crofer22APU/HJ11 glass-ceramic/Crofer22APU joined sample were in the range of 10^5-10^6 Ω.cm, higher than the minimum require limit (10^4 Ω.cm) for SOEC applications in order to avoid any short circuit during operation. The uniform electrical resistivity behavior also suggests that no chemical interaction between the HJ11 glass-ceramic and the Crofer22APU plates occurred.

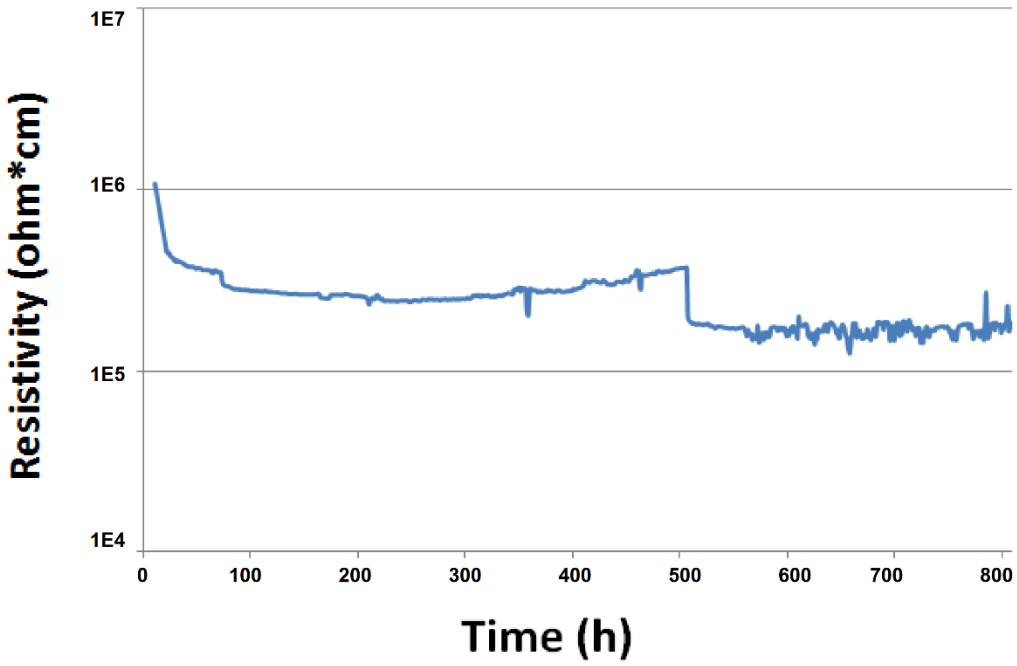

Figure 102. Electrical resistivity of the Crofer22APU/HJ11/Crofer22APU joined sample, as investigated in the dual atmosphere for 800 hours at 850 °C

After the electrical resistivity test, the post mortem analyses of the Crofer22APU/HJ11 glass-ceramic/Crofer22APU joined sample was carried out by the SEM in order to investigate the morphology of glass-ceramic and its compatibility with the Crofer22APU substrates. Figure 103 shows the Crofer22APU/HJ11 glass-ceramic/Crofer22APU joined sample after the electrical resistivity test in dual atmosphere for 800 hours. The SEM analyses shows that the HJ11 glass-ceramic is significantly dense; however, it contains few isolated pores. The pores size and overall level of porosity in the HJ11 glass-ceramic after the long-term resistivity test seems similar to that of as-joined HJ11 glass-ceramic as shown in Figure 99 (a). The presence of residual porosity is most likely due to the manual deposition of the glass. However, the HJ11 glass-ceramic showed good compatibility and strong bonding to the Crofer22APU substrates.

The Figure 103 also shows the magnified SEM images of the HJ11 glass-ceramic interfaces with negative and positive polarized Crofer22APU. The HJ11 glass-ceramic is well adherent to the both polarized Crofer22APU plates, after the long-term resistivity test. Despite of the presence of low CTE $BaAl_2Si_2O_8$ phase after ageing (as detected by XRD), no delamination or cracks were observed at the Crofer22APU/HJ11 glass-ceramic interfaces, with different polarized Crofer22APU substrates. The microstructure of HJ11 glass-ceramic is also uniform where different crystalline phases are evenly distributed though out the glass-ceramic without any segregation.

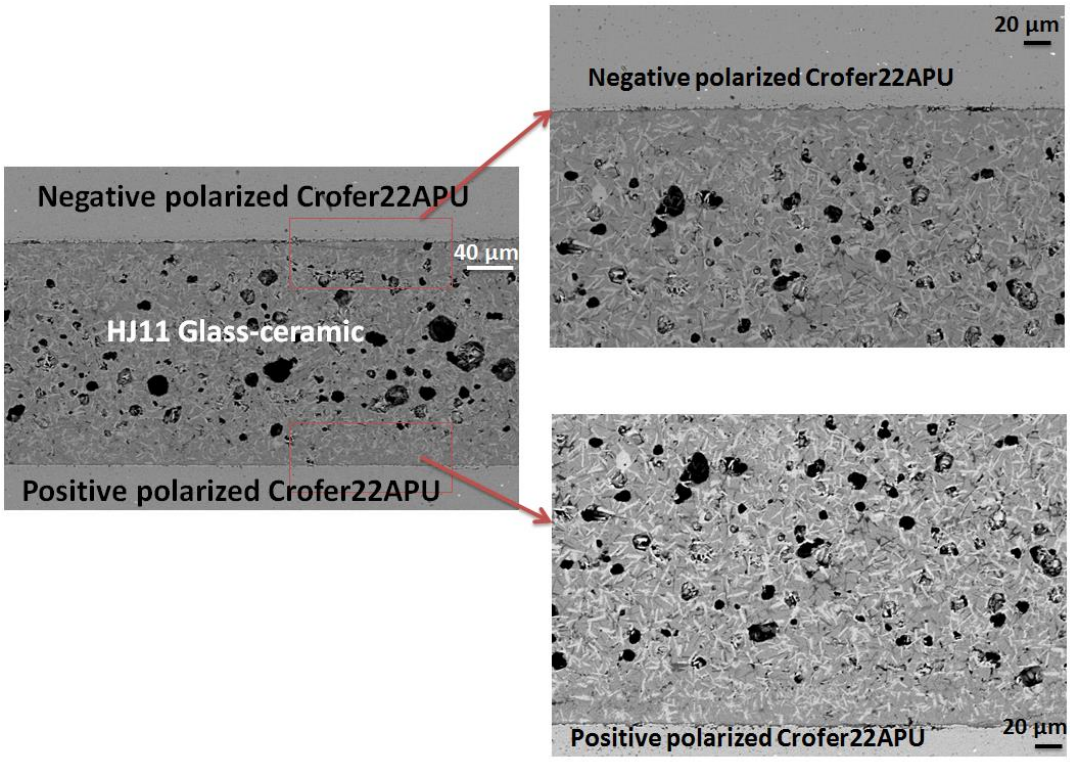

Figure 103. SEM image of Crofer22APU/HJ11/Crofer22APU joined sample interface after electrical resistivity test in the dual atmosphere for 800 hours at 850 °C

The morphology of the HJ11 glass-ceramic was further analyzed by EDS. For this purpose, the EDS point analyses were carried out on different crystalline phases shown in Figure 104. The corresponding EDS data is given in Table 33. The EDS analysis at bright phase (point 1) shows the presence of Ba, Si and O thus refer to $BaSi_2O_5$ phase. On the other hand, the EDS analysis at dark needle like phase (point 2) depicts that this phase contains significantly higher concentration of Al, in addition to Ba and Si. This Al-rich phase corresponds to the celsian ($BaAl_2Si_2O_8$). This dark phase ($BaAl_2Si_2O_8$) was not observed during the SEM analysis of as-joined HJ11 glass-ceramic and is formed as a result of long-term thermal ageing during the resistivity test. The region corresponding to the point 3 is the residual glassy phase. A minimal concentration of Ba (8 at.%) is present at the residual glass after the long term electrical resistivity test. The Ba concentration slight reduced in the residual glassy phase after long-term resistivity test as compared with the residual glass after joining. This is most likely due to the devitrification of more crystalline phases during the ageing. Nevertheless, the Ba concentration is still sufficient to maintain the CTE and viscous behavior of glass.

These SEM-EDS analyses also confirmed the XRD analyses performed on HJ11 glass-ceramic after the thermal ageing.

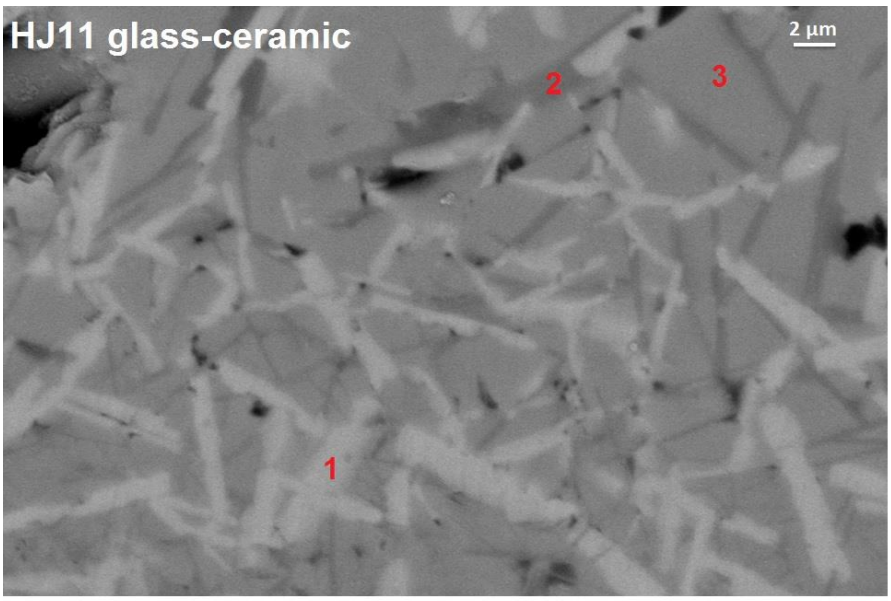

Figure 104. SEM image of HJ11 glass-ceramic after electrical resistivity test in the dual atmosphere for 800 hours at 850 °C

Table 33. EDS point analyses performed on the HJ11 glass-ceramic shown in Figure 104, after electrical resistivity test in the dual atmosphere for 1000 hours at 850 °C

	Point 1	Point 2	Point 3
O	50.0	63.4	69.6
Si	30.4	19.9	17.6
Ba	19.6	7.3	8.0
Al	---	8.1	1.3
Ca	---	1.3	3.4

The EDS line scans performed across the negative and positive polarized Crofer22APU/HJ11 glass-ceramic, after the electrical resistivity test in dual atmosphere is shown in Figure 105. According to the EDS line scans, no diffusion of elements across the Crofer22APU/HJ11 glass-ceramic interface was detected. Formation of no Cr_2O_3 oxide scale nor segregation of glass elements was observed at the Crofer22APU/HJ11 glass-ceramic interface. Therefore, there was no indication were found regarding the formation of undesirable high CTE $BaCrO_4$ phase or corrosion at the Crofer22APU/HJ11 glass-ceramic interface.

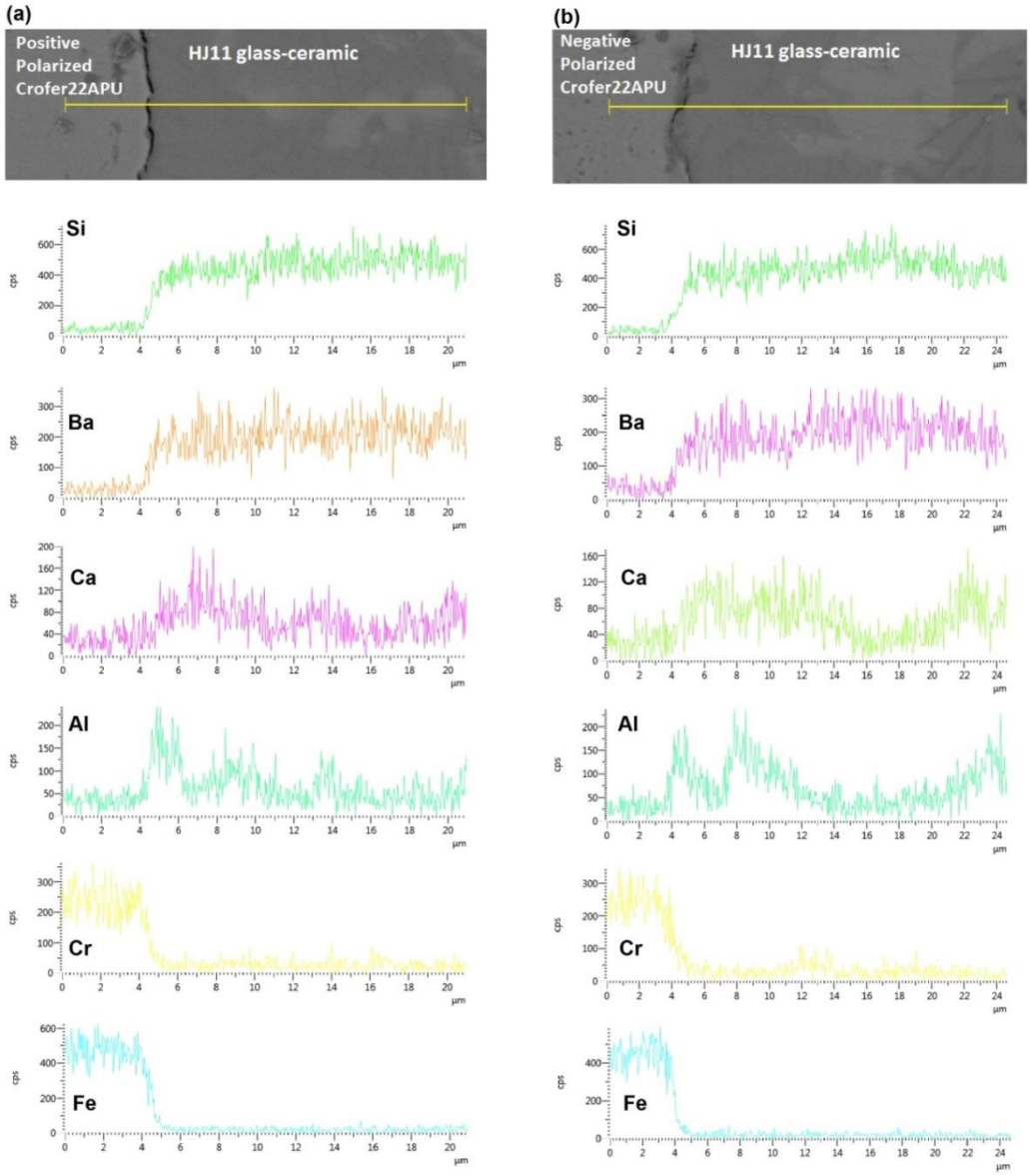

Figure 105. SEM-EDS line scan across (a) positive polarized Crofer22APU/HJ11 and (b) negative polarized Crofer22APU/HJ11 interfaces, after resistivity test in the dual atmosphere for 800 hours at 850 °C

The EDS mappings carried out at the positive and negative polarized Crofer22APU/HJ11 glass-ceramic after the electrical resistivity test are shown in Figure 106 and Figure 107 respectively. The EDS mapping results are in agreement with the EDS line scan analyses discussed above. No Cr rich layer was formed at both polarized Crofer22APU plates, therefore excluded the possible formation of $BaCrO_4$ phase. The presence of hard atmosphere i.e. H_2/H_2O, high working temperature and applied electrical load offer promotes the chemical interaction [28], however, the EDS analyses confirmed that no chemical interaction took place between the HJ11 glass-ceramic elements and that of Crofer22APU after the electrical resistivity test in dual atmosphere and consequently no corrosive products were formed at interface. In the glass-ceramic, the compositional difference between different crystalline phases is also clear

from the EDS mapping. The bright phases in the HJ11 glass-ceramic show the absence of Al and Ca, thus indicating the $BaSi_2O_5$ phase. The Ca and Al were detected at the residual glassy phase (dark phase).

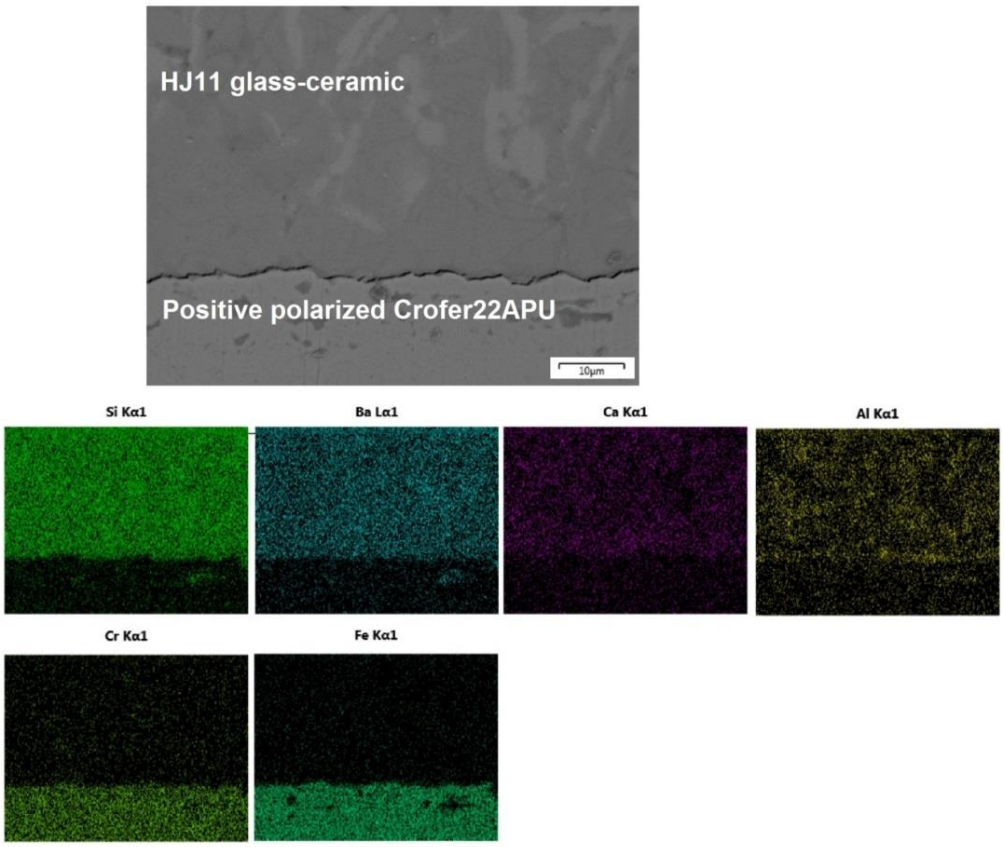

Figure 106. EDS mapping of positive polarized Crofer22APU/HJ11 interface after electrical resistivity test in the dual atmosphere for 800 hours at 850 °C

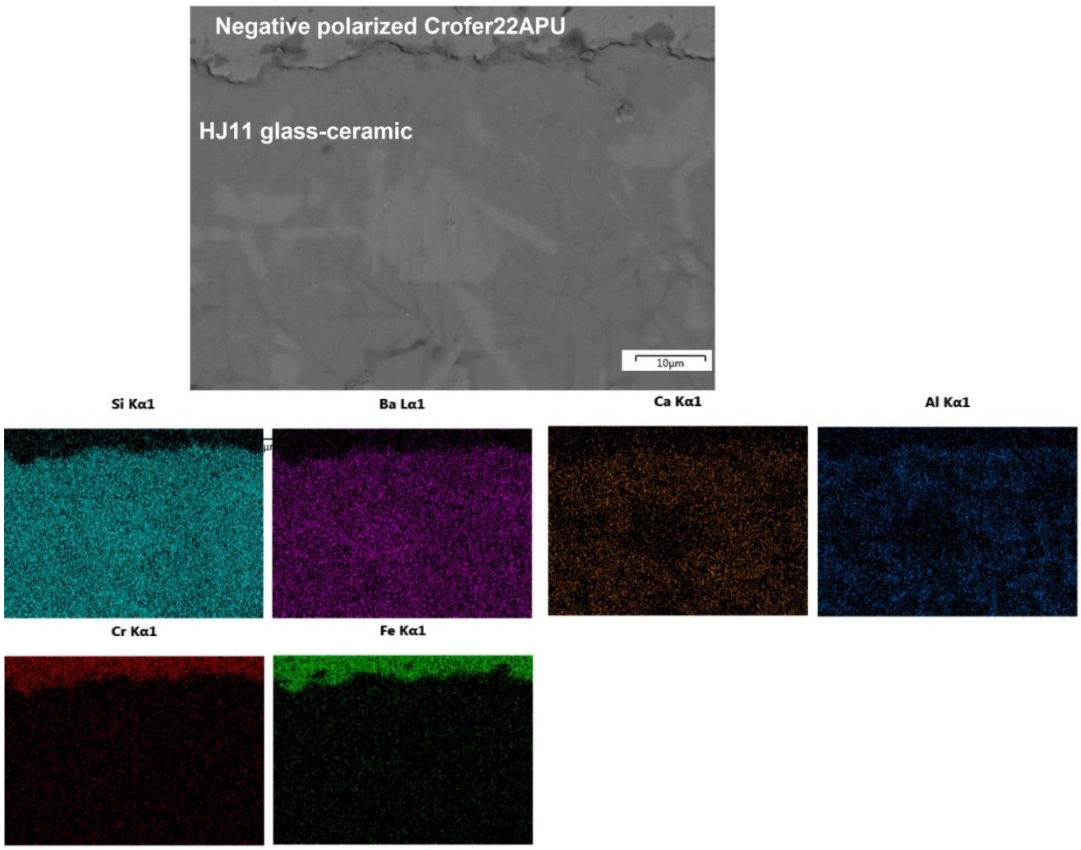

Figure 107. EDS mapping of negative polarized Crofer22APU/HJ11 interface after electrical resistivity test in the dual atmosphere for 800 hours at 850 °C

The electrical resistivity of the Crofer22APU/HJ28 glass-ceramic/Crofer22APU joined sample was investigated for 2000 hours at 850 °C in dual atmosphere. In order to simulate the real working conditions of SOEC, two thermal cycles were employed after 500 hours of initiation of resistivity test, where the Crofer22APU/HJ28 glass-ceramic/Crofer22APU joined sample was cooled down from 850 °C to room temperature. After the thermal cycles, the Crofer22APU/HJ28 glass-ceramic/Crofer22APU joined sample was reheated and aged for remaining 1500 hours following by cooling down to room temperature. The time-temperature profile for the long term electrical resistivity test of the HJ28 glass-ceramic is shown in Figure 108.

In this research work, the electrical resistivity of only HJ28 glass-ceramic has been investigated in the simulated SOEC conditions (dual atmosphere, thermal cycles etc.). The investigation of electrical resistivity of other glass-ceramics in such conditions is under progress.

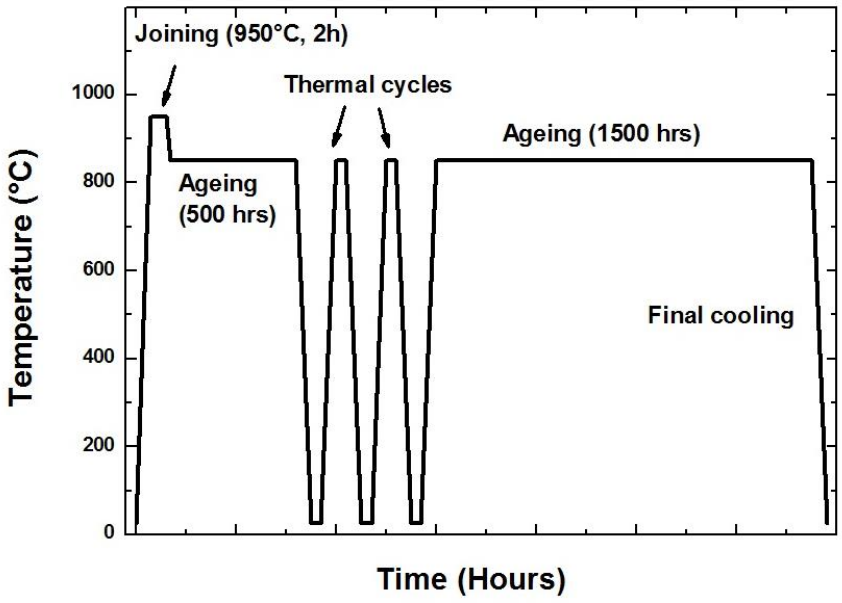

Figure 108. Time temperature profile for the long-term electrical resistivity test for the Crofer22APU/HJ28/Crofer2APU joined sample

The electrical resistivity curve for the Crofer22APU/HJ28 glass-ceramic/Crofer22APU joined sample is shown in Figure 109. The electrical resistivity for the Crofer22APU/HJ28 glass-ceramic/Crofer22APU joined sample was recorded in the range of 10^6 – 10^7 Ω.cm, thus higher than the minimum threshold (10^4 Ω.cm) required to ensure insulation between the two the conducting Crofer22APU plates. The electrical resistivity curve is quite uniform with small fluctuations that are most likely due to the polarized effect. At 500 hours, an abrupt increase in the electrical resistivity is due to the applied thermal cycles. However, after the thermal cycles the resistivity achieved the same values as prior to the thermal cycles. The smooth resistivity curve also indicates that neither corrosion phenomena nor any undesirable chemical interaction took place between the HJ28 sealant and Crofer22APU interconnects.

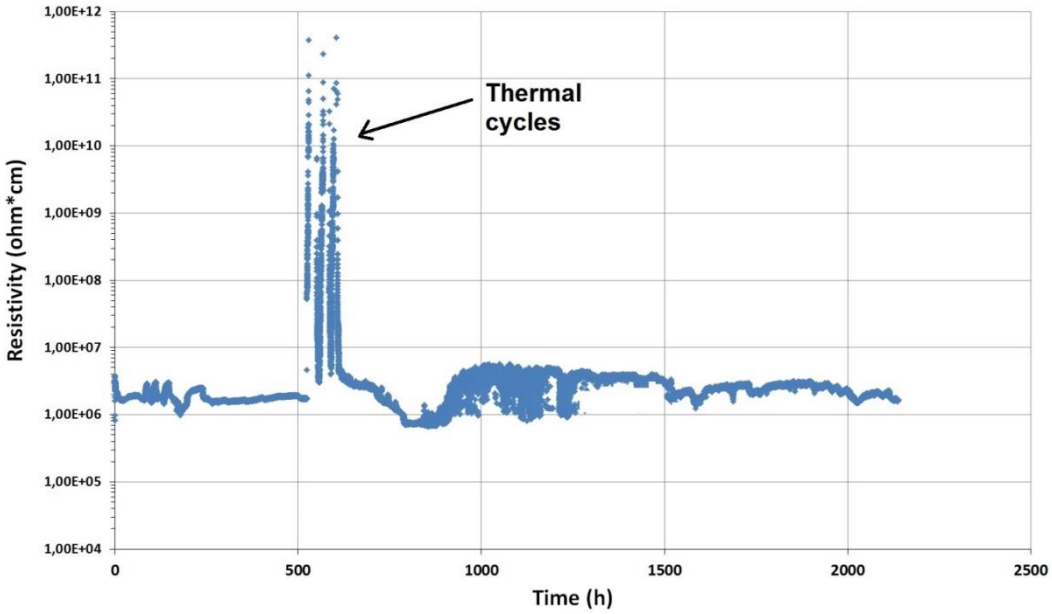

Figure 109. Electrical resistivity of Crofer22APU/HJ28 glass-ceramic/Crofer22APU joined sample, as measured for 2000 hours at 850 °C under the applied voltage of 1.6V.

The SEM-EDS post mortem analyses on the HJ28 glass-ceramic after the long-term resistivity are under progress.

Beside long term testing in dual atmosphere and under electric load, the Crofer22APU/HJ28 glass-ceramic/Crofer22APU joined sample was also aged in static air for 2000 hours according to heat treatment shown in Figure 108. The corresponding SEM post mortem analyses are shown in Figure 110. Figure 110 (a) shows the SEM analysis carried out at middle of Crofer22APU/HJ28 glass-ceramic/Crofer22APU joined sample. The HJ28 glass-ceramic seems to be strongly bonded to both the Crofer22APU plates. No cracks were found within the HJ28 glass-ceramic nor at Crofer22APU/HJ28 glass-ceramic interface after the long-term thermal ageing in static air. The HJ28 glass-ceramic microstructure is dense with little residual porosity. Figure 110 (b) shows the SEM image of Crofer22APU/HJ28 glass-ceramic/Crofer22APU joint at air side. Few small cracks are visible within the HJ28 glass-ceramic, close to air side. These cracks are not penetrating throughout the glass-ceramic, but seem to be present only close to the air side. Nevertheless, the HJ28 glass-ceramics seems to be strongly attached to both the Crofer22APU plates. Close to the air side, the HJ28 glass-ceramic also showed porosity; however, the glass-ceramic is still significantly dense to act as suitable sealant for SOEC applications.

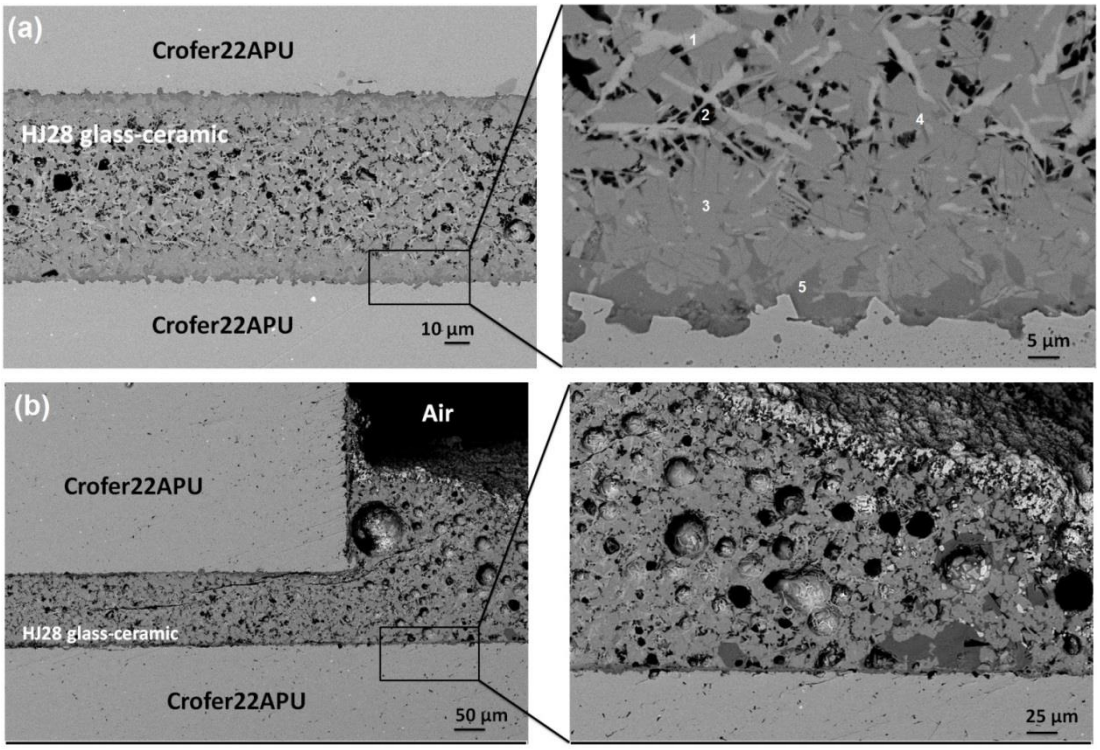

Figure 110. SEM post mortem analyses of Crofer22APU/HJ28/Crofer22APU joined sample tested in static air at 850 °C for 2000 hours. The shown images correspond to (a) middle of joint and (b) at Crofer22APU/glass-ceramic/air triple phase boundary. The labelled numbers in Figure 110 (a) represents different crystalline phases with corresponding EDS analysis given in Table 34.

The EDS point analyses carried out at different crystalline phases of the HJ28 glass-ceramic (Figure 110), after the long term thermal ageing are given in Table 34. The bright phase at point 1 shows presence of Si, Ba and O based phase thus refer to $BaSi_2O_5$ while the black phase (point 2) is cristobalite (SiO_2). Point 3 represent the residual glassy phase and contains significant concentration of Ba, Si, O in addition to Ca and Al. No Cr was detected into residual glass phase after long-term thermal ageing for 2000 hours. The EDS analysis at the needle like structure (point 4) shows prominent increase in the Al concentration. Besides Al, significant amount of Si, Ba and O are also measured. The presence of these elements indicates that the needle like phase corresponds to celsian $BaAl_2Si_2O_8$. The celsian is a low CTE phase and formed during long-term ageing. On the other hand, point 5 shows high concentration of Y (11.8 at. %) besides Ba, Si and O. The HJ28 glass system contains only 1 mol% of Y_2O_3, therefore the detection of such a high concentration of Y is most likely due to wrong estimation during EDS analysis. Nevertheless, the point 5 shows 2.3 mol% of Cr, therefore, probably this phase corresponds to the Cr-oxide scale.

Table 34. EDS point analyses (at.%) carried out at different regions of Figure 110 (a)

	Point 1	Point 2	Point 3	Point 4	Point 5
O	31.2	51.8	33.9	32.6	34.4
Si	19.9	42.3	17.9	18.0	17.9
Ba	47.0	5.9	41.9	40.5	28.6
Ca	1.9	---	5.2	2.7	2.7
Al	---	---	1.0	6.2	2.3
Y	---	---	---	---	11.8
Cr	---	---	---	---	2.3

Figure 111 shows the EDS mapping carried out at Crofer22APU/HJ28 glass-ceramic/Crofer22APU joint, at air side after long term ageing in static air. The EDS mapping shows the presence of chromates at the glass-ceramic/air interface. These chromates are formed most likely due to the chemical reaction between the Ba from glass-ceramic and Cr from Crofer22APU. These chromates have high CTE and can be a source of crack initiation. The cracks visible in the glass-ceramic, close to the air side, could probably due to these chromates. However, no chromates were formed at HJ28 glass-ceramic/Crofer22APU interface, thus no crack or delamination was detected at glass-ceramic/Crofere22APU interface. Furthermore, no signs were found regarding the diffusion or segregation of other elements within the glass-ceramic or at glass-ceramic/Crofer22APU interface.

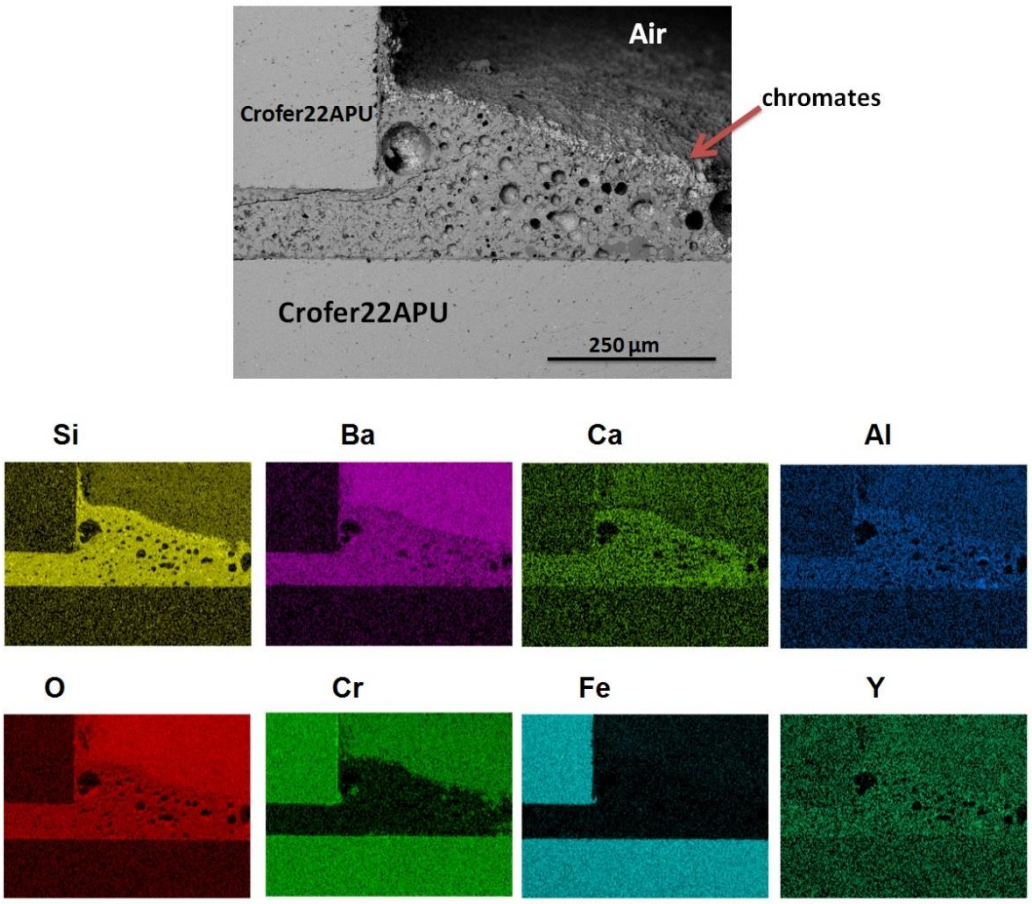

Figure 111. EDS mapping carried out at Crofer22APU/HJ28 glass-ceramic/Crofer22APU joint, at air side after long term ageing in static air.

Summary

The 3rd series of glasses (HJ11 and HJ28) contained BaO as main modifier. The as-joined glass-ceramics showed excellent compatibility with other cell components. XRD confirmed the presence of only desirable $BaSi_2O_5$ phase in both the glass-ceramics. However, the long-term treatment resulted in the formation of low CTE $BaAl_2Si_2O_8$ celsian phase in both glass-ceramics. The formation of cristobalite (SiO_2) phase was also detected after long term ageing of HJ28 glass-ceramic. Nevertheless, both glass-ceramics showed adequate electrical resistivity measured in dual atmosphere. In particular, the HJ28 showed the most promising results as it was tested under the electrical load for a total of 2000 hours with 3 applied thermal cycles.

4.4 Stencil printing of glass paste

The novel glass pastes were developed based on HJ28 glass system. The rheological properties such as viscosity, shear modulus and storage modulus of pastes were analyzed by using a rheometer (Physica, Anton Paar). The rheological properties of the most promising pastes are summarized in Table 35.

Table 35. Rheological properties of glass pastes

Property (unit)	
Viscosity (Pa.s)	16-18
Storage Modulus (Pa)	19-22
Loss Factor	0.4-0.6

The glass pastes were deposited on the real dimensioned Crofer22APU interconnect. Figure 112 shows the Crofer22APU interconnect, where glass paste was deposited by using automatic stencil printing. The deposited glass paste seems to be uniform, without any missing sections. The glass paste also did not slump after deposition.

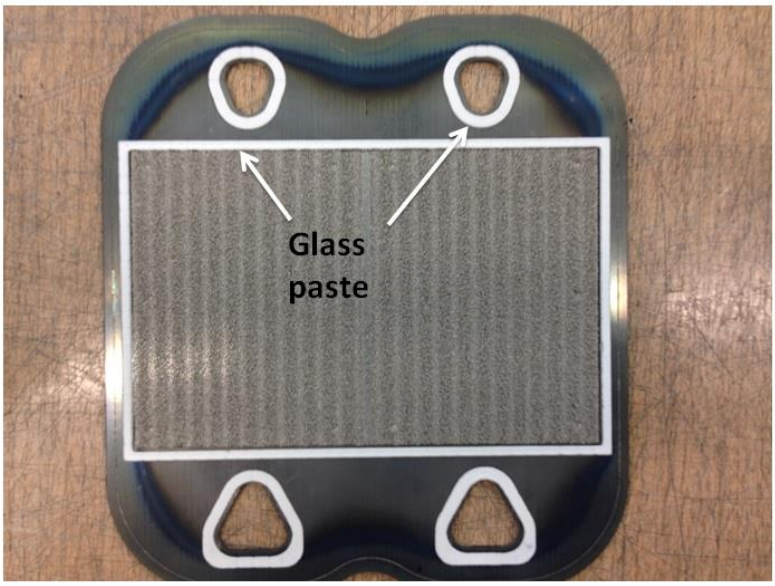

Figure 112. Glass paste deposited on the Crofer22APU substrate by stencil printing

After paste deposition, the 3YSZ electrolyte was placed on the stencil printed HJ28 glass paste. A short stack was build up using Crofer22APU plates containing stencil deposited HJ28 glass. The joining of the stack was carried out according to standard heat treatment of HJ28 glass system. The short stack was operated at 850 ºC for 4 hours. After joining and testing, the SEM post mortem analyses were performed to analyze the microstructure and compatibility of HJ28 glass-ceramic with other cell components.

Figure 113 shows the corresponding SEM images of Crofer22APU/HJ28 glass-ceramic/3YSZ joint sample. The SEM analyses were carried out at fuel-in side, air side and in middle of joint. The SEM images show that the HJ28 glass-ceramic deposit in the form of paste by stencil printing is dense throughout the joining regions. The microstructure of HJ28 glass-ceramic is quite homogenous. No cracks were found within the glass-ceramics or at either interface. These SEM

results also confirm that the novel paste formed was promising in order to obtain the dense sealant.

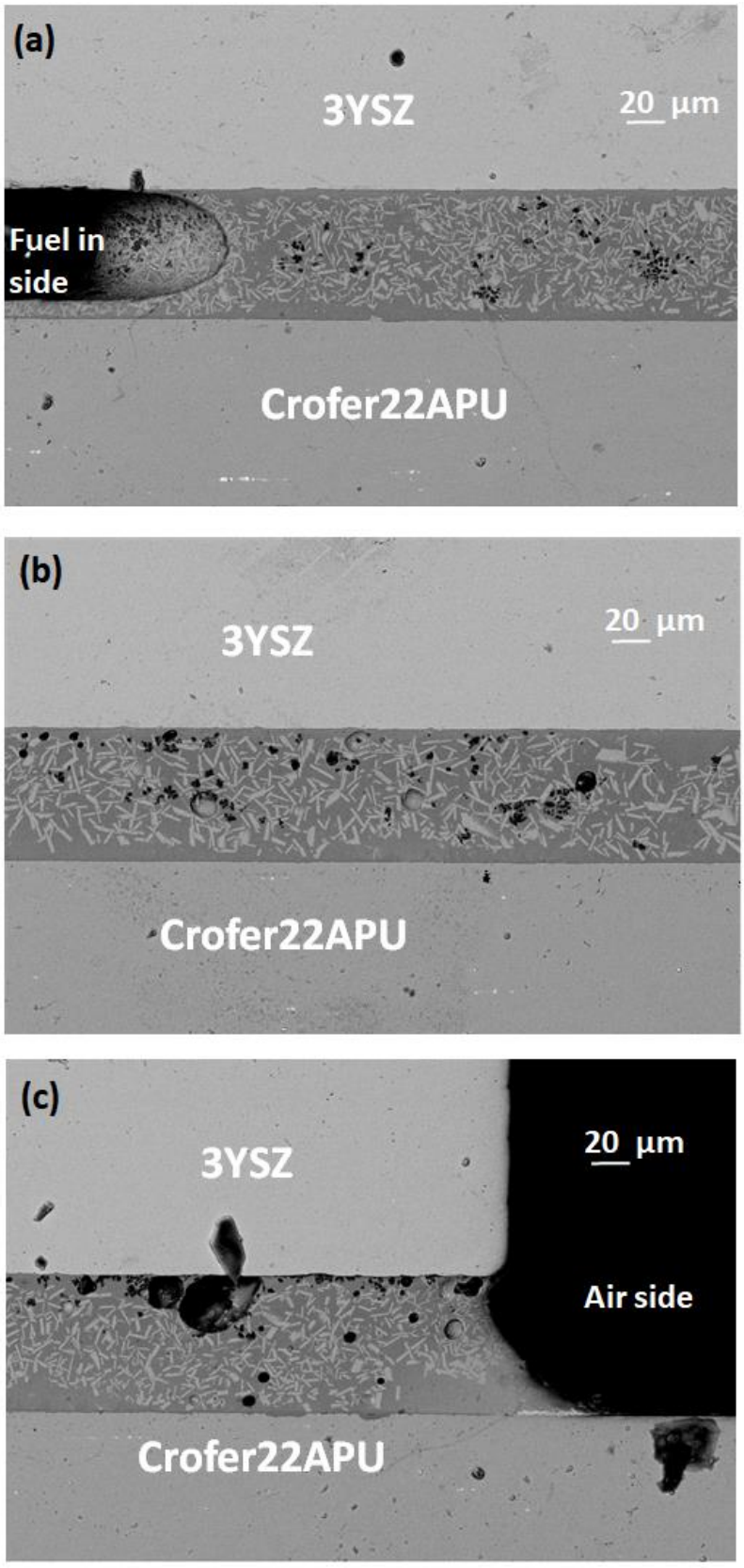

Figure 113. SEM analyses of Crofer22APU/HJ28 glass-ceramic/3YSZ joined sample. HJ28 glass paste was deposited by stencil printing. The shown images were taken at (a) fuel in side, (b) middle of joining and (c) air side

References

[1] J. W. Fergus, “Sealants for solid oxide fuel cells,” *Journal of Power Sources*, vol. 147, no. 1–2, pp. 46–57, 2005.

[2] D. U. Tulyaganov, A. A. Reddy, V. V. Kharton, and J. M. F. Ferreira, “Aluminosilicate-based sealants for SOFCs and other electrochemical applications - A brief review,” *Journal of Power Sources*, vol. 242, pp. 486–502, 2013.

[3] Q. Zhang, H. Yang, F. Zeng, S. Wang, D. Tang, and T. Zhang, “Development of the CaO – SrO – ZrO2 – B2O3 – SiO2 Sealing Glasses for Solid Oxide Fuel Cell Applications : Structure,” *RSC Advances*, vol. 5, no. April 2016, pp. 41772–41779, 2015.

[4] S. Ghosh, A. Das Sharma, P. Kundu, and R. N. Basu, “Glass-ceramic sealants for planar IT-SOFC: A bilayered approach for joining electrolyte and metallic interconnect,” *Journal of the Electrochemical Society*, vol. 155, no. 5, pp. B473–B478, 2008.

[5] K. M. Manu, S. Ananthakumar, and M. T. Sebastian, “Electrical and thermal properties of low permittivity Sr2Al2SiO7ceramic filled HDPE composites,” *Ceramics International*, vol. 39, no. 5, pp. 4945–4951, 2013.

[6] A. A. Reddy, A. Goel, D. U. Tulyaganov, M. Sardo, L. Mafra, M. J. Pascual, V. V. Kharton, E. V. Tsipis, V. A. Kolotygin, and J. M. F. Ferreira, “Thermal and mechanical stability of lanthanide-containing glass–ceramic sealants for solid oxide fuel cells,” *Journal of Materials Chemistry A*, vol. 2, no. 6, p. 1834, 2014.

[7] C. Thieme and C. Rüssel, “Thermal expansion behavior of SrSiO3 and Sr2SiO4 determined by high-temperature X-ray diffraction and dilatometry,” *Journal of Materials Science*, vol. 50, no. 16, pp. 5533–5539, 2015.

[8] S. Hillier, “Accurate quantitative analysis of clay and other minerals in sandstones by XRD: comparison of a Rietveld and a reference intensity ratio (RIR) method and the importance of sample preparation,” *Clay Minerals*, vol. 35, no. 1, pp. 291–291, 2000.

[9] H. T. Chang, C. K. Lin, and C. K. Liu, “Effects of crystallization on the high-temperature mechanical properties of a glass sealant for solid oxide fuel cell,” *Journal of Power Sources*, vol. 195, no. 10, pp. 3159–3165, 2010.

[10] Y. Zhao and J. Malzbender, “Elevated temperature effects on the mechanical properties of solid oxide fuel cell sealing materials,” *Journal of Power Sources*, vol. 239, pp. 500–504, 2013.

[11] T. Osipova, J. Wei, G. Pecanac, and J. Malzbender, “Room and elevated temperature shear strength of sealants for solid oxide fuel cells,” *Ceramics International*, vol. 42, no. 11, pp. 12932–12936, 2016.

[12] H. Javed, A. G. Sabato, K. Herbrig, D. Ferrero, C. Walter, M. Salvo, and F. Smeacetto, “Design and characterization of novel glass-ceramic sealants for solid oxide electrolysis cell (SOEC) applications,” *International*

Journal of Applied Ceramic Technology, vol. 15, no. February, pp. 999–1010, 2018.

[13] J. Milhans, S. Ahzi, H. Garmestani, M. A. Khaleel, X. Sun, and B. J. Koeppel, "Modeling of the effective elastic and thermal properties of glass-ceramic solid oxide fuel cell seal materials," *Materials and Design*, vol. 30, no. 5, pp. 1667–1673, 2009.

[14] Y. Zhao, J. Malzbender, and S. M. Gross, "The effect of room temperature and high temperature exposure on the elastic modulus, hardness and fracture toughness of glass ceramic sealants for solid oxide fuel cells," *Journal of the European Ceramic Society*, vol. 31, no. 4, pp. 541–548, 2011.

[15] M. D. Beals and S. Zerfoss, "Volume Change Attending Low-To-High Inversion of Cristobalite," *Journal of the American Ceramic Society*, vol. 27, no. 10, pp. 285–292, 1944.

[16] E. V. Stephens, J. S. Vetrano, B. J. Koeppel, Y. Chou, X. Sun, and M. A. Khaleel, "Experimental characterization of glass-ceramic seal properties and their constitutive implementation in solid oxide fuel cell stack models," *Journal of Power Sources*, vol. 193, no. 2, pp. 625–631, 2009.

[17] B. Dev, M. E. Walter, G. B. Arkenberg, and S. L. Swartz, "Mechanical and thermal characterization of a ceramic/glass composite seal for solid oxide fuel cells," *Journal of Power Sources*, vol. 245, pp. 958–966, 2014.

[18] W. Liu, X. Sun, and M. A. Khaleel, "Predicting Young's modulus of glass/ceramic sealant for solid oxide fuel cell considering the combined effects of aging, micro-voids and self-healing," *Journal of Power Sources*, vol. 185, no. 2, pp. 1193–1200, 2008.

[19] J. Milhans, D. S. Li, M. Khaleel, X. Sun, M. S. Al-Haik, A. Harris, and H. Garmestani, "Mechanical properties of solid oxide fuel cell glass-ceramic seal at high temperatures," *Journal of Power Sources*, vol. 196, no. 13, pp. 5599–5603, 2011.

[20] S. Ghosh, A. Das Sharma, P. Kundu, and R. N. Basu, "Glass-based sealants for application in planar solid oxide fuel cell stack," *Transactions of the Indian Ceramic Society*, vol. 67, no. 4, pp. 161–182, 2008.

[21] A. G. Sabato, G. Cempura, D. Montinaro, A. Chrysanthou, M. Salvo, E. Bernardo, M. Secco, and F. Smeacetto, "Glass-ceramic sealant for solid oxide fuel cells application: Characterization and performance in dual atmosphere," *Journal of Power Sources*, vol. 328, no. October, pp. 262–270, 2016.

[22] N. H. Menzler, D. Sebold, M. Zahid, S. M. Gross, and T. Koppitz, "Interaction of metallic SOFC interconnect materials with glass-ceramic sealant in various atmospheres," *Journal of Power Sources*, vol. 152, no. 1–2, pp. 156–167, 2005.

[23] P. Batfalsky, V. A. C. Haanappel, J. Malzbender, N. H. Menzler, V. Shemet, I. C. Vinke, and R. W. Steinbrech, "Chemical interaction between glass-ceramic sealants and interconnect steels in SOFC stacks," *Journal of Power Sources*, vol. 155, no. 2, pp. 128–137, 2006.

[24] A. Rost, J. Schilm, J. Suffner, M. Kusnezoff, and A. Michaelis, “Development and Testing of Sealing Glasses for SOFCs based on CFY-Interconnects,” *11th European SOFC and SOE Forum 2014*, no. July, pp. 1–9, 2014.

[25] M. Kerstan and C. Rüssel, “Barium silicates as high thermal expansion seals for solid oxide fuel cells studied by high-temperature X-ray diffraction (HT-XRD),” *Journal of Power Sources*, vol. 196, no. 18, pp. 7578–7584, 2011.

[26] G. Kaur, *Solid Oxide Fuel Cell Components: Seal glass for solid oxide fuel cells*, vol. 58, no. 8. 2006.

[27] M. Kerstan, M. Müller, and C. Rüssel, “High temperature thermal expansion of BaAl2Si2O8, CaAl2Si2O8, and Ca2Al2SiO7 studied by high-temperature X-ray diffraction (HT-XRD),” *Solid State Sciences*, vol. 38, pp. 119–123, 2014.

[28] M. K. Mahapatra and K. Lu, “Effect of atmosphere on interconnect-seal glass interaction for solid oxide fuel/electrolyzer cells,” *Journal of the American Ceramic Society*, vol. 94, no. 3, pp. 875–885, 2011.

Chapter 5

Protective Coatings - Results and Discussion

The following section will discuss the results related to electrophoretic deposition (EPD) and characterization of $Mn_{1.5}Co_{1.5}O_4$ (MCO) coatings on the Crofer22APU substrates, the up-scaling of EPD process from lab to industrial scale and long term area specific resistance (ASR) analyses of MCO coated Crofer22APU.

The following text, data and images are an adaptation of the results that were published in the article:

S. Molin, A. G. Sabato, H. Javed, G. Cempura, A. R. Boccaccini, and F. Smeacetto, "Co-deposition of CuO and $Mn_{1.5}Co_{1.5}O_4$ powders on Crofer22APU by electrophoretic method: Structural, compositional modifications and corrosion properties," *Materials Letters*, **2018**, 218, pp. 329–333.

It is partially reproduced in this chapter with the incorporation of more results and slight modifications.

5.1 Electrophoretic deposition and SEM characterization of MCO coatings on Crofer22APU

The deposition parameters used for the EPD deposition of MCO coatings have already been reported in chapter 3. The coatings were deposited on the 1.5x1.5 cm flat Crofer22APU samples and were sintered at 1000°C for 2h in static air. The Crofer22APU/coatings interface was characterized by using SEM in order to observe the uniformity and thickness of coatings.

The SEM images of the EPD deposited and subsequently sintered MCO coating on the Crofer22APU substrates are shown in Figure 114. The SEM

images shows that the EPD resulted in uniform deposition of MCO coating. The coatings have the thickness of ~15 µm.

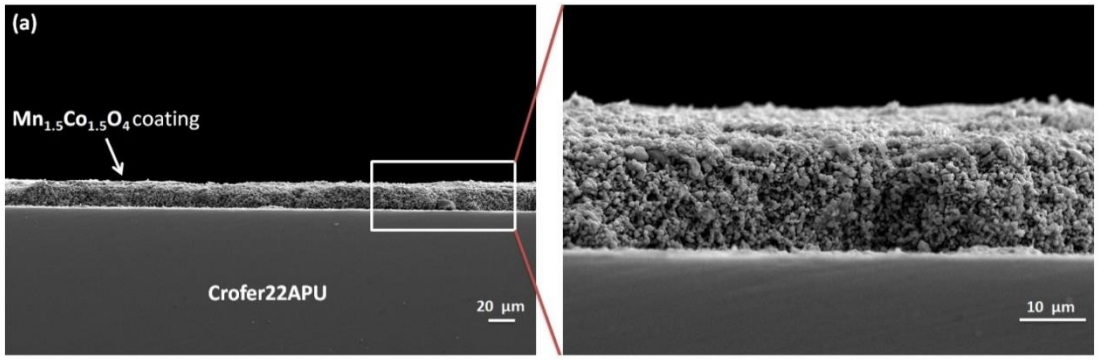

Figure 114. SEM images of EPD deposited and sintered MCO coating on the Crofer22APU interconnect

Despite satisfactory results in terms of thickness and uniformity of the coatings shown in Figure 114, the densification after the sintering process in air was still low. In order to improve this aspect a 2-step sintering process was also evaluated: a first step in reducing atmosphere (Ar/4% H_2 mixture) at 900°C for 2h and a subsequent step at 900°C for 2h in air. This process results in the formation of metallic Co and MnO during the first step and spinel form during the second step sintering in air. In this way, it is possible to take advantage from the presence of the metallic Co for improving the densification during the sintering. XRD carried out on MCO coating after the reducing step and reported in Figure 115, confirmed the formation of Co and MnO after the treatment in Ar/H_2.

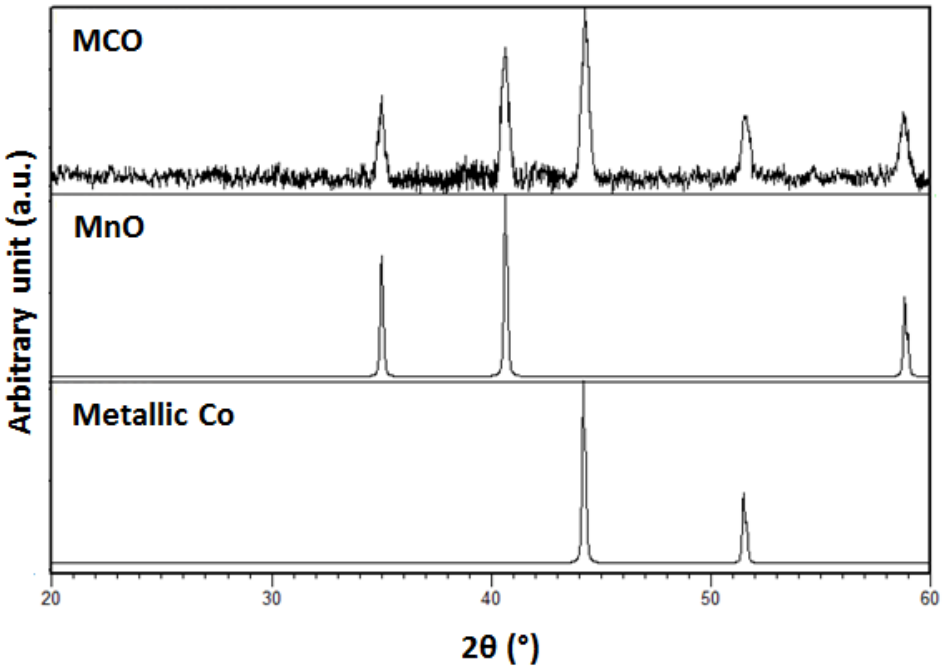

Figure 115. XRD pattern of MCO after sintering in reducing atmosphere

5.2 Up-scaling of EPD process at industrial scale

After optimization and successful deposition of uniform coating on the 1.5x1.5 cm samples, the EPD process was up-scaled in order to coat the real dimensioned (16 cm x 18 cm) corrugated Crofer22APU plates to be used into an SOEC stack. The Figure 116 shows the 16 cm x 18 cm Crofer22APU plate coated with MCO by EPD process.

Figure 116. MCO coated real dimensioned (16 x 18 cm^2) Crofer22APU interconnect by EPD

SEM analyses were carried out on samples in the as-prepared and sintered state. For this purpose, the real dimensioned MCO coated Crofer22APU plates were sintered in air (1000 ºC, 2 hours). For SEM, the samples were collected from the real dimension coated plates in order to have information about the

morphology of the coatings obtained on the real plate after the up-scaling of the EPD apparatus and the sintering treatments. Figure 117 shows the corresponding SEM images of Crofer22APU/MCO coating interface after one-step sintering in air.

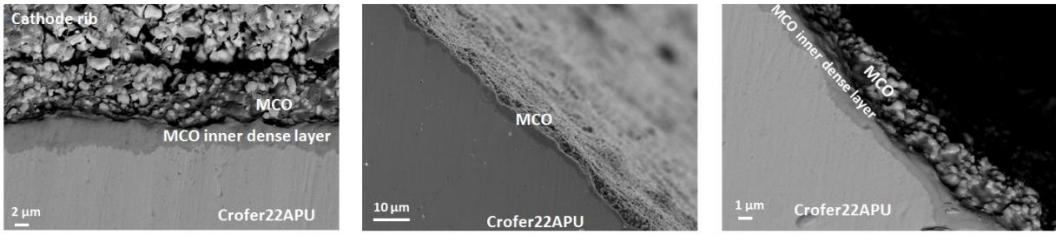

Figure 117. SEM pictures (cross-section) of MCO-EPD-1 step sintered

The MCO coating appeared to be denser in the first layer in contact with the Crofer22APU, for around 1-2 µm (labelled in the picture as "MCO inner dense layer"). On the contrary, it was found to be porous in the outer part. The porous area was also partially infiltrated by the cathode paste deposited to produce the cathode ribs (picture on the left). However, the coating is uniformly present on the horizontal region of the plate as well as on the "walls", thus confirming the good performances of EPD for coating channeled surfaces.

The effect of the 2-step sintering process was also investigated by carrying out SEM on the as-prepared MCO-EPD-2 step sintered coating. The results are reported in Figure 118. The densification of the coatings shown in here is much higher in comparison with one-step sintering, thus confirming the enhanced sintering due to the formation of metallic Co during the first reducing step of the sintering process. In addition, in this case the coating is homogeneously present on the horizontal surfaces as well as on the "walls".

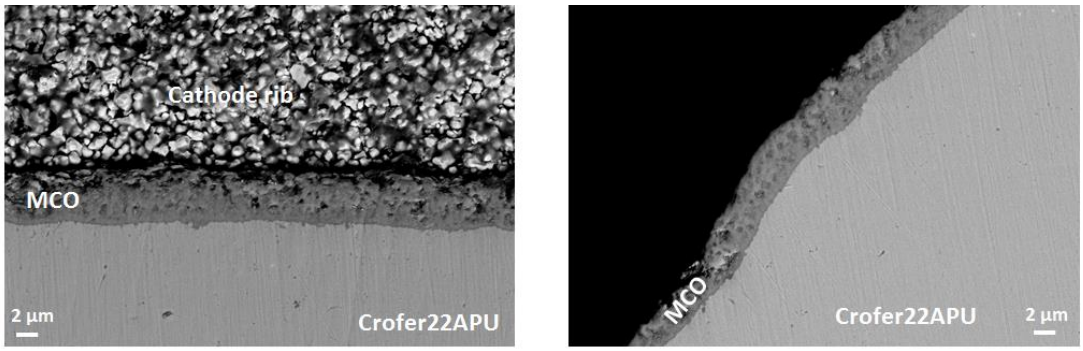

Figure 118. SEM pictures (cross-section) of MCO-EPD-2 steps sintered

In Figure 117 and Figure 118 the thickness of the coatings (≈ 4µm) appears to be reduced in comparison with the 10-15 µm obtained on 1.5x1.5cm samples. This was likely due to the upscaling of the experimental apparatus. Indeed, all the

deposition parameters (applied voltage, electrodes distance and time of deposition) were maintained constant after the upscaling.

5.3 Area specific resistance (ASR) measurements and post mortem analyses

The area specific resistance of the EPD coated MCO coating was measured up to 8600 hours at 850 °C. The details about the samples preparation have been already described in detail in the chapter 3. In order to investigate the effect of different sintering treatments, the MCO coatings were sintered by two following routes followed by the long term ASR measurements.

1. One-step sintering carried out in static at 900 °C for 2 hours at a heating/cooling rate of 10 °C/min.
2. Two steps sintering, first step sintering in the reducing atmosphere and second step sintering in static air. Sintering in both steps was carried out at 900 °C for 2 hours at a heating/cooling rate of 10 °C/min.

Figure 119 shows the long-term ASR data of the EPD deposited MCO coatings, sintered by two different routes as discussed above. The ASR test was conducted for total duration of 8600 hours, however, after 5000 hours the test was stopped due to some technical reasons and samples were cooled down to the room temperature. Later, the ASR test was restarted by heating the samples to 850 °C followed by the ageing.

According to the Figure 119, the MCO coating sintered by two different routes shows the quite steady ASR values up to 5000 hours (before the furnace shut down). However, after 5000 hours a sudden increase in the ASR data was recorded for both the samples. This abrupt increase in the ASR can be either due to the delamination of coatings from the Crofer22APU substrate or the delamination of cathode ribs from the top of coatings, because of applied thermal cycle.

Figure 119 also shows the ASR data before the thermal cycle i.e. up to 5000 hours. The direct comparison shows that the ASR values of the two steps sintered (reducing and oxidizing atmospheres) MCO coating are almost three times lower than MCO coating sintered in a single step (in oxidizing atmosphere). The higher ASR for the single step sintered MCO coating was probably due to the formation of Cr_2O_3 scale on the Crofer22APU surface because of sintering treatment only in static air. The Cr_2O_3 scale is electrical insulator and can increase the resistivity. On the other hand, in case of two steps sintering, the initial sintering treatment in reducing atmosphere can avoid the formation of Cr oxide scale.

The ASR results are also summarized in Table 36.In case of MCO-EPD-1 step sintering, ASR value after the shutdown of the apparatus are not reported, since they would be not meaningful. ASR degradation rate was evaluated with a linear interpolation of the data collected after 1000h thus excluding initial

consolidation of the samples (i.e. sintering of the contact paste). The degradation data after the shutdown (5000 hours) was not considered.

Table 36. Area specific resistance (ASR) and degradation rate of MCO coating up to 8.6kh at 850 °C

Variant	Description	ASR after 5kh (mΩ cm^2)	ASR after 8.6kh (mΩ cm^2)	Degradation rate (mΩ cm^2 kh^{-1})
1	MCO-EPD-2step sint.	28.1	n.a.	0.5*
2	MCO-EPD-1step sint.	94.7	n.a.	6.7

* ASR evaluated between 1000h and 5000h

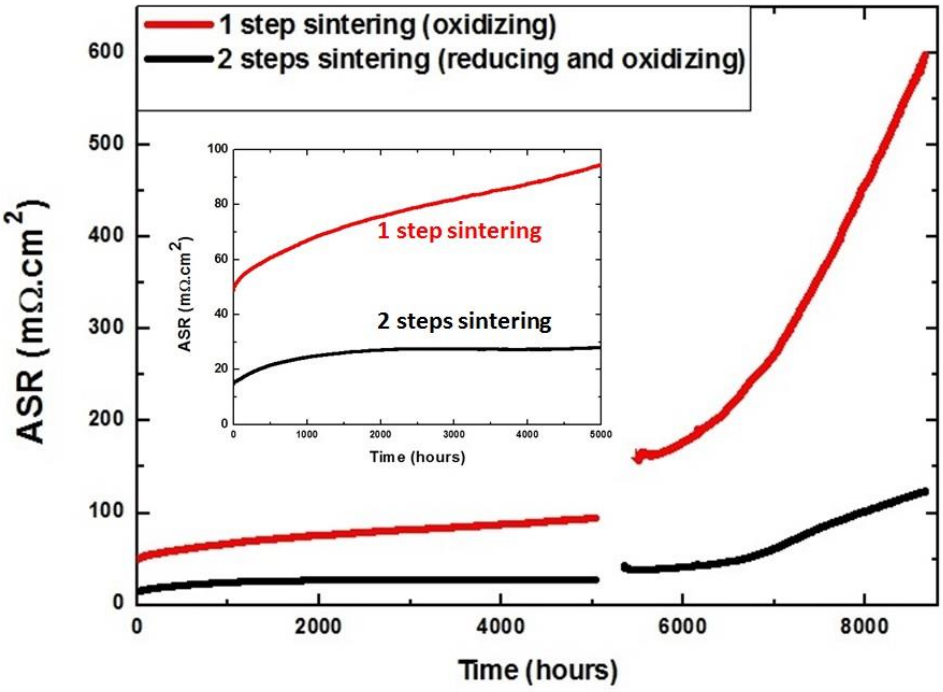

Figure 119. Area specific resistance (ASR) of the MCO coating sintered in one-step (red curve) and in two steps (black curve). The ASR was measured for 8600 hours at 850°C

For the single step sintered MCO coating the ASR values gradually increase with time, while in case of two steps sintered coating the ASR values are quite constant. The continuous gradual increase in the ASR of single step sintered coating is probably due to the fact that the density of coating after single step sintering is not sufficient to control oxygen diffusion. This oxygen diffusion can

facilitate the formation of non-conducting Cr oxide scale and consequently increase ASR. These results clearly show that the two steps sintering of MCO coating is necessary in order to achieve better electrical properties.

In order to correlate possible microstructural and chemical changes occurred during the test with the ASR behavior, SEM/EDS analyses were carried out on the samples after the ASR test up to 8600 hours.

The SEM post mortem images of the Crofer22APU/MCO coating interface sintered in two-steps are shown in Figure 120. The cathode ribs of LSMC are also visible above the MCO coating. A crack between the coating and cathode rib can be seen. This crack formation and consequent delamination was probably occurred during the thermal cycle applied after the 5000 hours of ASR test. This crack is most likely be the reason of increasing the ASR of coatings after 5000 hours as shown in Figure 119.

The red rectangles indicate the regions on which EDS semi-quantitative analyses were performed. In Figure 120(a) it is clearly visible the difference between the coated side and the uncoated side. In the latter case, the oxide scale grew up to ≈25µm. This is not the case for the coated side (Figure 120 (c) and (d)), where the oxide scale has a thickness of ≈3-5µm depending on the considered region. Although the cathode rib appears to be completely detached from the coating, however the coating appears to be still adherent to the underlying Crofer22APU substrate, more precisely to its oxide scale (Cr_2O_3). This together with the high degree of densification justifies the very good performances in terms of ASR and degradation rate recorded for this sample. The EDS analyses carried out on the coating and marked as region 3 (Table 37) detected an amount of Cr around 8.7 at%. This is due to the Cr diffusion from the steel into the coating, considering the very long duration of the ASR test (8.6kh). This could cause the formation of $(Mn,Cr,Co)_3O_4$ mixed spinel with higher electrical resistivity, leading to an increase of the overall electrical resistance of the coating/Crofer22APU system. Furthermore, also the Mn/Co ratio results to be higher than region 1 (as would be expected for MCO). This is due to fact that the Mn can diffuse toward the spinel from the cathode rib (LSMC) and Co can diffuse from the coating towards the cathode rib. The EDS carried out on region 2 did not detect any traces of Cr, suggesting that despite the diffusion of Cr from the Crofer22APU into the coating, Cr did not diffuse in to the cathode rib above the coating.

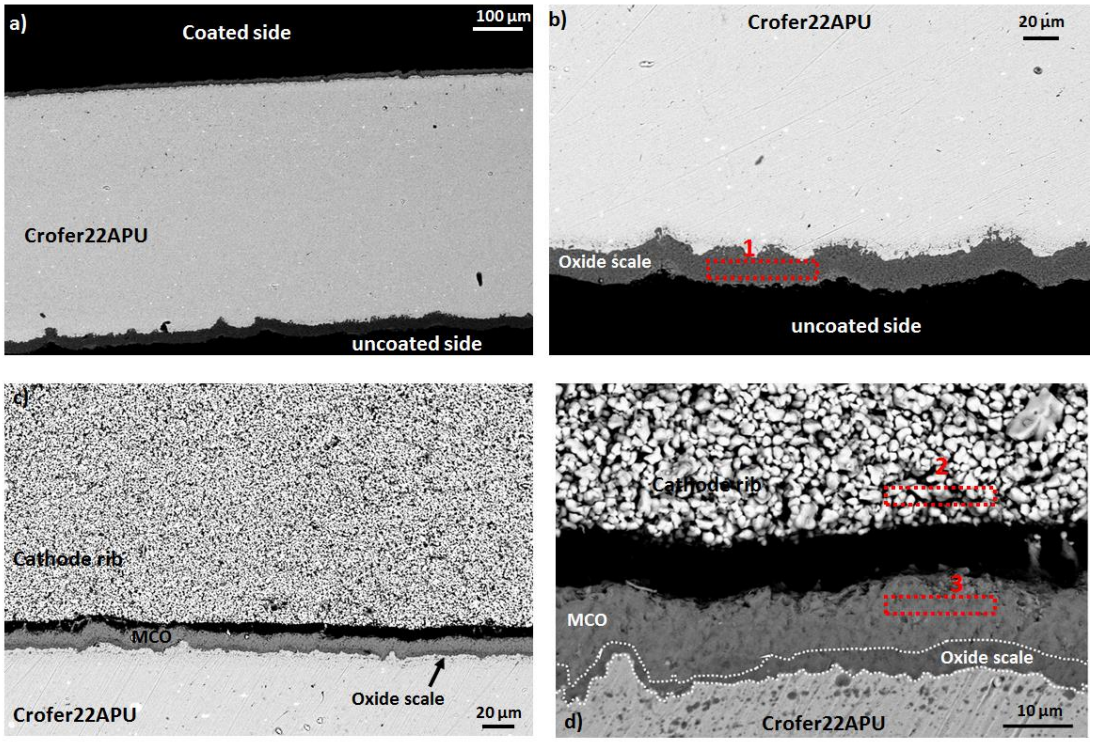

Figure 120. SEM post mortem image of MCO coated Crofer22APU after electrical resistivity test for 8600 hours at 850°C. Coating was sintered in two steps

Table 37. EDS analyses (at. %) carried out at different regions of Figure 120

Elements	Region 1	Region 2	Region 3
O	58	60.6	64.5
Cr	41.5	---	8.7
Mn	---	17	17.2
Co	---	2.1	8.6
Fe	0.5	0.6	1.0
La	---	16.2	---
Sr	---	3.5	----

Figure 121 shows the SEM post mortem images of the one-step sintered MCO coated Crofer22APU, after the long term ASR test. The coating seems very dense and uniform with a thickness of ~10 µm. No delamination was observed at the Crofer22APU/coating interface after the long-term ASR test. A Cr rich oxide scale is visible between the Crofer22APU and coating. The SEM analysis performed on the non-coated side (not shown here) of the Crofer22APU, showed the presence of ~20-25 µm thick Cr oxide scale. However, the oxide scale at coated side has thickness of ~5-7 µm, therefore confirmed that coatings successfully hindered the formation of Cr oxide scale. Nevertheless, the thickness of the oxide scale in case of two steps sintering (Figure 120) is less compared to

one-step sintered coating (Figure 121). This is due to the fact that two steps sintering treatment involved the first step sintering in reducing atmosphere. The sintering in reducing atmosphere not only improves the density of the coating, but also does not effectively promote the formation of oxide scale. In the second step, the already dense coating hinders the formation of oxide scale. However, on the other hand, the one-step sintering in air increase the possibility of oxide scale growth due to simultaneous densification of green coating.

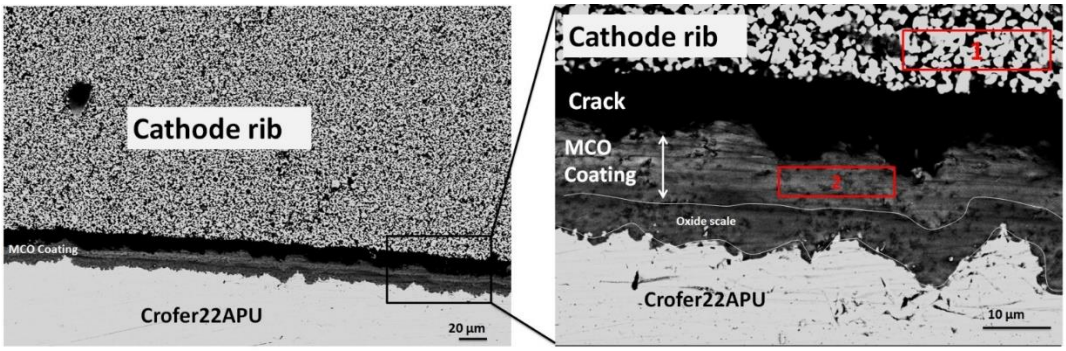

Figure 121. SEM post mortem image of MCO coated Crofer22APU after electrical resistivity test for 8600 hours at 850°C. The shown coating was sintered in one-step

The EDS analyses carried out on different regions of Figure 121 are given in Table 38. According to EDS analysis, the MCO coating hindered the Cr diffusion from the Crofer22APU substrate into the cathode rib. On the other hand, the EDS analysis performed on the MCO coating showed the presence of small concentrations of La due to its diffusion from cathode side towards the coating. Besides that, in the coating region the Mn concentration is more than twice as that of Co. This significant difference is due to possible diffusion of Mn from cathode side towards the coating.

Table 38. EDS analyses (at. %) carried out at different regions of Figure 121

Elements	Region 1	Region 2
O	43.2	63.2
Mn	25.6	19.9
Co	2.9	8.41
Cr	---	6.7
La	21.5	0.4
Sr	4.9	---
Fe	1.9	1.6

5.4 EPD deposition and characterization of Cu doped MCO coating

The EPD technique was used to co-deposit MCO and CuO particles on the Crofer22APU substrate. Formation of Cu-doped spinel by a co-deposition process using commercial powders can be considered a new and promising route for spinel modification. As earlier works show the CTE and electrical conductivity might be matched to a desired level by doping of the spinel by Cu and/or Fe, thus tailoring for specific alloy and possible operation temperature [1]–[5]. For this purpose, the MCO was doped with 5 wt% and 10 wt% CuO. The up-doped MCO coating were also deposited and investigated to have better comparison. The deposition parameters were kept same as that of pure MCO coating, and are described in chapter 3. The Cu doped MCO coating were also sintered at 900 °C in two steps i.e. first in reducing atmosphere and secondly in static air. The two steps sintering was carried out with the aim to form the metallic Co and Cu during the first step sintering in reducing atmosphere and consequently formation of Cu containing Mn-Co mixed spinel during the second step sintering in air. The formation of the metallic Co during sintering in reducing atmosphere and reformation of spinel in air has been studied by other researcher [6]–[9]. In addition to that, the two steps sintering also improves the densification of coating.

The SEM images of un-doped MCO and MCO coating doped with 5wt% and 10wt% of CuO, are shown in Figure 122. The un-doped and CuO doped MCO coatings are quite uniform and have thickness of almost 10 µm. By comparing the un-doped MCO coating (Figure 122 (a)) with the CuO doped MCO (Figure 122 (b) and (c)), it can be clearly seen that the Cu doping considerably improved the density of MCO coating.

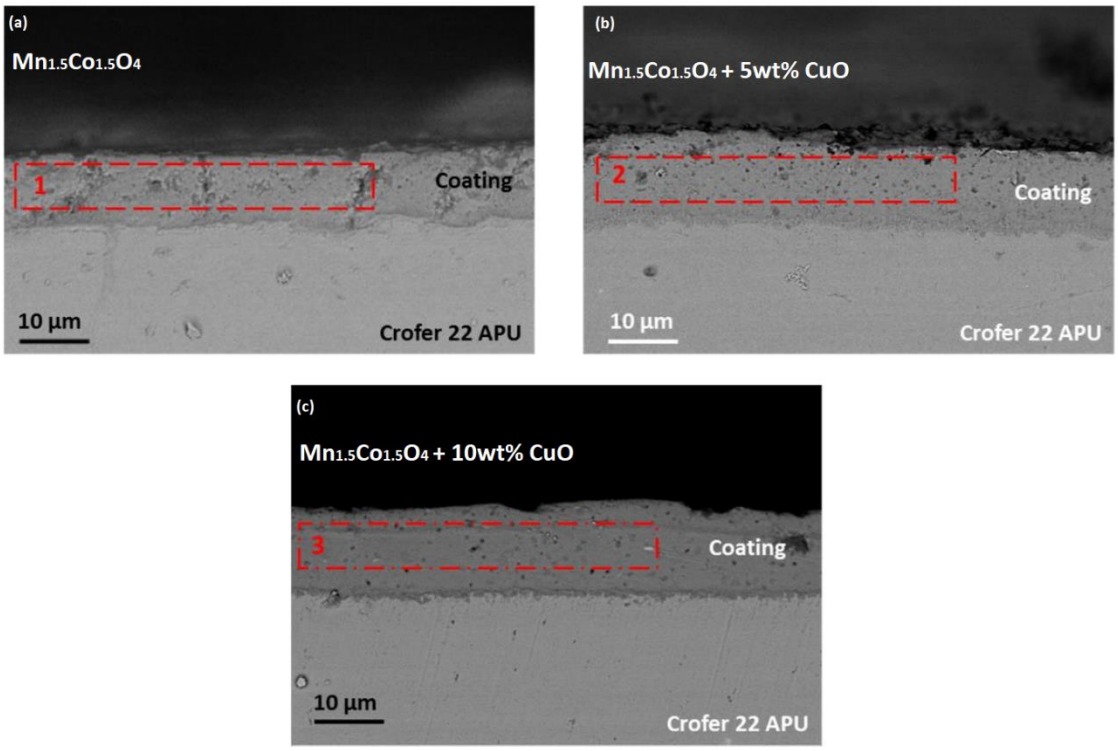

Figure 122. SEM images of EPD deposited and two steps sintered (a) MCO and MCO doped with (b) 5wt% (c) 10 wt% of CuO.

The EDS analyses were carried out on the EPD deposited un-doped and CuO doped MCO coatings (Figure 122). The corresponding EDS analyses are given in Table 39. From the EDS analyses, a negligible Cr concentration (below 0.5 at. %) were detected after the sintering.

Table 39. EDS analyses carried out at different regions of EPD coatings shown in Figure 122

	(a) MCO	(b) MCO+5 wt% CuO	(c) MCO+10wt% CuO
O	59.6	54.0	29.6
Cr	0.4	0.3	---
Mn	19.6	21.5	33.1
Co	20.4	22.0	32.6
Cu	---	2.1	4.7

EDS mapping carried out at Cu doped MCO coating is shown in Figure 123. The shown coatings contains 5 wt% (Figure 123 (a)) and 10 wt% of CuO (Figure 123(b)) and have been sintered in two steps. The EDS mapping shows that the Cu is distributed uniformly throughout the coatings without being precipitated, which indicates that the Cu form the solid solution with the Mn-Co spinel. Besides Cu, the Mn and Co is also homogenous within the entire coatings. On the other hand, the Cr seems to be mainly confined between the coatings and the Crofer22APU substrate. This is due to the formation of Cr oxide scale during the sintering

process. Nevertheless, the EDS mappings did not detect any Cr diffusion into the coatings region.

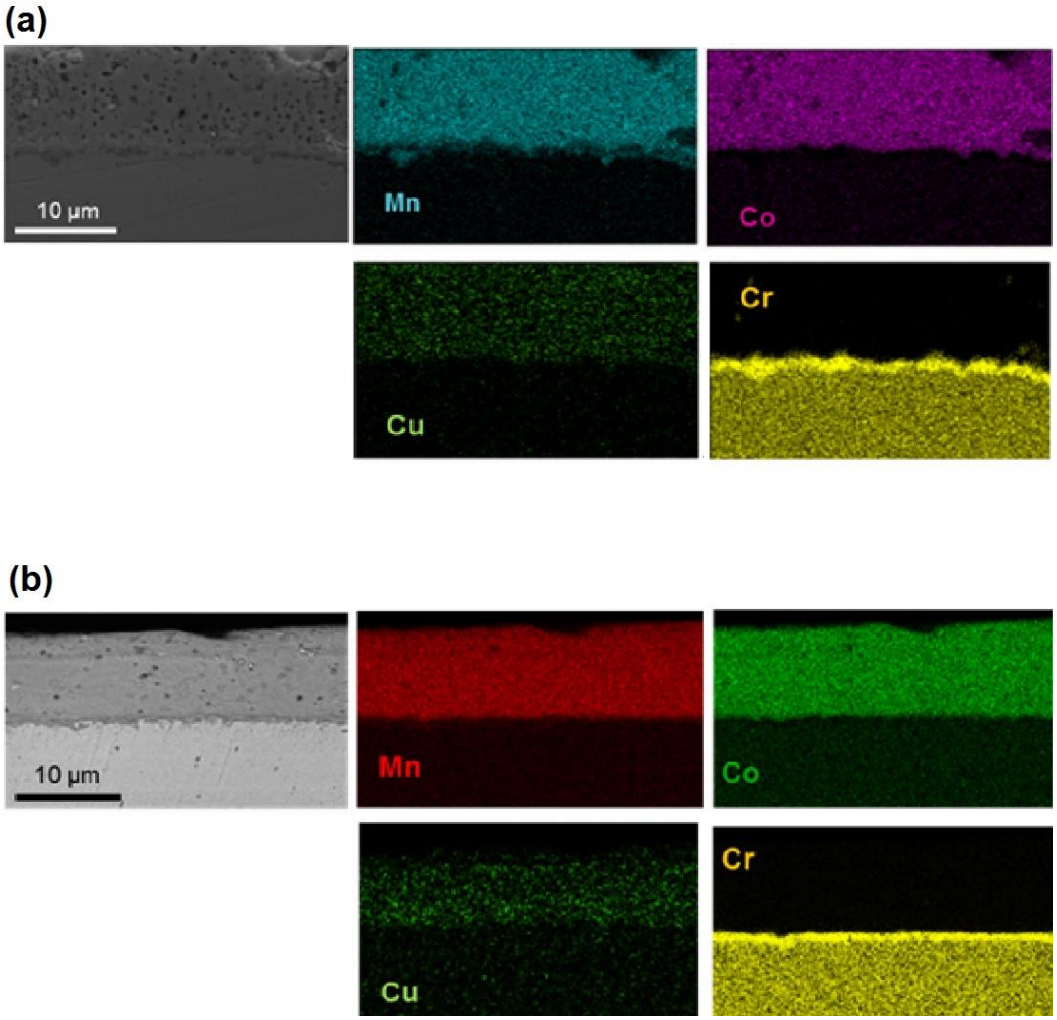

Figure 123. EDS carried out at Crofer22APU/ MCO coatings doped with (a) 5 wt% CuO and (b) 10 wt % CuO. The shown coatings are EPD deposited and sintered in two steps

Figure 124 shows the SEM images of the un-doped and CuO doped MCO coatings, after sintering in reducing (Figure 124 (A,B,C)) and subsequently in the oxidizing conditions (Figure 124 (D,E,F)). From the SEM images, the coatings sintered only in reducing atmosphere showed the presence of individual Co and Cu particles. These particles are bright in color and are uniformly distributed throughout the coatings without any agglomerates. However, after the re-oxidization (Figure 124 (D,E,F)) step, no individual Co or Cu particles were observed. This indicates that the sintering in reducing atmosphere leads to the reduction of CuO into metallic Cu, and decomposition of MCO spinel into the metallic Co and MnO. On the other hand, the second step sintering in oxidizing atmosphere results in the reformation of Mn-Co-Cu based mixed spinel. These results are in agreement with the EDS mapping results shown above (Figure 123) where Cu was found to be uniformly distributed after the two steps sintering.

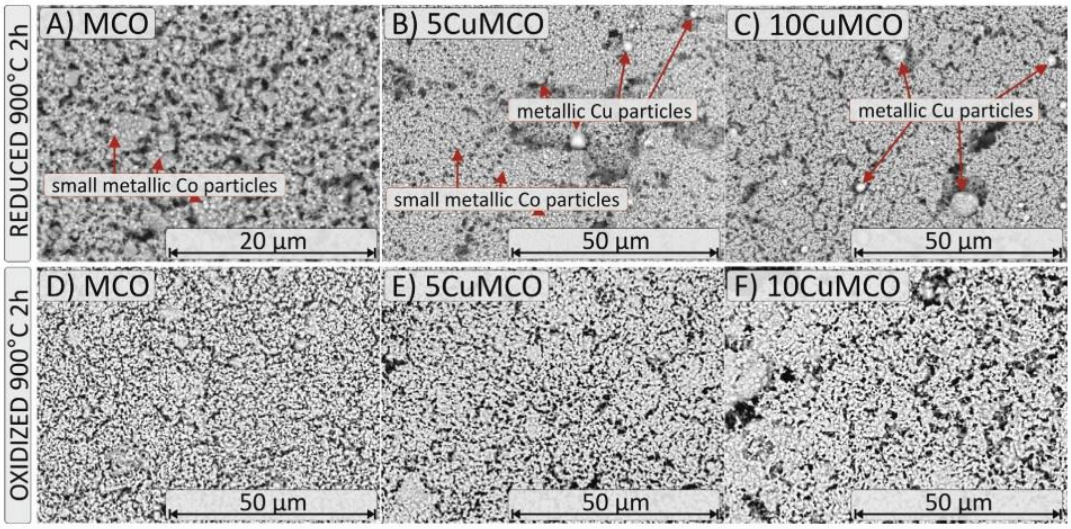

Figure 124. SEM surface images of reduced (top row) and re-oxidized (bottom row) coatings A, D) MCO, B, E) 5CuMCO and C, F) 10CuMCO and re-oxidized coatings

The XRD analyses were also carried out on un-doped and CuO doped coatings after sintered in reducing and oxidizing conditions. The corresponding XRD patterns are shown in figure. After sintering in reducing atmosphere, the presence of metallic Cu and Co was detected by the XRD. As discussed before, the heat treatment in the reducing condition can lead to the reduction of CuO into the metallic Cu in addition to decomposition of MCO into the MnO and metallic Co. However, after the heat treatment in static air, the XRD analyses does not detect metallic Co or Cu anymore. The absence of Co and Cu peaks after re-oxidization is due to the formation of Mn-Co-Cu based mixed spinel. These XRD results are in agreement with the EDS results shown in figure, thus confirm that in cased of CuO doped MCO, the two steps sintering resulted in incorporation of Cu into the MCO spinel. The Pt-peaks in the XRD analyses are due to the sample holder.

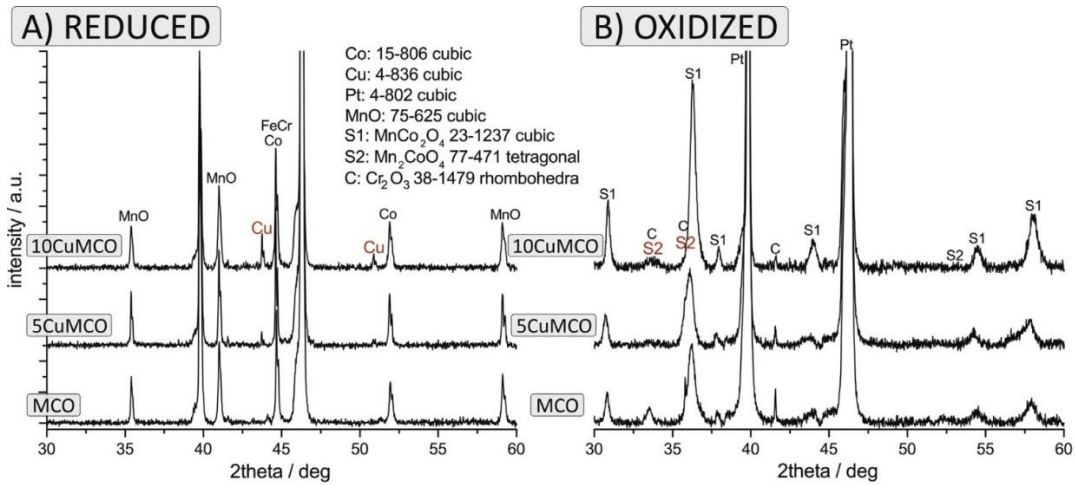

Figure 125. XRD patterns of the coated alloys. Spectra of (A) reduced coatings, and (B) after re-oxidation

The area specific resistance (ASR) of MCO coatings (un-doped, 5 wt% and 10 wt% doped with CuO) deposited on the Crofer22APU, was measured up to 2000 hours at 800 °C in the static air and under the applied current density of 500 mA x cm^{-2}. For comparison, the ASR data of the un-coated Crofer22APU was also recorded.

The Figure 126 shows the ASR data for the coated and un-coated Crofer22APU substrates as measured up to 2000 hours. For all the samples, the ASR values show a reduction up to almost 150 hours. This reduction is possibly due to the sintering of applied LSM paste or due to the formation of interface between the LSM paste and the sample. After the initial reduction, the ASR values started to increase gradually. For the uncoated Crofer22APU, the increase in the ASR values was most significant. Among the coated Crofer22APU, the CuO doped MCO coatings showed low ASR as compared with un-doped MCO coating. These results suggest that the doping of CuO into the MCO is beneficial in order to improve its electrical conductivity. The Figure 126 also shows the degradation rate for coated and uncoated samples. The degradation rate for the uncoated Crofer22APU (3.62 mΩ.cm^2/kh) is almost three times higher than coated Crofer22APU (1.35 mΩ.cm^2/kh).

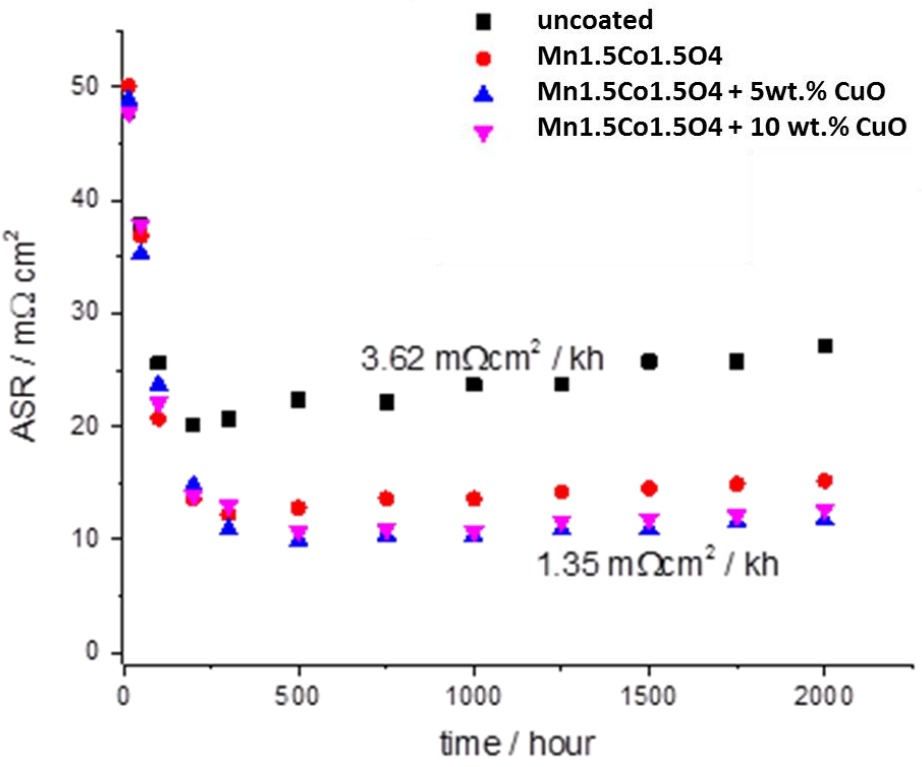

Figure 126. Long-term ASR analysis of the bare and coating Crofer22APU. The Crofer22APU was coated with pure MCO, and MCO doped with 5wt% and 10 wt% of CuO

The high temperature corrosion properties of the CuO doped MCO spinel were analyzed for 2000 hours at 800 °C and compared with the un-doped spinel by weight gain (corrosion kinetics). The corresponding weight gain data is shown in Figure 127. For the better comparison, the Figure 127 also shows the weight gain for the uncoated steel. The doping of CuO does not deteriorate the corrosion protection capability of the MCO spinel. However, as compared with the uncoated steel, these protective coatings improve the corrosion behavior by the factor of almost 10.

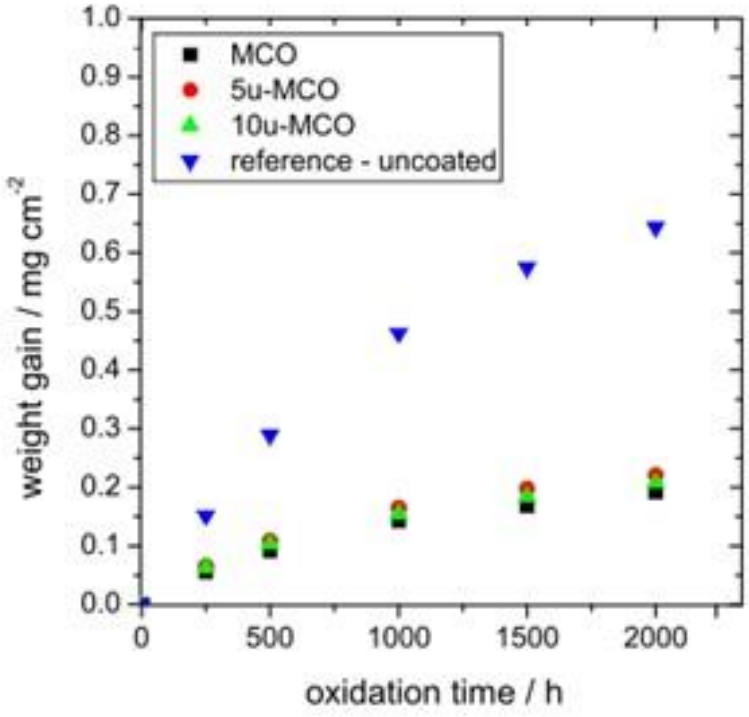

Figure 127. Comparison of thermo-gravimetric measurements of the coated samples

5.5 Flash sintering of un-doped MCO and MCO doped with CuO and Fe_2O_3

Flash sintering is a fascinating technique for achieving high dense ceramics in few min or even in seconds by applying pressure/electrical field [10]. Gaur et al. [11] studied the flash sintering behavior of $MnCo_2O_4$ spinel in terms of microstructure and phase analysis. Previously, the flash sintering was carried out on MCO spinel in powder form [11], [12], however, according to author best knowledge no studies have been carried out related to flash sintering of MCO spinel based coatings. The novelty of our research is to observe the flash sintering of EPD deposited MCO based spinel coatings in terms of coating density, oxide scale growth and microstructure.

The application of flash sintering was used to sinter the EPD deposited un-doped MCO and MCO doped with CuO and Fe_2O_3. For doping,10 wt% of the deponents (CuO and Fe_2O_3) were co-deposited with MCO by the EPD process. The coatings involving the flash sintering, were sintered in three different ways termed as S1, S2 and S3. The S1 treatment was one-step sintering i.e. by flash sintering, the S2 involved two steps sintering i.e. 1^{st} step in reducing atmosphere and 2^{nd} by flash sintering, while the S3 was a three steps sintering process i.e. 1^{st} step in reducing atmosphere, 2^{nd} by flash sintering and 3^{rd} step sintering in static air. Further details about these three heat treatments and their parameters have been already discussed in chapter 3.

Figure 128 shows the EPD deposited MCO coatings, sintered in the different ways as described above. It can be clearly seen from the Figure 128, that for all three types of sintering treatments, the coatings are very dense. Despite of fast heating and cooling rates (200 °C/min) during the flash sintering, no crack or delamination between the Crofer22APU substrate the MCO coatings was observed. The MCO coatings sintered in three different ways are strongly bonded with the Crofer22APU substrates.

The magnified SEM images of the MCO coatings (Figure 128) shows that the three different routes resulted in different morphologies of MCO coatings. As a result of one-step sintering (S1-flash sintering in vacuum), the coating microstructure is quite uniform, however, different phases are apparent in the coating. When the MCO coating sintered in two steps (1^{st} in reducing atmosphere and 2^{nd} step by flash sintering), the different phases are more clearly visible and distinguishable. The corresponding EDS point analyses performed on different phases are given in Table 40. The EDS point analyses show that the bright phase (point 1) is metallic Co while the dark phase (point 2) is MnO. The decomposition of MCO into MnO and metallic Co was according to expectation after the sintering in the reducing atmosphere. Similar behavior has been reported by many research groups, where the MnCo based spinel decompose while sintering in reducing conditions [6]–[9]. Although during the one-step sintering (S1-flash sintering), the treatment was performed in reducing conditions (vacuum), however, due to high heating/cooling rates (200 °C/min) and no dwell time at maximum temperature, the flash sintering (S1 treatment) did not cause complete decomposition of MCO spinel. On the other hand, in case of two steps sintering, the relatively slow heating/cooling rates (10 °C/min) and dwell of 2 hours during reducing step, mainly cause the reduction of MCO into metallic Co and MnO.

After the re-oxidation step in S3 treatment, the morphology of the MCO is very uniform and homogenous without any Mn or Co rich zones. This indicates that re-oxidation step resulted in the formation of MnCo spinel.

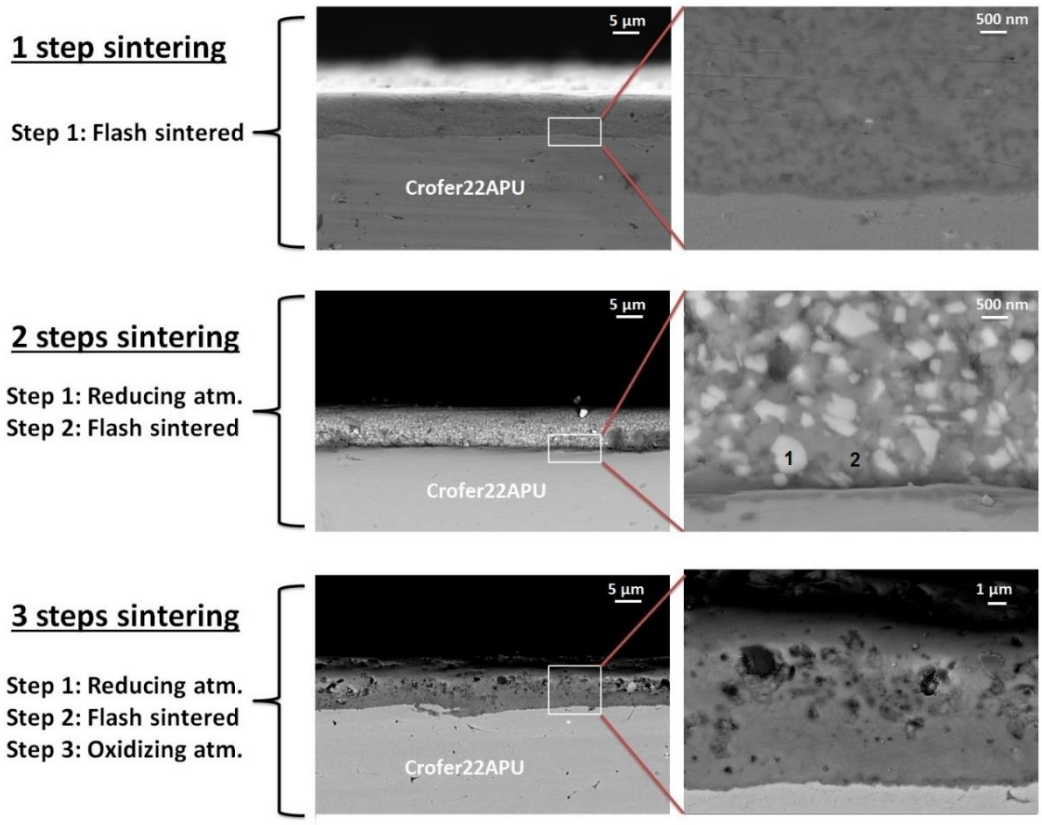

Figure 128. EPD deposited MCO coating on the Crofer22APU substrates. Sintering was performed according to three different treatments

Table 40. EDS point analyses (at. %) carried out in different regions of Figure 128

	O	Mn	Co
Point 1	19.3	9.2	71.6
Point 2	52.5	36.6	10.9

Figure 129 shows the EDS mapping carried out at Crofer22APU/MCO coating sintered by three different heat treatments i.e. S1, S2 and S3. From the one-step (S1) and two steps (S2) sintering treatments, no evidence was found either about the diffusion of elements across the interface or segregation of any element at interface. From the EDS mapping of two steps sintered (S2) coating, Co rich zones can been seen due to formation of metallic Co as a results of MCO decomposition as discussed above. After the three steps sintering, no Co rich zones are visible, thus indicating the re-formation of MnCo spinel. Besides that, in contract to S1 and S2 treatments, a Cr rich scale was formed after S3 (three steps) treatment, as clearly visible from the corresponding EDS mapping (Figure 129).

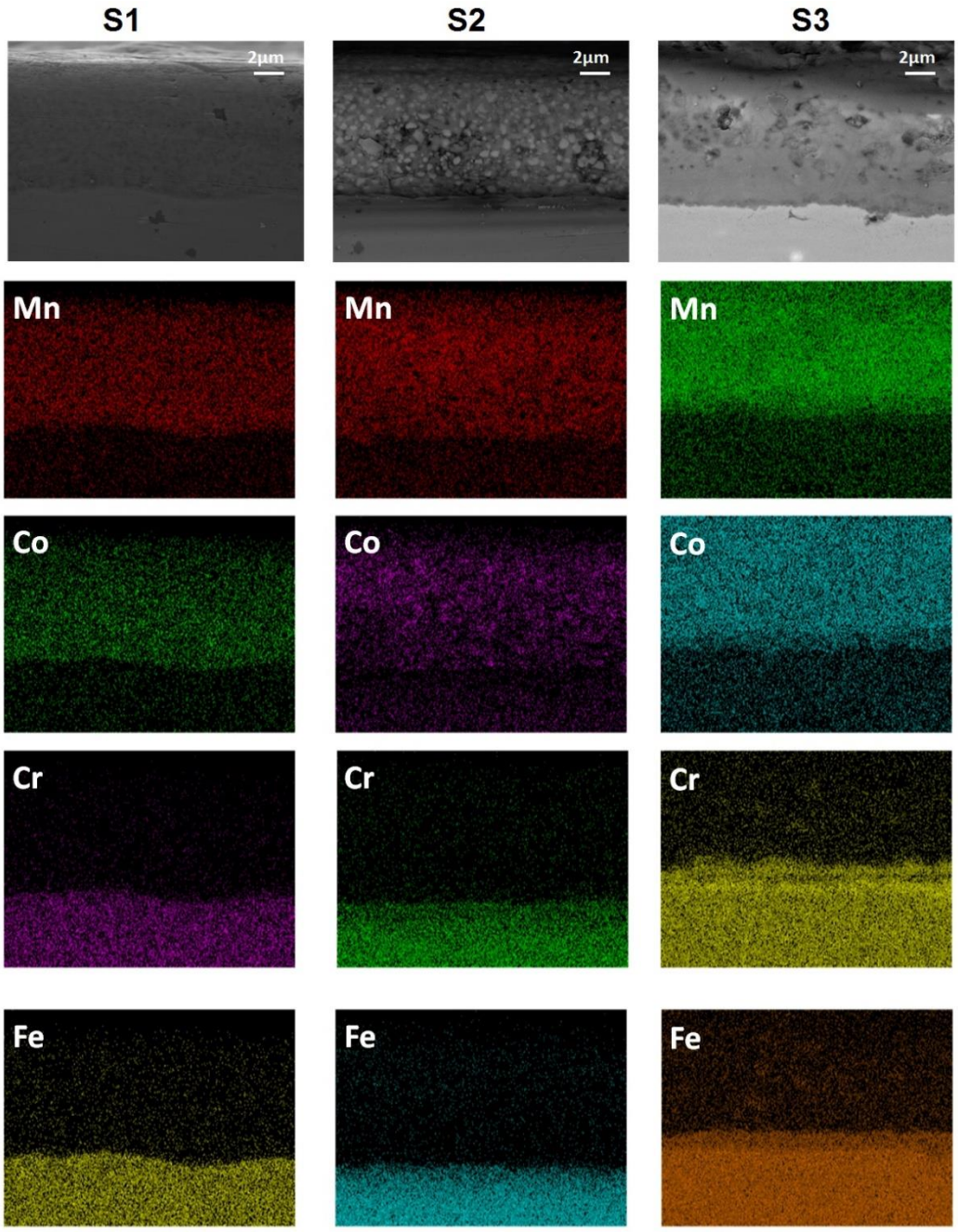

Figure 129. EDS mapping carried out at MCO coated Crofer22APU substrates. The MCO coatings were sintered according to three different treatments

Figure 130 shows the SEM images of the CuO doped MCO spinel coatings sintered by three different routes. The coatings are quite dense and have uniform thickness of ~10-15 µm. Different sintering treatments resulted in different microstructural morphologies of coatings. The one-step sintering (flash sintering) of CuO doped MCO coating contains randomly dispersed Cu particles. Beside Cu particles, the morphology of single step sintered coating is similar to the un-doped MCO coating sintered by similar treatment (Figure 128).

The SEM image of the CuO doped MCO coating after two steps sintering treatment (S2), show the presence of different distinguishable phases. Similar to

un-doped MCO coating, sintered according to the S2 treatment, the CuO doped MCO coating also contains metallic cobalt and MnO, formed due to decomposition of MCO, in addition to the Cu particle of the dopant.

The three steps sintering route (S3), that involves additional re-oxidation step after the S2 route, resulted in homogenous coating without presence of residual Cu or Co particle. The re-oxidation caused the formation of MnCoCu mixed spinel. The formation of MnCoCu mixed spinel after the re-oxidation has already been observed and discussed in the section 5.4 for the CuO doped MCO coatings.

The corresponding EDS mapping of the CuO doped MCO coatings sintered by three different ways are shown in Figure 131. In case of one-step and two steps sintering routes, the presence of Cu particles is clearly visible. Besides Cu, the Co rich zones are also present especially after two steps sintering (S2). However, in case of three steps sintering (S3) in air, and Cu became the part of Mn-Co spinel and therefore, Cu was found to be distributed uniformly in the overall coating. These EDS analyses further confirmed the formation of MnCoCu based mixed spinel as discussed above. The EDS mapping also shows the presence of Cr rich scale at Crofer22APU interconnect surface as a result of S3 sintering treatment. Besides Cr, no segregation or diffusion of elements across the Crofer22APU/coatings interface was detected.

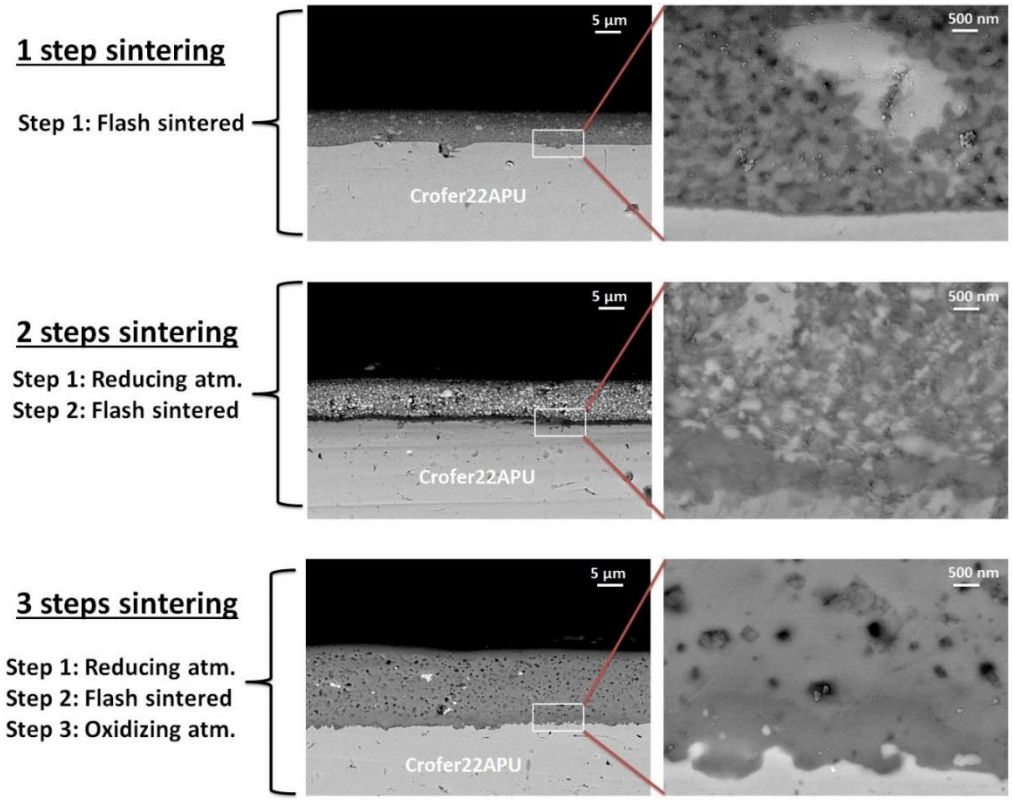

Figure 130. SEM images of Cu doped MCO coated Crofer22APU substrates. The CuO doped MCO coatings were sintered according to three different treatments

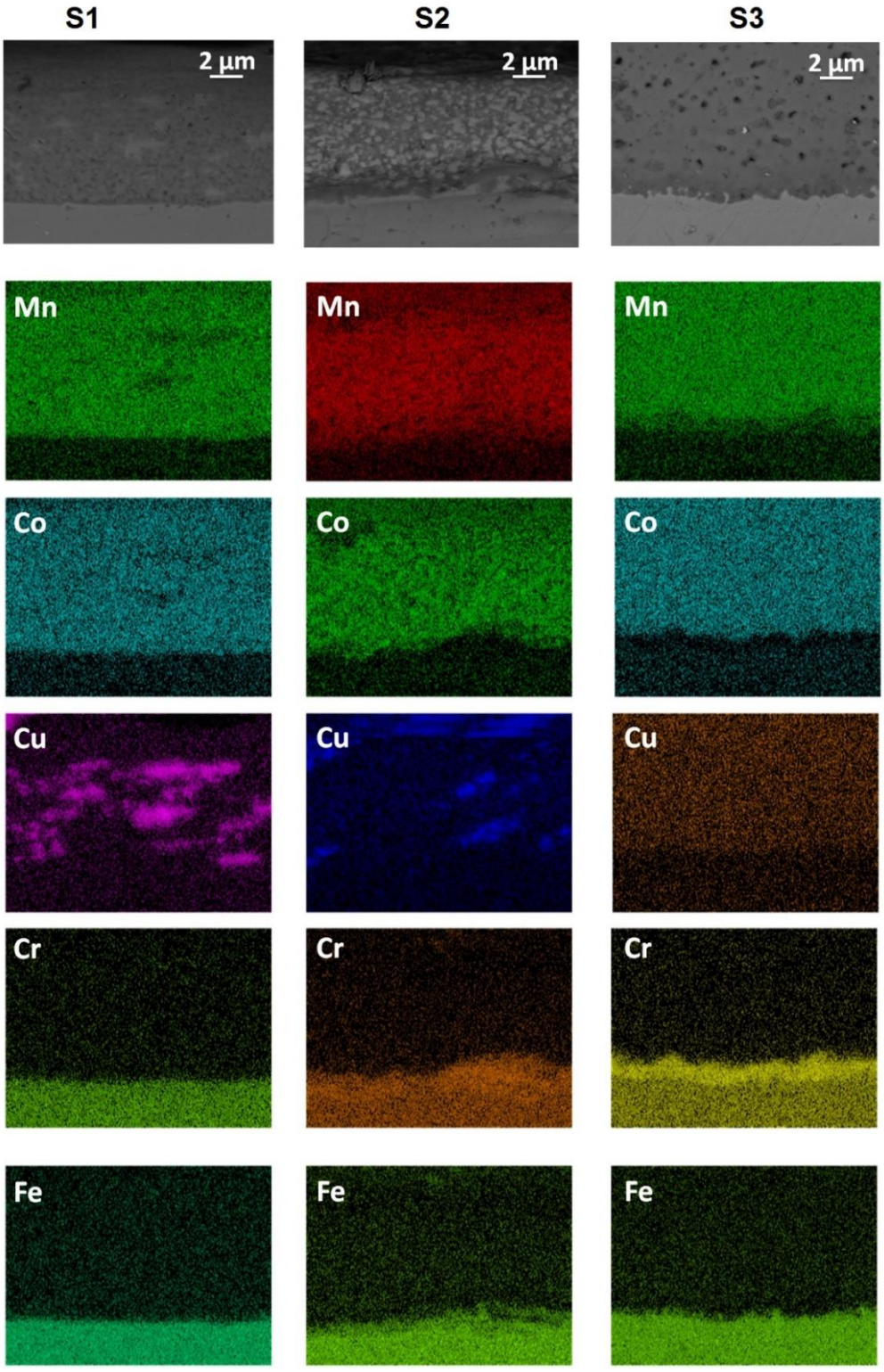

Figure 131. EDS mapping carried out at Cu doped MCO coated Crofer22APU substrates. The MCO coatings were sintered according to three different treatments

The XRD phase analyses were carried out on the Cu doped MCO coatings sintered by different heat treatments i.e. S1, S2 and S3. For this purpose, the sintered coated Crofer22APU samples were sonicated for 5 min in order to remove the boron nitride (BN) layer from the top. As discussed in chapter 3

(experimental) that a BN layer was deposited in order to avoid the direct contact of EPD deposited coatings with the mold during flash sintering. The corresponding XRD patterns are given in Figure 132.

The Figure 132 (a) shows the XRD analysis of Cu doped MCO coating after one step sintering conducted by flash sintering. According to XRD patterns, the flash sintering resulted in the formation of $(Co,Mn)_2O_4$ phase in addition to Cu_2O. The presence of reducing atmosphere caused the reduction of CuO to Cu_2O. In addition to these phases, the peaks of boron nitride (BN) were also found. The presence of BN peaks was due to the fact that sonication time was not sufficient to completely remove the BN layer from the top of Cu doped MCO coating.

The two steps sintering (first in reducing atmosphere followed by flash sintering) results in the decomposition of MCO spinel into MnO and metallic Co. The decomposition of MCO into MnO and Co after sintering in reducing atmosphere is according to expectation and has been observed before Figure 125. Furthermore, the two steps sintering also resulted in the complete reduction to CuO in to metallic Cu. The corresponding XRD analysis of Cu doped MCO coating after two steps sintering is shown in Figure 132 (b).

Figure 132 (c) shows the XRD pattern of the Cu doped MCO after three steps sintering i.e. in reducing atmosphere followed by the flash sintering and in air respectively. The third steps sintering in air resulted to reformation of MCO based spinel in addition to $CuMn_2O_4$. No peaks of metallic Cu or Co were detected after sintering in oxidation conditions. These XRD analyses are in accordance with the SEM-EDS results shown in Figure 131.

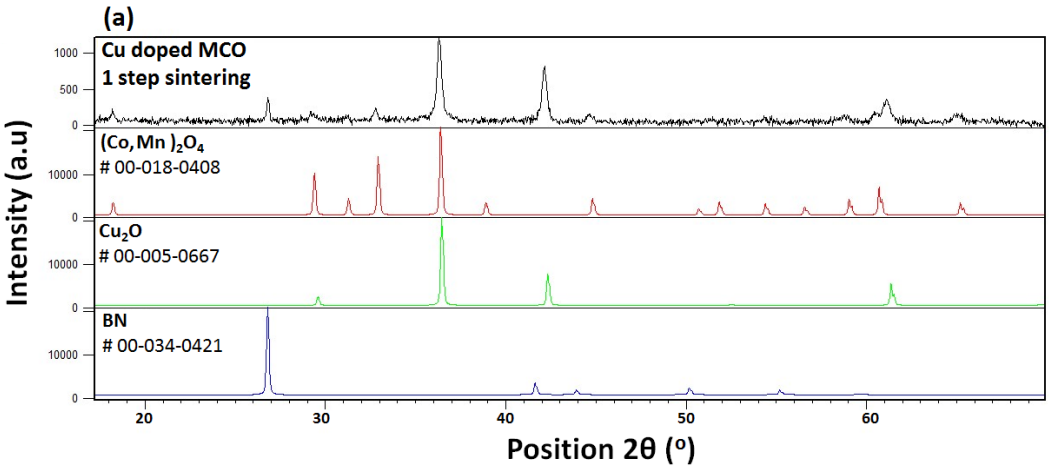

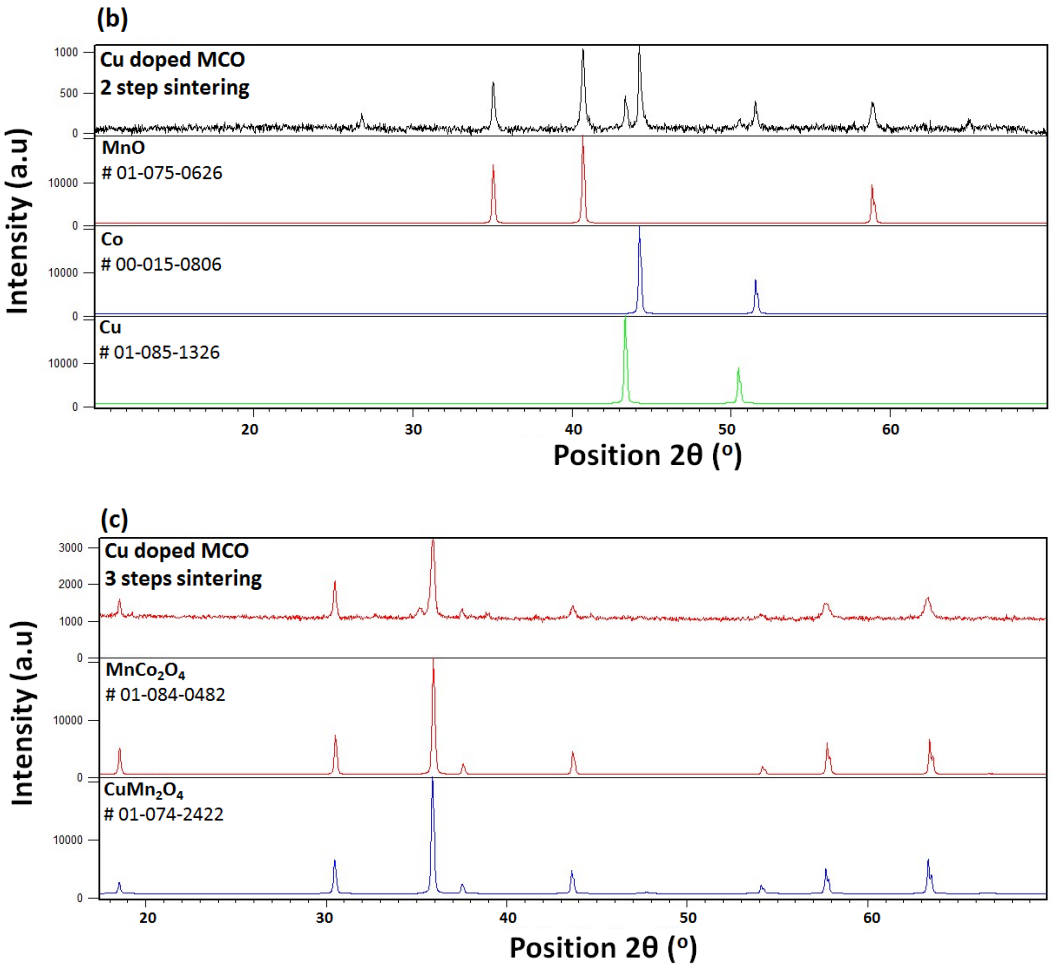

Figure 132. XRD patterns of Cu doped MCO after (a) one step-S1 (b) 2 steps- S2 and (c) 3 steps-S3 sintering

The SEM images of 10 wt% Fe_2O_3 doped MCO coatings, sintered by three different heat treatments are shown in Figure 133. In contrast to Cu doped MCO, no particles of the Fe were found after sintering carried out either by one-step (S1) or by two steps (S2). The corresponding EDS mapping shows that the Fe is uniformly distributes in the whole coating area after S1, S2 and S3 sintering treatments. However, after the S2 treatment, the bright metallic Co is clearly visible similar to what observed in un-doped MCO (Figure 129) and Cu doped MCO (Figure 131). The absence of Fe residual indicates that Fe forms some intermediate compound with either MnO or Co. Moreover, the Cr rich oxide scale is clearly visible from the EDS mapping of Fe doped MCO coating sintered by the S3 treatment. However, the S1 and S2 treatments do not form Cr oxide scale on the Crofer22APU surface. Besides that, no diffusion of elements was detected across the Crofer22APU/coating after three sintering treatments.

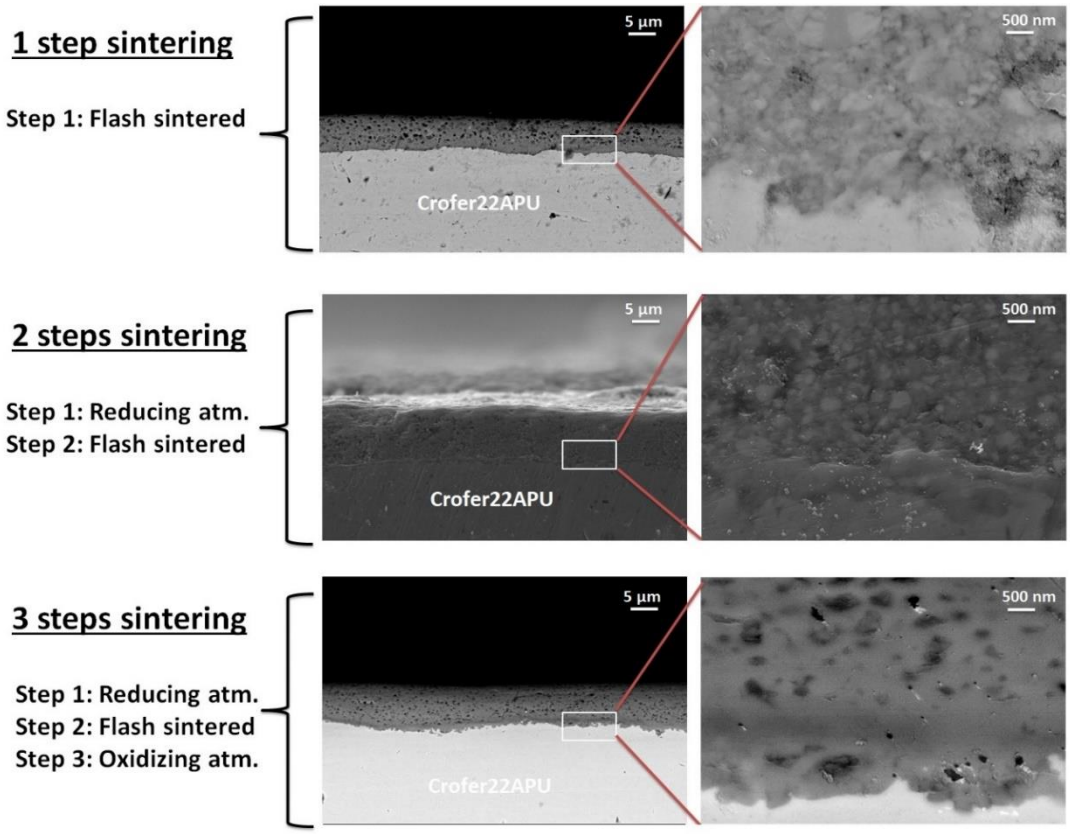

Figure 133. SEM images of Fe doped MCO coated Crofer22APU substrates. The Fe_2O_3 doped MCO coatings were sintered according to three different treatments

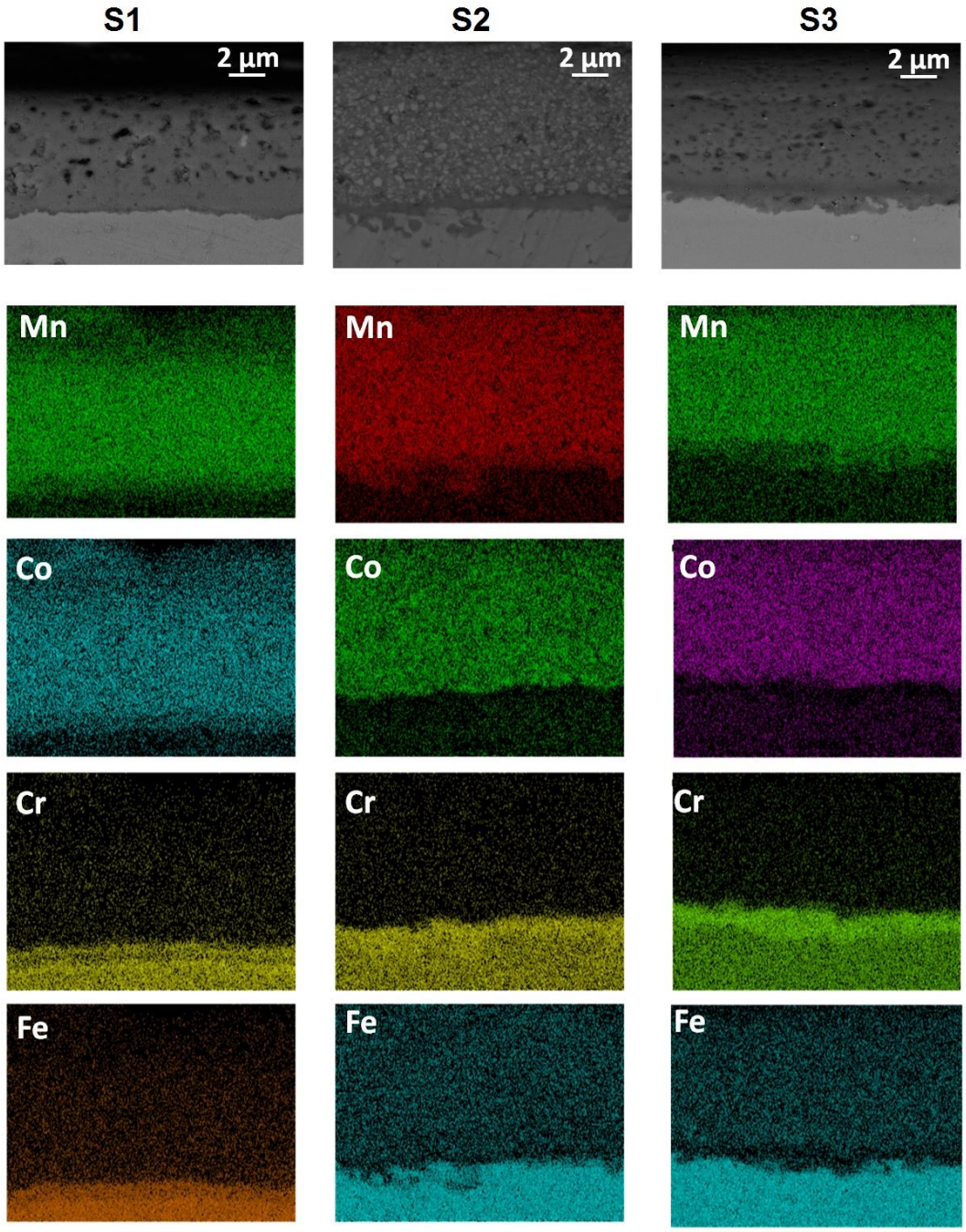

Figure 134. EDS mapping of Fe doped MCO coated Crofer22APU substrates. The Fe_2O_3 doped MCO coatings were sintered according to three different treatments

Summary

MnCo spinel based coatings were deposited by electrophoretic deposition (EPD) on Crofer22APU 1.5x1.5 cm samples. The suspensions and deposition parameters were optimized in order to obtain thick (10 µm) and uniform coatings. Subsequently the EPD experimental apparatus was up-scaled for coatings deposition on the real dimensions (16x18cm) Crofer22APU plates and real bipolar plates were successfully coated. The area specific resistance (ASR) of the MnCo coating was measured for 8.6k hours at 850 °C. The effect of two different sintering treatments was observed on the resultant ASR values of MnCo coating.

The ASR results indicate that as compared with one-step sintering (in air), the two steps sintering (1st in reducing atmosphere and 2nd in air) in beneficial to obtain low ASR values. The ASR values of two steps sintered MCO coating are in the range of 15-27 mΩ.cm^2 while that of single step sintered are in the range of 50-95 mΩ.cm^2, as measured up to 5000 hours. In addition to pure MCO, the Cu doped MCO coatings were also deposited by EPD process. The 5-10 wt% doping of CuO was found to improve the sintering ability and electrical properties of the MCO spinel. A two-steps sintering was found to be a viable method to obtain a Mn-Co-Cu mixed spinel.

Besides conventional pressure-less sintering, the flash sintering process was employed for rapid sintering. Flash sintering of un-doped MCO as well as Cu and Fe doped MCO coatings was carried out. Flash sintering was found to be a promising sintering method that involved less sintering time and results in higher level of densification with respect to conventional sintering. The effect of Cu doping to enhance the densification was also observed in flash sintering. The enhanced densification of Cu doped MCO coating was due to formation of metallic Cu during sintering in reducing atmosphere and formation of MnCo-Cu mixed spinel during re-oxidation. However, the Fe doped MCO coating sintered by flash sintering contain small porosity. Moreover, the presence of reducing atmosphere during flash sintering does not promoted the formation of any oxide scale at Crofer22APU substrate.

Besides the possibility of achieving high coating density, currently the flash sintering technique is not suitable for mass production. Due to geometrical constrains, it is not feasible to flash sinter the large size samples. Nevertheless, in future the issues related to geometrical constrains can be solve and it can be used in SOEC technology; where the coated interconnects can be sintered by flash sintering followed by sintering during stack consolidation. It would result in time saving and will limit sintering treatments.

References

[1] B. Talic, S. Molin, K. Wiik, P. V. Hendriksen, and H. L. Lein, "Comparison of iron and copper doped manganese cobalt spinel oxides as protective coatings for solid oxide fuel cell interconnects," *Journal of Power Sources*, vol. 372, no. August, pp. 145–156, 2017.

[2] A. Masi, M. Bellusci, S. J. Mcphail, F. Padella, P. Reale, J. Hong, R. Steinberger-wilckens, and M. Carlini, "Cu-Mn-Co oxides as protective materials in SOFC technology: The effect of chemical composition on mechanochemical synthesis, sintering behaviour, thermal expansion and electrical conductivity," *Journal of the European Ceramic Society*, 2016.

[3] A. Petric and H. Ling, "Electrical conductivity and thermal expansion of spinels at elevated temperatures," *Journal of the American Ceramic Society*, vol. 90, no. 5, pp. 1515–1520, 2007.

[4] B. Talic, P. V. Hendriksen, K. Wiik, and H. L. Lein, "Thermal expansion

and electrical conductivity of Fe and Cu doped MnCo2O4spinel," *Solid State Ionics*, vol. 326, no. July, pp. 90–99, 2018.

[5] A. Masi, M. Bellusci, J. Stephen, F. Padella, P. Reale, R. Steinberger-wilckens, A. Masi, M. Bellusci, S. J. Mcphail, F. Padella, P. Reale, J. Hong, and R. Steinberger-wilckens, "The Effect of Chemical Composition on High Temperature Behaviour of Fe and Cu Doped Mn-Co spinels," *Ceramics International*, vol. 43, no. 2, pp. 2829–2835, 2016.

[6] D. Szymczewska, S. Molin, V. Venkatachalam, M. Chen, P. Jasinski, and P. V. Hendriksen, "Assesment of (Mn,Co)33O4 powders for possible coating material for SOFC/SOEC interconnects," *IOP Conference Series: Materials Science and Engineering*, vol. 104, no. 1, 2016.

[7] M. Bobruk, S. Molin, M. Chen, T. Brylewski, and P. V. Hendriksen, "Sintering of MnCo2O4coatings prepared by electrophoretic deposition," *Materials Letters*, vol. 213, pp. 394–398, 2018.

[8] S. Molin, P. Jasinski, L. Mikkelsen, W. Zhang, M. Chen, and P. V. Hendriksen, "Low temperature processed MnCo2O4and MnCo1.8Fe0.2O4as effective protective coatings for solid oxide fuel cell interconnects at 750 °C," *Journal of Power Sources*, vol. 336, pp. 408–418, 2016.

[9] S. Molin, A. G. Sabato, H. Javed, G. Cempura, A. R. Boccaccini, and F. Smeacetto, "Co-deposition of CuO and Mn1.5Co1.5O4powders on Crofer22APU by electrophoretic method: Structural, compositional modifications and corrosion properties," *Materials Letters*, vol. 218, pp. 329–333, 2018.

[10] R. Raj, "Joule heating during flash-sintering," *Journal of the European Ceramic Society*, vol. 32, no. 10, pp. 2293–2301, 2012.

[11] A. Gaur and V. M. Sglavo, "Flash-sintering of MnCo 2 O 4 and its relation to phase stability," *Journal of the European Ceramic Society*, vol. 34, no. 10, pp. 2391–2400, 2014.

[12] A. L. G. Prette, M. Cologna, V. Sglavo, and R. Raj, "Flash-sintering of Co2MnO4 spinel for solid oxide fuel cell applications," *Journal of Power Sources*, vol. 196, no. 4, pp. 2061–2065, 2011.

Chapter 6

Conclusions and Future Perspectives

This PhD research was focused on the design and synthesis of glass-ceramics sealants and deposition of ceramic coatings on the metallic interconnect for the solid oxide electrolysis cell (SOEC) applications. The glass-ceramics were mainly divided into three series either on the basis of used modifiers or their relative concentration. The first two series of glasses contained SrO as main modifier while third series was focused on BaO-containing glass-ceramics. The rationale behind design novel glass compositions, their properties after joining and long term testing in SOEC working conditions were reviewed and discussed in this thesis. In addition to glass-ceramic sealants, the results related to the MnCo spinel based protective coating were also presented and discussed. The obtained results can be summarized as follows:

6.1 Glass-ceramics

Among the SrO containing glasses, the HJ14 glass-ceramic, coupled with the Crofer22APU showed an optimal electrical resistivity during 1000h of test @ 850°C in dual atmosphere and under the application of 1.6 V. Despite a slight decrease in resistivity observed during the test, the electrical resistivity values were always in the range 10^5-10^6 Ω cm, which are acceptable in a SOEC stack and considerably higher than the limit to avoid current shunting. HJ14 composition showed a very good glass-ceramic stability and an excellent compatibility with the Crofer22APU, both at the positive and negative polarised interfaces. No Cr diffusion phenomena occurred and no strontium chromate formation was detected neither at the three phase boundary nor at the interface.

Further research should be undertaken to investigate the possibility of increasing the amount of residual glassy phase in the HJ14 composition.

Considering BaO containing compositions, two compositions, labelled as HJ11 and HJ28 demonstrated very interesting properties in terms of electrical resistivity and capability to avoid the formation of barium chromate.

In particular, the HJ11glass-ceramic joined samples did not show any critical porosity or cracks induced by the aging test and no evidence of Ba-chromate formation was found; slight amounts of celsian ($BaAl_2Si_2O_8$) in addition to the sanbornite ($BaSi_2O_5$) were detected, determining a slight decrease of the overall CTE. On the other hand, the HJ28 system demonstrated an excellent stability concerning the electrical resistivity values (10^6 Ω cm) as tested in dual atmosphere for 2000 hours and under the applied thermal cycles. However, the HJ28 glass-ceramic showed the formation of slight amounts of celsian ($BaAl_2Si_2O_8$) and cristobalite phases in addition to parent sanbornite ($BaSi_2O_5$) phase after 2000 hours of test at 850°C.

Concerning BaO containing systems, further studies, which take these variables into account, will need to be undertaken, in order to minimize the presence of celsian and cristobalite while maintaining proper balance between the silica and barium oxide content.

In spite of an extensive amount of research, it is still not possible to define the universal or optimal sealing solution, since it depends on the SOEC working temperature and stack design. Furthermore, specific investigations are necessary to understand the possible poisoning effect from silica-based sealants on fuel electrode-electrolyte interface, for example. These research findings provide important insights for future sealing development, their characterization and validation in relevant conditions. In particular, different mechanical characterization (such as torsion tests) approaches will be very useful in the view of characterizing and improving the mechanical strength of glass-ceramic sealants as well to properly balance the crystalline/amorphous phase ratio, in order to limit possible sealant's failure at high temperatures, due to viscous flow of residual glassy phase.

6.2 Protective coatings

The MCO based protective coating deposited by electrophoretic deposition (EPD) resulted in uniform and homogenous coating having the thickness of~ 10-15 μm. The EPD process was scaled up to coat the real dimensioned (16 x 18 cm) Crofer22APU plates for industrial application. The effect of different sintering routes was examined on the area specific resistance (ASR) of MCO coating, as measured for 8600 hours at 850 ºC. According to ASR analyses, the two-steps sintering (first in reducing atmosphere followed by in air) of MCO coating resulted in low ASR and

degradation rate as compared with the MCO coating sintered by one-step i.e. in air. The ASR values of two steps sintered MCO coating are in the range of 15-27 $m\Omega.cm^2$ while that of single step sintered are in the range of 50-95 $m\Omega.cm^2$, as measured up to 5000 hours The ASR post mortem analyses also confirmed that the presence of protective coatings significantly reduced the growth of Cr-oxide scale on the Crofer22APU surface. Besides that, a strong bonding of MCO coating with the Crofer22APU substrate was examined by SEM-EDS post mortem analyses.

In addition to pure MCO, the CuO doped MCO coatings were also co-deposited by EPD technique. For this purpose, the MCO was doped with 5-10 wt% of CuO. The CuO doping enhanced the density of the MCO coating in addition to slight improvement in the electrical properties.

Cu was found to be highly effective in reaching higher density of the MnCo doped coatings; in the view of reaching lower rates of Cr evaporation from the steel, this result looks to be very interesting and promising.

However, it is not possible to absolutely define the optimal coating solution, since it depends on coating method and sintering procedure, costs, environmental issues etc; research findings reported in this thesis provide new insights for future coating development. By properly balancing the microstructural, thermomechanical and electrical properties of Cu (or other doped element) spinels by EPD co-deposition it will be possible to further optimize MnCo coatings or to substitute Co, due to critical environmental issue, to obtain proper functional requirements.

Furthermore, controlling and understanding the evolution of the oxide scale-spinel coating interface will provide useful tools to further improve SOC durability and performance issues.

Dissemination of the Results

- 2019, In-situ Cu-doped MnCo-spinel coatings for solid oxide cell interconnects processed by electrophoretic deposition, Sabato, Antonio Gianfranco; Sebastian, Molin; **Javed, Hassan**; Zanchi, Elisa; Boccaccini, Aldo Roberto; Smeacetto, Federico. Journal of Ceramic International. (Accepted)

- 2019, Shear performance at room and high temperatures of glass-ceramic sealants for solid oxide electrolysis cell technology, **Javed, Hassan**; Sabato, Antonio Gianfranco; Dlouhy, Ivo; Halasova, Martina; Bernardo, Enrico; Salvo, Milena; Herbrig, Kai; Walter, Christian; Smeacetto, Federico. *Materials* 12, 298. doi: org/10.3390/ma12020298.

- 2018, Design and characterization of novel glass-ceramic sealants for solid oxide electrolysis cell (SOEC) applications, **Javed, Hassan**; Sabato, Antonio Gianfranco; Herbrig, Kai; Ferrero, Domenico; Walter, Christian; Salvo, Milena; Smeacetto, Federico. International Journal of Applied Ceramic Technology. 15, 999–1010. doi:10.1111/ijac.12889.

- 2018, Novel glass-ceramic SOFC sealants from glass powders and a reactive silicone binder, Elsayed, Hamada; **Javed, Hassan**; Sabato, Antonio Gianfranco; Smeacetto, Federico; Bernardo, Enrico. Journal of European Ceramic Society. 38, 4245-4251. doi.org/10.1016/j.jeurceramsoc.2018.05.024

- 2018, Co-deposition of CuO and $Mn_{1.5}Co_{1.5}O_4$ powders on Crofer22APU by electrophoretic method: Structural, compositional modifications and corrosion properties, Sebastian, Molin; Sabato, Antonio Gianfranco; **Javed, Hassan**; Grzegorz, Cempura; Boccaccini, Aldo Roberto; Smeacetto, Federico. Materials Letters. 218, 329–333. doi:10.1016/j.matlet.2018.02.037.

- 2017, Poster Presentation: "New Glass-Ceramic Sealants for SOEC Applications" **Javed, Hassan**; Sabato, Antonio Gianfranco; Herbrig, Kai, Walter, Christian; Salvo, Milena; Smeacetto, Federico. Euromat Conference (Thessaloniki, Greece).

Secondments and Trainings

- The electrical properties of the glass-ceramics were measured at **Sunfire GmbH, Dresden Germany, 2nd May – 28th June 2016.**

- The 5th Stanislaw Gorczyca European School on Electron Microscopy and Electron Tomography was attended at **AGH University of science and technology, Krakow, Poland, 4th -9th July 2016.**

- The mechanical properties of glass-ceramics at room temperature and high temperature were analysed at Institute of **Physics of Materials (IPM), Brno Czech Republic, 1st – 31st March 2017.**

- Electrophoratic deposition of ceramics based coatings on the Crofer22APU interconnects was performed at **Institute of Biomaterials, Univeristy of Erlangen, Germany, 1st -28th April 2017.**

- The XRD characterizations of the glass-ceramics was carried out at **Università degli studi di Padova, Padova, Italy, 12th – 14th December 2017.**

- The glass paste development was carried out at **Sunfire GmbH, Dresden Germany, 11th March – 2nd May 2018** and **29th July – 24th August 2018.**

- The flash sintering of the ceramic coatings was carried out at Nanoforce Ldt, **Queen Mary University of London, UK, 27th August – 14th September 2018.**